buildings

Special Issue Reprint

Advances and Applications in Timber Structures

Edited by
Zeli Que

mdpi.com/journal/buildings

MDPI

Advances and Applications in Timber Structures

Advances and Applications in Timber Structures

Guest Editor

Zeli Que

MDPI

Basel • Beijing • Wuhan • Barcelona • Belgrade • Novi Sad • Cluj • Manchester

Guest Editor
Zeli Que
College of Materials Science
and Engineering
Nanjing Forestry University
Nanjing
China

Editorial Office
MDPI AG
Grosspeteranlage 5
4052 Basel, Switzerland

This is a reprint of the Special Issue, published open access by the journal *Buildings* (ISSN 2075-5309), freely accessible at: https://www.mdpi.com/journal/buildings/special_issues/0A7364TJ7U.

For citation purposes, cite each article independently as indicated on the article page online and as indicated below:

Lastname, A.A.; Lastname, B.B. Article Title. *Journal Name* **Year**, *Volume Number*, Page Range.

ISBN 978-3-7258-5927-6 (Hbk)
ISBN 978-3-7258-5928-3 (PDF)
https://doi.org/10.3390/books978-3-7258-5928-3

Contents

buildings

MDPI

Article

Analysis of Mechanical Properties of Four-Section Composite Columns of *Pinus sylvestris* var. *Mongolia* of Ancient Wooden Architecture under Axial Compression Load

Sheng Peng *, Yifan Qiao and Yang Song *

School of Urban Construction, Wuhan University of Science and Technology, Wuhan 430065, China
* Correspondence: pe_sh@sina.com (S.P.); songyang0506@wust.edu.cn (Y.S.)

Abstract: In order to study the influence of the cross-sectional area of hidden dovetail mortise (cross-sectional area of the projecting part after dovetail installation is completed) and length of tenon joint dimensions (axial length with dovetail installation completed) on the axial compressive behavior of four-section composite columns, the length of tenon joint dimensions was set to 30 mm, 60 mm, and 90 mm, and the cross-sectional area of hidden dovetail mortise was set to 360 mm^2, 562 mm^2 and 810 mm^2 as experimental variables. Some column models were designed and fabricated accordingly. Axial compression tests were conducted to observe failure modes, load–displacement curves, stress–strain curves, load–strain curves, ultimate bearing capacity, and stiffness of the timber column. The results of the study show that the influence of dark drum mortise and tenon cross-section size and tenon length on the axial compressive mechanical properties of four-section jointed wood columns should not be ignored; the load-carrying capacity of the wood columns decreases with the increase in tenon cross-section size and decreases with the decrease in tenon length; the stability decreases with the increase in tenon cross-section size; and the deformability of specimens of the tenon length group as a whole is obviously superior to the tenon cross-section area group. The increase in ultimate load-carrying capacity of the columns was 7–11.9% when the concealed cross-sectional area of the hidden dovetail mortise was reduced in the range of 30.5–55.5%. When the length of the tenon joint dimensions was reduced from 90 mm to 60 mm, its ultimate bearing capacity decreased by 9%; when it was reduced from 60 mm to 30 mm, its ultimate bearing capacity was almost unchanged, which indicated that after the length of tenon joint dimensions was lower than 60 mm, the influence on the ultimate bearing capacity of the column was more negligible. It is recommended that the length of tenon joint dimensions of 60 mm should be taken as the design standard value of the ultimate bearing capacity for the four-sectioned composite columns of the *Pinus sylvestris* var. *Mongolia (PSVM)*.

Keywords: four-section composite column; *Pinus sylvestris* var. *Mongolica (PSVM)*; hidden dovetail mortise; tenon joint dimensions; axial compressive mechanical properties

1. Introduction

Ancient wooden architecture is widely used throughout China due to its excellent mechanical and material properties. Due to its natural and low-carbon nature, wood is one of the future popular materials for civil engineering [1]. The unique mechanical properties of wood enable it to meet the requirements of modern structures in terms of seismic resistance, light weight, and large spans. Wood columns, as extremely important components of wooden structures, play a role in supporting the upper structure of wooden buildings and transmitting forces within the structure [2,3]. In addition to the complete wooden column, the wooden column can also be spliced into a column as a load-bearing member through different combinations, such as forming a glued wood column by bonding many wood laminates with structural adhesives, modifying the wooden column with a rigid sheath splice joint, and connecting the sections of the column through mortise and

tenon joints [4–6]. The four-section combined column is a unique type of ancient wooden structure where small pieces are connected and assembled into larger pieces through a mortise and tenon structure. As shown in Figure 1, the Ningbo Baoguo Temple Hall is an important example of this structure [7]. The building in the centre of the four small columns and embedded in the outside of the four auxiliary petals of small materials forms the eight petals of the Guarang column. The centre of the four small columns bears the load and is embedded in the outside of the four decorative petals. Overall, the structure has eight pieces in four columns. It has undergone several repairs due to long-term corrosion [8]. Segmental columns, due to their unique structural configuration, are connected to the superstructure (e.g., beams, slabs, etc.) by mortise and tenon joints, which are designed to ensure a solid bond between the columns and the other components in order to support the stability and load-bearing capacity of the overall building structure. The four-section composite column of *Pinus sylvestris* var. *mongolica (PSVM)* is widely used in ancient wooden buildings, mainly due to its excellent mechanical properties. The wood of *PSVM* has high bending and compressive strength, and its texture is straight and tough, which makes the four-section composite column composed of it perform well when bearing loads. *PSVM* is widely used in construction because of its moderate density and strength, its ability to provide good durability under the right conditions, and its ease of processing and handling, making it suitable for making use in various shapes and sizes [9]. In addition, the design of the four-section composite column also fully considers the mechanical properties of wood. Through reasonable splicing methods, it not only enhances the overall stability of the column but also effectively disperses stress concentration, thereby improving the load-bearing capacity and seismic performance of the entire building. Although there have been some studies on the mechanical properties of the four-section composite column of *PSVM*, there is still a lack of in-depth discussion on its specific mechanical characteristics and laws under axial compressive load. Axial compressive load is a common stress state in the practical use of wooden columns in ancient buildings, which has a crucial impact on the stability and load-bearing capacity of wooden columns [10–12]. Therefore, research on the mechanical properties and failure mechanisms of four-section composite wooden columns is of great significance for the protection and repair of ancient wooden architectural structures.

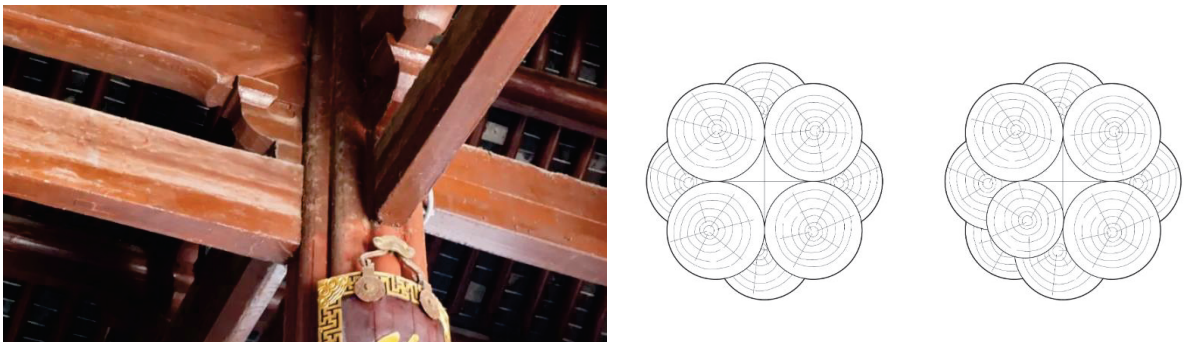

Figure 1. Collocated columns in ancient buildings.

Currently, domestic and international scholars have conducted numerous studies on the mechanical properties of wooden columns and established design formulas for the ultimate limit state of composite columns [13–18]. Malhotra et al. [19] described the development of reliability-based design formulas for the ultimate limit state of mechanically connected composite wooden columns, predicting and analyzing their mechanical properties. Song et al. [20] conducted material performance tests and biaxial eccentric compression tests on wooden columns. Theiler et al. [21] proposed a bearing capacity analysis model considering the strain of wooden columns and studied the degradation performance of wood and repair methods for damaged wooden columns. Li et al. [22] conducted axial compression tests on four wooden columns with different damages and

proposed a degradation model that can accurately predict the compressive strength of locally damaged wooden columns. Zhou et al. [23] conducted composite reinforcement on wooden columns, analyzed the mechanical properties of wooden columns with different reinforcement sections, and established a calculation model for the axial compressive bearing capacity of composite reinforced wooden columns. Wei et al. [24] studied the mechanical properties of orthogonal laminated wooden columns and laminated veneer lumber columns and established a stress–strain model for wooden columns. Research on the mechanical properties of log wooden columns and glued laminated wood columns under axial pressure is relatively mature, providing theoretical premises and experimental methods for the study of the mechanical properties of four-section composite wooden columns under axial pressure. Four-section composite wooden columns are commonly used in ancient wooden architectural structures, and the use of concealed mortise and tenon joints and wedges has typical historical and cultural characteristics, which are quite different from the force transmission mechanisms of modern wooden structures.

In order to reveal the force transmission mechanism and failure mechanism of the four-section composite wooden column, the classic four-section composite wooden column in the ancient wooden building structure system was selected as the object. Considering the influence of concealed mortise and tenon joints and the use of wedges, a series of axial pressure performance tests were carried out on the four-section composite wooden column. The test failure phenomena, load–longitudinal displacement curve, stress–strain curve, load–strain curve, bearing capacity, and stiffness changes were analyzed in detail, aiming to provide a theoretical basis and experimental basis for the design of this kind of ancient wooden building structure.

2. Test Design

2.1. Materials

The column body and mortise-and-tenon connectors of the four-section composite column were made of *PSVM* wood [25], which has high compressive and tensile strengths, medium density and moderate hardness, which gives it good workability and strength in the production of building structures. It has good corrosion resistance under dry conditions and is able to resist fungi and insects to some extent, and their elastic engineering constants are shown in Table 1. The moisture content and density of the wood are 10.3% and 0.46 g/cm^3, respectively.

Table 1. Elastic engineering constants of *PSVM*.

E_L/ MPa	E_R/ MPa	E_T/ MPa	M_{LR}	M_{LT}	M_{RT}	G_{LR}/ MPa	G_{LT}/ MPa	G_{RT}/ MPa
10562.4	563.4	796.5	0.3	0.35	0.51	706.4	706.4	191.8

Note: L. parallel to the grain direction; R. transverse to the grain direction; T. transverse to the chord direction; LR. radial section; LT. tangential section; RT. transverse section; E. elastic modulus; M. Poisson's ratio; G. shear elasticity.

2.2. Specimen Preparation

The four-section composite column was a method of constructing wooden columns in ancient architecture, where the column was not a single piece of raw wood but rather a structure made up of multiple pieces of wood connected by mortise and tenon joints. The concealed drum tenon was a tenon component inserted into a concealed drum mortise used to connect different structures. A full or half-hidden tenon, where the tenon head is not exposed, was called a concealed tenon. The wedge was a wooden block used to secure the concealed drum mortise and fit into the concealed drum mortise hole.

In order to study the impact of the cross-sectional dimensions of the concealed mortise and the size of the wedge on the mechanical properties of a four-section composite column under axial compression, this experiment designed five groups of test specimens. The dimensions of the corresponding components were determined with reference to the "Con-

struction Methodology" for the four-section composite column mortise and the "Standard for design of timber structures" [26]. The dimensions of the test specimens were all 360 mm in length and 90 mm in circular cross-sectional radius. Tenon lengths and mortise areas are set with reference to the ranges specified in the *Construction Method Style* and historical ancient timber building practices. The specific dimensions of the concealed mortise and the wedge are shown in Table 2.

Table 2. Specimen size design.

Specimens No.		Length of Upper and Lower Surfaces/mm	Length of the Lower Base/mm	Thickness /mm	Length of Tenon Joint/mm
A1	a	16	20	20	90
	b	16	20	20	90
	c	16	20	20	90
A2	a	20	25	25	90
	b	20	25	25	90
	c	20	25	25	90
A3	a	24	30	30	90
	b	24	30	30	90
	c	24	30	30	90
A4	a	24	30	30	60
	b	24	30	30	60
	c	24	30	30	60
A5	a	24	30	30	30
	b	24	30	30	30
	c	24	30	30	30

The specimen was composed of four smaller pieces of wood that were fitted together to match the dimensions of each tenon and mortise. The concealed tenon was inserted into the concealed mortise and moved up to the slot, followed by the insertion of a wedge to secure the concealed tenon. Then, the column was assembled. Figure 2 is a schematic diagram of the internal structure of a single piece of wood in the specimen. After all the above-mentioned test pieces were processed, the assembly of the test pieces was completed in the order of installing concealed mortise and tenon, wedging, and jointing the columns.

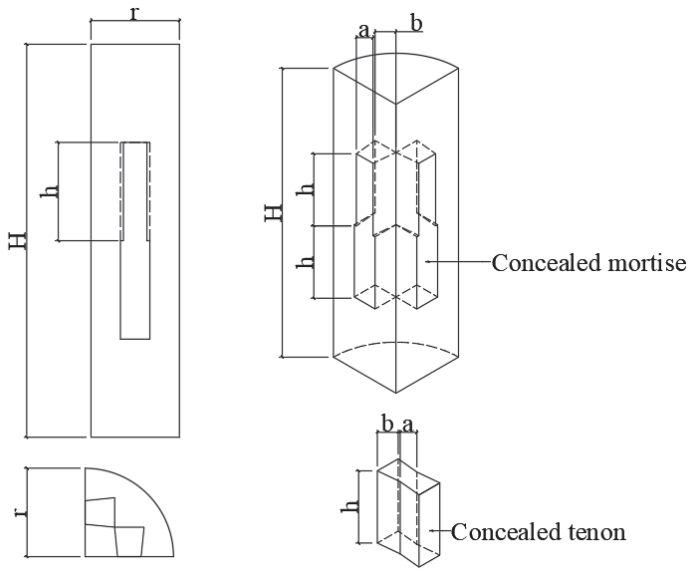

Figure 2. Internal construction of typical specimens.

2.3. Testing Procedures

The loading device used for the axial pressure test was an electro-hydraulic servo universal machine. The top of the specimen was connected to a ball joint through a loading plate, and the bottom was supported on a reaction base. The entire loading process can be viewed as one end being hinged and the other end being fixed.

In this experiment, resistance strain gauges were used to measure the lateral and longitudinal strains in the four-section composite column. One set of longitudinal and lateral strain gauges was placed at the centre of each side of the column. One lateral strain gauge was placed at a distance of 50 mm from the top of the column on the side where the wedge was installed for a total of 10 gauges. Electronic displacement meters were used to measure the lateral displacement in the column of the test specimen. One displacement meter was placed in the column on one of the adjacent surfaces of the test specimen, for a total of two meters. Figure 3 is a schematic diagram of the test setup.

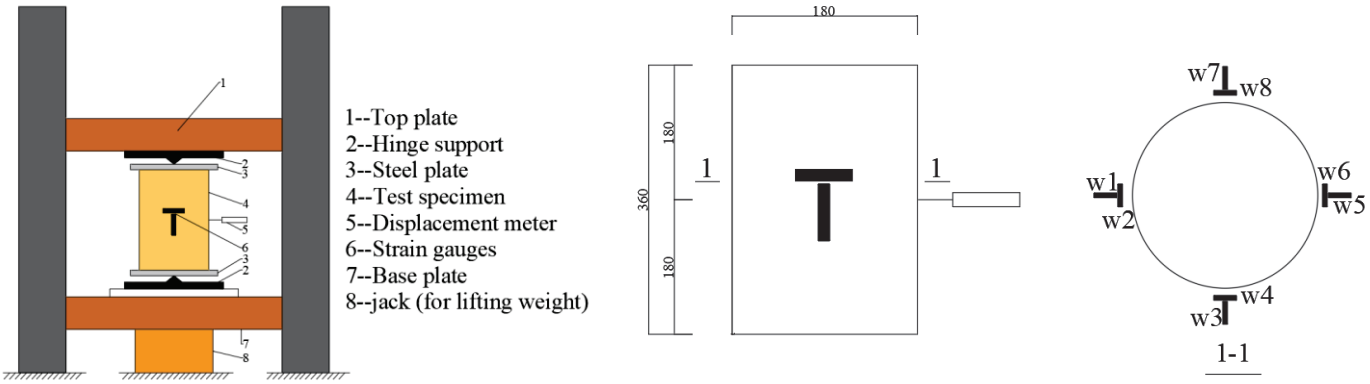

Figure 3. Test setup.

Before formal loading, the universal machine and the loading specimen were geometrically and physically aligned to ensure that the pressure application position of the universal machine was aligned with the axial pressure position of the specimen. Referring to the "Standard for Test Methods of Timber Structures" [27], the specimen is preloaded before formal loading. The test loading method and rate are selected according to the provisions of the "Standard for Test Methods of Timber Structures" [27]. Displacement loading was used for formal loading, with a loading speed of 1 mm/min. Uniform loading is applied throughout the process. When the bearing capacity of the specimen decreased to 80% of the ultimate bearing capacity, it was considered to be damaged and the test was terminated. During the formal loading of the specimen, the longitudinal and transverse strain values in the column were read at intervals of 10 s, and the load–axial displacement curve, stress–strain curve, and load–strain curve were drawn.

3. Analysis of Test Results

3.1. Experimental Phenomena

At the beginning of the specimen loading, there was no obvious experimental phenomenon. As the test load gradually increased, the longitudinal and transverse deformations of the specimen continuously increased, and longitudinal cracks and transverse wrinkles appeared on the surface of the specimen. When the test load was loaded to about 60% of the ultimate bearing capacity, the specimen began to produce a wood fiber extrusion sound. When the load reached its peak, the sound produced by the specimen was very obvious and uninterrupted, and the longitudinal cracks on the surface of the specimen continued to extend. As the bearing capacity of the specimen decreased, the transverse deformation and longitudinal cracks in the concealed bulge area became more obvious, and the middle part of the column showed outward bulging with large transverse displacement.

The knots experienced significant dislocation and outward bulging, and cracks appeared around the knots, while the surrounding wood was crushed and damaged.

3.2. Failure Modes

The failure modes of the test specimens in all groups mainly manifest as four types: lateral crushing failure (represented by rectangles), longitudinal cracking failure (represented by ellipses), diagonal shear failure (represented by circles), and local shear failure at the knots (represented by triangles), as shown in Figure 4. Longitudinal and lateral cracks and wrinkles on the surface of the wooden column are concentrated in the middle of the column, with more wood crushing occurring at the lower part of the column. For the specimens with a longer mortise, lateral wrinkles appear around the mortise tenon, and obvious longitudinal cracks appear inside the mortise, with the cracks being longer and almost penetrating the entire mortise, as shown in Figure 4c; this is because a large length of tenon length leads to a large vacancy inside the wooden post, and a large hazardous damaged area in the middle of the wooden post, and when a crack appears in the hazardous cross-section, the crack will develop rapidly in the hazardous area along the axial direction and ultimately form a crack through the mortise hole. For the specimens with a shorter mortise, the mortise tenon experiences greater compressive stress, resulting in obvious cracks accompanied by multiple lateral wrinkles around the mortise and crushing failure occurring at the mortise, with no obvious cracks. As shown in Figure 4d, this is due to the small length of the tenon length, the core stress area being small, and the tensile and compressive stresses being mainly concentrated in the mortise and tenon joints, causing cracks around the tenon and mortise holes. Under the action of the test load, the wooden column undergoes vertical compression and lateral deformation. The mortise in the column limits the lateral deformation inside the column, causing the longitudinal cracks to first appear in the middle of the outer surface of the column, gradually developing towards the inside of the column. As the test load increases, the tensile stress on the mortise continuously increases, and the longitudinal cracks on the surface of the column develop along the grain direction of the column, extending to the mortise area, eventually penetrating the middle of the column and developing to the lateral wrinkles at the upper and lower parts of the column. Diagonal cracks are concentrated near the knots. As the vertical load continues to increase, stress concentration occurs near the knots, resulting in local shear failure. The crack width further increases and the length continues to extend. Under the action of shear stresses in all directions, diagonal cracks and longitudinal cracks are produced.

3.3. Load–Displacement Behavior

The load–displacement curves of the test specimens in each group are shown in Figure 5, and the trends of the curves are basically consistent. The test specimens undergo three stages under axial pressure: elastic stage, elastic–plastic stage, and plastic stage. In the elastic stage, due to the influence of material properties and initial defects, the relationship between axial displacement and load of the wooden column shows a strong nonlinear relationship, followed by a linear relationship. The test specimens are in the elastic stage from the beginning of loading to the proportional limit load, which is defined in this article as 70% of the ultimate load; the second stage is the elastic–plastic stage, i.e., the load of the test specimens increases from the proportional limit load to the ultimate load. The curve has a small nonlinear stage before reaching the peak load, which is due to the wood fibers on the compression side of the test specimens reaching the yield stress. The load of the test specimens slowly increases between the proportional limit load and the ultimate load, and the displacement development is relatively slow in this stage; the third stage is the plastic stage, where the load of the test specimens increases from the ultimate load to the failure of the test specimens. After the load reaches the ultimate load, as the axial displacement continues to increase, the bearing capacity of the test specimens shows a significant downward trend, which is due to local compression buckling, shear failure, and cracking phenomena in the central region of the wooden column. The compressed wood

fibers are crushed, and the tensile wood fibers break. From the curves, it can be seen that the change in tenon cross-sectional area has a greater effect on the ultimate load capacity of the wooden columns, the performance of the wooden columns with large tenon cross-sectional area is optimal, and the reduction in tenon length makes the ultimate load capacity of the wooden columns decrease. In the mortise cross-sectional area group, the A2 specimen has the smallest axial damage displacement, and its deformation capacity is poorer than that of the remaining two groups, and the A1 specimen has the best deformation capacity and load-bearing capacity; in the mortise length group, the A3 specimen has the best load-bearing capacity, and the A3 specimen has the best deformation capacity. Overall, the deformation capacity of the tenon length group is better than that of the tenon area group, while the load-bearing capacity is insufficient. The peak load and failure displacement of each test specimen are shown in Table 3, and the axial stiffness and ductility coefficient of the test specimens are shown in Table 4 which will be further analyzed in Section 4.

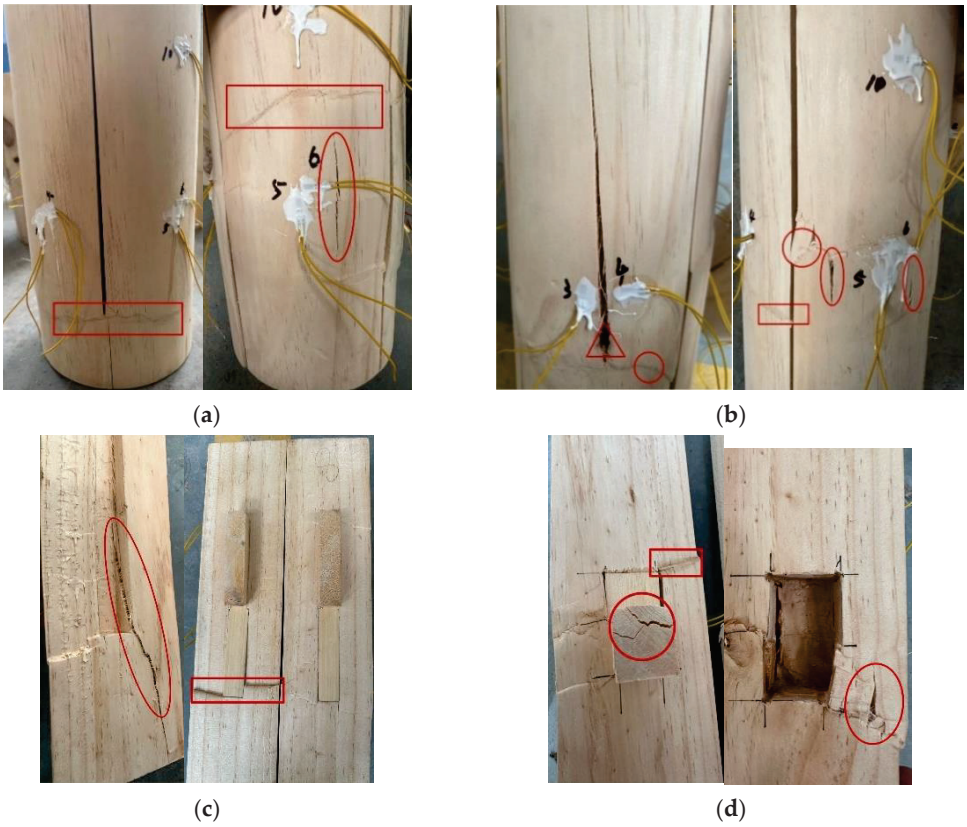

(**a**) (**b**) (**c**) (**d**)

Figure 4. Failure mode of specimens. (**a**,**b**) Cracks on the surface of the specimens and (**c**,**d**) cracks within the specimens.

Table 3. Axial pressure test results.

Specimens No.	*L*/mm	Δ_u/mm	P_u/kN	Failure Mode
A1-a/b/c	360	13.74	388.85	Strength failure
A2-a/b/c	360	12.82	372.9	Strength failure
A3-a/b/c	360	12.17	347.5	Strength failure
A4-a/b/c	360	15.05	316.1	Strength failure
A5-a/b/c	360	12.35	310.8	Strength failure

Note: Δ_u is the axial displacement corresponding to the load of the test piece falling to 80% of the ultimate load; P_u is the average ultimate bearing capacity of the test specimen.

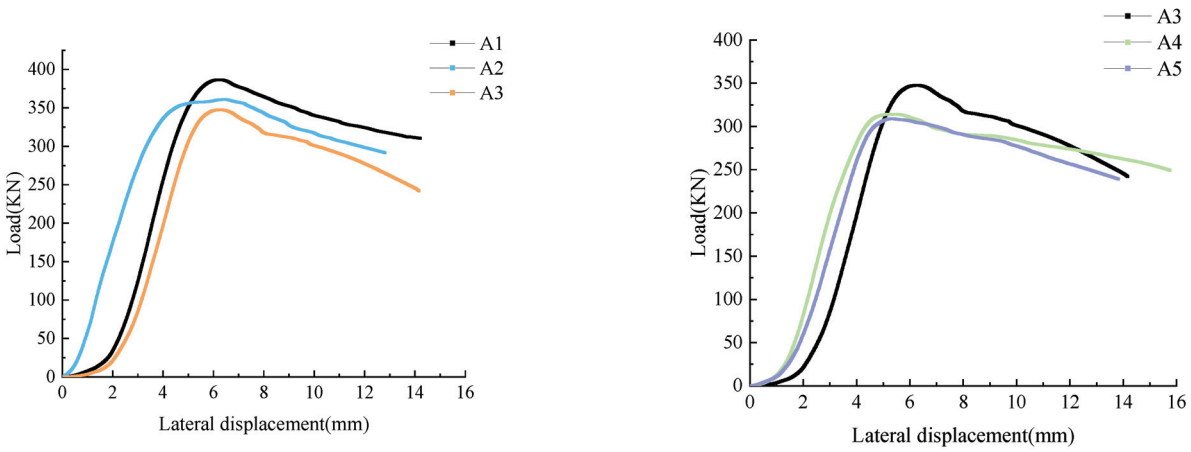

(**a**) (**b**)

Figure 5. Load–longitudinal displacement curves. (**a**) Load-displacement curve for the mortise cross-sectional area group and (**b**) Load-displacement curve for the tenon length group.

Table 4. Characteristic parameters of axial compression of four-section composite columns.

Spcimen No.	Ultimate Compressive Stress σ_{cu}/Mpa	Ultimate Strain $\varepsilon_{cu}/10^{-6}$	Proportional Limit Stress σ_{ce}/Mpa	Proportional Limit Strain $\varepsilon_{ce}/10^{-6}$	Failure Stress σ_{cf}/Mpa	Failure Strain $\varepsilon_{cf}/10^{-6}$	Initial Axial Stiffness *K*/(KN/mm)	Variation Coefficient of Initial Axial Stiffness CoV/%
A1-a	16.08	1825	11.26	1202.78	12.86	3815.56	107.63	
A1-b	15.03	1586.94	10.52	1082.22	12.1	3815.56	121.98	8.84
A1-c	15.02	1587	11.02	1084.54	12.55	3815.55	112.87	
A2-a	15.43	1836.39	10.8	981.39	12.34	3560.56	101.9	
A2-b	14.41	1101.94	10.01	560.83	11.52	3255	139.88	23.87
A2-c	14.55	1454.22	10.4	812.01	11.66	3335.2	129.56	
A3-a	12.80	1738.33	8.96	1087.78	10.24	2921.39	97.53	
A3-b	15.02	1732.50	10.52	1289.72	12.32	3815.56	123.93	16.86
A3-c	13.88	1735.42	9.58	1188.68	11.56	3541.26	112.86	
A4-a	13.19	1556.11	9.23	841.11	10.55	4180.28	130.57	
A4-b	12.1	1396.11	8.47	981.39	9.68	4376.39	92.23	24.31
A4-c	12.5	1486.52	8.88	912.08	9.85	4256.21	118.54	
A5-a	11.44	1272.78	8.08	869.17	9.15	3840.83	92.26	
A5-b	13.45	1480.28	9.42	1076.67	10.76	3431.67	98.02	4.28
A5-c	13.02	1345.20	9.12	956.42	10.22	3654.75	95.55	

3.4. Stress–Strain Behavior

Assuming that the tensile strain and compressive strain of the specimen are positive and negative, respectively, when the load reaches the ultimate bearing capacity of the specimen, some strain gauges stop working, and the load–strain curve given is a rising curve. The load–strain curves of each specimen are shown in Figure 6. From the curve, it can be seen that the changing trend of axial strain and transverse strain during the axial compression process of each group of specimens is basically the same, with obvious plastic deformation. At the beginning of loading, the load–strain curve is basically a straight line, indicating that the specimen was in the elastic stage. As the load continues to increase, the curve shows a nonlinear growth, which is due to the uneven distribution of micro-defects such as knots in the specimen. The specimen enters the plastic working stage, and the internal mortise and tenon structure constrains the lateral deformation of the specimen, while obvious local compressive buckling failure occurs. After reaching the peak load,

the axial strain increases rapidly, and the dangerous section reaches the ultimate strain, resulting in the destruction of the specimen.

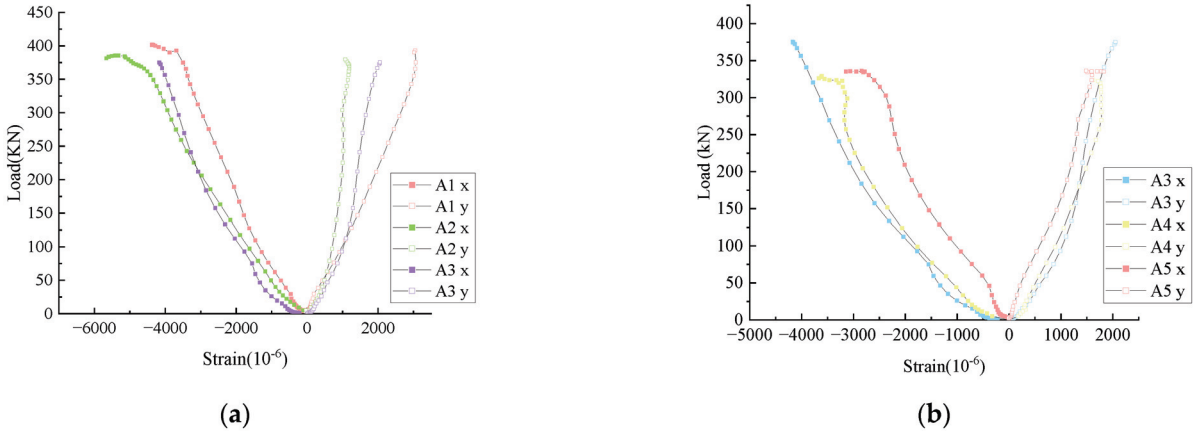

(**a**) (**b**)

Figure 6. Load–strain curves. (**a**) Load-strain curve of tenon cross-sectional area group and (**b**) Load strain curve of tenon length group.

In the group of tenon lengths, the variation in tenon length has a significant impact on the tensile and compressive strain. Comparing the same conditions in Figure 6b, the maximum compressive strain at the measuring point of the wooden column increases with the increase in tenon length. This is due to the increase in tenon length, which leads to an increase in the compression zone of the wooden column. The strain in the compression zone reaches the ultimate compressive strain of the wood, causing the specimen to fail. In addition, the increase in tenon length increases the cross-sectional area of the wooden column in the non-mortise area, strengthening the lateral constraint effect of the fibers and thereby reducing the lateral deformation of the wooden column.

4. Quantitative Analysis

4.1. Ultimate Bearing Capacity

To minimize the interference of initial defects in the wooden columns with the bearing capacity results, the ultimate stress σ_u is used to normalize the bearing capacity results of the test specimens. The ultimate stress σ_u is calculated using the formula $\sigma_u = P_u/A$, where P_u is the average peak load of the specimen and A is the original cross-sectional area of the column. The impact of the cross-sectional area of the tenon on the bearing capacity of the four-section composite column is quantified using the change ratio of ultimate stress (ζ). The change ratio of ultimate stress (ζ) is the ratio of the ultimate stress of the four-section composite column to that of specimen A3. The ultimate bearing capacity data for each specimen can be found in Table 4.

From Tables 3 and 4, it can be seen that the change in the cross-sectional area of the concealed tenon has a significant impact on the load-bearing capacity of the wooden column. As the cross-sectional area of the concealed tenon decreases, the ultimate bearing capacity of the specimen increases, with an increase of 7.3% to 11.9%. Compared with specimen A3, specimen A1 has a 55.5% reduction in the cross-sectional area of the concealed tenon, and the ultimate bearing capacity of the specimen increases by 11.9%. Compared to specimen A3, specimen A2 had a 30.5% reduction in the cross-sectional area of the mortise, resulting in a 7% increase in the ultimate bearing capacity. Compared to specimen A3, specimen A4 had a 30 mm reduction in the length of the mortise, resulting in a 9% decrease in the bearing capacity. Compared to specimen A4, specimen A5 had a 30 mm reduction in the length of the mortise, with no significant change in the ultimate bearing capacity. This indicates that the length of the mortise has an impact on the ultimate bearing capacity of the specimen within a certain range, with the ultimate bearing capacity increasing as the length of the mortise increases. Specimen A1 showed the best load-carrying capacity among all

the specimens, which may be due to the fact that specimen A1 had the smallest tongue and groove cross-sectional area, which made the cross-sectional area of the hazardous damage section the largest, and the tensile stress required for the fracture of the wood fibers in the vicinity of the hazardous damage section was greater. Figure 7 shows the relationship curve between the change ratio of ultimate stress and the ratio of mortise area for the group with varying mortise cross-sectional area. The curve indicates that the change ratio of ultimate strain for the four-section composite column decreases quadratically with the increase in the ratio of mortise area. As shown in Equation (1), the attenuation pattern of the bearing capacity of the specimens in this experiment with the ratio of mortise area can be expressed as:

$$\zeta = 2.54 \times 10^5 A^2 - 0.00582A + 1.2 \quad (1)$$

where ζ is the limit strain change ratio, and A is the ratio of the cross-sectional area of the tenon.

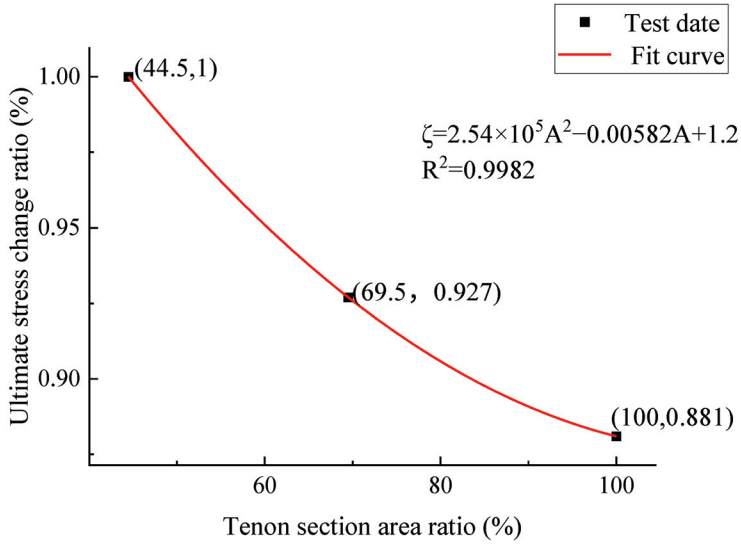

Figure 7. Relation curve of the tenon section area group and tenon section area ratio.

The change in tenon length has a minor impact on the ultimate stress of the specimens, and the ultimate stress of the specimens in the tenon length group is relatively similar. This may be because the change in tenon length does not alter the critical section of the wooden column, but only changes the lateral stiffness of the specimens. Similar results were obtained by Cheng [28], where the change in tenon length did not have a significant effect on the load-carrying capacity of the timber post.

4.2. Stiffness and Stability Coefficient

To compare the axial stiffness of the test specimens during the elastic phase, the initial nonlinear phase of the load–displacement curve is ignored to avoid its influence [29]. The initial axial stiffness K of the specimens is represented by the slope of the load–displacement curve from 20% to 40% of the peak load. The initial axial stiffness data of each specimen is shown in Table 5.

Table 5. Stabilization coefficients and related parameters.

Spciemens No.	$I_p/10^6$ mm^4	A_p/mm^2	i_p/mm	λ_p	φ
A1	50.4166	23846.9	45.98	7.829	0.985
A2	49.8841	22946.9	46.625	7.721	0.986
A3	49.2349	21846.9	47.472	7.583	0.965

From Table 4, it can be seen that the increase in the mortise cross-sectional area caused the axial stiffness of the wooden columns to first increase and then decrease with the decrease in the mortise length, with an overall decreasing trend, and the axial stiffness of the specimens in the mortise cross-sectional area group was significantly larger than that of the mortise length group. This may be due to the fact that the tenon lengths of the specimens in the tenon cross-sectional area group are all larger than those in the tenon length group, and the core region of the wood column is larger, which has better overall stability and thus exhibits greater stiffness. The specimens with larger knots in the column exhibited lower stiffness, resulting in an increase in the CoV value of the axial stiffness of the specimens.

For the four-section spliced wooden column, the mortise-and-tenon connection creates gaps inside the column, which changes the slenderness ratio of the column. The change in slenderness ratio leads to a change in the stability coefficient of the column, which in turn affects the bearing capacity of the column ($N \leq \varphi A_0 f_c$; this formula is used to calculate the bearing capacity of axial compression members during stability verification). The slenderness ratio of the specimen can be expressed as [26]:

$$\lambda = \frac{l_0}{i} \tag{2}$$

where l_0 (=kl; k is the length calculation coefficient, the hinge connection k at both ends of the specimen is taken as 1.0 and l is the actual length of the specimen) is the calculated length of the specimen, and i is the radius of gyration of the complete specimen section.

The slenderness ratio of a specimen with a notch in the same cross-section can be expressed as:

$$\lambda_p = \frac{l_0}{i_p} \tag{3}$$

where i_p is the radius of gyration of the four-segment combined column cross-section, $i_p = \sqrt{I_p / A_p}$. I_p represents the sectional moment of inertia of the four-section composite column, and A_p represents the net sectional area of the four-section composite column.

Figure 8 is a schematic diagram of the cross-section of a four-section composite wooden column. According to the calculation principle of sectional moment of inertia, the moment of inertia of the wooden column section can be calculated as:

$$I_p = \frac{\pi D^4}{64} - \frac{2\left(bt^3 + b^3 t\right)}{3} - \frac{R^2 bt}{2} + Rtb^2 \tag{4}$$

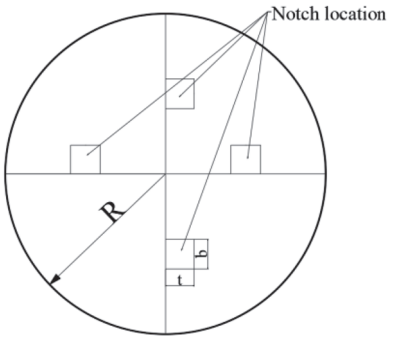

Figure 8. Schematic cross-section of a four-section composite wooden column.

The net cross-section of the wooden column can be obtained from Equation (5):

$$A_n = \pi R^2 - 4bt \tag{5}$$

According to the specification [26], the stability coefficient of the wooden column is defined as:

$$\varphi = \begin{cases} \left(1 + \frac{\lambda^2 f_{ck}}{b_c \pi^2 E_k}\right)^{-1}, \lambda \le \lambda_c \\ \frac{a_c \pi^2 E_k}{\lambda^2 f_{ck}} \quad , \lambda > \lambda_c \end{cases} \tag{6}$$

The wood used in this experiment is all scotch pine wood. According to the specifications [14], the relevant coefficients are taken as α_c = 0.95, b_c = 1.43, c_c = 5.28, β = 1.0, E_k/f_{ck} = 300, where $\lambda_c = c_c\sqrt{\beta E_k/f_{ck}} = 91.45$. The slenderness ratio of the test piece is less than 91.45, and the stability coefficient of the test piece can be calculated using the first calculation formula in Equation (6). The stability coefficient and related parameter calculation results of the test piece are shown in Table 5. From the table, it can be seen that when the length of the tenon is the same, the change in the cross-sectional area of the tenon has a small impact on the stability coefficient of the test piece, and the overall trend is decreasing. This indicates that when the length and slenderness ratio of the wooden column is small, the change in tenon dimensions does not have a large impact on the overall stability of the wooden column, and thus the specimens are all strength-damaged. At the same time, the tenon cross-sectional area of specimens 3, 4 and 5 did not change, and the length of the tenon did not lead to a change in the cross-sectional area of the specimen, so the calculation of the length and slenderness ratio and stability coefficient of specimen 3 were analyzed.

4.3. Ductility

Displacement ductility is an important indicator for measuring the elastic–plastic deformation capacity of a component or structure. To measure the elastic–plastic deformation capacity of a wooden column, the displacement ductility factor (μ) is used for quantification, calculated according to the following formula:

$$\mu = \frac{\Delta_u}{\Delta_v} \tag{7}$$

where Δ_u and Δ_v represent the displacements corresponding to the failure load and yield load, respectively. In this paper, the equivalent elastic–plastic energy method (EEEP) [30] is used to calculate the ductility index of the wooden column, and the displacement when the load decreases to 80% of the ultimate load is taken as the failure displacement Δ_u. The yield displacement is obtained by Equations (8) and (9):

$$\Delta_v = \frac{P_v}{K} \tag{8}$$

$$P_v = K\left[\Delta_u - \sqrt{\Delta_u^2 - \frac{2w}{K}}\right] \tag{9}$$

where P_v is the yield load of the specimen, K is the initial axial stiffness, and w is the energy lost before failure (the area enclosed by the load–displacement curve before failure), as shown in Figure 9. The relevant calculation coefficients for each specimen are shown in Table 5.

As shown in Figure 10, the ductility index of each specimen is greater than 4. This is because compressed wood is a material with good ductility, and wood columns with lower bearing capacities exhibit better ductility [31,32]. The ductility coefficient of the specimens increases with the decrease in the tenon length. When the tenon length is less than 60 mm, the ductility coefficient increases sharply. When the tenon length decreases from 90 mm to 60 mm and 30 mm, the ductility coefficients of the wood columns increase by 35.4% and 23.77%, respectively, indicating that the decrease in the tenon length is very effective in improving the deformation capacity of the wood columns. The wood column with a tenon length of 60 mm has the best ductility performance, followed by the 30 mm

wood column, and the worst is the wood column with a tenon length of 90 mm. At the same time, the ductility coefficients of the wood columns in the tenon cross-sectional area group are all smaller than those in the tenon length group, indicating that the tenon length has a more significant impact on the deformation capacity of the wood columns. In the restoration of some historical buildings and in antique architecture, this component combines moderate load-bearing capacity with excellent deformation capacity and can be used to restore original structural features while effectively coping with deformation caused by earthquakes or other loads.

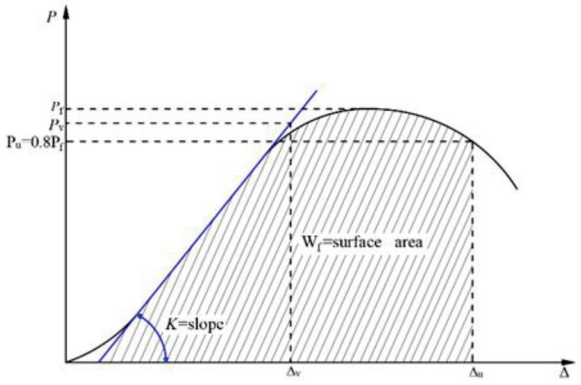

Figure 9. Schematic diagram for determining ductility index by equivalent elastic–plastic energy method (EEEP).

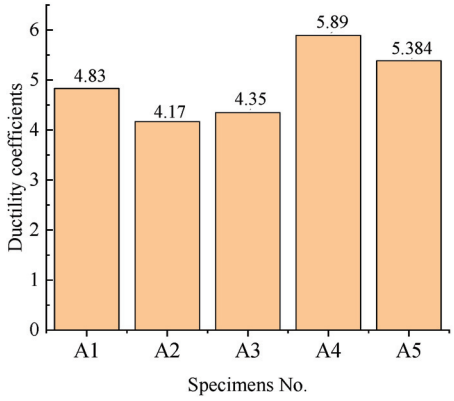

Figure 10. Ductility coefficients of specimens.

5. Conclusions

(1) When the length of the wooden column remains constant, changes in the cross-sectional size of the concealed mortise and the length of the wedge do not alter the failure mode of the specimen. The specimen mainly undergoes three working stages during axial compression: the elastic stage, the elastic–plastic stage, and the plastic stage.

(2) The tenon cross-sectional area has a significant effect on the load-carrying capacity, stiffness and ductility coefficients of the specimen and a relatively small effect on the stability coefficient. The ultimate load-carrying capacity decreases with increasing tenon cross-sectional area of the specimen and the ductility decreases with increasing tenon cross-sectional area. The ultimate load-carrying capacity of the specimens decreased by 7.3–11.9% for tenon cross-sectional area ratios of 44.5–100% compared to the specimens with the largest tenon cross-sectional areas. The axial stiffness of the specimen increases and then decreases with the increase in tenon cross-sectional area, which corresponds to the change rule of ductility. Stability coefficient with the increase in tenon cross-sectional area overall tendency to decrease.

(3) In addition, the length of the tenon also has an effect on the load-carrying capacity, stiffness and ductility of the specimen. The size of the tenon length has a more obvious effect on the ultimate load capacity of the specimen within a certain range. When the tenon length is reduced from 60 mm to 30 mm, the ultimate load capacity of the specimen does not change significantly, and 60 mm can be taken as the design standard value of the ultimate load capacity of the four-section joint column. At the same time, the ductility of the specimen is best when the tenon length is 60 mm, increasing the length of the tenon can effectively improve the load-bearing capacity and deformation capacity of the laminated timber columns.

(4) The current study was limited to sample data with a small sample size, which may affect the generalizability and statistical significance of the findings. Future studies try to increase the sample size and diversify the sources to verify the generalizability and reliability of the findings. Studies on ancient wood buildings should consider more carefully the effects of environmental conditions on material properties, such as humidity changes and long-term exposure conditions. It is hoped that the sample data in Table 4 will continue to be increased in the future, and the relevant mechanical property parameters of this component will continue to be supplemented, so as to provide the experimental basis for the establishment of the subsequent strength model and the constitutive relationship, which can provide a more scientific and reliable technical support for the protection and restoration of ancient buildings.

Author Contributions: Y.Q.: Data curation, Formal analysis, Writing—original draft, Visualization, Investigation. S.P. and Y.S.: Conceptualization, Funding acquisition, Writing—review and editing, Supervision. All authors have read and agreed to the published version of the manuscript.

Funding: This research is funded by 'Natural Science Foundation of Hubei Province of China (CN)'—'China' (Grant No. 2022CFB662), 'Hubei Construction Science and Technology Plan Project of China (CN)'—'China' (Grant No. 202144) and their support is gratefully acknowledged.

Informed Consent Statement: Not applicable.

Data Availability Statement: Some or all data, models, or code that support the findings of this study are available from the corresponding author upon reasonable request.

Conflicts of Interest: The authors declare no conflicts of interest.

References

1. King, W.S.; Richard, Y.J.Y.; Alex, Y.Y.N. Joint characteristics of traditional Chinese wooden frames. *Eng. Struct.* **1996**, *18*, 635–644. [CrossRef]
2. Zhao, H.T.; Zhang, F.L.; Xue, J.Y.; Xie, Q.; Zhang, X.; Ma, H. Research review on structural performance of ancient timber structure. *J. Build. Struct.* **2012**, *33*, 1–10.
3. Siha, A.; Zhou, C. Experimental study and numerical analysis of composite strengthened timber columns under lateral cyclic loading. *J. Build. Eng.* **2023**, *67*, 106077. [CrossRef]
4. Pang, S.J.; Oh, J.K.; Hong, J.P.; Lee, S.J.; Lee, J.J. Stochastic model for predicting the bending strength of glued-laminated timber based on the knot area ratio and localized MOE in lamina. *J. Wood Sci.* **2018**, *64*, 126–137. [CrossRef]
5. Li, H.; Qiu, H.X.; Lu, Y. An analytical model for the loading capacity of splice-retrofitted slender timber columns. *Eng. Struct.* **2020**, *225*, 111274. [CrossRef]
6. Li, Z.; He, M.; Tao, D.; Li, M. Experimental buckling performance of scrimber composite columns under axial compression. *Compos. Part B Eng.* **2016**, *86*, 203–213. [CrossRef]
7. Han, Y.; Chun, Q.; Xu, X.; Teng, Q.; Dong, Y.; Lin, Y. Wind effects on Chinese traditional timber buildings in complex terrain: The case of Baoguo Temple. *J. Build. Eng.* **2022**, *59*, 105088. [CrossRef]
8. Chu, Y.P.; Shi Bixin Gong, Y.D. Experimental study on compressive behavior of intermediate slender timber columns with local damage and the retrofitting techniques for the damaged columns. *Structures* **2022**, *46*, 1709–1725. [CrossRef]
9. Qin, G.Z.; Li, M.; Fang, S.Y.; Deng, T.; Huang, C.; Mao, F.; Zhao, Y.; Xu, N. Study of a grid-based regional localization method for damage sources during three-point bending tests of wood. *Constr. Build. Mater.* **2024**, *419*, 135348. [CrossRef]
10. Thamboo, J.; Navaratnam, S.; Poologanathan, K.; Corradi, M. Experimental investigation of timber samples under triaxial compression conditions. *J. Build. Eng.* **2022**, 104891. [CrossRef]
11. Kia, L.; Valipour, H.R.; Ghanbari-Ghazijahani, T. Experimental and numerical investigation of concentric axial loading on bar-reinforced composite timber columns at a large scale. *Structures* **2024**, *60*, 105920. [CrossRef]

12. Shi, F.; Wang, L.B.; Du, H.; Zhao, M.; Li, H.; Wang, F.; Wang, S. Axial Compression Behavior of FRP Confined Laminated Timber Columns under Cyclic Loadings. *Buildings* **2022**, *12*, 1841. [CrossRef]
13. Zhang, L.; Liu, C.; Zhou, T. Experimental study on mechanical properties of column foot of ancient timber structures—Take the drum-shaped plinth as an example. *Structures* **2022**, *40*, 1002–1013. [CrossRef]
14. Xu, F.Y.; Zhang, Z.; Meng, X.M.; Wu, X.; Gao, Y. Axial compressive performance of cruciform timber-encased steel composite columns: Experimental investigation and buckling analysis through 3D laser scanning. *Thin-Walled Struct.* **2024**, *201*, 111968. [CrossRef]
15. Wang, Y.; Huang, Q.Z.; Dong, H.; Wang, Z.Q.; Shu, B.Q.; Gong, M. Mechanical behavior of cross-laminated timber-bamboo short columns with different layup configurations under axial compression. *Constr. Build. Mater.* **2024**, *421*, 135695. [CrossRef]
16. Dubois, F.; Dopeux, J.; Pop, O.; Metrope, M. Long-term creep behavior of timber columns: Experimental and numerical protocols. *Eng. Struct.* **2023**, *275*, 115283. [CrossRef]
17. Navaratnam, S.; Thamboo, J.; Poologanathan, K.; Roy, K.; Gatheeshgar, P. Finite element modelling of timber infilled steel tubular short columns under axial compression. *Structures* **2021**, *30*, 910–924. [CrossRef]
18. Zheng, Y.B.; Zhou, C.D. Axial compressive properties of intermediately slender circular ancient timber columns reinforced with high-performance bamboo-based composites. *Structures* **2024**, *65*, 106720. [CrossRef]
19. Malhotra AS, K.; Sukumar, A.P. Reliability-based design of mechanically connected built-up wood columns. *Can. J. Civ. Eng.* **1991**, *18*, 171–179. [CrossRef]
20. Song, X.B.; Frank, L. Laterally braced wood beam-columns subjected to biaxial eccentric loading. *Comput. Struct.* **2009**, *87*, 1058–1066. [CrossRef]
21. Theiler, M.; Frangi, A.; Steiger, R. Strain-based calculation model for centrically and eccentrically loaded timber columns. *Eng. Struct.* **2013**, *56*, 1103–1116. [CrossRef]
22. Li, S.Y.; Xu, Q.F. Compressive behavior of damaged timber columns: Experimental tests, degradation model, and repair method. *Eng. Struct.* **2023**, *293*, 116579. [CrossRef]
23. A, S.H.; Zhou, C.D.; Yang, L.G. Experimental investigation on axial compression behavior of timber columns strengthened with composite reinforcement method. *China Civ. Eng. J.* **2021**, *54*, 1–9.
24. Wei, P.; Wang, B.J.; Li, H.; Wang, L.; Peng, S.; Zhang, L. A comparative study of compression behaviors of cross-laminated timber and glued-laminated timber columns. *Constr. Build. Mater.* **2019**, *222*, 86–95. [CrossRef]
25. Xie, Q.F.; Zhang, B.Z.; Zhang, L.P.; Miao, Z. Study on mechanical performance test and degradation model of naturally cracked timber columns. *J. Build. Struct.* **2022**, *43*, 210–222.
26. *GB 50005-2017*; Standard for Design of Timber Structures. Ministry of Housing and Urban-Rural Development: Beijing, China, 2017.
27. *GB/T 50329-2012*; Standard for Test Methods of Timber Structures. Ministry of Housing and Urban-Rural Development: Beijing, China, 2012.
28. Cheng, X.W.; Yu, H.R.; Shi, M.Y.; Sun, X.L.; Lu, W.D. Axial compression test of glulam columns based on traditional splicing method. *J. Nanjing Tech Univ.* **2022**, *44*, 654–663.
29. Kia, L.; Valipour, H.R. Composite timber-steel encased columns subjected to concentric loading. *Eng. Struct.* **2021**, *232*, 111825. [CrossRef]
30. André, J.; Massimo, F. General notes on ductility in timber structures. *Eng. Struct.* **2011**, *33*, 2987–2997.
31. Xu, F.Y.; Xuan, S.Q.; Li, W.; Meng, X.; Gao, Y. Compressive performance of steel-timber composite L-shaped columns under concentric loading. *J. Build. Eng.* **2022**, *48*, 103967. [CrossRef]
32. Karampour, H.; Bourges, M.; Gilbert, B.P.; Bismire, A.; Bailleres, H.; Guan, H. Compressive behaviour of novel timber-filled steel tubular (TFST) columns. *Constr. Build. Mater.* **2020**, *238*, 117734. [CrossRef]

buildings

MDPI

Article

Seismic Behavior of Bahareque Walls Under In-Plane Horizontal Loads

Karol Cristancho [1], Iván Fernando Otálvaro [1], Daniel M. Ruiz [2,*], Natalia Barrera [2], Jesús D. Villalba-Morales [2], Yezid A. Alvarado [2] and Orlando Cundumí [1]

[1] Department of Civil and Industrial Engineering, Pontificia Universidad Javeriana, Cali 760031, Colombia; kjcristanchob@javerianacali.edu.co (K.C.); ifotalvaro@javerianacali.edu.co (I.F.O.); orlando.cundumi@javerianacali.edu.co (O.C.)

[2] Department of Civil Engineering, Pontificia Universidad Javeriana, Bogotá 110231, Colombia; natalia.barrera@javeriana.edu.co (N.B.); jesus.villalba@javeriana.edu.co (J.D.V.-M.); alvarado.y@javeriana.edu.co (Y.A.A.)

* Correspondence: daniel.ruiz@javeriana.edu.co

Abstract: This study investigates the structural behavior of bahareque earth walls, a traditional construction system commonly used in rural areas of northern South America. Bahareque (wattle and daub) walls, consisting of guadua (a bamboo-like material) or wooden frames filled with soil mixes, have demonstrated considerable resilience in seismic zones due to their lightweight and flexible nature. Despite their widespread use in these communities, limited scientific data exist on their seismic performance under in-plane pseudo-static horizontal loading. This research addresses this gap by experimentally evaluating the seismic behavior of five wall models with different combinations of guadua, wood, and earth filling materials. The methodology included four main phases, namely field visits to document traditional construction techniques, material characterization, prototype testing under pseudo-static loads, and an analysis of mechanical behavior. Key material properties, including compressive strength and Young's modulus, were determined, alongside the mechanical and physical properties of the infill material, which incorporated natural fibers. Pseudo-static tests were conducted on five wall prototypes, featuring various configurations of guadua and wood frameworks, both with and without soil infill. The walls were subjected to horizontal in-plane loads to assess their deformation capacity, energy dissipation, and failure mechanisms. The results indicated that walls with soil mixture infill—specifically the GSHS (guadua frame with horizontal guadua strips and soil mixture infill) and TSHS (wood frame with horizontal guadua strips and soil mixture infill) configurations—demonstrated the best seismic performance, with maximum displacements reaching up to 166 mm and strengths ranging from 6.4 to 8.4 kN. The study concludes that bahareque walls, particularly those incorporating soil mixes and horizontal guadua strips, exhibit high resilience under seismic conditions and provide a sustainable construction alternative for rural regions. The scope of this study is limited by the exclusion of dynamic seismic simulations, which could offer additional insights into the behavior of bahareque walls under real earthquake conditions. The novelty of this research lies in the direct evaluation of the seismic performance of traditional bahareque configurations, specifically comparing walls constructed with guadua and wooden frameworks, while emphasizing the critical role of soil infill and guadua strips in structural performance.

Keywords: bahareque; earthen walls; seismic performance; guadua; bamboo; pseudo-static tests

1. Introduction and Background: Traditional Timber Structures

Traditional timber structures have played a vital role in the architectural heritage of many regions worldwide, especially in areas prone to seismic activity. Examples like the Chuan-dou timber frames in China, Japanese pagodas, and European half-timbered houses demonstrate remarkable resilience to seismic forces. Understanding their seismic performance is essential not only for preserving these historical structures but also for integrating their resilient design features into modern construction practices [1,2].

Timber's flexibility, lightweightness, and energy dissipation make it ideal for seismic resistance, along with its structural configuration and connections. Some joinery techniques found in traditional timber structures further enhance their seismic resilience, as mentioned in [3]. Timber's anisotropy, damping capacity, and ability to deform without failing are key to its seismic behavior [4,5]. Additionally, timber's flexibility and energy-dissipating capacity help reduce the impact of seismic forces [4,6].

The structural configuration of timber buildings plays a critical role in their seismic performance. The arrangement of beams, columns, and infill materials enhances the structure's ability to resist seismic forces. For instance, ref. [7] demonstrated that masonry infill in traditional Chinese timber frames significantly improves load capacity and energy dissipation, highlighting its importance in seismic resilience. Similarly, studies like [8,9] on Taiwanese timber shear walls revealed that traditional design elements, such as the friction between board units and beams, along with embedment resistance, are key factors in resisting lateral forces.

Likewise, joints between timber elements are crucial to a structure's seismic resilience. Traditional joinery, such as mortise–tenon and dovetail joints, allows for flexibility and energy dissipation. However, these joints can degrade under repeated seismic loading if not properly maintained. Reinforcing joints with modern materials, like steel plates or advanced adhesives, could significantly improve seismic performance while preserving the historical integrity of the structures.

Historical records and experiments show timber structures' resilience, as seen in the Great Kanto (Japan) and Sichuan (China) earthquakes, due to their flexible frameworks and energy-dissipating joints. Studies [1,2,7,10] highlight how these buildings have withstood significant seismic forces due to the effective combination of the inherent properties of wood and traditional construction techniques; for example, these traditional wood structures have shown outstanding earthquake performance due to their excellent deformation capacity and energy dissipation properties.

Experimental research has provided further evidence of the seismic resilience of traditional timber structures. For instance, ref. [11] demonstrated through shake table tests that proper structural configuration is critical, with column-and-tie timber frames showing excellent resistance to collapse under maximum earthquake scenarios. Similarly, ref. [12] performed pseudo-static cyclic tests on Chuan-dou timber frames with varying infill configurations, analyzing key parameters such as force deformation behavior, failure mechanisms, stiffness, and energy dissipation capacity using 1:2 scale models. More recently, ref. [13], inspired by traditional Romanian architecture, conducted pseudo-static tests on the TRAROM lightweight timber frame system, further validating the seismic performance of timber-based designs.

Detailed case studies provide further insight into the seismic performance of specific traditional wood structures around the world. For example, ref. [8] studied Taiwanese timber shear walls, while [14] analyzed European timber frames (a timber frame structure called "gaiola pombalina" used in downtown Lisbon after the 1755 earthquake), emphasizing how design details—such as the use of bamboo nails in Taiwanese structures and the integration of masonry infill in European designs—affect seismic performance. Ref. [15]

further investigated the seismic behavior (strength, stiffness, ductility, and energy dissipation) of traditional Mediterranean infilled timber frame walls subjected to pseudo-static tests. The infill consists of masonry lath and plaster. The authors also tested a timber frame without infill for comparison. The tests showed how the infill was able to guarantee greater stiffness, ductility, and the ultimate capacity of the wall. Ref. [16] performed static cyclic tests on timber frame specimens, which were constructed based on findings from field investigations of traditional Romanian buildings. Some of the specimens tested exhibited excellent deformation capacity, with drifts greater than 5%. Similarly, ref. [17] tested double-span traditional timber structure models, highlighting that the experimental pseudo-static tests had stable hysteretic loops and that the P–Δ effect could affect the response of timber frames.

Shaking table tests and cyclic loading experiments confirm timber-framed walls with infill materials like adobe or fired bricks can withstand lateral displacements and ground accelerations without collapsing [18]. The results indicated that walls with bamboo or timber frameworks provided superior seismic performance, particularly in terms of energy dissipation and the reduced likelihood of catastrophic failure.

Computational modeling has become an essential tool for predicting the seismic response of traditional timber structures. For example, ref. [19] developed a hysteretic model for "frontal" walls in Pombalino buildings, providing valuable insights into their seismic behavior. Finite element analysis (FEA) has also been widely applied to simulate the performance of timber frames with various infill materials, demonstrating how different configurations influence structural response. Similarly, ref. [20] created numerical models calibrated with the experimental results of timber frames, both with and without masonry infill, incorporating key effects such as flexural behavior, pinching, and strength degradation. Advancements in modeling techniques include shear spring models proposed in [21], which accurately replicate initial stiffness and peak strength, effectively capturing the complex interactions between structural elements during seismic events. Various software tools have facilitated these analyses, with OpenSees employed in [19] and ABAQUS utilized in [22] to assess the dynamic properties of timber frame masonry systems.

While the technical literature and several reports from Colombia (northern South America) have studied the behavior of cemented bahareque (a type of timber-framed structure) with bolted connections (actually included in the Colombian earthquake-resistant code) or contemporary systems such as prefabricated wattle and daub [23], there are few studies in the scientific literature focused on the structural behavior of traditional timber-framed bahareque modules used in the rural areas of northern South America.

The novelty of this research lies in providing the first scientific report on the structural behavior of traditional bahareque walls subjected to in-plane horizontal loads, as constructed in the Valle del Cauca and Cauca regions of Colombia. This study highlights the potential of bahareque as a safe and resilient construction system, particularly for seismically vulnerable areas. Furthermore, it offers a unique experimental comparison, under controlled and identical loading conditions, of the seismic performance of bahareque walls constructed with guadua (a bamboo-like material) versus wooden frameworks, incorporating insights into their distinct mechanical behaviors, emphasizing the role of soil infill and guadua strips in structural performance.

The primary objective of this study is to experimentally evaluate the seismic performance of traditional bahareque walls, focusing on the influence of material configurations (guadua, wood, and soil infill) on their ductility, stiffness, and failure mechanisms. Addressing a critical gap in the literature, this research provides much needed empirical data on the seismic behavior of bahareque systems, which have received limited attention despite their widespread use in rural South America. By grounding its findings in robust experimental analysis, this study not only preserves traditional construction knowledge but also lays the foundation for enhancing the seismic resilience of bahareque walls, aligning them with modern performance standards and sustainable building practices.

2. Methodology

The methodology implemented in the current study is presented in Figure 1, consisting of the four following phases:

- Phase 1: Field Visits: During field and technical visits, the materials and structural characteristics of bahareque constructions in rural areas of southern Colombia (northern South America) were documented. Material specimens, including wood, guadua, and soil, were collected for laboratory analysis. Existing houses were studied to determine the main dimensional characteristics of bahareque modules.
- Phase 2: Material Characterization: Given that earthen bahareque is composed of sawn timber frames combined with guadua and soil mixtures, with or without natural fibers, this phase involved the evaluation of the physical and mechanical properties of these materials. The characterization included testing for compressive strength and the modulus of elasticity for both wood and guadua. For the soil, Atterberg limits, maximum dry density, optimum water content, percentage passing through sieves, compressive strength, and indirect tensile strength were determined.
- Phase 3: Pseudo-Static Tests on Five Models: To evaluate the in-plane behavior of bahareque walls and components, pseudo-static tests were conducted. The wall specimens included vertical and diagonal elements made of wood and guadua. The dimensions of the test modules were based on observations from the field visits and on typifications of heritage construction systems, as described in [24] in the Colombian Coffee Cultural Landscape and as reported [25]. All prototypes were constructed with a base width of 2.2 m and a height of 2.2 m.
- Phase 4: Conclusions and Recommendations: Based on the experimental results from the material characterization and pseudo-static tests, conclusions were drawn regarding the performance of the bahareque system, along with recommendations for future research and applications.

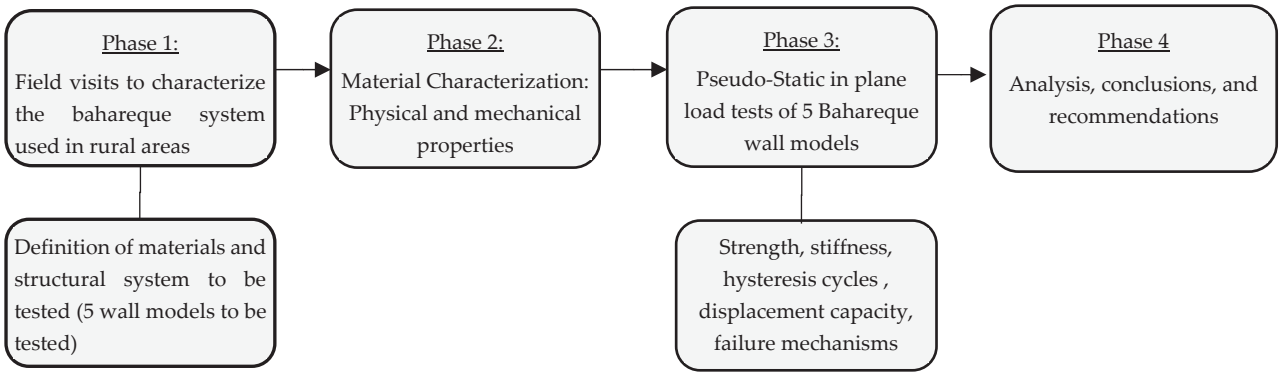

Figure 1. The proposed methodology to assess the mechanical characteristics of Bahareque walls.

3. Characteristics of Bahareque-Framed Earthen Walls and Field Visits

A typology of traditional wooden structures, used for centuries in South America, Central America, and Asia [26–29]), is known as bahareque in Colombia and Ecuador (quincha in Peru, taipa de mão in Brazil). This system is renowned for its use of natural materials such as bamboo, wood, and earth, making it not only sustainable but also highly resilient in seismic zones [30]. In recent years, these construction techniques have seen renewed interest due to their low environmental impact and inherent seismic resistance. The basic characteristic of the bahareque system (native from the Andean region of South America) is the reliance on a bamboo or wooden framework (braced and with sill beams), infilled with a mixture of soil and fibers (organic). According to [31], this framework is usually plastered or coated with mortar to protect it from the weather.

In reference [32], the authors mention that bamboo is a natural construction material found in tropical, sub-tropical, and mild temperate regions of at least four continents (America, Oceania, Asia, Africa). This natural material is particularly widespread in Colombia (Northern Andean region of South America), where it serves as the primary structural element of some rural and urban dwellings due to its abundance and favorable mechanical properties [33]. As indicated in [34], modern adaptations often use engineered bamboo products, such as laminated bamboo, which provide enhanced strength and uniformity by bonding layers of bamboo strips, making them stronger and more durable than traditional bamboo. Bamboo's rapid growth also makes it a highly renewable resource [35].

Bahareque is a traditional construction technique that weaves bamboo or wooden strips with mud or clay, creating walls that are both thermally efficient and highly durable. As reported in [36], these walls can endure harsh environmental conditions and remain functional for decades with minimal maintenance. A key advantage of bahareque systems lies in their capacity to absorb and dissipate seismic energy, a result of the materials' flexibility and lightweight nature. Bamboo-framed structures, in particular, demonstrate exceptional seismic performance due to their ability to undergo large deformations without failure. Research in [37] highlights the critical role of joint design, such as bolted steel-to-bamboo connections, in ensuring structural strength. Similarly, ref. [38] showed that adding diagonal bamboo strips to the walls significantly enhances seismic performance, improving both lateral load capacity and stiffness.

Field studies conducted after the 1999 Armenia earthquake in Colombia revealed that bahareque structures performed remarkably well compared to modern construction technologies. Ref. [33] reported that houses constructed with well-maintained bahareque walls suffered minimal damage, whereas those with poorly maintained walls experienced significant failures. This underscores the importance of maintenance and the use of high-quality materials to ensure the longevity and seismic resilience of these structures.

Additionally, several studies have highlighted the potential of combining traditional materials with modern construction techniques. For instance, ref. [23,39] explored bahareque in contemporary construction, demonstrating its viability as an alternative to conventional materials, especially for low-income housing projects in seismic regions. Combining traditional bahareque techniques with modern materials, such as reinforced concrete for foundations, can further enhance the seismic performance of these structures.

Hybrid wood–soil systems (HWSs), particularly those integrating bamboo, wood, and soil, have gained attention for their potential to meet global housing demands sustainably. Traditional systems like bahareque, prevalent in Latin America, utilize natural materials such as bamboo, soil, and mortar, providing low-cost and environmentally friendly solutions [31]. Modern iterations of HWSs have adapted these techniques to incorporate engineered materials, improving performance under seismic and environmental conditions [34]. Studies demonstrate that combining traditional materials with engineered

components enhances durability, resilience, and adaptability, making HWSs a promising solution in addressing housing deficits while reducing environmental impacts.

Comparative evaluations of traditional and modern HWSs reveal significant advantages for engineered systems in terms of environmental impact and scalability. Ref. [40] conducted a comprehensive life cycle assessment of bamboo-based construction systems, showing that engineered bamboo, particularly glue-laminated bamboo, significantly reduces CO_2 emissions compared to traditional systems. The environmental savings result from reduced material weight and lower energy consumption during processing and transport, allowing for its use in multi-story construction. Similarly, ref. [35] highlighted the superior renewability of bamboo as a resource, noting its rapid growth and carbon sequestration capabilities, which further enhance the sustainability of HWSs.

The bahareque construction system stands out as a highly sustainable solution due to its reliance on locally available and renewable materials, such as guadua (a bamboo-like material) and soil. Studies have shown that guadua angustifolia, a species widely used in Colombia, captures significant amounts of CO_2 during its growth cycle, contributing to carbon sequestration and reducing the overall environmental footprint of the material. According to [40], bamboo-based construction systems, including traditional bahareque-cemented systems (bahareque coated with a thin layer of cement mortar), exhibit lower carbon emissions compared to conventional materials like concrete and brick, particularly when transportation distances are minimized. The minimal energy required to process bamboo or guadua and the use of soil further reduce the embodied energy of bahareque walls, making them an eco-friendly choice for construction in rural and low-income regions. Additionally, promoting the use of the local and decentralized production of materials (as suggested by [40]) can significantly lower transportation impacts, making the system even more viable for remote regions. However, challenges remain regarding the optimization of the bahareque system to enhance its environmental benefits. Traditional bahareque-cemented systems use mortar or cement plaster for weather protection, which can increase its carbon footprint. Efforts to reduce this dependency through natural coatings or alternative binders could further improve sustainability.

Structural performance is another key advantage of HWSs. Ref. [28] analyzed cemented bahareque systems under seismic loads, concluding that their structural behavior meets earthquake resistance criteria. These findings align with the work presented in [34], which demonstrated that multi-story bamboo frames achieve high levels of seismic resilience through improved joint design and dynamic load management. Furthermore, ref. [41] emphasized that hybrid construction systems like engineered bahareque housing maintain affordability while offering enhanced strength and durability, making them particularly suited for low-income housing in seismically active regions.

Despite these advancements, challenges remain in expanding the adoption of HWSs. Traditional bahareque systems are labor-intensive, requiring significant manual effort for construction [31], while engineered systems depend on centralized production and advanced manufacturing, increasing costs [40]. Optimizing transport logistics and decentralizing production centers, as suggested in [40], can mitigate these challenges. Moreover, integrating sustainable design principles, as outlined in [35], and leveraging bamboo's environmental benefits can further strengthen the role of HWSs in promoting sustainable development. These systems exemplify how traditional knowledge and modern engineering can converge to provide affordable, resilient, and sustainable housing solutions.

In addition, studies such as [42] emphasize the importance of preserving and adapting traditional construction methods (in response to modern challenges), such as timber framing like frontal real in Portugal or bahareque in Colombia. These traditional techniques not only provide a connection to cultural heritage but also offer practical solutions for building in seismic zones. The application of these methods in contemporary contexts is further supported by environmental and sustainability considerations.

Globally, traditional seismic-resistant systems have developed to address earthquake challenges, sharing commonalities with bahareque walls in their use of natural materials and energy-dissipating features. For instance, Japanese timber pagodas rely on mortise and tenon joinery to dissipate seismic energy, while Chuan-dou timber frames in China use diagonal bracing and infill panels for lateral stiffness and ductility. Similarly, gaiola pombalina structures in Portugal integrate timber frames with masonry infill, combining flexibility and strength, and bamboo-based construction in South Asia demonstrates the importance of lightweight, flexible materials for seismic resilience.

These global examples highlight the universality of traditional systems in prioritizing resilience and sustainability. Bahareque walls, like these practices, provide a heritage-based yet innovative approach to seismic-resistant construction. This study builds on these global lessons by experimentally analyzing bahareque walls under controlled conditions, emphasizing their potential as a sustainable and seismic-resistant solution.

Furthermore, contemporary research has begun to formalize traditional practices into hybrid approaches. Engineered bamboo frames and advanced joinery techniques, for example, combine traditional materials with modern performance standards. This aligns with the objectives of this study, bridging traditional bahareque methods with experimental validation to strengthen their integration into global practices for resilient construction.

In Colombia, the bahareque construction system is characterized by a structural framework made of sawn wood or guadua bamboo (guadua). The Colombian bahareque consists of upper and lower sill beams, vertical elements, and braces (inclined diagonal members). The infill bahareque walls are built using strips of guadua, approximately 4 to 5 cm wide, placed lengthwise to secure the filler (an earth mixture). These strips are nailed horizontally on both sides of the frame, leaving a gap of about 10 cm between them to facilitate the hand application of the mixture. The mixture itself consists of clay with high moisture content, combined with natural fibers such as ficus, straw, and grass. Additionally, a protective coating of manure or a mixture of cement and sand is applied, with lime used in some cases. These characteristics were documented during technical visits, which enabled the observation and analysis of construction techniques used in bahareque structures in rural areas of southern Colombia (northern South America). During these visits, specimens were collected from existing houses, facilitating the analysis of materials, soil properties, and natural fibers. Various construction styles were observed, ranging from houses built 50 years ago to those constructed within the past two years. Examples of these buildings are shown in Figure 2. In many cases, these structures are owned by individuals with low socio-economic status.

During field visits to rural areas, several site-specific challenges were observed that highlight the complexities of traditional bahareque construction. One major issue was the variability in construction techniques and materials across different communities, leading to significant differences in structural configurations and joint integrity. Additionally, many existing bahareque structures exhibited signs of aging and poor maintenance, inadequate connections, high humidity and exposure to rainfall, and loss of soil infill cohesion. Another challenge was the limited use of standardized practices for soil mixture preparation, resulting in variations in mechanical properties of the infill material.

The use of bahareque walls in rural South America is deeply rooted in local traditions, which have shaped their construction techniques, material selection, and cultural significance over generations. These practices are informed by the availability of natural materials like guadua and soil, as well as by the collective knowledge passed down through communities. For instance, the incorporation of natural fibers in the soil mixture or the specific arrangement of guadua strips reflects adaptations to regional climatic conditions and seismic risks. Additionally, bahareque construction is often carried out collaboratively within communities, reinforcing its role as a sustainable and affordable solution for low-income families. Understanding these traditional influences is essential for preserving the cultural heritage associated with bahareque while promoting its adaptation to modern seismic standards.

Figure 2. Bahareque dwellings with guadua strips located in the village of "La Estrella" near the municipality of Jamundí, in the Valle del Cauca Department, southwest Colombia.

However, based on the collected information, models were designed for the construction of prototypes, which were experimentally evaluated under in-plane pseudo-static loads in the Structures Laboratory at the Pontificia Universidad Javeriana. Figure 3 illustrates the construction process of a Colombian bahareque module in four phases as follows: placing the sill beams and vertical elements (Figure 3a), installing the braces (Figure 3b), attaching horizontal strips (Figure 3c), and filling the wall with the soil mixture (Figure 3d). Steel nails were used to secure all joints and connections between the various elements (vertical members, sill beams, braces, and strips).

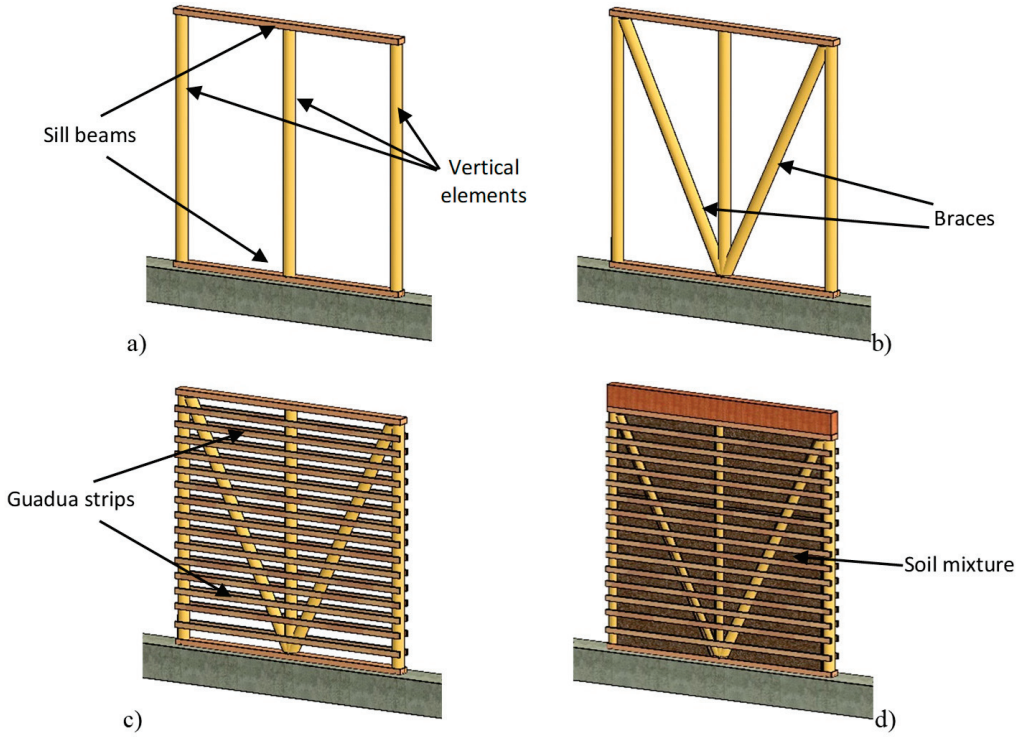

Figure 3. The construction process of a Colombian bahareque module. (**a**) The configuration of the wood/guadua frame, with sill wood beams and vertical elements (guadua or wood). (**b**) The placement of structural braces (guadua or wood). (**c**) The installation of guadua bamboo strips. (**d**) Infill of the wall with soil mixture.

4. Material Characterization

The soil specimen studied is classified as elastic silt with sand (MH) based on the Unified Soil Classification System (USCS). According to the classification, gravels are defined as particles with diameters greater than 4.75 mm, sands range from 0.075 mm to 4.75 mm, silts from 0.002 mm to 0.075 mm, and clays consist of particles smaller than 0.002 mm. Following the ASTM D422 [43], the grain size distribution of the soil revealed a gravel content of 1%, sand content ranging from 17.4% to 21.1%, silt content between 61.6% and 64.7%, and clay content between 13.1% and 20%. The soil behavior is primarily influenced by its fine-grained fraction, particularly silt. Additionally, the compaction characteristics were determined using the ASTM D698 test method [44], resulting in a maximum dry density of 14.1 kN/m^3 with an optimum water content of 23.5%.

A natural fiber native to the study region (Valle del Cauca, municipality of Jamundí), identified as Andropogon glomeratus of the Poaceae family, was incorporated into the soil mixtures following local construction practices. The production process did not adhere to standardized methods; instead, the community manually mixed the soil with pre-cut fibers and placed the mixture within the bahareque walls without compaction. The fibers were cut to two lengths—2.5 cm and 5 cm—based on traditional techniques, and fiber content ranged from 0% to 5% across ten mixtures for each length. Cylindrical specimens were subsequently prepared to estimate the material's compressive and indirect tensile strengths. The results for compressive strength are presented in Figure 4, while the indirect tensile strength results are shown in Figure 5.

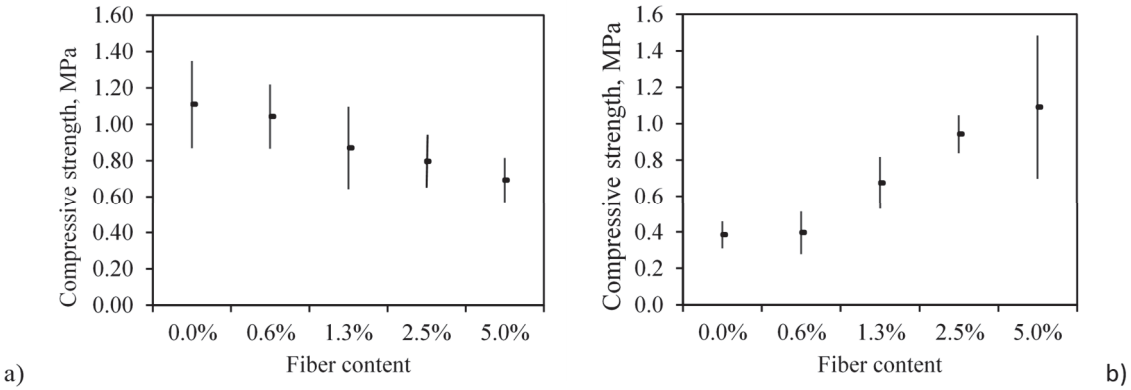

Figure 4. (**a**) Compressive strength of the soil mixture for varying fiber contents with 2.5 cm long fibers; (**b**) compressive strength of the soil mixture for varying fiber contents with 5.0 cm long fibers.

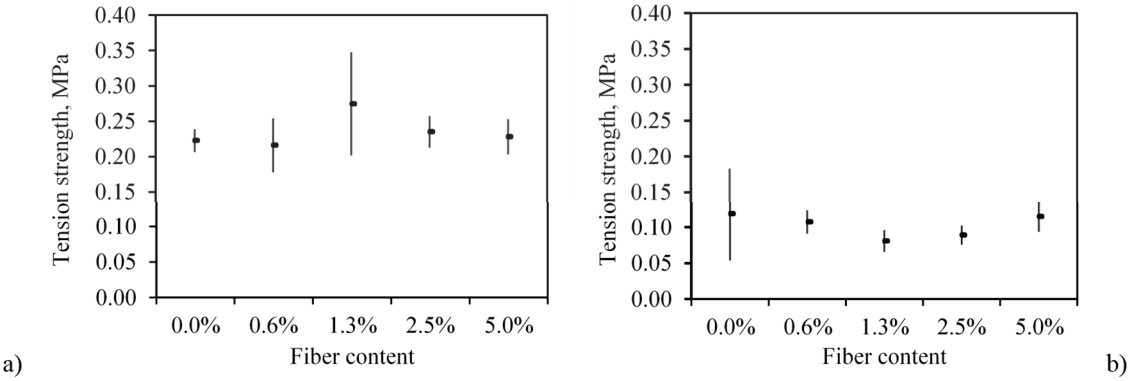

Figure 5. (**a**) Indirect tensile strength of the soil mixture with varying fiber contents for 2.5 cm long fibers; (**b**) indirect tensile strength of the soil mixture with varying fiber contents for 5.0 cm long fibers.

Compression test results after 28 days of drying indicated strengths from 0.3 MPa to 1.5 MPa. However, due to the high variability in the results, no clear relationship could be established between fiber content, length, and compressive strength. In contrast, the indirect tensile strength results indicated better performance for the soil mixture with 2.5 cm long fibers, achieving tensile strengths of up to 0.35 MPa. The soil mixture with 5 cm long fibers exhibited lower tensile strength, with a maximum value of 0.18 MPa.

Compression tests on guadua specimens were performed according to the ISO standard [45]. Both specimens, with and without biodeterioration, (Figure 6c) were evaluated one year after the materials were obtained. It is important to note that biodeterioration, as referred to in this study, is defined as the degradation or damage of the guadua material caused by biological agents such as insects, fungi, or microorganisms, which can compromise the structural integrity of untreated specimens. In all cases presented in Figure 6, the slenderness ratio was 2:1, with specimens measuring approximately 10 cm in diameter.

The mean compressive strength of the guadua specimens without biodeterioration was 54.9 MPa, with a coefficient of variation of 25.6% (Figure 6a), while biodeteriorated specimens averaged 43 MPa. Compressive Young's modulus tests revealed an average modulus of 9.3 GPa for the guadua without biodeterioration (Figure 6b). Additionally, the average density of the guadua without biodeterioration was 508.3 kg/m^3 (standard deviation of 55.78 kg/m^3). The wet wood density was 691.0 kg/m^3 (standard deviation of 73.7 kg/m^3). After drying, the density of the wood decreased to 613.6 kg/m^3 (standard deviation of 67.0 kg/m^3). The maximum compressive strength of the tested wood elements was 54.1 MPa, the average of the results was 34.5 MPa, and the standard deviation was 14 MPa (Figure 6d). Figure 6e shows the stress–strain curves of the 20 wood specimens

tested in compression. The variability in strength (which is consistent with the data in Figure 6d) is evident, as is the variability in maximum strain. Nevertheless, it can be seen that the material has a good inelastic deformation capacity.

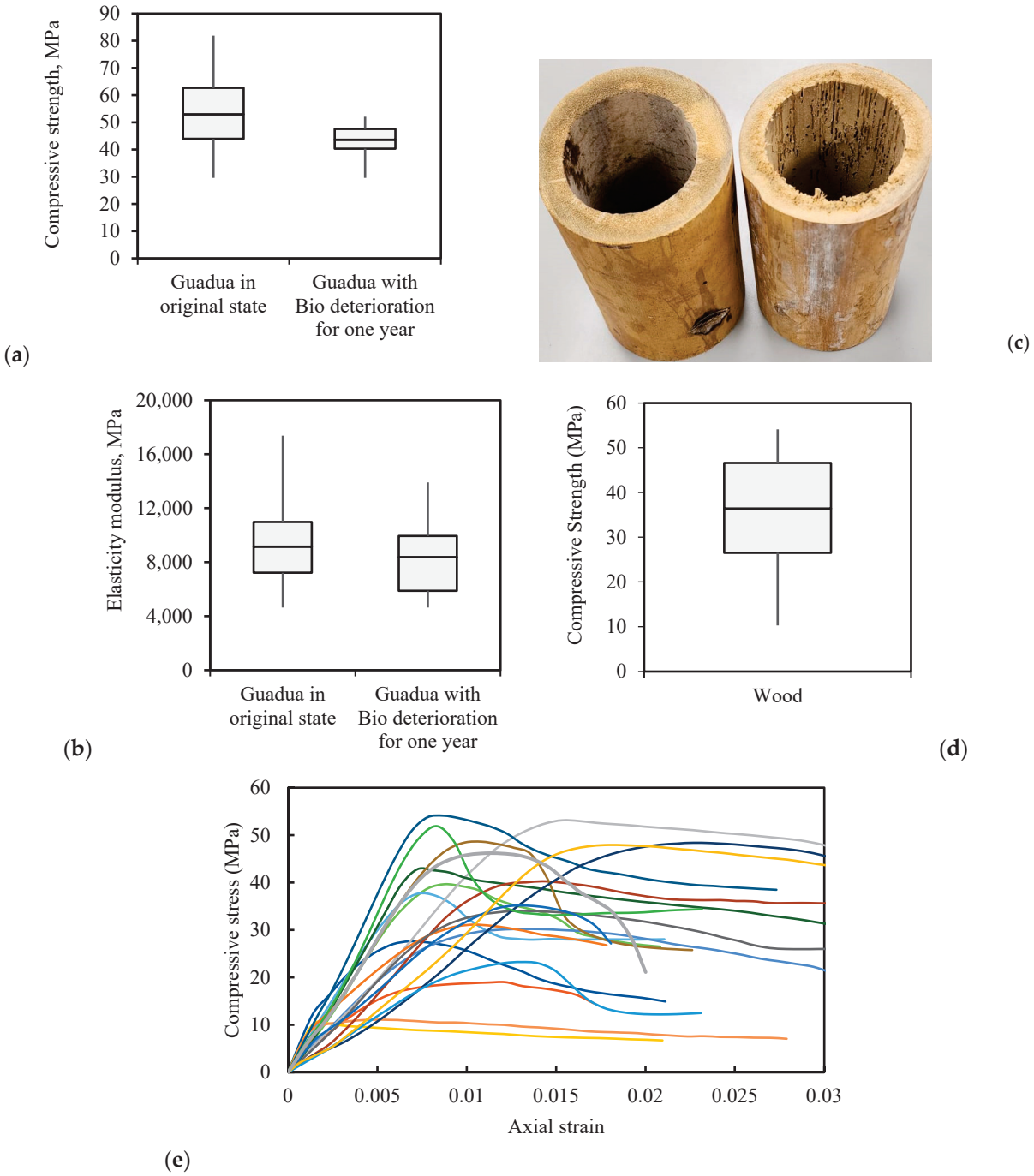

Figure 6. (**a**) Compressive strength of guadua specimens; (**b**) elastic modulus of guadua specimens; (**c**) comparison of guadua without biodeterioration (**left**) and guadua with biodeterioration (**right**); (**d**) compressive strength of wood specimens; (**e**) stress–strain curves of used wood.

5. Pseudo-Static In-Plane Load Tests of Bahareque Walls

Pseudo-static in-plane load tests of bahareque walls were conducted on the five following prototypes, designed and constructed based on field observations and the technical literature: (a) guadua skeleton (GS), (b) timber skeleton with horizontal strips (TSH), (c) guadua skeleton with horizontal guadua strips (GSH), (d) guadua skeleton with horizontal guadua strips and soil mixture filling (GSHS), and (e) timber skeleton with horizontal

guadua strips and soil mixture filling (TSHS). Figure 7 illustrates these prototypes. Each measured 2.2 m in both height and base width, with two 1.1 m panels and lower sill beams made of wood with cross-sectional dimensions of 10 cm wide by 5 cm high. Detailed descriptions of each prototype are provided as follows:

- GS: Constructed of two panels made entirely of guadua (approximately 10 cm in diameter), joined by three vertical elements and two diagonal braces, with sawn wooden sill beams. This prototype did not include guadua strips or soil mix infill (Figure 7a).
- TSH: Featured vertical sawn timber elements with a square cross-section of 10 cm by 10 cm and incorporated horizontal guadua strips spaced 9–10 cm. The strips had an average width of 4–5 cm and thickness of 1 to 2 cm (Figure 7b).
- GSH: included three vertical elements and two diagonal braces, all made of guadua (approximately 10 cm in diameter), with horizontal guadua strips installed similarly to the TSH prototype (Figure 7c).
- GSHS: Comprised three vertical guadua elements and two diagonal braces, with horizontal guadua strips spaced 9–10 cm apart. The strips were 4–5 cm wide and 1–2 cm thick, with the wall filled using a mixture of soil and natural fibers, as described in the Methodology section (Figure 7d).
- TSHS: Consisted of vertical sawn timber elements and two diagonal braces with a 10 cm by 10 cm cross-section. Like the TSH, GSH, and GSHS prototypes, guadua strips were installed and the wall was infilled with a mixture of soil and fibers (Figure 7e).

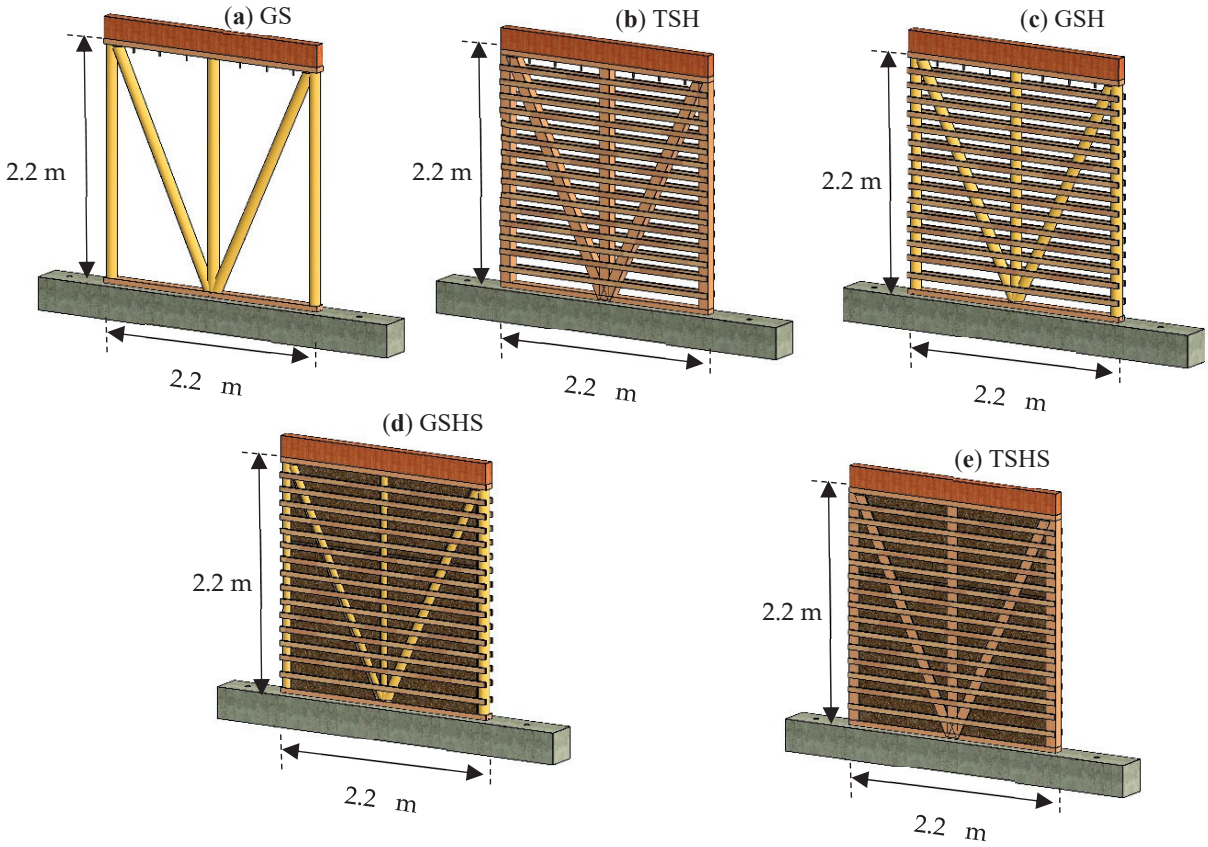

Figure 7. (**a**) Guadua skeleton (GS); (**b**) timber skeleton with horizontal guadua strips (TSH); (**c**) guadua skeleton with horizontal guadua strips (GSH); (**d**) guadua skeleton with horizontal guadua strips and soil mixture infill (GSHS); and (**e**) timber skeleton with horizontal guadua strips and soil mixture infill (TSHS).

Field observations revealed foundations made of cyclopean concrete, stone, or standard concrete. To replicate these foundations, the lower sill beam of each prototype was anchored to a concrete beam, secured to the reaction plate in the Structures Laboratory at Pontificia Universidad Javeriana. The connections between the structural elements (vertical members, braces, and sill beams) were based on typical field practices using 3-inch steel nails. Figure 8 illustrates examples of these connections for both wood and guadua elements.

Figure 8. (**a**) An example of a steel nail connection at the central joint of a bahareque wall with a guadua skeleton (vertical element and two braces) (Blue points indicate the position of the steel nails); (**b**) an example of a steel nail connection at the central joint of a bahareque wall with a wooden skeleton (vertical element and two braces); (**c**) an example of a connection between a guadua vertical element and a wooden sill beam; (**d**) an example of a connection between a wooden vertical element and a wooden sill beam.

The test setup included an MTS hydraulic actuator used to apply in-plane shear loads to the specimens. Figure 9 illustrates the test setup with the actuator attached to the reaction wall, with QR codes in Figure 9b,c providing 360° views of the test setup. To simulate the weight of a typical building roof, a vertical load of 1.9 kN was applied to all specimens, as determined during the site visits. The dynamic actuator was connected to the bahareque wall using two steel components and four rods, allowing for reversible displacement in accordance with the test protocol. Figure 10 presents the displacement protocol (pseudo-static).

The loading procedure followed the provisions of ref [46] and Test Method B of ref. [47], and it was displacement-controlled, with displacement cycles grouped into phases of increasing levels at a frequency of f = 0.01 Hz. The protocol was designed for a target maximum drift of 6% based on the consulted references but allowed for drifts up to 10%.

A servo-controlled dynamic hydraulic actuator was used to apply the in-plane cyclic loads to the bahareque walls. All walls were instrumented with displacement sensors using LVDT technology, with ranges of ±25 mm, ±50 mm, ±100 mm, and ±150 mm and a sampling rate of 10 Hz. The LVDTs were distributed as follows (Figure 11): LVDT 1 (±150 mm) on the upper sill beam; LVDT 2 (±100 mm) at wall center height; LVDT 3 (±50 mm) for the wall–foundation relative displacement; LVDTs 4 and 6 (±50 mm) for vertical displacements of the vertical (side) elements of the bahareque walls; and LVDTs 5 and 7 for the relative vertical displacement of the sill beam anchored to the foundation. It is important to note that the control sensor for the test was LVDT 1. Finally, the hydraulic actuator was also equipped with an LVDT with a range of ±250 mm.

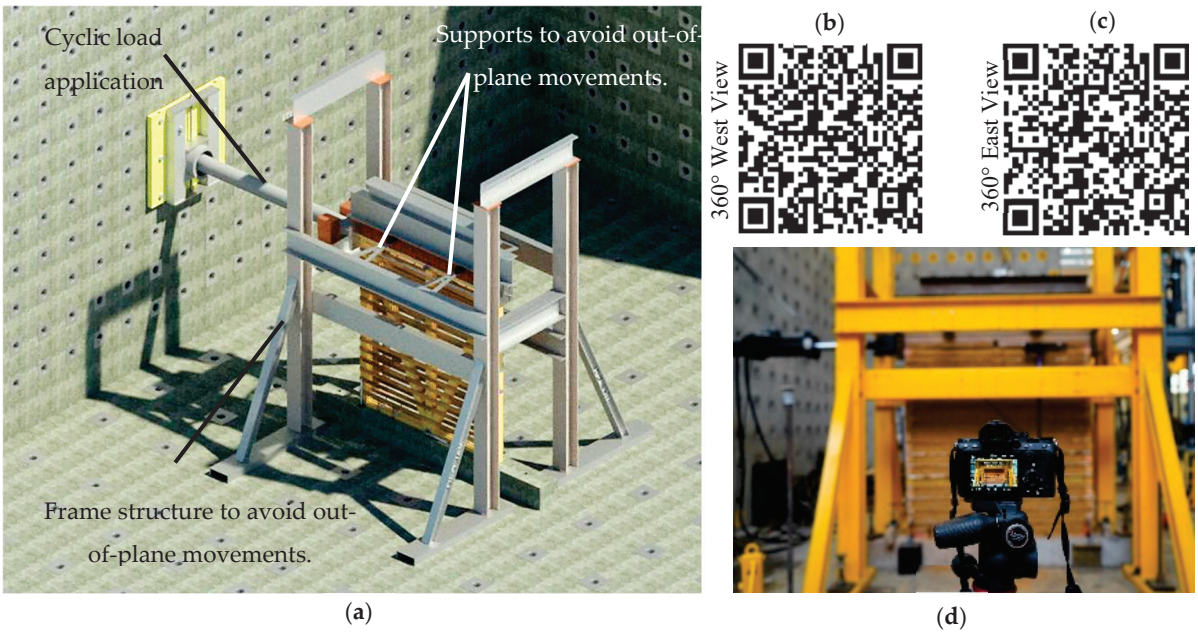

Figure 9. The setup for the pseudo-static in-plane loading of Bahareque walls. (**a**) A 3D view of the setup (showing the reaction wall and the laboratory's strong floor); (**b**) QR code—360° west view of the test setup (Revit—Autodesk®) https://pano.autodesk.com/pano.html?mono=jpgs/3de5ecb8-5939-430f-88ff-d503156a7f9a&version=2 (accessed on 19 December 2024); (**c**) QR code—360° east view of the test setup (Revit—Autodesk®) https://pano.autodesk.com/pano.html?mono=jpgs/9c315f5e-dc84-40a1-9301-1767a28a0b18&version=2 (accessed on 19 December 2024); (**d**) the final setup of a Bahareque wall test.

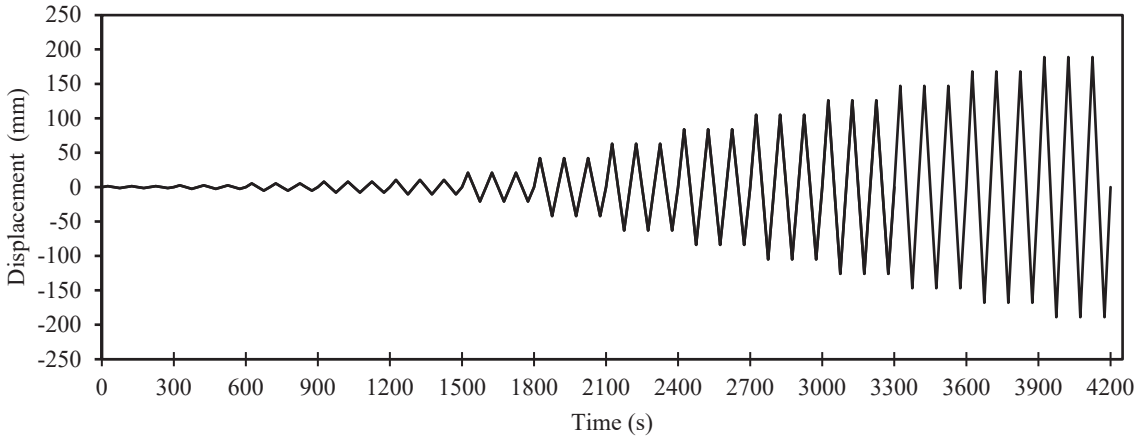

Figure 10. The load protocol applied to the upper section of the bahareque walls (displacement-controlled).

Figure 12 illustrates the failure mechanisms for each of the five bahareque wall specimens. In the GS wall, failure initiated with a crack in the lower zone of the wooden sill beam. Subsequently, joint failures occurred between the wood and guadua, leading to the detachment of the vertical elements (Figure 12a—1). This was primarily due to the steel nails becoming dislodged and unanchored (Figure 12a—3). During loading, the connection of the central vertical member to the braces failed as steel nails loosened and were reinserted repeatedly, eventually causing misalignment. Notably, neither the wood nor the guadua elements fractured. In the TSH specimen, detachment of the steel nails was observed at the joints between the bottom sill and the vertical elements (Figure 12b—1), causing the central vertical member became separated from the bottom sill, along with the diagonals at the joint. Similarly to the GS wall, the steel nails repeatedly detached

during loading cycles and reattached during unloading until some were crushed. Minor detachment also occurred in the upper region, though less significant than in the lower region. It is important to note that despite these issues, no fractures were detected in the wood, although a crack appeared in the guadua strips (Figure 12b—2). In addition, the vertical members completely detached from the lower sill beam joint (Figure 12b—3). For the GSH specimen, steel nails were pulled out at the joint of the central vertical member and the top sill beam (Figure 12c—1), resulting in the separation of the elements. During the final loading cycles, the left vertical member completely detached from the lower sill beam joint (Figure 12c—2). By the test's end, a crack appeared in the bottom sill beam near a vertical member connection (Figure 12c—3), but the guadua strips and their connections remained intact. Prior to the pseudo-static testing of the GSHS wall, a one-month drying process was conducted in the structures laboratory to assess the impact of the infill soil on structural performance. The drying process took place in the structures laboratory, with the wall exposed to solar radiation. The moisture content was measured at two stages, namely during wall construction and at the end of the drying period. Initially, when the soil mix was prepared, the moisture content was set at 26.3%, corresponding to the optimum value determined through compaction tests. After one month of drying, by the time the pseudo-static test was conducted, the moisture content had reduced to a range of 5.2% to 8.2%. Upon applying the loading protocol, the failure mechanism was found to be similar to those observed in the previous walls tested (Figure 12d). The failure mechanism included lifting of the vertical elements with respect to the bottom sill beam (Figure 12d—1), the removal of steel nails at the connection of the central vertical element, and cycles of removal and insertion of steel nails in the vertical elements, which resulted in a loss of alignment in the lower zone of the wall. Additionally, fissures and cracks developed in the infill soil (Figure 12d—2,3), along with a noticeable separation between the infill and the skeleton formed by the guadua strips. The soil fill exhibited loss and spalling during the loading and unloading cycles applied to the wall.

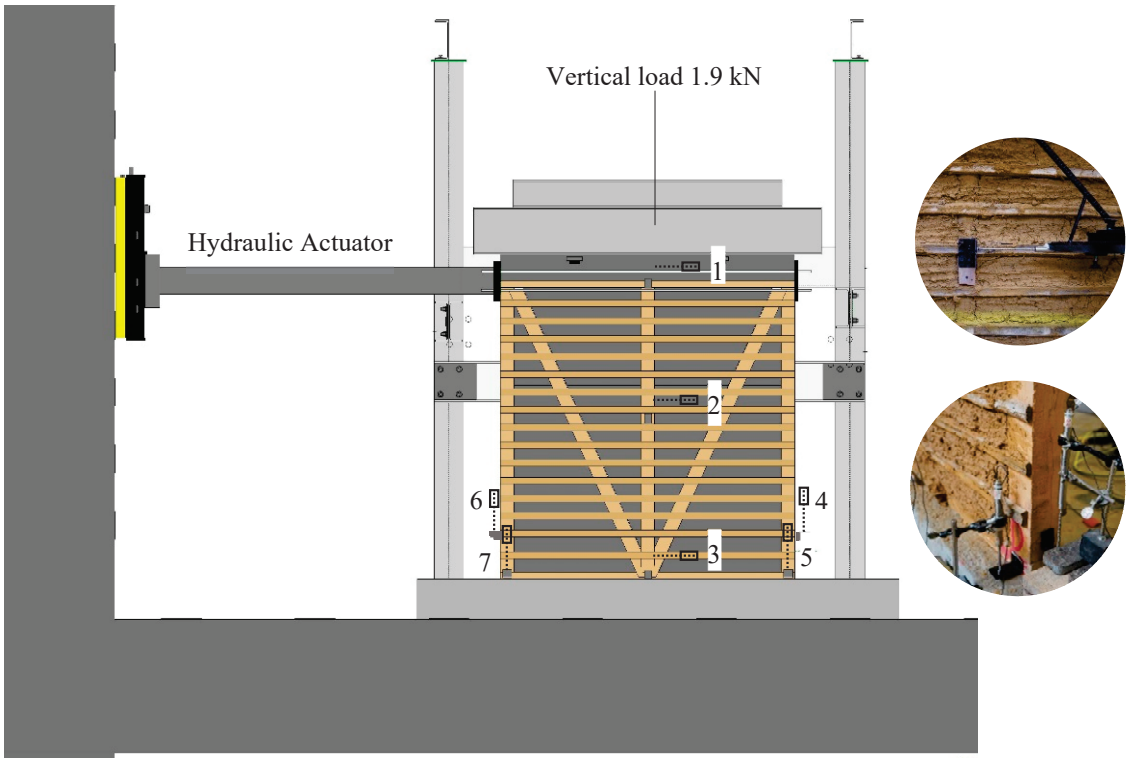

Figure 11. The instrumentation of the bahareque walls with LVDT sensors (Each number represents an installed LVDT sensor).

Figure 12. Mechanisms of failure for each of the 5 bahareque walls tested (Each number indicates the respective location of the photograph). (**a**) Photographs of failures after testing the GS prototype; (**b**) photographs of failures after testing the TSH prototype; (**c**) photographs of failures after testing the GSH prototype; (**d**) photographs of failures after testing the GSHS prototype; (**e**) photographs of failures after testing the TSHS prototype.

Similarly, to the previous wall, the TSHS bahareque wall was constructed with soil mix filler between the guadua strips, which was applied in three layers. Prior to the pseudo-static test, a drying period of one month was allowed. After drying, the filler soil shrank without delamination. Testing of the TSHS wall revealed steel nail detachment in some joints and lifting of vertical elements at the wall's ends (Figure 12e—1) and fractures in some guadua strips at the steel nail joints with the wooden elements (Figure 12e—2). Although noise was noted during the failure of the bahareque walls in all tests, the TSHS

wall exhibited particularly pronounced noise during the failure of the guadua strips, which showed multiple fractures. Additionally, the infill soil demonstrated a significant degree of delamination and separation from the wooden skeleton at the lower and upper sill beams, vertical members, and bracing (Figure 12e—3). Evidence of spalling and loss of soil fill was also observed at the conclusion of the experimental test.

In order to avoid the connection failures found in the tested bahareque models, reference [48] proposed a connection system that resists tensile and compressive forces. For walls made of guadua, the elements must be connected to the foundations according to the scheme shown in Figure 13. The system is based on a mortar–bahareque, where the internode elements of the guadua are filled with mortar. The guadua must not be in direct contact with the soil, masonry, or concrete; therefore, the guadua elements must be supported on a steel plate or other impermeable material separator. Compressive forces are transmitted through the separator, which must always rest on the foundation. Tensile forces are transmitted through pin connections. A pin passes through the first or second internode of the guadua element (filled with mortar), and this pin is anchored to the foundation with steel rods. This type of connection resists tensile forces but is not suitable for resisting bending moments. Reference [48] also includes examples of improved connections for wooden bahareque.

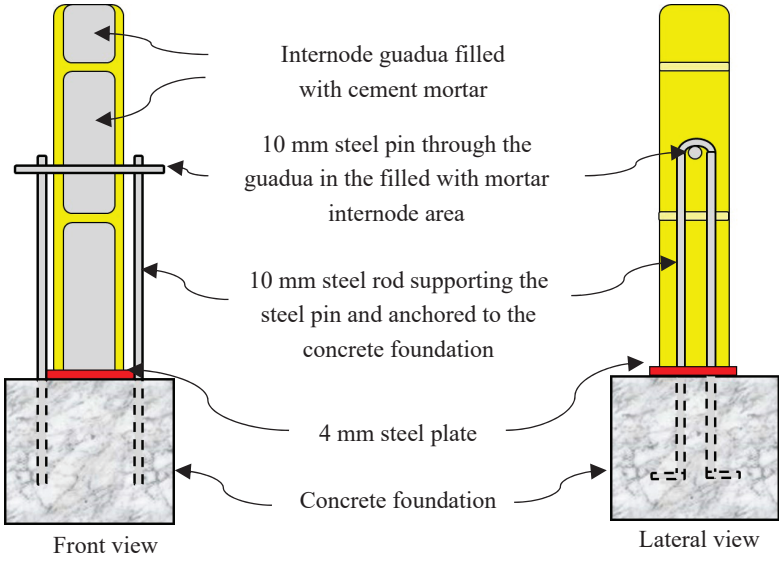

Figure 13. Example of improved connection between vertical guadua elements and foundation.

The enhanced connection design illustrated in Figure 13 provides a feasible solution to improve the performance of traditional bahareque systems. However, implementing such enhancements in rural and low-income areas faces significant logistical and economic challenges. The reliance on materials like mortar, cement, and steel introduces barriers due to their high cost and limited availability in remote regions. Transporting these materials to isolated areas, where infrastructure is often lacking, adds to the complexity and expense of adopting these improvements. Moreover, traditional construction practices in these communities are deeply rooted in locally sourced materials and techniques, making it challenging to introduce new methods without comprehensive training and support.

Figure 14 presents the in-plane hysteresis loops for the bahareque prototypes tested. The guadua skeleton (GS) wall exhibits narrow loops, indicating limited energy dissipation. Its force–displacement curve indicates relatively linear behavior during the initial loading cycles, with slight stiffness degradation as displacement increases.

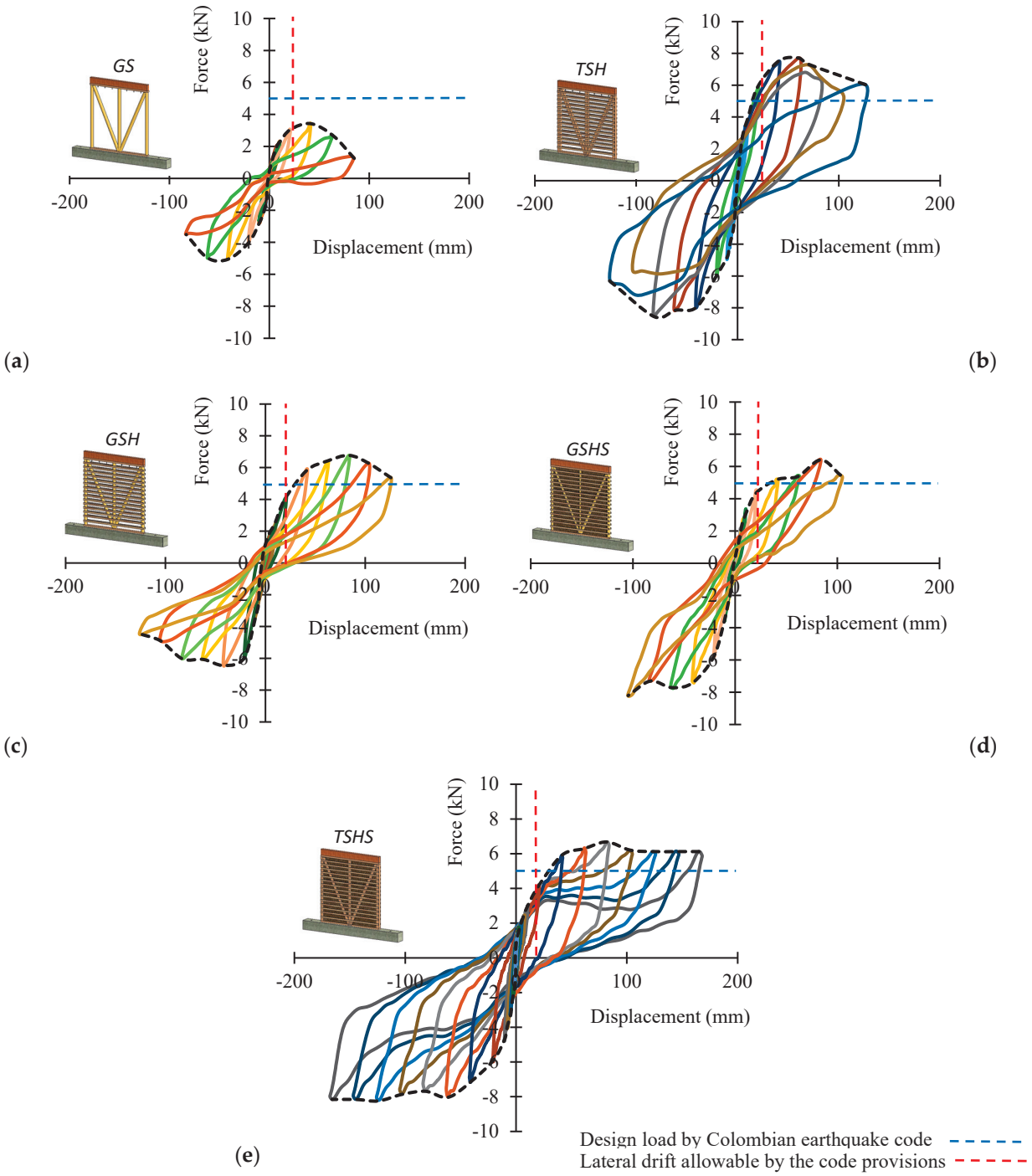

Figure 14. In-plane hysteresis loops for the tested bahareque prototypes. (**a**) Guadua skeleton (GS); (**b**) timber skeleton with horizontal strips (TSH); (**c**) guadua skeleton with horizontal strips (GSH); (**d**) guadua skeleton with horizontal strips and soil mixture infill (GSHS); and (**e**) timber skeleton with horizontal strips and soil mixture infill (TSHS).

The loops do not significantly expand, suggesting low energy absorption and moderate deformation capacity. Overall, the wall exhibits a stiff response with minimal nonlinear behavior. In contrast, the timber skeleton with horizontal guadua strips (TSH) shows more pronounced pinching effects in its hysteresis loops, indicative of reduced stiffness as displacement increases. The force–displacement curve reveals moderate energy dissipation, with wider loops suggesting greater ductility and a higher capacity for larger displacements and effective energy absorption compared to the GS wall.

The hysteresis cycles for the guadua skeleton with horizontal guadua strips (GSH) demonstrate a more stable cyclic behavior, with larger hysteresis loops compared to both the GS and TSH walls. Enhanced energy dissipation reflects a better balance between stiffness and ductility. The wider loops illustrate an improved capacity to absorb energy under cyclic loading, accompanied by a noticeable increase in displacement capacity.

The GSHS wall's wider hysteresis loops indicate greater ductility and better energy dissipation than previous wall types. The incorporation of the soil mixture improves structural performance under cyclic loading, enabling larger displacements with a gradual reduction in stiffness. This response demonstrates strong energy absorption characteristics, making the GSHS wall more suitable for seismic applications. Overall, this wall type exhibits excellent cyclic performance, with a superior ability to absorb energy and sustain larger displacements, rendering it the most resilient among the tested configurations.

The TSHS wall exhibited the best performance in terms of hysteresis cycles, establishing itself as the most effective bahareque wall type tested. The TSHS wall demonstrated remarkable ductility and resilience under load. The enhanced energy absorption capabilities of this wall are clearly reflected in its wide hysteresis loops, which indicate a higher capacity for energy dissipation during cyclic loading. Moreover, the hysteresis loops for the TSHS wall illustrate a significant ability to recover after unloading, suggesting effective energy absorption and dissipation mechanisms. The favorable hysteresis response of the TSHS wall underscores the importance of combining timber elements with soil mixture infill to enhance the seismic performance of traditional bahareque construction methods. It is important to note that Figure 14 includes the design load and lateral drift allowed by the code as horizontal (blue) and vertical (red) dotted lines. According to the results, all models except the GS specimen would be able to withstand the seismic forces and drift limit specified in the earthquake resistance code.

Finally, Table 1 summarizes the results of each tested bahareque wall, considering the following variables: maximum displacement achieved (both positive maximum and negative minimum), yield displacement (both positive and negative), strength, and yield force (both positive and negative). The GS wall has the lowest load and displacement capacity, with forces of 3.4–5.1 kN and 85 mm displacement. The TSH and GSH walls (timber skeleton and guadua skeleton with horizontal strips) demonstrate intermediate performance, achieving forces of 8.1 kN and 6.8 kN, respectively, and displacement capacities of 126 mm. In contrast, the GSHS and TSHS walls (those with soil mixture filling) exhibit the highest capacities, achieving maximum forces of about 8.4 kN and displacement capacities up to 166 mm.

Table 1. Strength, yield force, displacement capacity, and yield displacement for the bahareque tested walls.

Bahareque Wall	Strength + (kN)	Strength − (kN)	Yield Force + (kN)	Yield Force − (kN)	Max. Displ. + (mm)	Min. Displ. + (mm)	Yield Disp. + (mm)	Yield Disp. − (mm)
GS	3.4	−5.1	2.1	−3.0	85.0	−83.4	7.5	−10.5
TSH	7.7	−8.1	4.9	−5.4	126.0	−126.0	14.9	−15.4
GSH	6.8	−6.0	4.0	−4.7	125.6	−126.1	19.5	−15.5
GSHS	6.4	−8.4	4.3	−5.8	103.0	−104.7	20.2	−20.7
TSHS	6.7	−8.3	4.1	−5.3	165.1	−166.1	20.0	−15.4

The stiffness degradation curves are presented in Figure 15 to complement the analysis of the hysteresis loops by highlighting the differences in stiffness behavior among the five tested bahareque wall models. The GS wall exhibits the most rapid degradation, becoming the least stiff at larger displacements. In contrast, the GSHS and TSHS walls, which demonstrate the widest hysteresis loops and highest energy dissipation, exhibit more stable

stiffness degradation at larger displacements. This underscores the significance of the soil mixture infill and guadua strips in enhancing the seismic in-plane performance. Overall, the walls with wooden skeletons (TSH and TSHS) provide superior performance, combining good initial stiffness with gradual degradation. Based on the data of Figure 15, it was found that the walls with guadua skeletons (GSH and GSHS) had an average initial stiffness of about 0.6 kN/mm, while the walls with wooden skeletons (TSH and TSHS) had an average initial stiffness of about 0.9 kN/mm, which is 50% higher. At a drift level of 1% (0.01), the stiffness degradation observed in the GSHS and TSHS walls from the present study aligns with trends reported in similar traditional seismic wall systems. For example, the TSHS specimen shows improved stiffness retention compared to findings in [49] and [15], where walls without infill exhibited a sharper reduction in stiffness. Similarly, the GSHS model, with its soil infill and guadua strips, demonstrates a more gradual stiffness degradation than the results presented in [14] for timber walls with masonry infill. However, the stiffness degradation in the present study is comparable to results reported in [38]. On the other hand, the results in [16] emphasize the role of structural connections, which appear to be a limiting factor in the GSHS model due to the influence of nail pullout and joint behavior under cyclic loading.

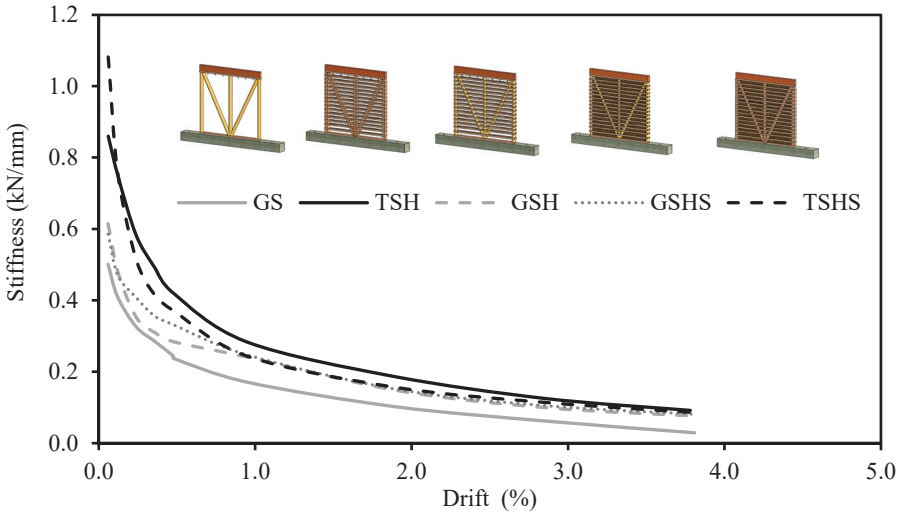

Figure 15. Stiffness degradation of the bahareque walls tested.

Finally, the comparison between bahareque walls with and without soil infill highlights significant differences in seismic performance, which can be attributed not only to the presence of the soil infill but also to the role of the horizontal guadua strips installed to contain it. Walls with soil infill, such as the GSHS and TSHS prototypes, demonstrated good energy dissipation and ductility. The soil infill acted as an energy-absorbing buffer during cyclic loading, while the horizontal guadua strips provided additional lateral confinement, enhancing structural stability. These walls showed a delayed onset of failure, higher displacement capacities (up to 166 mm), and improved stiffness retention compared to walls without infill (e.g., GS), which reached a maximum displacement of only 85 mm. In contrast, non-infill walls had premature joint failure due to nail pullout and limited load distribution. This combination of soil infill and guadua strips not only increased the walls' energy dissipation capacity but also reduced the risk of brittle failures by enhancing the ductility and integrity of the overall system.

Several studies have reported the energy dissipation of bahareque or wooden frames under pseudo-static loading, as observed in experimental hysteresis loops. The amount of energy dissipated depends on factors such as the specimen's size, resistance, and system flexibility. Consequently, this energy (measured in joules or kilojoules) is not directly

comparable across models from different studies due to variations in these geometric and mechanical parameters. To address this, researchers often report the evolution of equivalent hysteretic damping as a function of drift, which provides a standardized metric. Equivalent damping relates the energy dissipated through hysteresis to the elastic energy, offering a consistent basis for comparison. Based on the above, Table 2 presents a comparison of equivalent damping values reported by various authors. These values, measured at a 1% drift, are contrasted with the results obtained for the GSHS and TSHS models.

Table 2. A comparison of equivalent viscous damping ratios for timber/bamboo frame walls reported and the present study (measured at a 1% drift).

Reference	Type of Model Tested	Equivalent Viscous Damping Ratio
[38]	Composite mortar bamboo walls with diagonal bamboo strips	16.5%
[14]	Timber-framed walls: unreinforced, with GFRP at the connections; with brick masonry infill	10~19%
[49]	Timber frame with no masonry infill and timber frame with masonry infill	7% and 14%
[3]	Timber-framed structures filled with natural stones and adobe	13~27%
[15]	Timber frame walls infilled with brick masonry, lath and plaster, no infill	10.5~16%
[16]	Timber frame wall infilled with mud masonry featuring two different types of bracing system connections	5% and 14%
[6]	Timber frame with wooden panel infills and timber frames with brick masonry infills	8~12.5%
Present study	TSHS	14.7%
Present study	GSHS	11.3%

According to Table 2, TSHS and GSHS models exhibit equivalent viscous damping ratios of 14.7% and 11.3%, respectively. When compared with the data from previous studies, these values align closely with those reported for timber frame walls with masonry or panel infills. Notably, the TSHS model demonstrates comparable performance to systems such as timber frames with brick masonry infills and composite mortar bamboo walls, highlighting its superior energy dissipation capacity. In contrast, the GSHS model shows slightly lower damping values but still outperforms some timber walls without masonry infill. These findings suggest that the incorporation of soil infill and guadua strips significantly enhances the energy dissipation performance of bahareque walls.

6. Conclusions

This study provides a comprehensive evaluation of the seismic performance of bahareque walls constructed with guadua and timber frames. Key conclusions from this study are summarized below.

Displacement capacity was a key finding of the study and prototype TSHS (timber skeleton with horizontal guadua strips and soil mixture infill) exhibited an enhanced displacement capacity with recorded maximum displacements up to 166 mm (and wider hysteresis loops indicating higher energy dissipation). This displacement capacity is important for dissipating seismic energy without compromising overall structural integrity. The hysteresis loop analysis showed that wooden skeletons with guadua strips infilled with soil mix exhibited notably wider loops, an indication of superior energy dissipation during cyclic loading. In contrast, the GS wall had the worst displacement capacity, with a maximum reached displacement of 83 mm. However, it is important to note that the results are based on laboratory-controlled conditions, which may not fully represent the variability of traditional construction practices in the field.

The strength of the system showed differences between configurations; for instance, the results indicate that the strength of the bahareque system with a wood skeleton is on average 23% higher than that of the guadua skeleton (when comparing TSH and GSH). In

addition, the soil-infilled walls showed improvements in load-bearing capacity, achieving maximum in-plane shear strengths of up to 8.4 kN (TSHS wall). This fact highlights the importance of infill materials and guadua strips in seismic design, which can improve structural performance under lateral forces. While these results highlight the importance of material combinations, the influence of long-term environmental factors, such as moisture or soil degradation, was not evaluated and could affect performance over time.

The horizontal guadua strips affect the performance of the structural system, and an example of this fact is the notable difference between the GSH and the GS walls, where the guadua strips contribute significantly to the strength, displacement capacity, and ductility of the structure by allowing for energy absorption and reducing the risk of brittle failure under load reversals. While the average strength of the GS wall was 4.2 kN (average between maximum positive force and maximum negative force in absolute value), the strength of the GSH wall was 6.4 kN (51% higher). The same observation applies to the displacement capacity, since the wall without guadua strips (GS) had an average displacement capacity of 84 mm (average between maximum positive displacement and maximum negative displacement in absolute value), while the GSH wall (with guadua strips) had an average maximum displacement of 126 mm (50% higher). Nevertheless, the variability in guadua properties and the nail connections introduces uncertainties, which should be explored in subsequent investigations.

Failure mechanisms differed between models with and without infill; for example, infill models generally retained structural integrity longer, with cracks occurring in the soil infill rather than in the primary load-bearing members, suggesting that the infill acted as an energy-dissipating buffer. In contrast, the non-infill models exhibited early failure at the joints, primarily due to the detachment of vertical members from the lower sill beams as a result of nail pullout. This behavior indicates that without the added stability of the infill, structural weaknesses at the joints become critical failure points. Among the materials tested, the wood skeleton models generally demonstrated superior performance compared to the guadua-based structures, highlighting the role of material selection in joint performance.

The stiffness of the structures also varied by design and materials; according to the stiffness analysis, it was found that the wood-framed walls (TSH and TSHS) had an average initial stiffness 50% higher than the guadua-framed walls (GSH and GSHS). In addition, the soil infill and the guadua strips not only increase the energy absorption capacity but also contribute to maintaining the structural stiffness throughout the loading cycle.

The seismic suitability of the models was evident in the results, as the soil-infilled, guadua strip, wood frame model improved load-bearing and energy-dissipating capacity, along with improved structural stability over repeated load cycles, making it preferable for applications in seismically active areas. However, the results are limited to the tested prototypes, and additional dynamic testing under simulated earthquake conditions is required to confirm their performance in real scenarios. To promote the adoption of these systems in seismically active regions, public policies should focus on providing technical guidance, financial incentives, and training programs for rural communities. These measures can facilitate the integration of improved bahareque techniques into local construction practices, enhancing safety and sustainability.

7. Future Works

Future work will extend the scope of this study by incorporating a detailed analysis of the shear and tensile strength of guadua, wood, and soil filling materials, since these properties influence the behavior of structural joints, the cohesion, and the interaction between the frame and the soil mix under lateral loads. Another important aspect to

explore is the long-term durability of bahareque systems; future studies should evaluate the effects of environmental factors such as moisture, soil degradation, and exposure to humidity on the mechanical properties of the soil infill and the structural elements. In addition, dynamic testing under simulated seismic conditions will be important to validate the seismic suitability of the prototypes beyond static loading scenarios. Finally, the variability in natural materials, such as guadua and soil, presents a challenge to ensuring repeatable performance. Subsequent investigations should focus on characterizing this variability and identifying practical methods to improve standardization during material preparation and construction.

Author Contributions: Conceptualization: I.F.O., J.D.V.-M., O.C. and D.M.R.; funding acquisition: I.F.O., J.D.V.-M., O.C. and D.M.R.; formal analysis: K.C., I.F.O., D.M.R. and N.B.; methodology: K.C., D.M.R., N.B., I.F.O. and Y.A.A.; project administration: I.F.O. and J.D.V.-M.; supervision: I.F.O., D.M.R. and Y.A.A.; resources: Y.A.A., D.M.R. and I.F.O.; writing—original—draft: D.M.R. and K.C.; visualization: N.B., D.M.R. and K.C.; writing—review and editing: N.B., J.D.V.-M. and I.F.O. All authors have read and agreed to the published version of the manuscript.

Funding: This research was funded by the Pontificia Universidad Javeriana through, project ID: 20406, "Investigar PUJ" code 2112, entitled "Propuesta de edificación rural eco-amigable con muros de bahareque no cementado—Etapa 1".

Data Availability Statement: The data are available upon request.

Acknowledgments: The research was developed in the Structures Laboratory of Pontificia Universidad Javeriana, Bogotá. The authors thank the technical staff, particularly Jaime Cruz for building the bahareque earthen walls.

Conflicts of Interest: The authors declare no conflicts of interest. The funders had no role in the design of the study; in the collection, analyses, or interpretation of data; in the writing of the manuscript; or in the decision to publish the results.

References

1. Huang, H.; Wu, Y.; Li, Z.; Sun, Z.; Chen, Z. Seismic behavior of Chuan-Dou type timber frames. *Eng. Struct.* **2018**, *167*, 725–739. [CrossRef]
2. Xie, Q.; Wang, L.; Zhang, L.; Hu, W.; Zhou, T. Seismic behaviour of a traditional timber structure: Shaking table tests, energy dissipation mechanism and damage assessment model. *Bull. Earthq. Eng.* **2019**, *17*, 1689–1714. [CrossRef]
3. Champagne, A.; Doudak, G.; Dolan, J.D. Experimental analysis of seismic resistance of timber-framed structures. *Eng. Struct.* **2014**, *60*, 48–59. [CrossRef]
4. Crayssac, E.; Song, X.; Wu, Y.; Li, K. Lateral performance of mortise-tenon jointed traditional timber frames with wood panel infill. *Eng. Struct.* **2018**, *161*, 223–230. [CrossRef]
5. Meng, X.; Li, T.; Yang, Q. Experimental study on the seismic mechanism of a full-scale traditional Chinese timber structure. *Eng. Struct.* **2019**, *180*, 484–493. [CrossRef]
6. Guo, T.; Yang, N.; Zhou, H.; Wang, S. In-plane behavior of Chuan-Dou style wooden frames with infill under cyclic loading. *Structures* **2022**, *41*, 1311–1328. [CrossRef]
7. Xie, Q.; Tong, Y.; Zhang, L.; Li, S.; Wang, L. Seismic Behavior of Chinese Traditional Timber Frames with Masonry Infill Wall: Experimental Tests and Hysteretic Model. *Int. J. Archit. Herit.* **2021**, *15*, 1130–1144. [CrossRef]
8. Chang, W.S.; Komatsu, K. On mechanical behavior of traditional timber shear wall in Taiwan I: Background and theory derivation. *J. Wood Sci.* **2007**, *53*, 17–23. [CrossRef]
9. Chang, W.-S.; Komatsu, K. On mechanical behavior of traditional timber shear wall in Taiwan II: Simplified calculation and experimental verification. *J. Wood Sci.* **2007**, *53*, 24–30. [CrossRef]
10. Xie, Q.; Zhang, B.; Li, S.; Wu, F.; Yang, F. Effects of timber infill walls on the seismic behavior of traditional Chinese timber frames. *Earthq. Eng. Eng. Vib.* **2022**, *21*, 999–1018. [CrossRef]
11. Xue, J.; Guo, R.; Xu, D.; Qi, L.; He, Z. Shaking Table Test on 1/2-Scale Model of Column-and-Tie Timber Structure Filled with Wooden Walls. *J. Struct. Eng.* **2020**, *146*, 04020281. [CrossRef]
12. Liang, W.; Lan, J.; Zou, Z.; Zhu, Z.; Zhai, S.; Mo, Y.; Li, X.; Meng, S.; Cai, Y. Seismic behavior of Chuan-dou timber frames with different infilled walls. *Constr. Build. Mater.* **2022**, *327*, 126906. [CrossRef]

13. Dutu, A.; Barbu-Mocanescu, D.; Niste, M.; Spatarelu, I.; Yamazaki, Y.; Kober, D. In-plane static tests on a structural timber frame system proposal (TRAROM) inspired from traditional architecture and using local materials. *Eng. Struct.* **2020**, *212*, 110491. [CrossRef]
14. Vasconcelos, G.; Poletti, E.; Salavessa, E.; Abílio, M.; Lourenço, P.; Pilaon, P. In-plane shear behaviour of traditional timber walls. *Eng. Struct.* **2013**, *56*, 1028–1048. [CrossRef]
15. Poletti, E.; Vasconcelos, G. Seismic behaviour of traditional timber frame walls: Experimental results on unreinforced walls. *Bull. Earthq. Eng.* **2015**, *13*, 885–916. [CrossRef]
16. Dutu, A.; Niste, M.; Spatarelu, I.; Dima, D.; Kishiki, S. Seismic evaluation of Romanian traditional buildings with timber frame and mud masonry infills by in-plane static cyclic tests. *Eng. Struct.* **2018**, *167*, 655–670. [CrossRef]
17. Li, X.; Zhao, J.; Ma, G.; Chen, W. Experimental study on the seismic performance of a double-span traditional timber frame. *Eng. Struct.* **2015**, *98*, 141–150. [CrossRef]
18. Panoutsopoulou, L.; Meimaroglou, N.; Mouzakis, C. Shaking table tests on single-bay timber-framed wall specimens with fired brick and adobe block infills and mortise-tenon joints. *J. Build. Eng.* **2023**, *76*, 107380. [CrossRef]
19. Meireles, H.; Bento, R.; Cattari, S. A hysteretic model for "frontal" walls in Pombalino buildings. *Bull. Earthq. Eng.* **2012**, *10*, 1481–1502. [CrossRef]
20. Lukic, R.; Poletti, E.; Rodrigues, H.; Vasconcelos, G. Numerical modelling of the cyclic behavior of timber-framed structures. *Eng. Struct.* **2018**, *165*, 210–221. [CrossRef]
21. Dutu, A.; Yamazaki, Y.; Sakata, H. Shear spring model proposed for seismic evaluation of a timber framed masonry infilled wall. *Eng. Struct.* **2018**, *167*, 201. [CrossRef]
22. Gani, A.; Banday, J.M.; Rai, D.C. Seismic evaluation of traditional timber framed masonry systems using shake table tests and finite element modelling. *Innov. Infrastruct. Solut.* **2023**, *8*, 231. [CrossRef]
23. Herrera, J.C.; Takeuchi, C. Comportamiento de pórticos en Guadua angustifolia, rigidizados mediante páneles prefabricados en bahareque. *Rev. Ing. E Investig.* **2009**, *29*, 5–12. Available online: https://repositorio.unal.edu.co/handle/unal/29173 (accessed on 19 December 2024).
24. Muñoz, J. Tipificación de los Sistemas Constructivos de "Bahareque" en el Paisaje Cultural Cafetero de Colombia. 1–101. 2010. Available online: https://repositorio.unal.edu.co/bitstream/handle/unal/64733/9789588280400.pdf?sequence=2&isAllowed=y (accessed on 19 December 2024).
25. Silva, M.; Lopez, L. Comportamiento Sismo-Resistente de Estructuras en Bahareque Mechanical Properties Characterization of Philippine Bamboos View Project. Ph.D. Thesis, Universidad Nacional De Colombia Manizales, Caldas, Colombia, 2000. [CrossRef]
26. Lopez, M.; Bommer, J.; Mendez, P. The seismic performance of bahareque dwellings in El Salvador. In Proceedings of the 13th World Conference on Earthquake Engineering, Vancouver, BC, Canada, 1–6 August 2004.
27. Rizo, A.; Garay, L.; Monsalve, F. El bahareque y el adobe, como técnica constructiva sismo-resistente. *Form. Estratégica* **2021**, *3*, 1–13. Available online: https://www.formacionestrategica.com/index.php/foes/article/view/46 (accessed on 19 December 2024).
28. Mite, F.; Tello, K.; García, N.; Silva, C.; Malaga, C.; Arévalo, K.; Villao, D. Structural behavior of cemented bahareque for social housing: A case study in Guayaquil City, Ecuador. *Front. Built Environ.* **2022**, *8*, 922397. [CrossRef]
29. Neves, C. *Materiais de Construção e Sistemas Construtivos com Terra*; Ed. da Autora: Salvador, Brazil, 2023. Available online: https://redeterrabrasil.net.br/publicacoes/ (accessed on 19 December 2024).
30. Henneberg, A. Tradición Constructiva del Bahareque y su Resistencia Sísmica. Arquitectura en Tierra. Patrimonio Cultural. *XII CIATTI*. Congreso de Arquitectura en Tierra en Cuenca de Campos 2015. Valladolid. 2015. Available online: https://www5.uva.es/grupotierra/publicaciones/digital/libro2015/024henneberg.pdf (accessed on 19 December 2024).
31. Palacios, A.; Angumba, P. Bahareque as a Sustainable Construction System: Analysis of Unit Prices. *IOP Conf. Ser Mater. Sci. Eng.* **2021**, *1203*, 032118. [CrossRef]
32. Manandhar, R.; Kim, J.H.; Kim, J.T. Environmental, social and economic sustainability of bamboo and bamboo-based construction materials in buildings. *J. Asian Archit. Build. Eng.* **2019**, *18*, 49–59. [CrossRef]
33. Gomez, B. *Evaluación del Comportamiento de Viviendas de Bahareque con el Sismo del 25 de enero de 1999*; Universidad Nacional de Colombia: Bogotá, Colombia, 2002. Available online: https://repositorio.unal.edu.co/handle/unal/70184 (accessed on 19 December 2024).
34. Zhao, J.; Qiu, H. Seismic performance assessment of a multi-story bamboo frame structure. *Adv. Bamboo Sci.* **2023**, *2*, 100011. [CrossRef]
35. Van der Lugt, P.; Van den Dobbelsteen, J. An environmental, economic and practical assessment of bamboo as a building material for supporting structures. *Constr. Build. Mater.* **2006**, *20*, 648–656. [CrossRef]
36. Cutiño, G.; Esteves, A. Wattle and daub experimental workshop: Durability testing after 14 years of uninterrupted use. *Eur. J. Eng. Res. Sci.* **2018**, *3*, 78–83. Available online: https://sryahwapublications.com/article/download/2637-5796.0104003 (accessed on 19 December 2024). [CrossRef]

37. Zhang, M.; Fan, H.; Li, W.; Wu, H.; Yu, Z.; Zhao, S.; Zhou, Q.; Liu, C.; Li, Y.; Luo, H.; et al. Study on the elastic stiffness calculation method of single-bolted steel-bamboo scrimber-steel shear connections. *Eng. Struct.* **2024**, *301*, 117331. [CrossRef]
38. Hao, J.; Cai, Z.; Kou, Y. Effect of diagonal bamboo strips on seismic behavior of sprayed composite mortar-original bamboo composite walls: An experimental study. *J. Build. Eng.* **2023**, *79*, 107829. [CrossRef]
39. Puri, V.; Chakrabortty, P.; Anand, S.; Majumdar, S. Bamboo reinforced prefabricated wall panels for low cost housing. *J. Build. Eng.* **2017**, *9*, 52–59. [CrossRef]
40. Zea, E.; Habert, G.; Correal-Daza, J.; Archilla, H.; Echeverry, J.; Trujillo, D. Industrial or Traditional Bamboo Construction? Comparative Life Cycle Assessment (LCA) of Bamboo-Based Buildings. *Sustainability* **2018**, *10*, 3096. [CrossRef]
41. Kaminski, S.; Lawrence, A.; Trujillo, D. Design Guide for Engineered Bahareque Housing. Inbar Technical Report N° 38. 2016. Available online: https://www.researchgate.net/publication/311583390_Design_Guide_for_Engineered_Bahareque_Housing (accessed on 19 December 2024).
42. Ortega, J.; Vasconcelos, G.; Rodrigues, H.; Correia, M.; Lourenço, P. Traditional earthquake resistant techniques for vernacular architecture and local seismic cultures: A literature review. *J. Cult. Herit.* **2017**, *27*, 181–196. [CrossRef]
43. *ASTM D422*; ASTM-American Society for Testing and Materials. Standard Test Method for Particle-Size Analysis of Soils: West Conshohocken, PA, USA, 2007.
44. *ASTM D698*; ASTM-American Society for Testing and Materials. Standard Test Methods for Laboratory Compaction Characteristics of Soil Using Standard Effort: West Conshohocken, PA, USA, 2021.
45. *ISO 22157*; Bamboo Structures—Determination of Physical and Mechanical Properties of Bamboo Culms—Test Methods. ISO: Geneva, Switzerland, 2019.
46. *ASTM E2126*; ASTM-American Society for Testing and Materials. Standard Test Methods for Cyclic (Reversed) Load Test for Shear Resistance of Vertical Elements of the Lateral Force Resisting Systems for Buildings: West Conshohocken, PA, USA, 2007.
47. *ISO 16670*; Timber structures—Joints made with mechanical fasteners—Quasi-static reversed-cyclic test method. ISO: Geneva, Switzerland, 2003.
48. AIS (Asociación Colombiana de Ingeniería Sísmica). Manual de Construcción Sismo Resistente de Viviendas en Bahareque Encementado [Manual for Earthquake Resistant Construction of Cemented Bahareque Housing]. 2001. Available online: https://catalogo.sgc.gov.co/cgi-bin/koha/opac-detail.pl?biblionumber=73720 (accessed on 19 December 2024).
49. Dutu, A.; Sakata, H.; Yamazaki, Y.; Shindo, T. In-Plane Behavior of Timber Frames with Masonry Infills under Static Cyclic Loading. *J. Struct. Eng.* **2015**, *142*, 04015140. [CrossRef]

buildings

MDPI

Article

Research on the Lateral Resistance of Column Frames in the Tang Dynasty: A Case Study of the Straight Tenon Joints Under Varied Vertical Load Levels

Xiang Gan †, Fanxu Kong †, Ziyi Wang, Xinran Li, Tingyu Meng, Jiayang Wang, Qin Wang, Jinqiu Xie and Zeli Que *

College of Material Science and Engineering, Nanjing Forestry University, Nanjing 210037, China; xianggan@njfu.edu.cn (X.G.); fanxukong@njfu.edu.cn (F.K.); wzy020709@njfu.edu.cn (Z.W.); lixinran@njfu.edu.cn (X.L.); 1547376061@njfu.edu.cn (T.M.); jiayangwang@njfu.edu.cn (J.W.); 2110401220@njfu.edu.cn (Q.W.); jinqiuxie@njfu.edu.cn (J.X.)

* Correspondence: zelique@njfu.edu.cn

† These authors contributed equally to this work.

Abstract: Column frames connected using Tang Dynasty straight tenon joints represent a unique structural system characterized by historical significance and architectural ingenuity. Consequently, an experimental model, resembling the straight tenon joint style of the Tang Dynasty Foguang Temple East Hall, was constructed using two square beams (Fangs) and three columns in this study. Through low-cycle repeated load tests, hysteretic curves, stiffness degradation, energy dissipation capabilities, and certain other indicators were analyzed under four distinct vertical load levels. The results reveal that increasing the vertical load can effectively improve the fullness of the hysteresis curve and the peak restoring force of the column frame. Moreover, a pronounced pinch effect was found in the hysteretic curve of the column frame, indicating that a higher vertical load can strengthen the frame's restoring force within a specific range of horizontal displacement, thereby maintaining its structural stability. With increasing vertical loads, the maximum restoring force and stiffness of the column frame are elevated, enhancing the structure's energy dissipation capacity and partially mitigating its stiffness degradation. However, it is noteworthy that as the horizontal load displacement increases, higher vertical loads result in a more rapid decline in the frame's restoring force, reducing the effectiveness of improving the energy dissipation capabilities of the column frame.

Keywords: Foguang Temple; column frame structure; straight tenon joints; vertical load; lateral resistance

1. Introduction

China is an earthquake-prone country with multiple seismic zones, among which the North China seismic zone covers Shanxi, Beijing, and other places where ancient buildings are richly preserved [1,2]. Ancient buildings in many earthquake-prone areas have been under the threat of earthquakes for hundreds of years. It can be seen that traditional wooden buildings can be preserved to a large extent due to their good seismic performance [3]. The East Main Hall of Foguang Temple represents the sole surviving example of a Tang Dynasty hall-style timber structure within China and is a seminal representation of the wooden architectural heritage from the Tang era [4,5]. Situated in Shanxi province, this historical monument has endured several seismic activities, including three significant earthquakes with magnitudes exceeding 7 in the years 1038, 1626, and 1683 [6]. The remarkable seismic restoring force exhibited by traditional wooden structures is intimately associated with the

mortise-and-tenon joints that characterize their construction, with a particular emphasis on the joints within the column frames [7–9].

In the East Hall of Foguang Temple, the tenon configuration utilized is of the straight tenon variety. The column capitals feature grooves, and the beams maintain a consistent thickness and are directly inserted into the grooves of the column capitals [10]. This construction method is widely recognized by the academic community as one of the defining characteristics of Tang Dynasty architecture. In lateral resistance testing of mortise–tenon joints, a vertical load has been applied to the column top using a jack to simulate weight, while a horizontal cyclic load has been applied via an actuator or booster, controlled by displacement. These tests produced hysteresis loops that were fairly complete, showing the joints' effective deformation and energy dissipation [11–13]. The primary failure mode for straight mortise–tenon joints was the tenon being compressed against the mortise during rotation, leading to tenon pull-out failure [14–16].

In addition, the lateral resistance of column frames is also affected by vertical loads and repeated loads. Studies have shown that increasing vertical loads can significantly reduce the seismic displacement response of column frames [11], which is due to the increase in the roof weight, the decrease in the structural natural vibration frequency, and the increase in the final restoring force of the column frame [17]. With an increase in the vertical load, the lateral stiffness of the column frame will also increase, and an increase in the horizontal loading displacement will weaken the positive effect of the vertical load on the lateral stiffness [18]. However, these studies have mainly focused on single-span and four-beam, four-column models. The research results for single-span models have certain limitations when they are applied to the protection and restoration of actual multi-span ancient buildings, and they may not accurately simulate the performance of the overall structure. Although the four-beam, four-column model can clearly demonstrate the collaborative working relationship between the columns and beams, it still cannot cover the influence of multi-span combinations and other factors on the structural performance. Suzuki et al. [19] and Maeno et al. [17] examined the seismic performance of traditional Japanese wooden structures, revealing that the total restoring force of such structures is derived from column sway and the bending moment resistance of the mortise-and-tenon joints. Furthermore, they observed that the vertical load significantly impacts the restoring force generated by column sway. Although this study clarified that the total restoring force consists of the bending moment resistance from tie beams, as well as the restoring force due to column sway, the test model was of Japanese traditional wooden structures, which still significantly differed from the processing method of column frame joints during the specific historical period of the Tang Dynasty. Shi et al. [20] revealed deformation due to swing column rotation, friction slip, and embedded plastic deformation, which ultimately led to the degradation of the column frame's stiffness, in a single-span full-scale experiment model of Song Dynasty architecture. In addition, it was pointed out that repeated loading would reduce the energy dissipation, lateral stiffness, and bearing capacity of the column frame but basically did not affect the deformation ability of the column frame [11].

Despite extensive investigation into the stress performance of mortise-and-tenon joints, it is pertinent to highlight that the loading conditions simulated in certain experimental setups do not accurately replicate the conditions experienced by these joints in actual column frames. Consequently, examining mortise-and-tenon joints within the context of their application in real column frames yields a more precise understanding of their impact on the lateral resistance of the frame. Furthermore, the current body of research on the lateral resistance performance of traditional Chinese wooden building column structures predominantly concentrates on the various mortise-and-tenon joint configurations. In addition, there is a notable absence of studies that investigate the influence of differing vertical loads

on the resistance performance of these column structures, despite the considerable effect of vertical loads on the restoring force in response to sway and, by extension, the lateral resistance of the entire structure. Moreover, traditional buildings, such as the East Hall of Foguang Temple, are mostly multi-span structures in China. A double-span model can, to a certain extent, simulate the structural system of actual buildings better, and the research results are of greater reference value for understanding and protecting such buildings.

Thus, a two-span experimental model inspired by the East Hall of Foguang Temple was fabricated in this study, presenting the actual mechanical characteristics of ancient wooden structures more realistically. The influence of diverse vertical loads on the lateral resistance of the column frame was systematically investigated through low-cycle reversed loading tests at four levels of vertical loads, disclosing their impact on key parameters like the hysteresis curve, skeleton curve, stiffness degradation, and energy dissipation capacity. The behavior of the column frame was analyzed in depth, such as the relationship between the pinching effect of the hysteresis curve and the vertical load, offering a novel perspective for comprehending the complex mechanical behavior and facilitating the optimization of the design of and protection strategies for such structures.

2. Material and Methods

2.1. Material

The material used for the specimens was Fujian Chinese fir (*Cunninghamia lanceolata* (Lamb.) Hook.). After the completion of the test, the specimens were evaluated in accordance with current standards [21–27], wherein their physical and mechanical properties (Table 1) were assessed at a moisture content of 13.8% and an air-dry density of 0.371 g/cm^3.

Table 1. Physical and mechanical properties of the Chinese fir specimens (MPa).

Label	E_L	E_R	E_T	E_b	f_l	f_r	f_t	f_b
Average	11,959	1337	832	7670	28.7	2.5	2.0	49.4
Standard deviation	2550	244	121	1100	3.3	0.4	0.3	7.3

Notes: E_L: modulus of elasticity parallel to the grain direction; E_R: modulus of elasticity perpendicular to the grain direction; E_T: modulus of elasticity in the tangential direction; E_b: modulus of elasticity in bending; f_l: compressive strength parallel to the grain direction; f_r: compressive strength perpendicular to the grain direction; f_t: compressive strength in the tangential direction; f_b: bending strength.

2.2. The Test Model

This study presents the case of a test model of the East Hall of Foguang Temple. As illustrated in Figure 1, the model's dimensions are detailed, with the columns and Fangs interconnected using a straight tenon joint and brackets implemented to facilitate load transfer. In line with traditional Chinese wooden architecture, the reference building's column height-to-diameter ratio ranges from 8.54 to 9.91. Consequently, the columns are designed with a diameter of 232 mm and a height of 2110 mm (at a ratio of 9.09), with a center-to-center spacing of 1820 mm. The selection of these specific values mainly refers to existing study [28]. In addition, the Fangs are dimensioned with a length of 1720 mm, a thickness of 168 mm, and a width of 84 mm, which corresponds to the 84 mm diameter of the columns in the East Hall of Foguang Temple. The specified brackets (consisting of Dou and Gong, as shown in Figure 1) have a diameter of 232 mm and a height of 151 mm and include inserts with dimensions of 83 mm (width), 104 mm (height), and 571 mm (length) in two directions, designed to effectively transfer vertical loads. And the above dimensions were all obtained through scaling based on the ratio of the diameter of the test column to the diameter of the column of the East Hall of Foguang Temple.

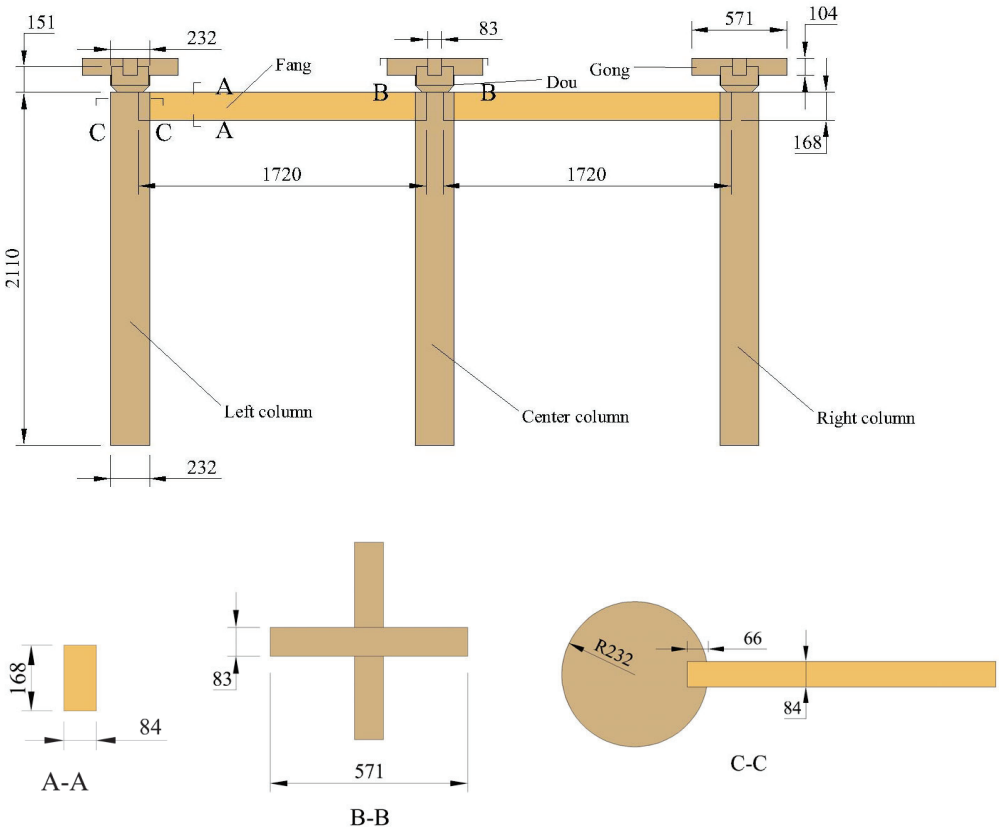

Figure 1. Test model (mm).

2.3. Testing Procedures

The testing procedure involved the use of a microcomputer-controlled o-hydraulic servo combined shear wall test system (model YAW-250J) for applying loads. Figure 2 depicts the test loading setup, where the horizontal actuator load in the left direction is designated as the forward load. The horizontal actuator has a travel range of ±250 mm and a maximum load capacity of 250 kN. The vertical loads, represented by P, were applied using a movable vertical hydraulic jack to simulate the roof load. These vertical loads were transmitted through steel beams to the distributing beams, which then allocated the loads to each column. Hence, the middle column received half of the total load ($P/2$), while the side columns received one-quarter of the total load ($P/4$), allowing for the simulation of two different loading scenarios in a single test [28]. The distributing beams were connected to the steel beams and the horizontal actuator via M24 high-strength bolts. The loading point of the horizontal actuator was located 2400 mm above the column base. The direction of horizontal push was defined as the positive direction, while the direction of horizontal pull was defined as the negative direction.

2.4. The Loading Scheme

In this testing procedure, four distinct levels of vertical loading were applied consecutively. The initial vertical load was set at 45 kN, reflecting the roof load of traditional ancient structures [11]. The second vertical load was adjusted to 50.5 kN, corresponding to the roof load of the main hall at Foguang Temple. To examine the impact of the vertical load on the lateral resistance of the column frame further, the third and fourth vertical loads were increased to 75.5 kN and 90 kN, respectively.

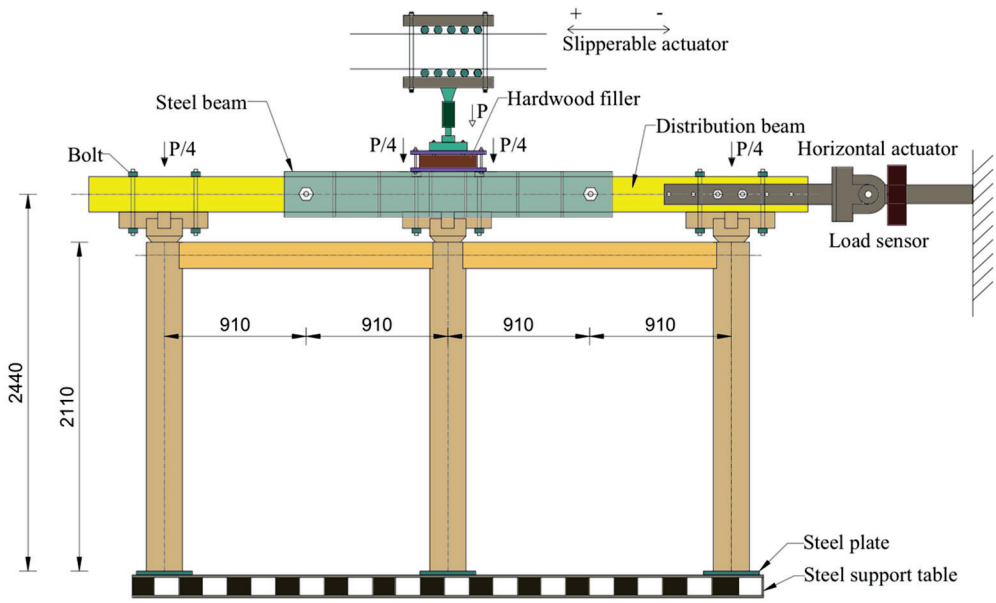

Figure 2. Test setup (mm).

The vertical load was applied to the steel beam using a sliding driver, which evenly distributed the load to each column through a distribution beam. The horizontal loading displacement was precisely controlled using a horizontal actuator to test the reference wooden frame shear wall system. As detailed in Figure 3 and Table 2, during the test, each cycle was replicated once; that is, one positive and one negative horizontal displacement were imposed each time, followed by progression to the next cycle [28]. The horizontal restoring force (F) and displacement (X) of the specimen were automatically recorded using a microcomputer-controlled electro-hydraulic servo system designed for shear wall experiments.

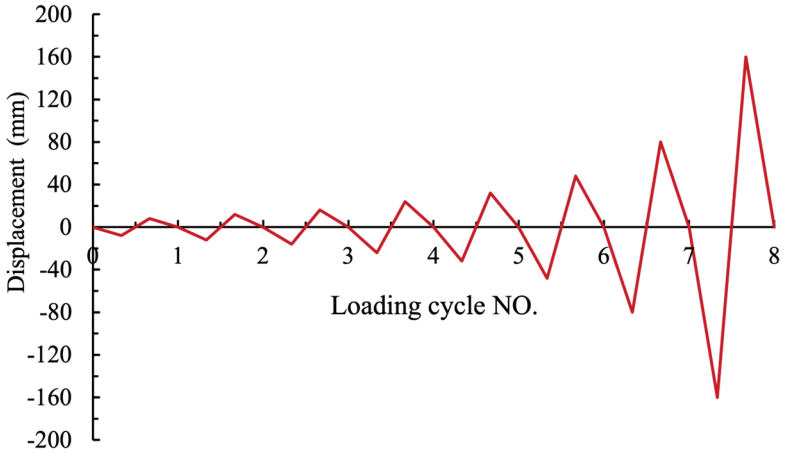

Figure 3. Loading procedure adopted in the cyclic tests.

Table 2. Scheme of horizontal loading cycle.

Label	Loading Cycle No.							
	1	**2**	**3**	**4**	**5**	**6**	**7**	**8**
Displacement/mm	±8	±12	±16	±24	±32	±48	±80	±160
Angle of roll/rad	±1/300	±1/200	±1/150	±1/100	±1/75	±1/50	±1/30	±1/15

3. Results and Discussion

3.1. Experimental Phenomena

The deformation patterns observed in the column frame across the four tests were largely consistent, with no signs of failure or significant slippage at the column bases. Initially, under horizontal loading, no remarkable phenomena were detected during the observation tests. However, as the horizontal displacement increased, extrusion and frictional slippage became evident at the mortise-and-tenon joints between the columns and the Fangs. This extrusion led to variable compression on the upper and lower surfaces of the mortise-and-tenon joints. At a horizontal displacement of $|X| = 160$ mm (1/15 rad), an assessment of the column frame's deformation under four different vertical load conditions revealed that despite a 45 kN range in the vertical loads, the rotational deformation of the column frame, as depicted in Figure 4, exhibited negligible differences. A detailed examination of the four vertical load test sets indicated that the pull-out lengths of the tenons, as shown in Figure 5, remained fairly stable, with measurements of 12.5 mm, 12.6 mm, 12.9 mm, and 13.5 mm for vertical loads of 45 kN, 50.5 kN, 75.5 kN, and 90 kN, respectively. This uniformity suggests that vertical load has a minimal impact on the rotational deformation of the column frame or the rotation of the Fangs. Furthermore, when the column frame was subjected to a horizontal displacement of 160 mm, a slight difference in inclination was recorded at the bases of the left and right columns, with the left column exhibiting a slightly greater tilt, as illustrated in Figure 6.

(**a**) 45 kN (**b**) 90 kN

Figure 4. Rotational deformation of the column frame under varied vertical loads: a comparison of 45 kN and 90 kN load conditions.

Following the unloading process, a detailed inspection of each component was conducted. The column exhibited negligible extrusion deformation at the mortise-and-tenon joints. In contrast, the end of the Fangs displayed more pronounced extrusion deformation. This discrepancy is attributed to the substantial difference in the compressive strength between the longitudinal and transverse directions of the grain. Columns mainly withstand longitudinal compression in the vertical direction, and their superior longitudinal performance results in the relatively minor deformations of the columns. However, the ends of the Fangs are exposed to complex stress states in both the tangential and radial directions under horizontal loads, and anisotropy renders them more susceptible to large deformations. As depicted in Figure 7, the extrusion deformation at the ends of Fangs is more conspicuous.

Figure 5. Pull-out lengths of tenons across four different load conditions.

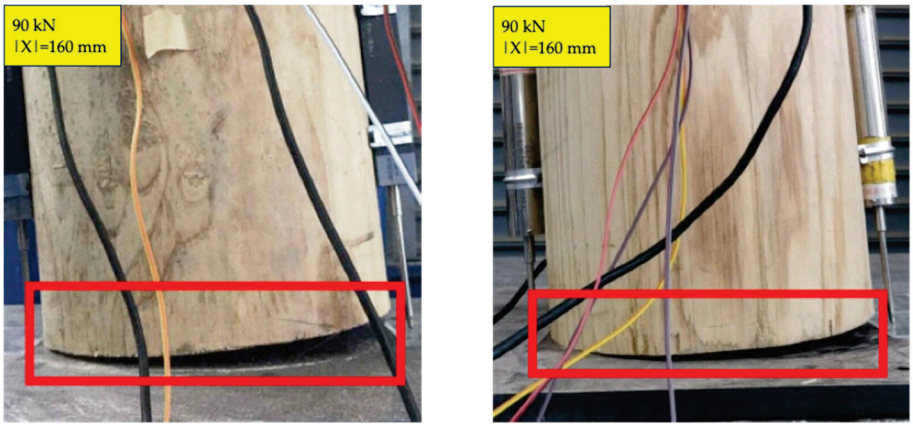

(**a**) Left column (**b**) Right column

Figure 6. Rotation angles at column bases under forward loading at 90 kN vertical load with 160 mm horizontal displacement.

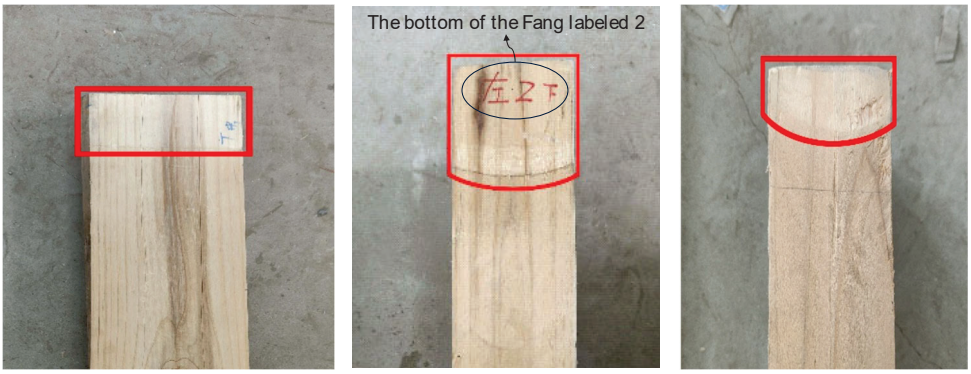

(**a**) Side view (**b**) Bottom view (**c**) Top view

Figure 7. Extrusion observations on the sides and surfaces of the Fangs.

3.2. Hysteretic Curves

Figure 8 illustrates the hysteretic curves of the column frame subjected to four different vertical loads. The hysteretic loops for the Tang Dynasty column frame structure are observed to have full loops at the ends, with an S-shaped middle section that exhibits a clear pinching effect. This pinching suggests that the structure experiences significant sliding friction between the mortise-and-tenon joints.

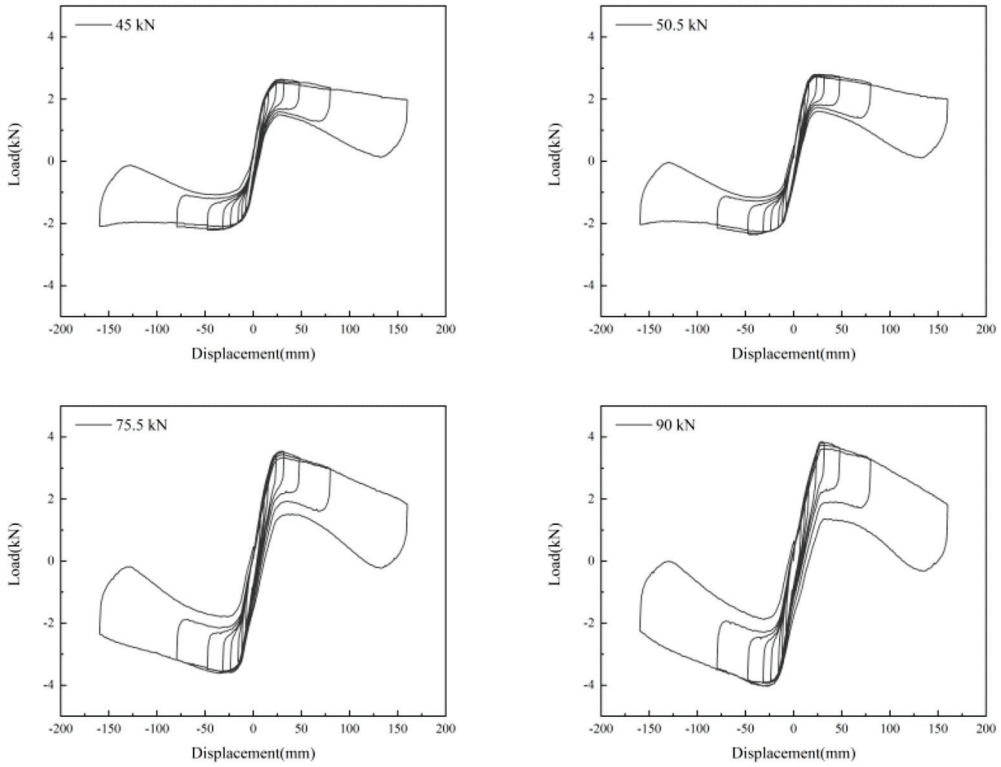

Figure 8. Hysteretic curves across four different load conditions.

From the hysteretic curves, it is evident that at low levels of horizontal loading displacement, the swinging of the columns contributes positively to the lateral resistance of the column frame, and this positive contribution increases with the application of greater vertical loads. However, as the horizontal loading displacement increases, the beneficial effect of the swinging column diminishes, and the extrusion of the components intensifies. A comparison of the four sets of curves reveals that the restoring force of the column frame subjected to a higher applied vertical load decreases more rapidly. This phenomenon can

be attributed to the fact that within a certain range of loading displacement, an increase in the vertical load can effectively enhance the column's lateral resistance and maintain its structural stability. But when the load exceeds this range, the larger swing of the columns means that an additional vertical load no longer improves the lateral resistance of the column frame. Instead, it exacerbates the column's swinging motion, leading to a faster decline in the restoring force.

Inspecting Figure 8, it is clear that the hysteresis loop for the 90 kN vertical load is the most well defined. The loops appear to become more complete as the vertical load increases. This can be understood by considering that higher vertical loads lead to greater compression between the components. When a horizontal load is applied, this increased compression boosts the frictional resistance, which, in turn, heightens the structure's ability to dissipate energy. Furthermore, the additional compression aids in absorbing energy, resulting in hysteresis loops that are more fully formed. The calculation results show that the peak restoring force of the column under the four different vertical loads is 2.43 kN, 2.58 kN, 3.55 kN, and 3.89 kN, respectively. As the vertical load rises from 45 kN to 50.5 kN, then to 75.5 kN, and finally to 90 kN, the column's peak restoring force increases by 6.17%, 46.09%, and 60.08%, respectively. Along with this, the horizontal displacement at which the column frame exhibits the maximum restoring force also increases. This demonstrates that a higher vertical load contributes to a stronger restoring force in the column frame. This enhanced restoring force seems to be due to the structure's improved ability to dissipate energy through friction and compression. This allows the column frame to absorb more of the energy from the loads applied without significant loss of its structural integrity. Therefore, during the repair or maintenance process for historical architectural heritages like Foguang Temple in this study, any increase or decrease in the vertical loads, such as those on the roof, should be controlled reasonably to ensure the stability and safety of the structure.

3.3. Skeleton Curves and the Simplified Model

Figure 9 displays the skeleton curves of a wooden column frame subjected to four different vertical load conditions. The symmetry of the skeleton curves, both in the positive and negative directions, is relatively good, although some deviation is present. To mitigate these deviations, an average of the positive and negative data points was used for the analysis of the skeleton curves. The trends observed in the four types of skeleton curves are consistent, encompassing an elastic stage, an elastic–plastic ascending stage, and a descending stage.

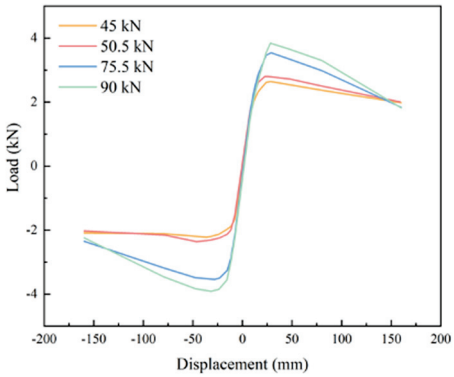

Figure 9. Skeleton curves under different load conditions.

To qualify the different loading stages under the four vertical load conditions, a three-stage model of the simplified skeleton curve is proposed and illustrated in Formula (1).

This model aims to capture the essential behavior of the column frame during loading by breaking down the response into three distinct phases:

(1) Elastic stage (k_e): This stage represents the initial loading where the column frame behaves elastically. The stiffness during this phase is denoted by k_e, and the corresponding restoring force is F_e. The displacement at this stage is below the yield point, X_e.

(2) Elastic–plastic ascending stage (k_p): As the loading continues, the column frame enters the elastic–plastic region where plastic deformation begins to occur. The stiffness in this phase is represented by k_p, with F_p being the restoring force. The peak displacement, X_p, is reached in this stage, which is approximately $|X| = 30$ mm as indicated by the data.

(3) Descending stage (k_u): Finally, as the load is increased further, the column frame enters a descending stage, where the stiffness decreases, represented by k_u, and the restoring force is F_u. The maximum displacement, X_{max}, is reached at this stage.

$$F = \begin{cases} k_e X, & 0 \le X \le X_e \\ k_e X_e + k_p(X - X_e), & X_e \le X \le X_p \\ k_e X_e + k_p(X_p - X_e) + k_u(X - X_p), & X_p \le X \le X_{max} \end{cases} \quad (1)$$

Here, F is the restoring force, and X is the displacement. The transition points X_e, X_p, and X_{max} are determined from the experimental data, and the stiffness parameters k_e, k_p, and k_u, as well as the restoring forces F_e, F_p, and F_u, are calculated based on the loading and unloading behavior of the column frame under the different vertical load conditions using Pickpoint software (version 3.292) [29]. This simplified model allows for a clearer understanding of the column frame's structural response and aids in predicting its behavior under varying loads.

The skeleton curves using the simplified three-stage model are shown in Figure 10, and the parameters in the different loading conditions are shown in Table 3. During the elastoplastic ascending stage, the column stiffness increases with the vertical load, with the peak displacement occurring at approximately $|X| = 30$ mm. As depicted in Figure 10, the increment in the vertical load enhances the performance characteristics at all stages in the skeleton curve model. Consequently, augmenting the vertical load can enhance the structural performance of the column frame.

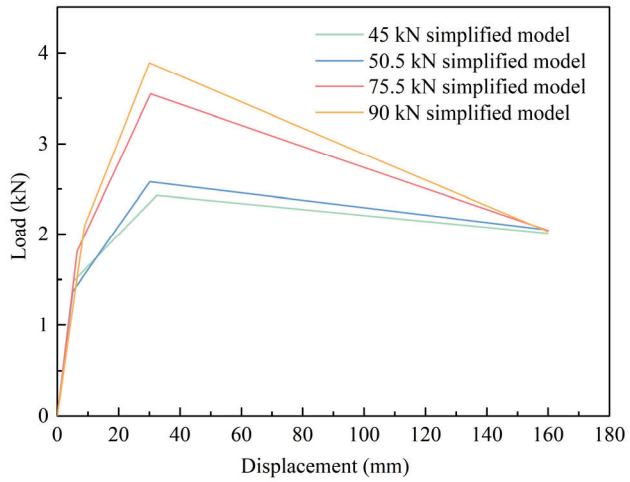

Figure 10. The skeleton curves using the simplified three-stage model.

Table 3. Parameters of the simplified model for the skeleton curves.

F (kN)	F_e (kN)	X_e (mm)	k_e (kN·mm^{-1})	F_p (kN)	X_p (mm)	k_p (kN·mm^{-1})	F_u (kN)	X_{max} (mm)	k_u (kN·mm^{-1})
45	1.48	5.26	0.2814	2.43	32.42	0.0350	2.01	159.91	−0.0033
50.5	1.37	5.01	0.2735	2.58	30.19	0.0481	2.05	159.03	−0.0041
75.5	1.81	6.46	0.2802	3.55	30.38	0.0727	2.04	160.07	−0.0116
90	2.09	8.88	0.2354	3.89	30.02	0.0851	2.03	159.83	−0.0143

3.4. Stiffness Degradation

This paper employs the line cutting stiffness method to compute the overall horizontal lateral stiffness of the column frame, adhering to the guidelines specified in the "Specification for Seismic Testing of Buildings" [30]. The calculation is derived from the following formula:

$$K_i = \frac{(|+F_i| + |-F_i|)}{(|+X_i| + |-X_i|)} \tag{2}$$

In this equation, $+F_i$ and $-F_i$ denote the maximum loads for the i-th forward and reverse loadings, respectively; $+X_i$ and $-X_i$ correspond to the horizontal displacements for the maximum loads of the i-th forward and reverse loadings, respectively. The stiffness degradation curves for the column frame under various vertical loads are depicted in Figure 11, and the trend in the stiffness degradation for the column frame under four distinct vertical loads is generally consistent. During the initial five loading cycles ($|X| = \pm 32$ mm), the stiffness of the column frame diminishes rapidly. For vertical loads of 45 kN, 50.5 kN, 75.5 kN, and 90 kN, the column stiffness decreases by 68.01%, 59.77%, 57.17%, and 40.52%, respectively, indicating a notable reduction in stiffness. As the horizontal loading displacement increases, the horizontal lateral stiffness of the column frame decreases swiftly and then stabilizes. In addition, it can be observed that the stiffness slightly increases after the sixth loading cycle. This behavior is attributed to the fact that the position where the straight tenon squeezes into the mortise gradually deepens as the cycling progresses, and after the sixth loading cycle, the position at which the tenon squeezes into the mortise at the start of loading is significantly deeper than that in previous loading cycles.

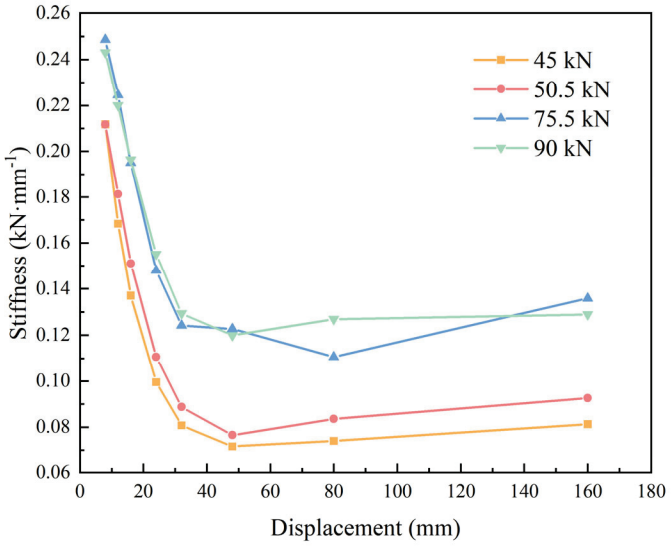

Figure 11. The stiffness degradation curves under different load conditions.

3.5. Energy Dissipation Capacity

The experiment thoroughly assesses the energy dissipation capacity of the structure through the equivalent viscous damping coefficient and energy dissipation metrics. In accordance with the "Specification for Seismic Testing of Buildings" [30], the equivalent viscous damping coefficient (ξ_{eq}) is determined using Formula (3) and interpreted using Figure 12.

$$\xi_{eq} = \frac{1}{2\pi} \times \frac{S_{(ABC+CDA)}}{S_{(OBE+ODF)}} \tag{3}$$

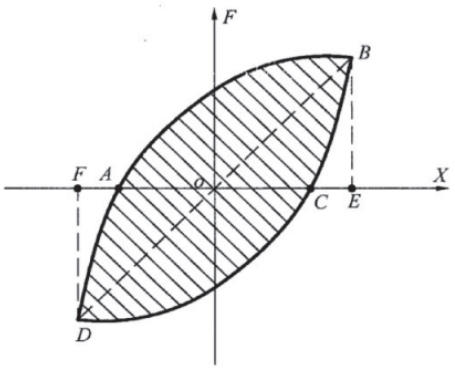

Figure 12. Diagram of calculation of equivalent viscous damping coefficient.

This formula takes into account the area enclosed by the hysteresis loop, which represents the energy dissipation of the column frame over a single loading cycle ($S_{(ABC+CDA)}$). This area is analogous to the energy absorbed by an elastic body at an equivalent displacement ($S_{(OBE+ODF)}$). The equivalent viscous damping coefficient serves as an indicator of the column frame's efficiency in dissipating energy, while the energy dissipation quantifies the frame's energy expenditure.

As illustrated in Figure 13, the equivalent viscous damping coefficients of the column frame both exhibit the trend of an initial decrease followed by an increase as the horizontal loading displacement progresses under different load conditions. This phenomenon can be attributed to the inherent softness of the wood material and the difficulty in achieving a perfectly flat surface during the manufacturing of wooden components. As a result, plastic deformation may occur at specific points of the component early in the lateral displacement process, leading to significant energy dissipation. However, as the gaps close and frictional slip diminishes, the node rotation angle and compression effects become minimal, causing a decrease in the energy dissipation during the initial loading cycles. With continued horizontal loading displacement, the rotation angle of the mortise-and-tenon joint intensifies, accumulating the plastic deformation and substantially augmenting the energy dissipation capacity.

Furthermore, this study reveals that the vertical loads exert a significant influence on the point at which the column frame's energy dissipation capacity begins to escalate. When the vertical loads are at 45 kN and 50.5 kN, an enhancement in the energy dissipation is observed following the third loading cycle, corresponding to a displacement of $\pm$16 mm. In contrast, at vertical loads of 75.5 kN and 90 kN, this enhancement is noted only after the fourth loading cycle, at a displacement of $\pm$24 mm. This suggests that an increase in the vertical load serves to postpone the initiation of the frame's enhanced energy dissipation capacity. The effect of increasing the vertical load is relatively subtle prior to the seventh cycle, at which point the displacement reaches $\pm$80 mm. However, subsequent to the seventh cycle, the rate at which the energy dissipation capacity increases becomes notably more rapid. An analysis of the data shows that under the maximum vertical load, the

eighth cycle sees marked increases in the energy dissipation of 47.6%, 52.7%, 104.9%, and 124.6% compared to that in the seventh cycle, respectively. This underscores the fact that the positive impact of vertical load increments on energy dissipation becomes more discernible with a greater horizontal loading displacement.

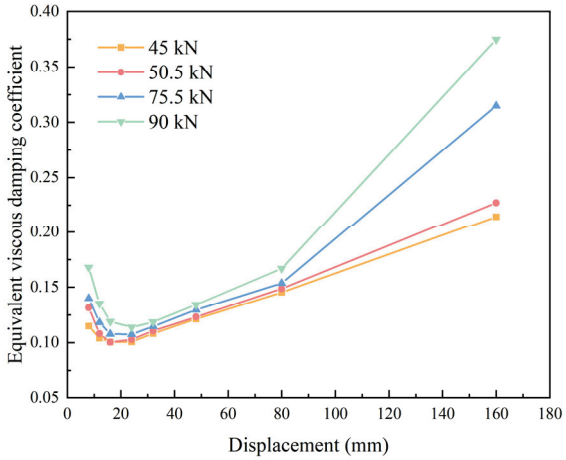

Figure 13. Equivalent viscous damping coefficients.

Figure 14 also shows that under a constant vertical load, the energy dissipation of the column frame escalates rapidly with an increase in the horizontal loading displacement. By analyzing the cumulative increment in the energy dissipation for each cycle relative to the previous one (as detailed in Table 4), it is evident that higher vertical loads correspond to greater increments in the energy dissipation per cycle for the column frame. Increasing the vertical load is advantageous for enhancing the structure's cumulative energy dissipation. However, a deeper analysis of the impact of the unit vertical load on energy dissipation (Figure 15) reveals that lower vertical loads contribute more significantly to the energy dissipation per unit load, particularly at larger horizontal loading displacements. This suggests that while increasing the vertical load can enhance the column frame's energy dissipation, the efficiency of this enhancement diminishes with the increment in the vertical load. Based on the abovementioned findings, in contemporary seismic structure design, structural deformation can be controlled and energy dissipation can be enhanced through the rational distribution of vertical loads. For instance, a structure resembling a bracket can be employed to adjust the magnitude and transfer path of vertical loads, thereby optimizing the overall performance of the structure.

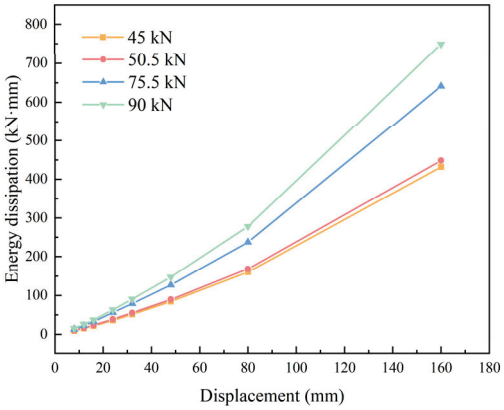

Figure 14. Energy dissipation.

Table 4. Accumulated energy dissipation increments per cycle.

Label	Vertical Load Conditions			
	45 kN (kN·mm)	**50.5 kN (kN·mm)**	**75.5 kN (kN·mm)**	**90 kN (kN·mm)**
Cycle 2-1	6.121	6.636	9.355	10.605
Cycle 3-2	6.509	6.983	10.294	11.235
Cycle 4-3	14.298	15.159	23.478	25.911
Cycle 5-4	15.462	16.327	22.858	27.627
Cycle 6-5	32.974	34.438	47.650	56.443
Cycle 7-6	75.823	78.762	110.515	131.262
Cycle 8-7	271.721	279.855	404.230	470.635

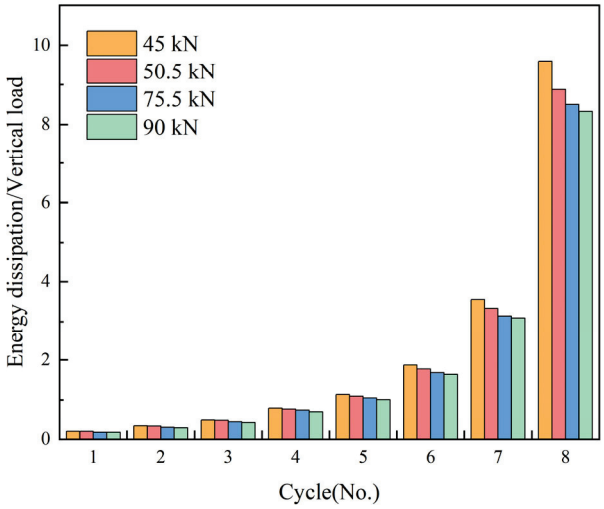

Figure 15. Accumulated energy dissipation per cycle/vertical load.

4. Conclusions

This experimental model, featuring two Fangs and three columns, was designed by drawing inspiration from the tenon joint style of the East Hall of Foguang Temple from the Tang Dynasty. Over the course of several weeks, this research conducted repeated load tests to investigate the deformation characteristics, hysteresis behavior, skeleton curves, stiffness degradation, and energy dissipation capacity of the column frame under four varying vertical loads. This study arrived at the following key conclusions:

(1) A pinch effect is observed in the hysteresis loops of the wooden column frame structure, with the intensity of this effect increasing in correlation with the vertical load. As the vertical load is augmented, it also exerts a more pronounced influence on the swaying motion of the columns, with the impact becoming more significant as the load increases.

(2) The stiffness of the column frame is positively correlated with the vertical load; an increase in the vertical load leads to a substantial enhancement in the frame's stiffness. During the initial stages of loading, the components within the column frame experience compression and sliding, which results in a rapid decline in stiffness. However, a higher vertical load slows down this stiffness degradation, indicating that increasing the vertical load can mitigate the rate of stiffness deterioration.

(3) The column frame demonstrates a notable capacity for energy dissipation. Elevating the vertical load can boost the equivalent viscous damping coefficient of the column frame. While increasing the vertical load can enhance the column frame's energy dissipation, it may also lead to a diminishing return on the efficiency of energy

dissipation improvements. Therefore, in practical construction, it is not necessary for elements such as the roof, which contribute to the vertical load, to be excessively heavy to achieve the optimal performance. It is essential to calculate and establish an optimal load range to avoid unnecessary waste and to maintain economic efficiency.

Author Contributions: Conceptualization: X.L. Data curation: X.G. and X.L. Formal analysis: X.G., F.K., and Z.W. Funding acquisition: Z.Q. Investigation: Z.W., X.L., J.X., and J.W. Project administration: Z.Q. Supervision: Z.Q. Validation: Q.W. Visualization: X.G. and F.K. Writing—original draft: X.G. Writing—review and editing: F.K. and T.M. All authors have read and agreed to the published version of the manuscript.

Funding: This research was financially supported by the Japan Society for the Promotion of Science (JSPS) under its project grant (the funding number: 14301613230001). Our sincere gratitude is extended to Professor Kohei Komatsu of Kyoto University for his guidance and support in advancing this research topic. Furthermore, we acknowledge the additional support provided by the Jiangsu Province University Students' Practical and Innovative Training Program Project, which significantly contributed to the success of our study.

Data Availability Statement: Some or all of the data, models, or code that support the findings of this study are available from the corresponding author upon reasonable request.

Conflicts of Interest: The authors declare no conflicts of interest.

References

1. Wang, J.; Main, I.G.; Musson, R.M.W. Earthquake Clustering in Modern Seismicity and Its Relationship with Strong Historical Earthquakes around Beijing, China. *Geophys. J. Int.* **2017**, *211*, 1005–1018. [CrossRef]
2. Li, Y.; Zhang, Z.; Xin, D. A Composite Catalog of Damaging Earthquakes for Mainland China. *Seismol. Res. Lett.* **2021**, *92*, 3767–3777. [CrossRef]
3. Shiping, H. The Earthquake-Resistant Properties of Chinese Traditional Architecture. *Earthq. Spectra* **1991**, *7*, 355–389. [CrossRef]
4. Li, Z.Y.; Gu, Y.; Zhang, R. Toward a Wider Audience, Systematic Approach of Reinterpretation and Representation of the East Main Hall of Foguang Temple Based on Digital Documentation and 3D Visualization Techniques. *Int. Arch. Photogramm. Remote Sens. Spat. Inf. Sci.* **2021**, *XLVI-M-1–2021*, 395–402. [CrossRef]
5. Jing, S.; Wang, W.; Masui, T. Analysis for Conservation of the Timber-Framed Architectural Heritage in China and Japan from the Viewpoint of Authenticity. *Sustainability* **2023**, *15*, 1384. [CrossRef]
6. Tsinghua University Architectural Design and Research Institute; Beijing Tsinghua Institute of Urban Planning and Design; Institute of Cultural Heritage Conservation. *Architectural Reconnaissance Study of the Main Hall of Foguang Temple*; Antiquities Press: Beijing, China, 2011. (In Chinese)
7. Zhang, B.; Song, X.; Xie, Q.; Xue, J. Seismic Behavior of Looseness-Induced Inclined Mortise and Tenon Joints in Ancient Timber Structures: Experimental Tests, Multi-Scale Finite Element Model, and Behavior Degradation. *Eng. Struct.* **2024**, *318*, 118680. [CrossRef]
8. Xie, Q.; Zhang, B.; Zhang, L.; Guo, T.; Wu, Y. Normal Contact Performance of Mortise and Tenon Joint: Theoretical Analysis and Numerical Simulation. *J. Wood Sci.* **2021**, *67*, 31. [CrossRef]
9. Sha, B.; Wang, H.; Li, A. The Influence of the Damage of Mortise-Tenon Joint on the Cyclic Performance of the Traditional Chinese Timber Frame. *Appl. Sci.* **2019**, *9*, 3429. [CrossRef]
10. Zhang, B.; Xie, Q.; Li, S.; Zhang, L.; Wu, Y. Effects of Gaps on the Rotational Performance of Traditional Straight Mortise-Tenon Joints. *Eng. Struct.* **2022**, *260*, 114231. [CrossRef]
11. Meng, X.; Yang, Q.; Wei, J.; Li, T. Experimental Investigation on the Lateral Structural Performance of a Traditional Chinese Pre-Ming Dynasty Timber Structure Based on Half-Scale Pseudo-Static Tests. *Eng. Struct.* **2018**, *167*, 582–591. [CrossRef]
12. Xie, Q.; Zhang, L.; Wang, L.; Zhou, W.; Zhou, T. Lateral Performance of Traditional Chinese Timber Frames: Experiments and Analytical Model. *Eng. Struct.* **2019**, *186*, 446–455. [CrossRef]
13. Xue, J.; Guo, R.; Qi, L.; Xu, D. Experimental Study on the Seismic Performance of Traditional Timber Mortise-Tenon Joints with Different Looseness Under Low-Cyclic Reversed Loading. *Adv. Struct. Eng.* **2019**, *22*, 1312–1328. [CrossRef]
14. Huang, H.; Wu, Y.; Li, Z.; Sun, Z.; Chen, Z. Seismic Behavior of Chuan-Dou Type Timber Frames. *Eng. Struct.* **2018**, *167*, 725–739. [CrossRef]

15. Chen, C.C.; Qiu, H.X.; Xu, M.G. Experimental Study on Flexural Behavior of Typical Mortise-Tenon Joints. *Appl. Mech. Mater.* **2014**, *578–579*, 160–163. [CrossRef]
16. Aras, F.; Krstevska, L.; Altay, G.; Tashkov, L. Experimental and Numerical Modal Analyses of a Historical Masonry Palace. *Constr. Build. Mater.* **2011**, *25*, 81–91. [CrossRef]
17. Maeno, M.; Suzuki, Y.; Ohshita, T.; Kitahara, A. Seismic Response Characteristics of Traditional Wooden Frame by Full-Scale Dynamic and Static Tests. In Proceedings of the 13th World Conference on Earthquake Engineering, Vancouver, BC, Canada, 1–6 August 2004.
18. Shi, X.; Li, T.; Chen, Y.F.; Chen, J.; Yang, Q. Full-Scale Tests on the Horizontal Hysteretic Behavior of a Single-Span Timber Frame. *Int. J. Archit. Herit.* **2020**, *14*, 398–414. [CrossRef]
19. Suzuki, Y.; Maeno, M. Structural Mechanism of Traditional Wooden Frames by Dynamic and Static Tests. *Struct. Control Health Monit.* **2006**, *13*, 508–522. [CrossRef]
20. Shi, X.; Chen, Y.F.; Chen, J.; Yang, Q.; Li, T. Experimental Assessment on the Hysteretic Behavior of a Full—Scale Traditional Chinese Timber Structure Using a Synchronous Loading Technique. *Adv. Mater. Sci. Eng.* **2018**, *2018*, 5729198. [CrossRef]
21. *GB/T 1927-4*; Physical and Mechanical Properties of Wood. Test Methods for Small Clear Wood Specimens. Part 4: Determination of Moisture Content. Standards Press of China: Beijing, China, 2014.
22. *GB/T 1927-5*; Physical and Mechanical Properties of Wood. Test Methods for Small Clear Wood Specimens. Part 5: Determination of Density. Standards Press of China: Beijing, China, 2014.
23. *GB/T 1927-9*; Physical and Mechanical Properties of Wood. Test Methods for Small Clear Wood Specimens. Part 9: Determination of Bending Strength. Standards Press of China: Beijing, China, 2014.
24. *GB/T 1927-10*; Physical and Mechanical Properties of Wood. Test Methods for Small Clear Wood Specimens. Part 10: Determination of Modulus of Elasticity in Bending. Standards Press of China: Beijing, China, 2014.
25. *GB/T 1927-11*; Physical and Mechanical Properties of Wood. Test Methods for Small Clear Wood Specimens. Part 11: Determination of Ultimate Stress in Compression Parallel to Grain. Standards Press of China: Beijing, China, 2014.
26. *GB/T 1927-12*; Physical and Mechanical Properties of Wood. Test Methods for Small Clear Wood Specimens. Part 12: Determination of Strength in Compression Perpendicular to Grain. Standards Press of China: Beijing, China, 2014.
27. *GB/T 1927-13*; Physical and Mechanical Properties of Wood. Test Methods for Small Clear Wood Specimens. Part 13: Determination of the Modulus of Elasticity in Compression Perpendicular to Grain. Standards Press of China: Beijing, China, 2014.
28. Komatsu, K.; Kitamori, A.; Nakagawa, T.; Nakashima, S.; Isoda, H. Experimental Study on The Restoring Force Characteristics of Traditional Timber Frame Consisting of *"Daitohijiki"* (Large Bearing Brock with Bracket Arms), *"Kasiranuki"* (Head Tie-Beams), and Three Circular Columns and on The Moment-Resisting Performance Evaluated in Each Structural Element. *J. Struct. Constr. Eng. Trans. AIJ* **2023**, *88*, 609–620. [CrossRef]
29. Masahiko, K. Automatic Software for Deciding Characteristics of Load-Displacement Curves. In Proceedings of the 8th World Conference on Timber Engineering WCTE2004, Lahti, Finland, 14–17 June 2004; Volume III, pp. 565–568.
30. *JGJ/T 101*; Specification for Seismic Test of Buildings. China State Engineering and Construction Press: Beijing, China, 2015.

buildings

MDPI

Article

Dynamic Characteristics and Seismic Response of Multi-Story Wooden Tower Considering the Influence of a High Stylobate

Hao Xue [1], Jianyang Xue [1,2,*], Dejun Song [1], Mengjie Li [1], Bowen Xue [3], Chenwei Wu [1] and Yan Sui [1,4]

[1] School of Civil Engineering, Xi'an University of Architecture & Technology, Xi'an 710055, China; ling960102@xauat.edu.cn (H.X.); songdejun@xauat.edu.cn (D.S.); zhourui@xauat.edu.cn (M.L.); willionms_wu@xauat.edu.cn (C.W.); suiyanmyy@163.com (Y.S.)
[2] Key Lab of Structural Engineering and Earthquake Resistance, Ministry of Education (XAUAT), Xi'an 710055, China
[3] College of Architecture, Xi'an University of Architecture & Technology, Xi'an 710055, China; renguoqi@xauat.edu.cn
[4] Xauat Engineering Technology Co., Ltd., Xi'an 710055, China
* Correspondence: jianyang_xue@163.com

Abstract: In situ dynamic tests were conducted on Caiyunjian Tower to investigate the influence of a high stylobate on its dynamic characteristics and seismic response through time–domain and frequency–domain methods. Finite element models were developed for Caiyunjian Tower (wooden structure and platform) and the overall structure including the high stylobate. Subsequently, models were subjected to El Centro, Taft, and Lanzhou waves at varying amplitudes. The seismic response results indicate that the overall structure model exhibits a low natural vibration frequency with closely spaced modal frequencies. As the peak seismic wave acceleration increases, both models exhibit increased acceleration, displacement, and shear responses. The Caiyunjian Tower model shows greater sensitivity to the El Centro wave, whereas the overall structure model is more responsive to the Taft wave. Under seismic waves with identical peak acceleration, the overall structure model exhibits greater dynamic responses than the Caiyunjian Tower model. The high stylobate minimally affects the lower-order frequencies of the upper structure but significantly influences the higher-order frequencies. Therefore, the high stylobate has an adverse influence on the seismic behavior of Caiyunjian Tower.

Keywords: high stylobate; multi-story tower timber structure; in situ dynamic test; dynamic characteristics; seismic response

1. Introduction

As one of the most remarkable architectural structures in modern history, Caiyunjian Tower in Xingqing Palace Park showcases the extraordinary craftsmanship of ancient times and carries significant cultural heritage value [1]. The Xingqing Palace site is currently on the tentative list of UNESCO World Cultural Heritage sites along the Silk Road, with significant historical, scientific, and artistic values. Unlike architectural landscapes on low plains or mountainous ancient buildings on elevated peaks, Caiyunjian wooden tower, situated at the park's highest point with a bluestone platform and high stylobate, complicates the seismic performance of its overall structure.

Caiyunjian Tower is a three-story hexagonal tower constructed with a Dou-gong bracket, featuring a double-eave roof adorned with green glazed tiles (Figure 1). The high stylobate, composed of manually compacted fill soil and loess, is 10 m high with a slope ratio of approximately 1:2. Caiyunjian Tower stands at a height of 20.8 m, comprising a

1.5 m platform and a 19.3 m wooden structure. The hexagonal wooden structure consists of three visible floors and two flat-floored layers, with a decreasing projected area from bottom to top. The center of the wooden tower is a reinforced concrete core column with a variable cross-section through the top. Wood braces and steel plates are employed between the eave columns and core columns of the flat-floored layers. The dimensions of the first floor are 6 m in length and 5.2 m in width, with six columns measuring 0.32 m in diameter and 3.65 m in height, spaced 3 m apart. The second floor measures as 5.4 m in length and 4.65 m in width, with columns that are 0.3 m in diameter and 4.8 m in height. The third floor measures as 4.6 m in length and 3.75 m in width, with columns that are 0.28 m in diameter and 4.2 m in height. The platform is a hexagonal structure with a length of 8.1 m from east to west and a width of 7.2 m from south to north. It is covered with bluestones and boulder strips on the outside and filled with compacted clay and loess inside. Figure 2 shows the plan view of the platform and the first floor. The numbers and letters in Figure 2b are column grid axis numbers for east-west and north-south directions, respectively. Key components such as hypostyle columns, eave columns, braces, and diagonal beams are detailed in Table 1, including their cross-sectional dimensions.

Figure 1. The typical multi-story wooden tower.

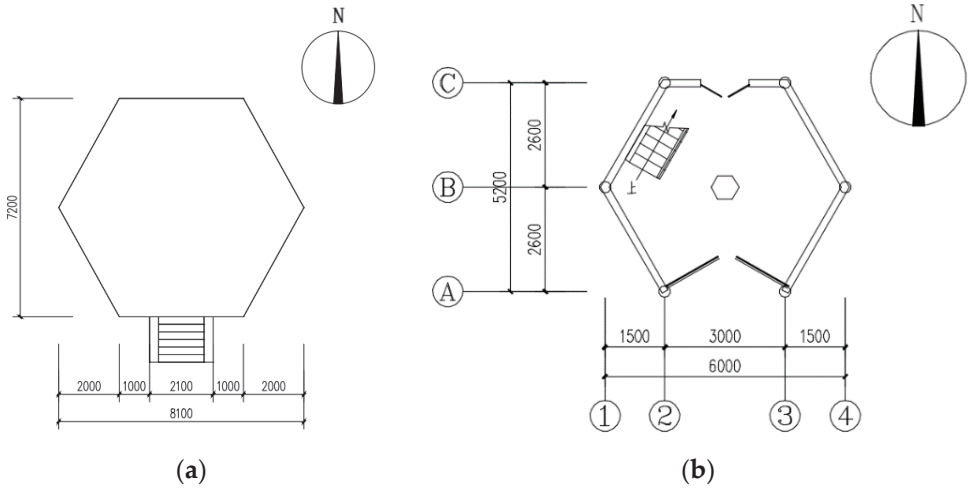

(**a**) (**b**)

Figure 2. The structure of Caiyunjian Tower. (**a**) Plan view of the platform; (**b**) plan view of the first floor.

Table 1. Main component section dimensions.

Component	D (mm)	Component	$b \times h$ (mm)
First eave column	320	First architrave	200 × 250
Second hypostyle column	320	First Rufu	280 × 500
Third hypostyle column	280	Brace	120 × 180

D, b, and h are the diameter, width, and height of the component section, respectively.

Some scholars have carried out a lot of research to study the soil–structure interaction. Zhang and Far [2] performed simulation analysis of rigid base and flexible base frame-core tube structures. The results showed that the soil–structure interaction has a remarkable impact on the seismic behavior of high-rise frame-core tube structures as it can increase the lateral deflections and inter-story drifts and decrease the story shear forces of structures. Through a numerical analysis considering the interaction between soil and structure carried out for low- to medium-rise buildings, Bolisetti and Whittaker [3] pointed out that the presence of the deep basement reduces uplift in the footings and results in smaller peak spectral accelerations at the roof. Heiland et al. [4] studied the soil–structure interaction on the dynamic characteristics of railroad frame bridges. The results showed that the natural frequencies react robustly to the soil–structure interaction and are thus mainly influenced by the structural stiffness of the frame. The above studies indicated that the interaction between soil and structure makes the foundation affect the dynamic characteristics and seismic response of the superstructure [5,6]. However, the above studies mainly focused on the interaction between soil and structure in modern structures, with less research on historical buildings.

To investigate the influence of the substructure on the upper wooden structures of historic buildings, Zhao et al. [7,8] developed a finite element model of the Drum Tower in Xi'an. A modal analysis indicated that the impact of the stylobate on the dynamic characteristics of the upper wooden structure is significant and should be considered. Xue et al. [9] conducted a numerical analysis on the seismic response of the Yingxian Wooden Pagoda, and the results showed that the high stylobate amplifies the acceleration and displacement of the wooden structure. A 3D finite element model of wood structure–abutment–foundation of Xi'an Bell Tower was established by Meng et al. [10]. The results indicated that the relative displacement of the second floor of the timber structure is increased by 2.12 times and the displacement of tower base relative to the ground is increased by 44%. Their findings revealed that when the natural frequencies of the upper wooden structure align closely with those of the high stylobate, the latter significantly affects the dynamic characteristics of the former. As a famous palace-style timber building with a high stylobate, Guangyue Tower was studied by Sun et al. [11] and Meng et al. [12]. The results indicated that when the soil–structure interaction is considered, the natural frequency of the structure is reduced, and its influence on the high-order natural frequency of the structure is greater than the influence on the low-order natural frequency. Pan et al. [13–15] carried out a detailed analysis of the ancient wooden buildings on a slope from the aspects of failure mode, dynamic characteristics, and seismic mechanism. The research shows that the high-slope structure reduces the seismic performance of the upper wooden structures. The above research revealed the impact of the high stylobate on the superstructure should not be overlooked for historical structures [16–18]. However, in the existing research, the superstructure is mostly palace-style buildings, and there are few tower buildings.

Based on the study of palace-style historical buildings, tower-type historical buildings have been widely studied. Gao et al. [19] carried out an in situ dynamic test on the Jiufeng Temple ancient masonry pagoda and obtained its modal characteristics. On this basis,

the finite element model of the pagoda was established to study the failure mechanism. The results showed that the top of the pagoda was the weak position. Yuan et al. [20] analyzed the dynamic characteristics and seismic response of Luoshan Temple Tower. The results show that the displacement angle of the bottom floor of the tower is large under earthquakes of various intensities, and the whipping effect at the top of the tower is obvious. The damage of the masonry at the bottom of the pagoda body and the openings of each layer of arch coupons is relatively serious. Xu et al. [21] studied the influence of inclination on the seismic performance of brick masonry toter. The results revealed that the resonant frequency of the inscribed tower model was 41% lower than the original model. Inclination enhances the acceleration and displacement responses. Abruzzese et al. [22] established a numerical model of masonry ancient pagoda while considering architectural characteristics and damage conditions, which provided a basis for the risk assessment of ancient pagodas. Zhang et al. [23] studied the influence of topographic effect on the seismic response of ancient pagodas. The results show that the hilly terrain can amplify the relative displacement, acceleration, and inter-story displacement angle of masonry pagodas. Therefore, the influence of high slope soil should be considered when studying the seismic performance of ancient pagodas. However, the research on the seismic performance of the tower structures mentioned above mainly focuses on the tower itself, and there is relatively little research on the influence of a high stylobate and high slope soil on the upper tower.

To predict the seismic response and evaluate the seismic performance of high-stylobate structures, this study uses Caiyunjian Tower, a multi-story wooden structure, as a case study. El Centro, Taft, and Lanzhou waves were selected for dynamic analyses, for which the reason are listed below: El Centro wave and Wenchuan waves include east–west, north–south, and vertical directions, and these waves are often used to calculate the dynamic response of the structure, which is located in the III-type site classification. The Lanzhou wave is an artificial wave with a duration of 20.00 s, which is statistically significant and often used for seismic performance analysis.

Through in situ dynamic testing and finite element simulation [24,25], the influence of a high stylobate on the dynamic characteristics and seismic response of wooden tower structures is discussed. Figure 3 shows a flowchart of dynamic characteristics and seismic response analysis.

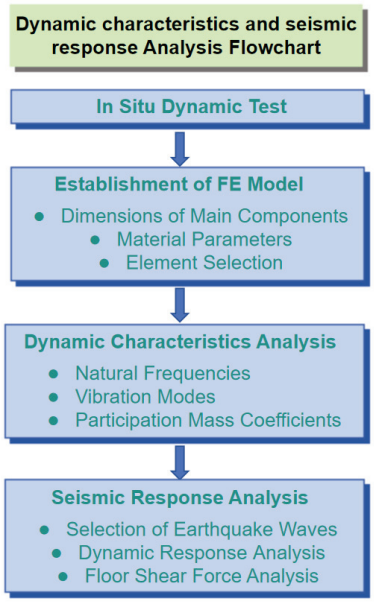

Figure 3. Flowchart of the dynamic characteristics and seismic response analysis.

2. In Situ Dynamic Test

2.1. Experimental Scheme and Measurement Point Arrangement

The 941B seismometer and the INV3062S/V network distributed data acquisition instrument were employed for measuring vibration signals and collecting data during in situ dynamic characteristic tests [26]. The seismometer has excellent ultra-low frequency performance and is a versatile ultra-low- or low-frequency vibration measurement device widely used for pulsation measurements in buildings. The seismometers were calibrated in advance to ensure the accuracy of the measurements. The seismometer is depicted in Figure 4. Different excitation conditions were applied for dynamic testing, encompassing environmental excitation, artificial bouncing, and hammer impacts. Xingqing Palace Park was closed to the public during the tests to maintain an undisturbed environment.

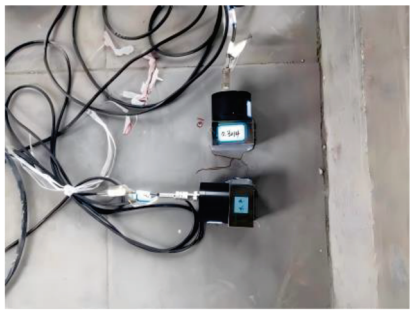

Figure 4. Photo of the seismometer.

Measurement points were selected at both the top and base of columns on each floor [27]; the outdoor ground served as a stationary reference point. The tests were conducted in multiple phases due to limited seismometers and the large number of measurement points. Each floor was divided into three orders, resulting in a total of nine orders. Each order included 5 measurement points and 3 stationary reference points, leading to 16 testing channels and 16 seismometers, totaling 48 measurement points.

The hypostyle column of Caiyunjian Tower extends vertically within the tower, anchored at each floor level on the platform, illustrated in Figure 5. Multiple measurement points are established using two sensors arranged horizontally and orthogonally. Vibration signals in the east–west and north–south directions were simultaneously recorded during transient excitation. And the measurement points are positioned as indicated in Figure 5.

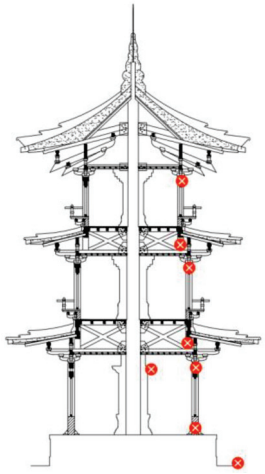

Figure 5. Diagram of measuring points.

2.2. Test Results

The structure underwent transient excitations under five different conditions. Data from the in situ dynamic characteristic tests were analyzed using an FFT (fast Fourier transform) spectral analysis with DASP V-11. This analysis yielded a peak power spectral density–frequency curve showing the natural frequencies of the structure. The first-order frequency was 3.821 Hz, and the second-order frequency was 4.106 Hz, as depicted in Figure 6. Here, S_a stands for the power spectral density, and f stands for the frequency. A3, C2, B1, B4, A2, and C3 represent the column numbers, which are composed of letters and numbers in the two directions, as shown in Figure 2. A modal analysis of Caiyunjian Tower was conducted using the random subspace identification (SSI) method [28]. After removing unstable modes, modal shapes for the first and second modes were determined, illustrated in Figures 7 and 8. Here, X, Y, and Z stand for the south–north direction, east–west direction, and vertical direction, respectively.

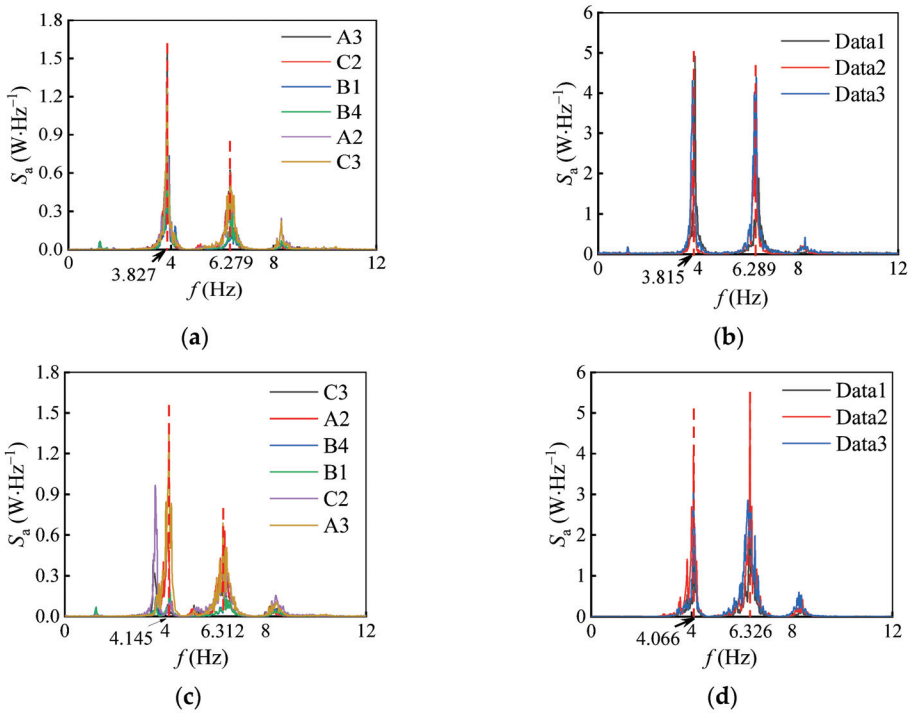

Figure 6. Power spectral density–frequency curves of measuring points. (**a**) The column top of first floor (east–west), (**b**) the ground of second floor (east–west), (**c**) the column top of first floor (north–south), and (**d**) the ground of third floor (north–south).

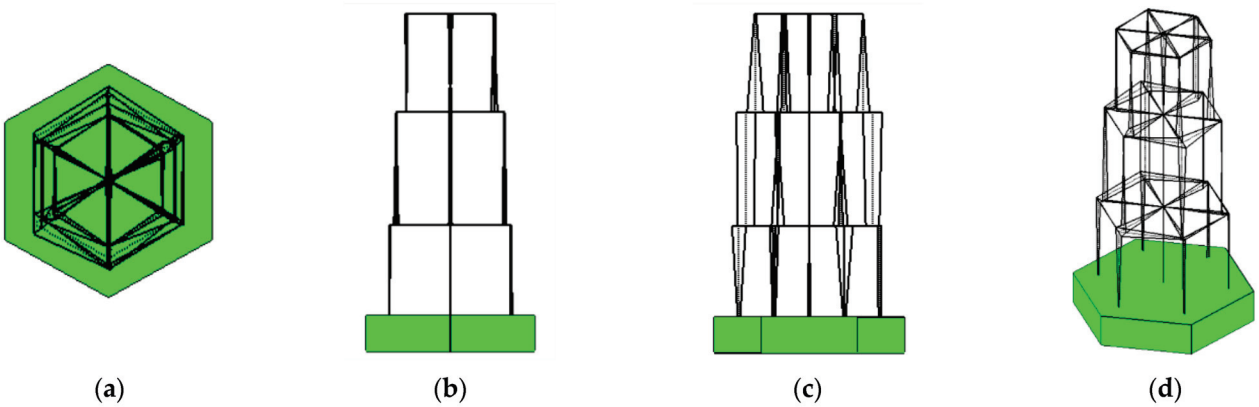

Figure 7. First-order mode shape diagram. (**a**) X–Y, (**b**) X–Z, (**c**) Y–Z, and (**d**) X–Y–Z.

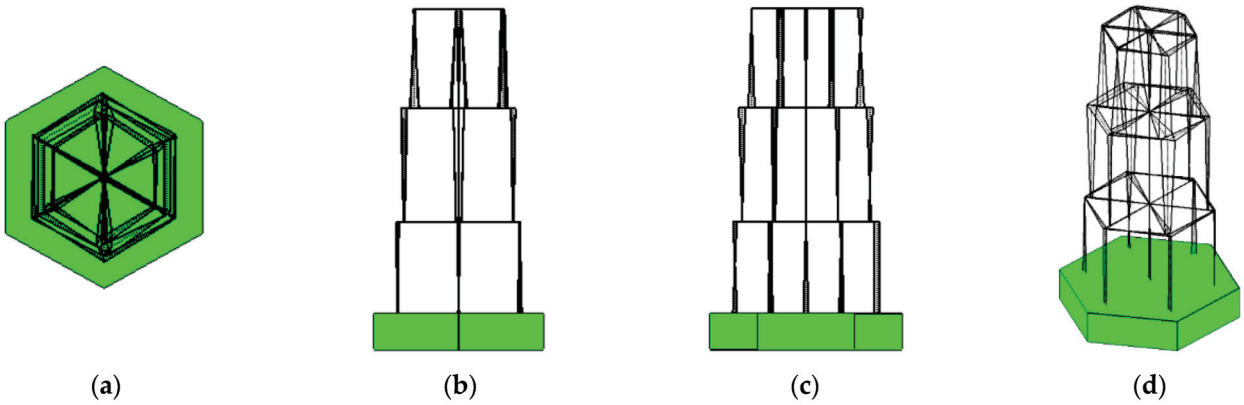

Figure 8. Second-order mode shape diagram. (**a**) X–Y, (**b**) X–Z, (**c**) Y–Z, and (**d**) X–Y–Z.

Acceleration responses were integrated to derive displacement responses. The peak-picking method was then used to analyze the amplitude spectrum curve. Displacement amplitudes in the respective directions were extracted at each measurement point corresponding to the resonant frequencies. Subsequently, average displacement amplitudes at the same height were calculated and compared with the maximum displacement response amplitude of the structure to determine the mode shape coefficient of Caiyunjian Tower. Torsional modes were observed in the mode shapes, with north and east being designated as positive directions, leading to spatial ambiguity, as indicated in Figure 9. This finding suggests possible issues with the experimental test point placement or distinguishing linearly related test modes [27].

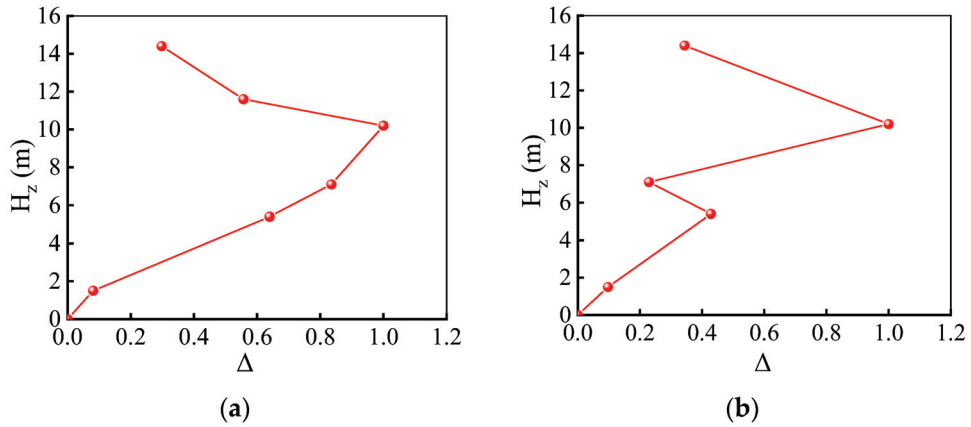

Figure 9. Vibration mode of Caiyunjian Tower. (**a**) The first mode (east–west); (**b**) the second mode (north–south).

3. Establishment of the Finite Element Model

3.1. Dimensions of Main Components

The finite element model of the wooden structure and platform was established based on the dimensions and construction details derived from the structural construction drawings.

3.2. Material Parameters

Material tests were performed on wooden columns sampled from Caiyunjian Tower to determine the material parameters. Pine wood [29] is used in the wooden structure, and its material parameters are detailed in Table 2. The Poisson's ratio is approximately 0.43, and the wood density is 493 kg/m^3. According to the "Standard for Evaluation of Concrete Compressive Strength" (GB/T 50107-2010) [30], the 300-grade concrete of the core

column corresponds to Grade C 28. Material parameters for the core column are provided in Table 3.

Table 2. Material parameters of wood.

E_L (MPa)	E_R (MPa)	E_T (MPa)	G_{RT} (MPa)	G_{LR} (MPa)	G_{LT} (MPa)
10,000	200	200	180	600	750

E and *G* are the elastic modulus and shear modulus of wood, respectively, and the subscripts *L*, *R*, and *T* represent the longitudinal, radial, and tangential direction of wood, respectively.

Table 3. Concrete material parameters of the core column.

Material	*E* (MPa)	ρ (kg/m^3)	μ
Concrete	28,500	2500	0.2

ρ and μ are the density and Poisson's ratio of concrete, respectively.

The hexagonal platform is filled with rammed soil internally and surrounded by a 400 mm thick bluestone exterior, which greatly enhances its rigidity. The material parameters of bluestone are provided in Table 4 [31].

Table 4. Material parameters of platform.

Material	*E* (MPa)	ρ (kg/m^3)	μ
Bluestone	5000	2500	0.3

Caiyunjian Tower stands on a 10 m high stylobate. The lower layers consist primarily of fill soil and Tertiary Pleistocene aeolian loess (Q3eol), characterized by soft-plastic to flow-plastic behavior and localized saturation. The material parameters are detailed in Table 5.

Table 5. Material parameters of foundation soil.

Material	*E* (MPa)	μ	ρ (kg/m^3)	*c* (kPa)	φ (°)
Rammed soil	20	0.3	1867	60	30.4

c and φ are the cohesive strength and angle of internal friction of the soil, respectively.

The geometric parameters in the finite element model were established based on real measurement data. As for the material parameters, firstly, the load–displacement curves of different materials were obtained through material tests, and the obvious fluctuation and abnormal data were deleted. Then, the simplified load–displacement curves were obtained through statistical analysis and data fitting, and finally, the stress–strain curves of materials were obtained so as to calibrate the material parameters.

3.3. Element Selection and Model Establishment

The models of Caiyunjian Tower (wooden structure and platform, model 1) and the overall structure (Caiyunjian Tower and high stylobate, model 2) were established by ANSYS finite element software (R18.2). The wooden structure's beams, columns, and braces were simulated with the BEAM188 element. The meshing dimensions of beams, columns, and braces are determined as 500 mm. Column bases are assumed to be hinged, neglecting base slip. The Dou-gong and are simulated by the COMBIN39 spring element. Spring stiffness values are mortise-tenon joints determined from both research team experiments [32] and actual tower construction, detailed in Tables 6 and 7, respectively.

Table 6. Stiffness of mortise-tenon joints.

Stiffness	Direction	K_1	K_2
Translational stiffness/(kN/m)	x y z	1.81×10^6 (0.102 m)	1.1×10^6 (0.16 m)
Rotational stiffness/(kN·m/rad)	rotx roty rotz	800 (0.06 rad)	200 (0.1 rad)

The numbers inside the parentheses of translational stiffness K_1 and K_2 represent the ultimate tensile strength d_1 and yield strength d_2, respectively. The numbers inside the parentheses of rotational stiffness K_1 and K_2 represent the ultimate tensile strength θ_1 and yield strength θ_2, respectively.

Table 7. Stiffness of Dou-gong joints.

Stiffness	Direction	K_1	K_2
Translational stiffness/(kN/m)	x y	3500 (0.03 m)	850 (0.04 m)
	z	12,000 (0.014 m)	2920 (0.02 m)
Rotational stiffness/(kN·m/rad)	rotx roty rotz	3000 (0.035 rad)	740 (0.05 rad)

The roof was simulated using the MASS21 element to represent the mass. Based on the principles of area equivalence, the roof load was calculated and applied to the top of each column as concentrated masses uniformly, which is listed in Table 8.

Table 8. Column top load.

Floor	First	Second	Third
Load (kN)	75.242	50.187	78.060

The platform and the compacted soil of the high stylobate were simulated with the SOLID45 element, assuming material homogeneity throughout. The soil is simplified as an independent frustum, employing the Drucker–Prager yield criterion to establish the DP soil model. The upper part of the frustum is unrestricted on all four sides, while the soil bottom is fixed. A multi-point constrained contact algorithm is used between the platform and the frustum, defining MPC contact with face-to-face interaction [33]. CONTA173 and TARGE170 elements were chosen to designate the platform's bottom surface as the contact area and the frustum's upper surface as the target. The meshing dimensions of the platform are determined as 300 mm.

Both models are shown in Figure 10, where the *X*-axis represents the north–south direction, the *Y*-axis represents the east–west direction, and the *Z*-axis represents the vertical direction.

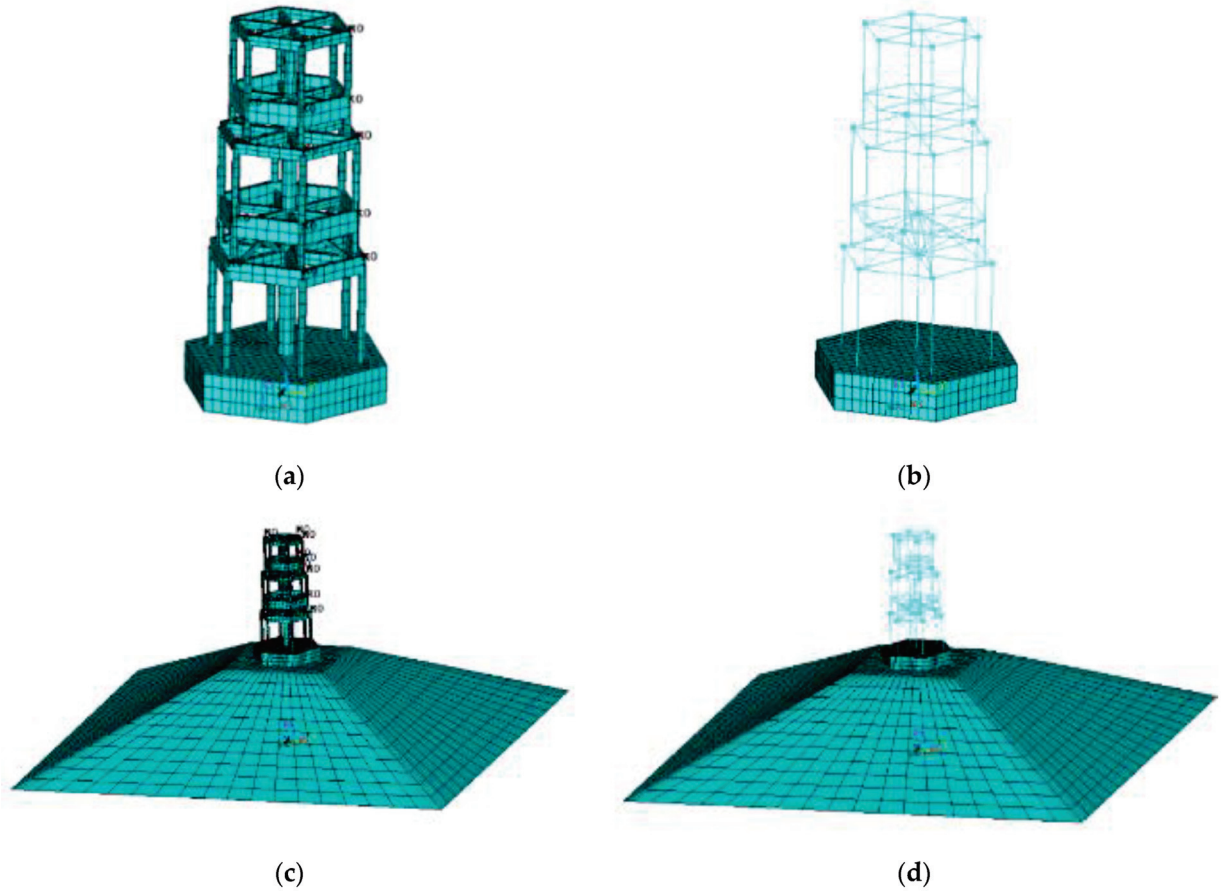

Figure 10. Finite element model. (**a**) Model 1 (with unit section), (**b**) model 1 (without unit section), (**c**) model 2 (with unit section), and (**d**) model 2 (without unit section).

4. Dynamic Characteristics Analysis

The natural frequencies and corresponding vibration mode of model 1 were obtained by modal analysis using the block Lanczos algorithm, and the method has been widely used and calibrated in the references [34,35].

A comparison of simulated and in situ measured values in Table 9 shows a relative error of under 10%, confirming the validity of model 1. Model 2 is derived from model 1.

Table 9. Comparison of natural vibration frequencies between simulated and experimental values of model 1.

Order	Experimental Value (Hz)	Simulated Value (Hz)	Relative Error (%)
First	3.821	3.767	1.413
Second	4.106	3.771	8.159

As shown in Figure 11, the first three order frequencies in model 1 are similar, but the fourth order and higher frequencies show significant variation, suggesting instability attributed to platform influence. Both models exhibit similar first three order frequencies, with model 2 accounting for the high stylobate's impact. Model 2 displays minimal frequency variation as the order rises, with little effect from the high stylobate on low-order frequencies but significant influence on high-order frequencies. The soil–structure interaction leads to a decrease in the structure's natural frequencies. The fundamental natural frequencies of model 1 and model 2 are, respectively, 3.7669 Hz and 2.0633 Hz, which means that the involvement of flexible soil reduces the fundamental frequency of the overall structure.

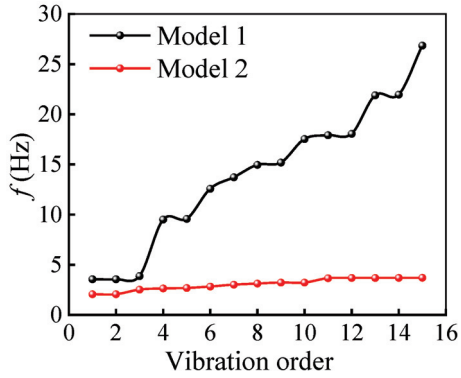

Figure 11. The front fifteen order frequencies of the models.

The first three mode shapes of model 1 and model 2 are nearly identical; the first and second modes show translational movements along the east–west and north–south directions, while the third mode exhibits torsional motion, as illustrated in Figures 12 and 13. In model 2, the amplitude of soil vibration increases notably for the fourth and fifth modes, particularly for higher modes, owing to the low stiffness of the high stylobate.

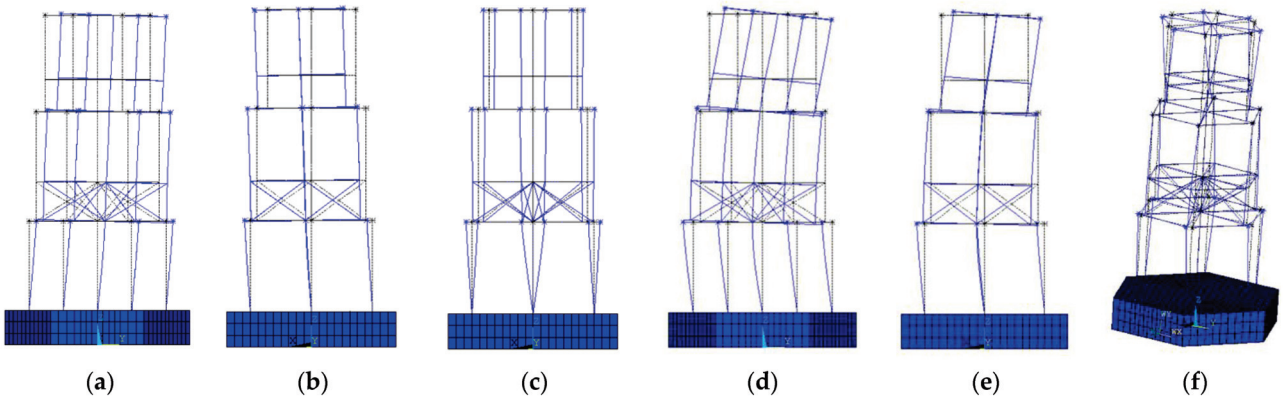

Figure 12. The finite element model mode diagram of model 1. (**a**) The first mode, (**b**) the second mode, (**c**) the third mode, (**d**) the fourth mode, (**e**) the fifth mode, and (**f**) the sixth mode.

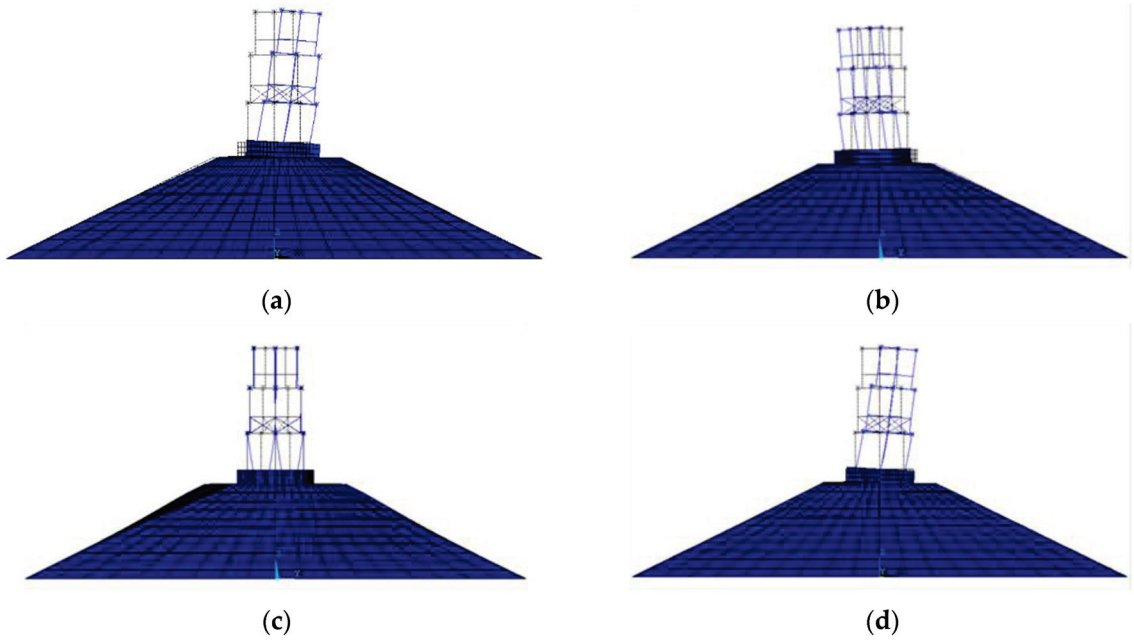

Figure 13. *Cont.*

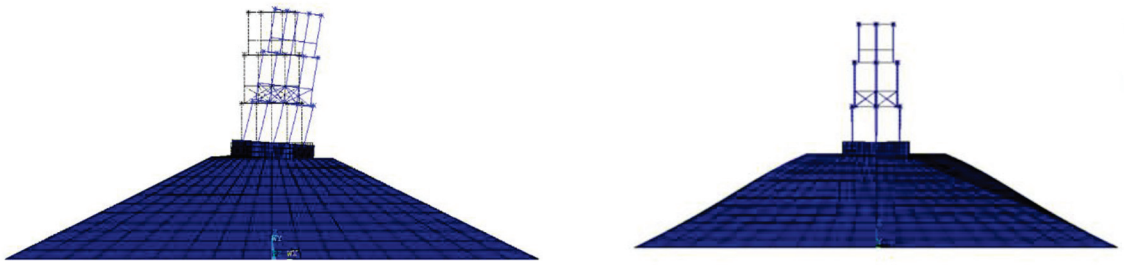

(**e**) (**f**)

Figure 13. The finite element model mode diagram of model 2. (**a**) The first mode, (**b**) the second mode, (**c**) the third mode, (**d**) the fourth mode, (**e**) the fifth mode, and (**f**) the sixth mode.

Modal participation factors for vibration modes are presented in Tables 10 and 11 for model 1 and model 2, respectively, illustrating each mode's contribution to the structural seismic response.

Table 10. Modal participation mass coefficient of model 1.

Mode	North–South		East–West	
	γ	*r*/%	γ	*r*/%
First	0	0	0.8525	85.25
Second	0.8831	88.31	0	85.25
Third	0	88.31	0	85.25
Fourth	0	88.31	0.1333	98.58
Fifth	0.1029	98.60	-	-

γ is the modal participation mass coefficient, r is the mode contribution; $r = \sum_1^i \gamma\%$, i is the order of the mode.

Table 11. Modal participation mass coefficient of model 2.

Mode	North–South		East–West	
	γ	*r*/%	γ	*r*/%
First	0.7063	70.63	0	0
Second	0	70.63	0.7096	70.96
Third	0	70. 63	0	70.96
Fourth	0.0740	78.03	0	70.96
Fifth	0	78.03	0.0750	78.46
Sixth	0	78.03	0	78.46
Seventh	0	78.03	0	78.46
Eighth	0	78.03	0	78.46
Ninth	0.1859	96.62	0	78.46
Tenth	-	-	0.1826	96.72

The first two modes of model 1 significantly contribute to the seismic response, whereas the platform minimally affects the fourth mode along the east–west (Y-axis) and the fifth mode along the north–south (X-axis). Considering the high stylobate's influence, modes 1 and 2 make the largest contributions to the seismic response. Furthermore, the influence of the ninth soil mode amplifies, thereby making the contributions of the first 10 modes substantial. Considering the high stylobate's influence alters the response direction of the first mode, underscoring the significance of a high stylobate in the study of the dynamic properties of ancient wooden structures.

5. Seismic Response Analysis

5.1. Selection of Earthquake Waves

Caiyunjian Tower is situated in Xi'an City, Shaanxi Province. It falls under seismic design category class B, with a design seismic intensity of eight and a design basic earthquake acceleration of 0.2 g. The site is classified as category III, with a design earthquake grouping of group 1. The site has a characteristic period of 0.45 s, categorizing it as a class B building. According to the "Code for Seismic Design of Buildings" (GB 50011-2011) [36], the selection of actual strong motion records and artificially simulated acceleration time history curves should be based on the building's site category and design seismic grouping when employing the time history analysis method. At least two-thirds of the total number of actual strong motion records should be selected. Therefore, seismic excitations such as the EI Centro wave, Taft wave, and Lanzhou wave were chosen [37].

The initial 20 s of earthquake waves were selected as seismic excitations, simultaneously applied in both the X- and Y-directions. The peak accelerations of earthquake waves were adjusted to 70 cm/s^2 for frequent earthquakes, 200 cm/s^2 for design scenarios, and 400 cm/s^2 for rare events. Calculations show that model 1 had weaker horizontal stiffness in the Y-direction; thus, earthquake wave accelerations were set at a ratio of 0.85:1 between the X- and Y-directions. Model 2 exhibited weaker horizontal stiffness in the X-direction; therefore, earthquake wave accelerations were set at a ratio of 1:0.85 between the X- and Y-directions. The output data of the two models take the larger value in two directions, respectively. Model 1 and model 2 produce response results in the Y-direction and X-direction, respectively. According to prior research, the damping ratio of the structure is 0.03 [26].

5.2. Results and Analysis

Figure 14 displays the time history curves of the displacement and acceleration response of the reference point located at the top of the hypostyle column on the third floor subjected to three types of seismic waves with a modulation amplitude of 400 cm/s^2. Table 12 shows the maximum inter-story displacement response Δ, maximum acceleration response a, and maximum inter-story displacement angle θ under three seismic wave excitations with peak accelerations of 70 cm/s^2, 200 cm/s^2, and 400 cm/s^2.

Table 12. The maximum displacement, acceleration, and displacement–angle response of the models.

The Waveform Input	a_{peak} (cm/s^2)	Model 1			Model 2		
		Δ (mm)	a (cm/s^2)	θ (rad)	Δ (mm)	a (cm/s^2)	θ (rad)
El Centro wave	70	7.16	281.80	1/545	23.86	1933.36	1/164
	200	20.00	782.47	1/195	57.03	4669.17	1/68
	400	38.51	1362.44	1/101	157.98	12,533.90	1/25
Taft wave	70	5.59	216.39	1/697	27.67	2297.59	1/141
	200	15.63	616.95	1/499	80.11	6570.58	1/49
	400	29.95	1198.11	1/130	144.82	12,109.30	1/27
Lanzhou wave	70	6.97	223.13	1/560	13.72	1218.79	1/284
	200	17.17	620.93	1/227	33.78	3119.63	1/116
	400	32.96	1166.31	1/118	58.44	5369.79	1/67

As can be seen from Figure 14, under the action of different seismic waves, the peak times of displacement and acceleration responses of model 1 and model 2 are different. Both the displacement and acceleration of the models increase with the increase in peak acceleration of the seismic waves from Table 12. Moreover, the displacement and acceleration responses of model 2 are greater than those of model 1, the amplification factors

under El Centro wave excitation range from 5.53 to 7.64, the amplification factors under Taft wave excitation range from 9.18 to 10.65, and the amplification factors under Lanzhou wave excitation range from 4.07 to 5.46. Under the same peak acceleration, model 1 exhibits a larger response to El Centro wave excitation, while model 2 exhibits a larger response to Taft wave excitation. Under the wave of a peak acceleration of 400 cm/s^2, the displacement response and acceleration response absolute values of the model 2 are ordered as Taft wave > El Centro wave ≈ Lanzhou wave.

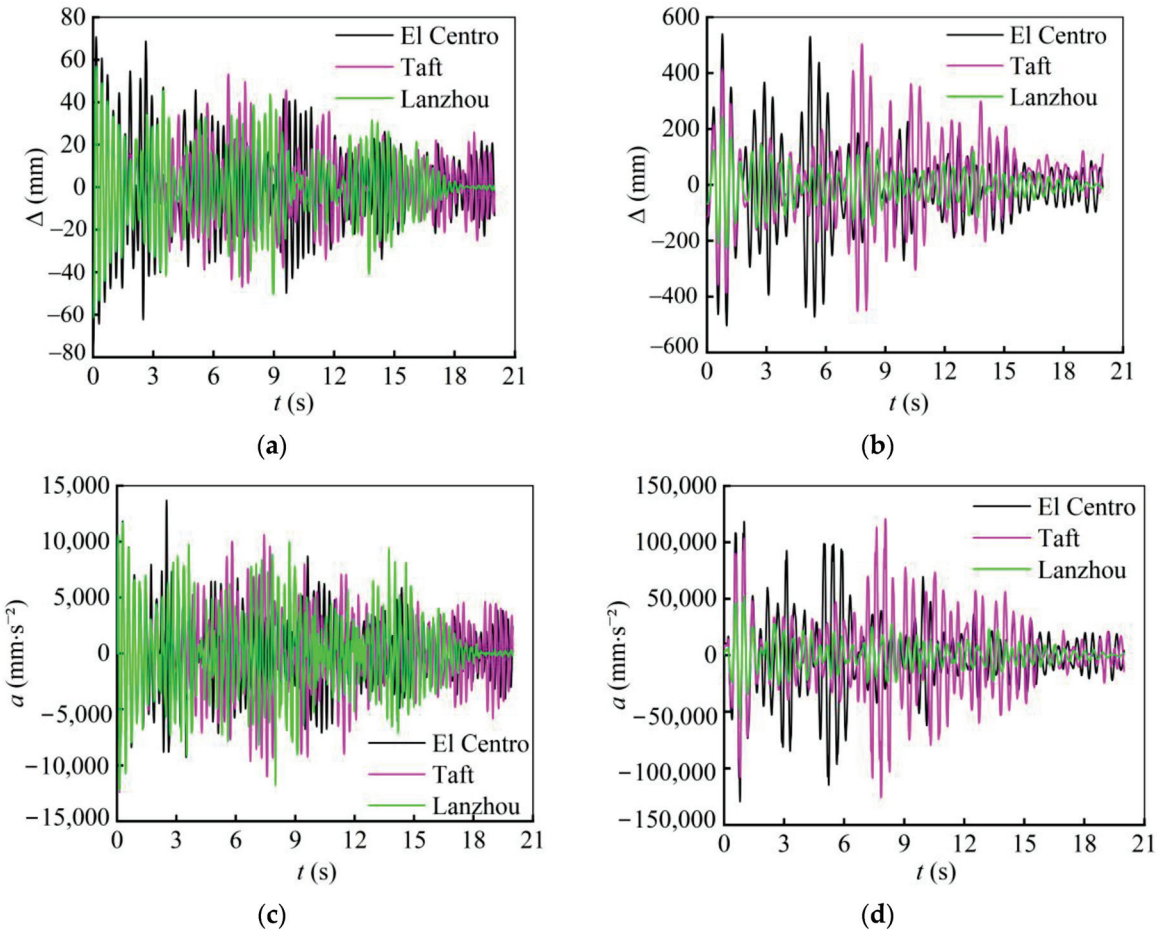

Figure 14. Time history curves of the reference points of the two models under a local seismic excitation at the peak acceleration of 400 cm/s^2. (**a**) Displacement–Time curve of model 1, (**b**) displacement–time curve of model 2, (**c**) acceleration–time curve of model 1, and (**d**) acceleration–time curve of model 2.

As indicated in Table 12, the maximum displacement angle is 1/25, which exceeds the 1/30 limit specified in "Standards for Maintenance and Strengthening of Ancient Building Wood Structures" (GB/T 50165-2020) [38]. Previous research pointed out that inter-story displacement angles above 1/20 significantly increase the risk of structural collapse [39]. Therefore, adopting 1/20 as the limit for inter-story displacement angle aligns with practical conditions [40]. The presence of soil significantly amplifies displacement and acceleration responses, as well as inter-story displacement angles, particularly compacted soil, exacerbating the seismic vulnerability of Caiyunjian Tower and potentially leading to structural overturning.

As shown in Table 12, the maximum displacement response and maximum acceleration response of the overall structure show a significant increase when the peak acceleration of the El Centro wave increases from 200 cm/s^2 to 400 cm/s^2. The increase factor is not approximately proportional to the increase in peak acceleration. It can be reasonably spec-

ulated that when the input excitation is an El Centro wave with a peak acceleration of 400 cm/s^2, Caiyunjian Tower may have been damaged.

By summing up the shear time history responses of each column top of the models, the maximum floor shear forces under various seismic conditions are obtained. Tables 13 and 14 show the maximum shear force of the two models. Figure 15 shows the shear force distribution from the base of the first floor to the top of the third floor for the models under partial working conditions. The trend of the maximum floor shear force along the structural height is basically consistent for both models under different seismic conditions. The addition of the cross-bridging on the second floor results in a small increase in the shear force at the column foot of the second floor compared with the column top of the first floor in all conditions. Due to the gradual inward displacement design of the upper column foot and the lower column top, the shear force on the node of the upper floor greatly reduces compared with the lower floor in the overall structure model. In response to EI, Taft, and Lanzhou wave excitations, the amplification factors of shear force for Caiyunjian Tower range from 2.96 to 3.38, 5.10 to 5.43, and 2.36 to 2.51, respectively, due to the high stylobate.

Table 13. The maximum floor shear response of model 1 under each working condition.

The Waveform Input	a_{peak} (cm/s^2)	Model 1 V_{max} (kN)					
		First Floor		Second Floor		Third Floor	
		Column Foot	Column Top	Column Foot	Column Top	Column Foot	Column Top
El Centro wave	70	68.73	55.47	59.55	19.92	5.19	7.16
	200	193.15	155.06	166.47	55.68	14.51	20.01
	400	371.88	298.55	320.52	107.20	27.95	38.52
Taft wave	70	48.49	37.87	38.07	13.31	4.45	5.13
	200	136.07	105.84	106.40	37.19	12.45	14.35
	400	260.76	202.83	203.90	71.26	23.85	27.50
Lanzhou wave	70	64.26	40.33	49.89	17.91	5.51	6.44
	200	158.36	112.71	122.95	44.15	13.58	15.86
	400	303.98	216.36	236.03	84.75	26.07	30.45

Table 14. The maximum floor shear response of model 2 under each working condition.

The Waveform Input	a_{peak} (cm/s^2)	Model 2 V_{max} (kN)					
		First floor		Second Floor		Third Floor	
		Column Foot	Column Top	Column Foot	Column Top	Column Foot	Column Top
El Centro wave	70	203.43	179.98	34.21	62.59	9.25	30.96
	200	653.38	577.14	154.45	176.08	21.51	97.40
	400	1200.27	1062.12	237.80	290.89	47.58	195.43
Taft wave	70	257.55	229.00	54.26	67.52	9.28	40.40
	200	738.69	656.61	155.71	193.55	26.63	115.74
	400	1330.78	1180.73	297.95	348.68	47.18	204.32
Lanzhou wave	70	151.62	134.60	53.64	54.22	2.26	18.32
	200	397.37	352.61	140.51	141.97	5.95	47.96
	400	721.05	639.32	254.78	257.16	14.31	86.83

Under the Taft wave excitation with a peak acceleration of 400 cm/s^2, the maximum shear force of model 2 increases substantially, with the increase in each layer relative to the bottom floor being 9.55%, 7.72%, 13.81%, 22.78%, 38.58%, and 26.89% from bottom to top, respectively. Soil makes the floor shear increase multiplier of the superstructure

between 6.66 and 8.59, so if the seismic response of the superstructure is analyzed without considering the effect of the base soil, the calculation results will be biased and insecure.

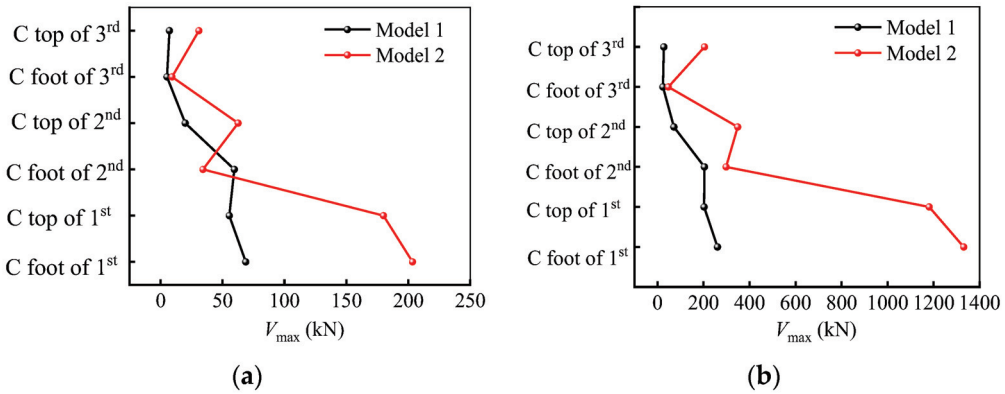

Figure 15. Distribution diagram of floor shear force (C means column). (**a**) El Centro a_{peak} = 70 cm/s^2; (**b**) Taft a_{peak} = 400 cm/s^2.

6. Conclusions

In situ dynamic characteristic tests were conducted on Caiyunjian Tower of Xingqing Palace, and finite element models for both Caiyunjian Tower and the overall structure were established. Three different seismic waves with different peak values were used to analyze the seismic responses for both models. The following conclusions were obtained:

(1) The first-order frequency of Caiyunjian Tower is 3.821 Hz, and the vibration mode is translation in the east–west direction. The second-order frequency is 4.106 Hz, and the vibration mode is translation in the north–south direction. The frequency in the east–west direction is less than that in the north–south direction, so the east–west direction is the weak stiffness direction of Caiyunjian Tower.

(2) The natural frequency of the high stylobate is low, and the frequencies of each order are similar. There is little difference between the front three frequencies of Caiyunjian Tower and the overall structure, but the fourth and higher frequencies of the overall structure are significantly smaller than Caiyunjian Tower. Therefore, the high stylobate reduces the natural frequency of the upper structure and soil–structure interaction has a significant impact on higher mode frequencies.

(3) The displacement and acceleration of Caiyunjian Tower and the overall structure increase with the increase in the peak acceleration of seismic waves, but the high stylobate increases the seismic response of the overall structure. The maximum inter-story drift angle of Caiyunjian Tower and the overall structure is 1/101 and 1/25, respectively, which is within the allowable limit for structural collapse.

(4) The maximum shear force of Caiyunjian Tower and the overall structure increase as the peak acceleration of seismic waves increases. The variation trend of the maximum shear force on each floor in both models is the same under different conditions. The high stylobate increases the maximum shear force of the overall structure.

(5) Due to the influence of the high stylobate, model 2 has different amplification factors for the displacement response, acceleration response, and maximum shear force on each floor under different seismic wave excitations. Caiyunjian Tower is more sensitive to excitation from the El Centro wave, while the overall structure is more sensitive to excitation from the Taft wave. The high stylobate amplifies the oscillation of the structure, which harms the seismic resistance of the structure.

(6) Terrain effect, material properties, modeling details, and other parameters will affect the performance of wooden towers with high stylobates. Limitations such as imperfect

modeling details and failure to consider multi-layer soil distribution need to be considered in future research.

Author Contributions: Writing—original draft preparation, H.X.; conceptualization, methodology, resources, project administration, and funding acquisition, J.X.; investigation and validation, D.S.; software and formal analysis, M.L.; data curation, B.X.; supervision and writing—reviewing and editing, C.W.; visualization, Y.S. All authors have read and agreed to the published version of the manuscript.

Funding: This research was funded by the National Natural Science Foundation of China (Grant No. 52308328, 52278317, 51908454), the China Postdoctoral Science Foundation (No 2023M732748), and the Preventive Conservation and Inheritance of Ancient Architecture "Scientist + Engineer" Teams (No. 2024QCY-KXJ-169).

Data Availability Statement: The data presented in this study are available on request from the corresponding author.

Conflicts of Interest: Author Yan Sui was employed by the company Xauat Engineering Technology Co., Ltd. The remaining authors declare that the research was conducted in the absence of any commercial or financial relationships that could be construed as a potential conflict of interest.

References

1. Jian, W.N.; Yue, B.R.; Song, G.M. The evolving role of Xingqing Palace in urban space. *Landsc. Archit.* **2012**, *2*, 33–37. [CrossRef]
2. Zhang, X.F.; Far, H. Effects of dynamic soil-structure interaction on seismic behaviour of high-rise buildings. *Bull. Earthq. Eng.* **2022**, *20*, 3443–3467. [CrossRef]
3. Boliseetti, C.; Whittaker, A.S. Numerical investigations of structure-soil-structure interaction in buildings. *Eng. Struct.* **2020**, *215*, 110709. [CrossRef]
4. Heiland, T.; Aji, H.D.B.; Wuttke, F.; Stempniewski, L.; Stark, A. Influence of soil-structure interaction on the dynamic charactitics of railroad frame bridges. *Soil. Dyn. Earthq. Eng.* **2023**, *167*, 107800. [CrossRef]
5. Bapir, B.; Abrahamczyk, L.; Wichtmann, T.; Prada-Sarmiento, L.F. Soil-structure interaction: A state-of-the-art review of moeling techniques and studies on seismic response of building structures. *Front. Built. Environ.* **2023**, *9*, 1120351. [CrossRef]
6. Anand, V.; Satish Kumar, S.R. Seismic Soil-structure Interaction: A State-of-the-Art Review. *Structures* **2018**, *16*, 317–326. [CrossRef]
7. Ma, H.; Xue, J.Y.; Zhao, H.T. Analysis of response of ancient timber buildings on the high pedestal under random earthquake excitations. *Ind. Archit.* **2014**, *44*, 45–49+54. [CrossRef]
8. Zhao, H.T.; Ma, H.; Xue, J.Y.; Zhang, F.L.; Zhang, X.C. Analysis of dynamic characteristics and seismic responses of the ancient timber building on high-platform base. *J. Earthq. Eng. Eng. Vib.* **2011**, *31*, 115–121. [CrossRef]
9. Xue, J.Y.; Wu, C.W.; Zhai, L.; Wang, R.P.; Ma, L.L. Finite element analysis on seismic response of Yingxian Wooden Tower by considering the effect of the stylobate. *J. Civ. Environ. Eng.* **2022**, *44*, 22–29. [CrossRef]
10. Meng, Z.B.; Wu, M.Z.; Hu, W.B.; Zhang, K.; Yuan, J. Seismic response analysis of Xi'an Bell Tower considering soil-structure interaction. *World Earthq. Eng.* **2008**, *24*, 125–129.
11. Sun, S.J.; Meng, Z.B.; Zhao, Q.S.; Zhao, T.F.; Jin, J. Dynamic performance analysis of ancient buildings based on soil-structure interaction. In Proceedings of the 7th International Conference on Environmental Science and Civil Engineering, Nanchang, China, 9–10 January 2021; Volume 719, p. 022010.
12. Meng, Z.B.; Hu, B.S.; Zhao, Q.S.; Jin, J.; Song, D.K. Dynamic response analysis of Liaocheng Guangyue Tower under the ground traffic load. In Proceedings of the 4th International Conference on Sensors, Measurement and Intelligent Materials, Shenzhen, China, 27–28 December 2015; Atlantis Press: Amsterdam, The Netherlands, 2016; pp. 1142–1146.
13. Pan, Y.; Chen, J.; An, R.B.; Yi, D.Y. A review on seismic performance of ancient timber structures on a slope. *J. Civ. Environ. Eng.* **2022**, *42*, 10–21.
14. Pan, Y.; Li, D.H.; Okuta, A.; Chen, J. Seismic performance of a historic timber structure on a slope. *J. Build. Eng.* **2023**, *71*, 106434. [CrossRef]
15. An, R.B.; Yuan, J.C.; Pan, Y.; Li, D.H. Experimental study on the seismic performance of a full-scale two-story traditional timber frame on sloped land. *Eng. Struct.* **2024**, *300*, 117139. [CrossRef]
16. Silva, F.D. Influence of soil-structure interaction on the site-specific seismic demand to masonry towers. *Soil. Dyn. Earthq. Eng.* **2020**, *131*, 106023. [CrossRef]
17. Liao, R.M. Dynamic Performance Analysis of Historic Architecture Based on Soil-Structure Interaction. Master's Thesis, Liaocheng University, Liaocheng, China, 2019.

18. Wang, Y. Seismic Analysis of the Soil-Structure System in Marine Soft Soil for Mid-Rise and High-Rise RC Frames. Master's Thesis, Southeast University, Nanjing, China, 2019.
19. Gao, Z.W.; Yang, X.B.; Zhang, J.F.; Tang, H.Y.; Du, Y.; Zhao, S.Y. Modal modification based analysis of seismic performance of the Jiufeng Temple Ancient Masonry Pagoda. *Soil. Dyn. Earthq. Eng.* **2025**, *188*, 109087. [CrossRef]
20. Yuan, Z.Y.; Lu, J.L.; Li, Z.; Chen, Y.F. Dynamic characteristics and seismic response analysis of Luoshan Temple Pagoda. *Constr. Technol.* **2024**, *53*, 13–17.
21. Xu, D.F.; Xie, Q.F.; Zhang, Y.; Hao, W.M. Effects of inclination on the seismic performance of Chinese historical masonry tower identified through shaking table tests. *J. Earthq. Eng.* **2023**, *27*, 1458–1481. [CrossRef]
22. Abruzzese, D.; Miccoli, L.; Yuan, J.L. Mechanical behavior of leaning masonry Huzhu Pagoda. *J. Cult. Herit.* **2009**, *10*, 480–486. [CrossRef]
23. Zhang, F. Study on Seismic Response Characteristics of Masonry Pagodas in Hill Site. Master's Thesis, Yangzhou University, Yangzhou, China, 2023.
24. Xue, J.Y.; Wu, C.W.; Hao, F.H.; Ma, L.L. In situ experiment and finite element analysis on dynamic characteristics of Yingxian Wooden Tower. *J. Build. Struct.* **2022**, *43*, 85–93. [CrossRef]
25. Bai, F.; Yang, N.; Liu, W.; Zhang, S.H. Study on condition assessment of Dingzhou Kaiyuan Pagoda under ambient vibration. *J. Build. Struct.* **2022**, *43*, 105–115. [CrossRef]
26. Xue, J.Y.; Wu, C.W.; Zhou, S.Q.; Zhang, F.L. Analysis on dynamic characteristics and seismic response of the Anding Gate Tower in Xi'an considering high stylobate. *J. Build. Struct.* **2021**, *42*, 12–21. [CrossRef]
27. Zhao, J. Studies on Optimal Design of Measurement Point Layout for Structural Health Monitoring. Doctor's Thesis, Jinan University, Guangzhou, China, 2011.
28. Xu, X.Z.; Hua, H.X.; Chen, Z.N. Review of modal identification method based on ambient excitation. *J. Vib. Shock.* **2002**, *3*, 3–7+91. [CrossRef]
29. Li, S.C.; Wang, P.X.; Zhang, S.J.; Macchioni, N. Parameter estimation on material properties of timber beams in ancient building based on test and evaluation. *Ind. Archit.* **2019**, *49*, 77–82. [CrossRef]
30. *GB/T 50107-2010*; Standard for Evaluation of Concrete Compressive Strength. China Building Industry Press: Beijing, China, 2010. (In Chinese)
31. Chang, S.P. *Geological Engineering Handbook*, 5th ed.; China Building Industry Press: Beijing, China, 2018.
32. Xue, J.Y.; Ling, H.Q.; Song, D.J.; Wu, C.W.; Guo, H.Z. Experimental study and finite element analysis on seismic behavior of Pingshenke Dou-Gong Brackets. *J. Build. Struct.* **2023**, *44*, 74–85. [CrossRef]
33. Zhang, Y.X. Seismic Response Analysis of High-Deck Wood Structure in Ancient Buildings Considering Soil-Structure Dynamic Interaction. Master's Thesis, Xi'an University of Architecture and Technology, Xi'an, China, 2017.
34. Wu, C.W.; Xue, J.Y.; Zhang, X.C.; Bai, F.Y.; Ma, H.D. Seismic assessment and fragility analysis of traditional Chinese timber frame building considering degraded connections. *Int. J. Archit. Herit.* **2023**, *17*, 553–572. [CrossRef]
35. Wu, C.W.; Zhang, X.C.; Xue, J.Y.; Ma, H.D.; Wu, J.B. Effect of performance degradation and infilled walls on seismic fragility assessment of traditional Chinese timber-frame structure. *Int. J. Archit. Herit.* **2022**, *16*, 1252–1269. [CrossRef]
36. *GB 50011-2011*; Code for Seismic Design of Buildings. China Building Industry Press: Beijing, China, 2016. (In Chinese)
37. Zhou, S.Q. Dynamic Characteristics and Seismic Response Analysis of Xi'an Andingmen Gate Building. Master's Thesis, Xi'an University of Architecture and Technology, Xi'an, China, 2019.
38. *GB/T 50165-2020*; Standards for Maintenance and Strengthening of Ancient Building Wood Structures. China Building Industry Press: Beijing, China, 2020. (In Chinese)
39. Tanahashi, H.; Suzuki, Y. Analytical simulations of full-scale static and dynamic tests of traditional wooden frames. *Hist. Urban Disaster Prev. J.* **2010**, *4*, 181–188. [CrossRef]
40. Zhang, X.C.; Hu, C.M.; Wu, C.W.; Ma, H.D. Analysis of anti-collapse performance of ancient timber frame buildings of grand style with Dou-gong under horizontal earthquake. *Conserv. Archaeol. Sci.* **2020**, *32*, 10–18. [CrossRef]

buildings

MDPI

Article

Biaxial Resistance of Pre-Engineered Beam Hangers in Glulam

Houman Ganjali, Fei Tong and Thomas Tannert *

School of Engineering, University of Northern British Columbia, Prince George, BC V2N 4Z9, Canada; ganjali@unbc.ca (H.G.); fei.tong@unbc.ca (F.T.)
* Correspondence: thomas.tannert@unbc.ca

Abstract: In timber construction, Glulam post-and-beam systems are commonly used to transfer vertical loads to the foundation. In such systems, the connections play a critical role in structural performance. Pre-engineered connectors, which facilitate fast and efficient assembly, are typically designed to resist only vertical shear loads. However, during seismic and wind events, post-and-beam systems deform horizontally, and axial forces develop at the connections. In this research, the performance of RICON and MEGANT pre-engineered connectors was studied under biaxial loading involving concurrent shear and axial forces. A total of 12 full-scale tests on Glulam frame segments were conducted. Neither type of connector experienced any resistance loss under concurrent shear loads equal to the factored shear resistance and axial loads equal to 5% of the factored shear resistance. The axial load-carrying capacity of the RICON and MEGANT connectors was up to 124% and 97% of their factored shear resistance, respectively. The global failure of all the studied connectors demonstrated both ductility and residual deformation capacity. These results provide valuable information for engineers designing Glulam post-and-beam systems in seismic regions.

Keywords: mass timber construction; post-and-beam systems; self-tapping screws; glue-laminated timber; experimental testing

1. Introduction

Historically, timber structures were limited by the size of local trees. The shift from solid sawn timber to glue-laminated timber (Glulam), pioneered by Hetzer [1], marked a significant technological advance, expanding timber's use in construction. Glulam allowed for the creation of continuous lamellae, reducing material defects and enabling larger, more complex shapes with a high load-bearing capacity [2].

Timber structures provide significant environmental benefits; trees capture CO_2 during growth, storing carbon within the building for its lifespan. This, combined with the lower carbon emissions from timber production compared to materials like steel and concrete, highlights their environmental advantages [3]. As a result, timber construction has advanced significantly, particularly in North America, where building codes now allow timber buildings of up to 18 stories [4,5]. This progress is based on the success of projects like the Wood Innovation and Design Centre (WIDC) in Prince George, home to the Wood Engineering program of the University of Northern British Columbia [6].

Gravity load-resisting systems transfer vertical loads (e.g., dead, live, and snow loads) downward through a structure to the foundation. Among the various structural systems used in timber construction, the post-and-beam system is one of the most common [7]. Vertical posts support horizontal beams, most often made of Glulam, allowing for open interior spaces such as in WIDC, as shown in Figure 1. The gravity system must be able

to deform with the structure during a seismic event. It is designed to provide minimal lateral stiffness, as this function is primarily handled by the lateral force-resisting system, which addresses lateral loads such as wind or earthquakes. Additionally, the connections within the gravity system must have an adequate deformation capacity to preserve the structural integrity as they move in coordination with the lateral system 'going along with the ride' [4]. A failure in these connections could result in a partial or complete collapse of the structure.

Figure 1. Glulam post-and-beam gravity system; Photography Credit: Ema Peter.

Timber members can be joined using carpentry joints, such as rounded dovetail joints (RDJs) [8], mechanical fasteners like self-tapping screws (STSs) [9], adhesive bonding [10], or combinations of these methods [11]. Traditional fasteners, such as bolts and rivets, depend on the relative displacement between components for load transfer. Recently, STSs have emerged as the state-of-the-art in timber connector technology, utilizing their axial withdrawal resistance for enhanced performance [9]. Among metal dowel-type fasteners, STSs are preferred because they typically require no predrilling [9]. The strength, stiffness, and ductility of STS connections vary based on the installation angle, with screws acting in both withdrawal and shear and providing a combination of high stiffness and ductility [12,13].

To connect posts to beams, a traditional method to connect beams to columns is light-gauge metal joist hangers, for which the ASTM D7147 testing method for joist hangers [14] was developed. Such joist hangers are assumed to freely rotate, but have been shown to exhibit some moment restraint, with the latter support condition leading to larger shear load resistance [15]. Popovski et al. [16] tested heavy timber connections using steel bolts and glulam rivets. Bolted connection ductility was dependent on bolt slenderness, with smaller diameters exhibiting more yielding. Rivet connections, designed for rivet failure, outperformed bolted connections in seismic performance and energy dissipation. Other research focused on bolted beam–column connections using STSs as reinforcement to avoid brittle failure and to increase ductility [17–19]. The axial load-carrying capacity resistance of post-to-beam connections has scarcely been investigated, but it was shown that RDJs exhibit considerable tension and bending resistance [20]. Hybrid timber–steel moment-resisting connections that consist of a steel link between the timber column and beam were tested for both the bending moment and shear resistance, without consideration of biaxial loading states [21,22]. He and Liu [23] examined timber post-to-beam connections with slotted-in steel plates where the moment resistance is typically neglected in the design; however, they determined that the STSs used to reinforce the timber increased the moment resistance. The reinforcement mitigated wood splitting, changing the failure mode from brittle to ductile.

While experimental testing of structural systems is vital to understanding their behavior under a load, due to space and budget constraints, scaled-down tests are often used, enabling parameter investigations that are rarely feasible in full-scale tests. Tests on the moment and shear responses of beam-to-column connectors in full-scale and quarter-scale mass timber systems showed that quarter-scale connections closely replicate full-scale responses [24]. One barrier to using timber in tall buildings is the limited fire resistance of the connections. Palma et al. [25] studied the fire behavior of timber beam-to-column shear connections under perpendicular grain loading and showed that dowelled connections achieved up to 60 min of fire resistance. Another experimental study tested eight glulam beam–end connections with concealed, mechanically fastened steel rods and showed that smaller washers improved wood protection, while longer rod anchorages enhanced shear resistance. Combining these features enabled a two-rod connection to achieve one hour of fire resistance without added protection [26].

These recent advances in connector technology have improved the construction of Glulam frames, enabling faster and more efficient assembly. Using pre-engineered connections, such as MEGANT and RICON, reduces installation errors, accelerates construction, and lowers costs [8]. One notable development is the beam-hanger system, which provides high-capacity, fully concealed, and fire-rated connections for mass timber structures. Beam hangers often use a clamping mechanism or dovetail joint to slot the plates together, and they may be recessed into the primary or secondary member to meet fire resistance requirements. Such pre-engineered beam hangers are widely used in buildings with large members [27]. They typically feature pre-installed plates on the beam end and the supporting post [28], and are connected to the timber with STSs.

The research conducted to date on the structural performance of pre-engineered beam-hanger connections was limited to the sub-sections of frames. The MEGANT connector was tested under interstorey drift and surpassed interstorey drifts of 2.5%, while failing due to a combined tension and pull-out failure of the STSs. It was observed that the gravity load has a significant effect on the interstorey drift capacity and energy dissipation of the connector. Leach et al. [29] evaluated the performance of different beam hangers, including the MEGANT and RICON systems, under shear and reversed cyclic loading to assess their seismic behavior. A constant shear force, simulating a gravity load, was applied near the beam–post connection, while cyclic displacement was imposed at the beam end. The MEGANT connectors sustained interstorey drifts exceeding 2.5%, surpassing the National Building Code of Canada (NBCC) [4] maximum allowable drift. In contrast, the RICON connectors failed at drift levels slightly below 2.0%. The failure modes included both bending of the steel connector plates and partial screw withdrawal. The MEGANT beam hanger was deemed more suitable for seismic applications due to its higher drift capacity and more ductile failure modes.

Madland et al. [30] tested four beam-to-column connections, including MEGANT E beam hangers, to evaluate their deformation compatibility under lateral displacements of frame segments. The test set-up included 3.7 m and 4.3 m Glulam posts. The column was supported by a pin connection at the base, allowing for free rotation. A constant gravity load was applied to the beam, and the frame was laterally displaced using a cyclic loading protocol. The MEGANT connection reached a yield load of 16 kN at a displacement of 34 mm and sustained a 7.2% drift without collapse. Damage was observed on the beam–side connector, including plate bending and screw withdrawal from the bottom of the plate, while the column connection plate showed no signs of damage.

In timber engineering, connections in post-and-beam frames are typically designed as either pinned or rigid. Pinned connections primarily resist shear forces and allow for rotational movement, while rigid connections resist both shear forces and bending

moments. In practice, however, connections exhibit behavior that falls between these two extremes. Despite this, contemporary timber design generally assumes that connections in the gravity load-resisting system are pinned, simplifying the structural analysis. While the connections in post-and-beam frames are not expected to contribute to a structure's lateral stiffness, during seismic events, gravity load-bearing frames deform horizontally. The deformation of the frame causes axial forces, in the beam direction, to develop at the beam-to-column connections. These axial forces interact with vertical shear forces, resulting in a biaxial load state.

2. Materials and Methods

2.1. Objective

The objectives of the research presented herein were to (i) investigate the ability of RICON and MEGANT pre-engineered beam hangers to resist biaxial loading of concurrent factored shear resistance and an axial load equal to 5% of the factored shear resistance as per ASCE/SEI-7-22 [31] requirements; and (ii) determine the axial load-carrying capacity and failure mechanisms under concurrent shear and axial loads. To achieve these objectives, a total of 12 full-scale post-to-beam connections were fabricated and tested in the UNBC Wood Innovation Research Lab in Prince George, Canada.

2.2. Timber Elements and Connectors

Glulam Douglas Fir 24F-EX 265 × 646 and Douglas Fir 16C-E 265 × 380 were used for beams and posts, respectively. The moisture content was determined using an electric resistance meter and had an average value of 10.7%.

Four types of pre-engineered connectors [8] were used to connect the beams to the posts: (1) RICON S vs. 290 × 80 mm (referred to as "RCN 290"); (2) RICON S vs. XL 390 × 80 mm (referred to as "RCN 390"); (3) MEGANT 430 × 150 mm (referred to as "MGT 430"); and (4) MEGANT 550 × 150 mm (referred to as "MGT 550"). The RICON beam-hanger system, shown in Figure 2a, is made from mild steel [28], featuring a welded "collar bolt". RICON consists of two identical components and is installed using Ø 10 × 100 mm ASSY VG CSK STSs to columns and Ø10 × 200 mm ASSY VG CSK STSs to beams. The MEGANT beam-hanger system, shown in Figure 2b, is made from aluminum [28]. The system includes two connector plates, two clamping jaws (one threaded and one unthreaded), and two threaded rods, along with washers and nuts that secure the assembly. The system utilizes ASSY VG CSK Ø 8 × 160 mm STSs, installed at 45° and 90° to the surface.

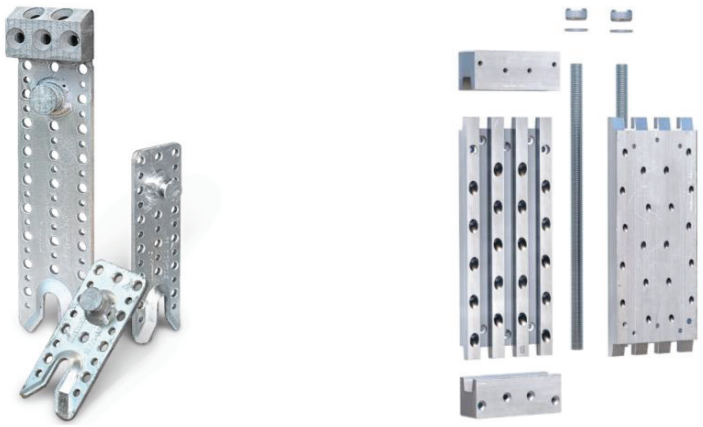

(**a**) (**b**)

Figure 2. Connectors [8]: (**a**) RICON; and (**b**) MEGANT.

The connectors were assembled according to the MTC Solutions "Beam Hanger Design Guide" [28]. First, one of the two identical parts of each connector was installed on the primary member and the other on the secondary member. Afterwards, the part mounted on the secondary member was slid in place, forming the connection. This procedure allowed for streamlined workflow and reduced shop time. For the ease of installation, all connectors were surface mounted. Examples of installed RICON and MEGANT connectors are presented in Figure 3.

(**a**) (**b**) (**c**) (**d**)

Figure 3. Installed connectors: (**a**) RCN 290; (**b**) RCN 390; (**c**) MGT 430; and (**d**) MGT 550.

2.3. Test Set-Up

The connectors were tested under biaxial loading, under a combined shear in direction of the post and axial tension in direction of the beam, as shown in Figure 4. The primary (post) member was oriented horizontally and tied to the strong floor using HSS profiles and threaded rods to prevent uplift during the test, while the secondary member (beam) was oriented vertically. In order to apply the shear load, a hydraulic jack was placed horizontally on the face of the post applying the load through a loading plate at the end of the beam. The axial load was applied through two hydraulic actuators and by means of two tension straps on the sides of the beams.

Figure 4. Biaxial loading test set-up.

Five calibrated linear string potentiometers (string pots) were used to measure the displacements as shown in Figure 5. A set of two sting pots was used on each corner of the beam (on the back and the front) to measure the relative axial displacement between beam and post. One string pot was used to measure the relative shear displacement between column and beam.

Figure 5. Test specimen instrumentation.

2.4. Loading Protocol

The loading protocol, adopted from ISO 6891 [32], is depicted in Figure 6. The loading procedure consisted of four steps as follows: (1) a shear load equal to the factored download resistance (factored shear resistance) of the connector was applied at a rate of approx. 5 mm/min; (2) a nominal axial load equal to 5% of the factored shear resistance of the connector, taken from [8], (target axial load) was applied at a rate of 5 mm/min; (3) the shear load was reduced to 40% of the factored shear resistance of the connector; and (4) the axial load was increased at a rate of 5 mm/min until failure. In these tests, failure was defined as a 20% drop in the resisted axial load.

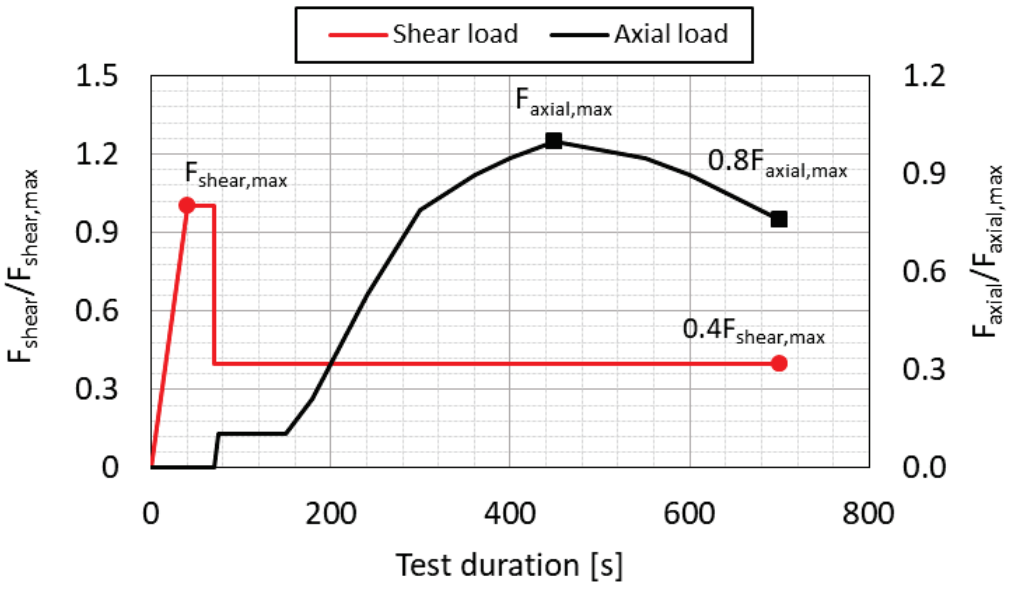

Figure 6. Biaxial loading protocol.

2.5. Stiffness and Ductility Analysis

The initial stiffness k was defined from the slope of the force–displacement curve in the range of 10% to 40% of the peak load; the ultimate stiffness (k_{ult}) was defined from the slope of the force–displacement curve in the range of 10% to 100% of the peak load. Ductility, μ, was defined as the ratio of ultimate displacement, d_{ult}, to yield displacement, d_y, of the axial force–displacement curves as per ISO/TR 21141 [33], with d_{ult} being the deflection at failure. Ductility was evaluated using the scale proposed by Smith et al. [34] with brittle ($\mu \leq 2$), low ductility ($2 \leq \mu \leq 4$), moderate ductility ($4 \leq \mu \leq 6$), and high ductility ($\mu > 6$).

3. Results

3.1. Load–Displacement Behavior and Failure Modes

The axial and shear load vs. displacement curves of the tested series are presented in Figure 7. The axial load vs. displacement of the RICON connectors can be divided into three parts: an initial linear part, a subsequent non-linear phase with a reduced stiffness leading to the peak load, and eventually, it enters a non-linear phase characterized by a gradual loss in stiffness, leading to a 20% drop in the load-carrying capacity, as shown in Figure 7a,b. In two of the RCN 390 specimens, this loss of stiffness was sudden, taking place right after the peak load, as seen in Figure 7b for Tests #1 and #3. On the other hand, the axial load vs. displacement of the MEGANT connectors had two distinct phases: an initial quasi-linear part up that occurred up to the peak load, which was followed by multiple load drops and load distributions until the failure point, as shown in Figure 7c,d. Studying the initial part of the axial load vs. displacement curves, the tested connectors within each series exhibited similar initial stiffnesses.

The shear load vs. displacement behavior of both the RICON and MEGANT connectors followed a semi-linear trend up to the factored shear resistance of the connector without any loss of strength. In the initial part of the RICON connectors' shear load–displacement curves, however, a plateau can be observed, which happened due to local compression that was perpendicular to grain deformation at the point of shear load introduction on the beam. This was minimized in the MEGANT connectors by increasing the shear load introduction surface area by means of a steel plate.

The connector failure modes are shown in Figure 8. In the RICON connectors, at an axial load equal to 5% of the factored shear resistance of the connectors, no signs of connector or wood element failures were observed. The global failure of the RICON connectors was plastic deformation taking place in the "collar bolt" of the connector as well as bending of the connector plate, as shown in Figure 8a,b. At the ultimate axial load, no screw failure was detected in the RICON connectors. In the MEGANT connectors, no failure was observed when the axial load was equal to 5% of the factored shear resistance of the connectors (Figure 8c,d). The global connection failure was a combination of connector yielding, uplift of the plate's end without the clamping jaw, and residual deformations, which could be observed as a gap between the two plates at the ultimate load. The clamping jaw of the MEGANT connectors experienced no uplift or deformation.

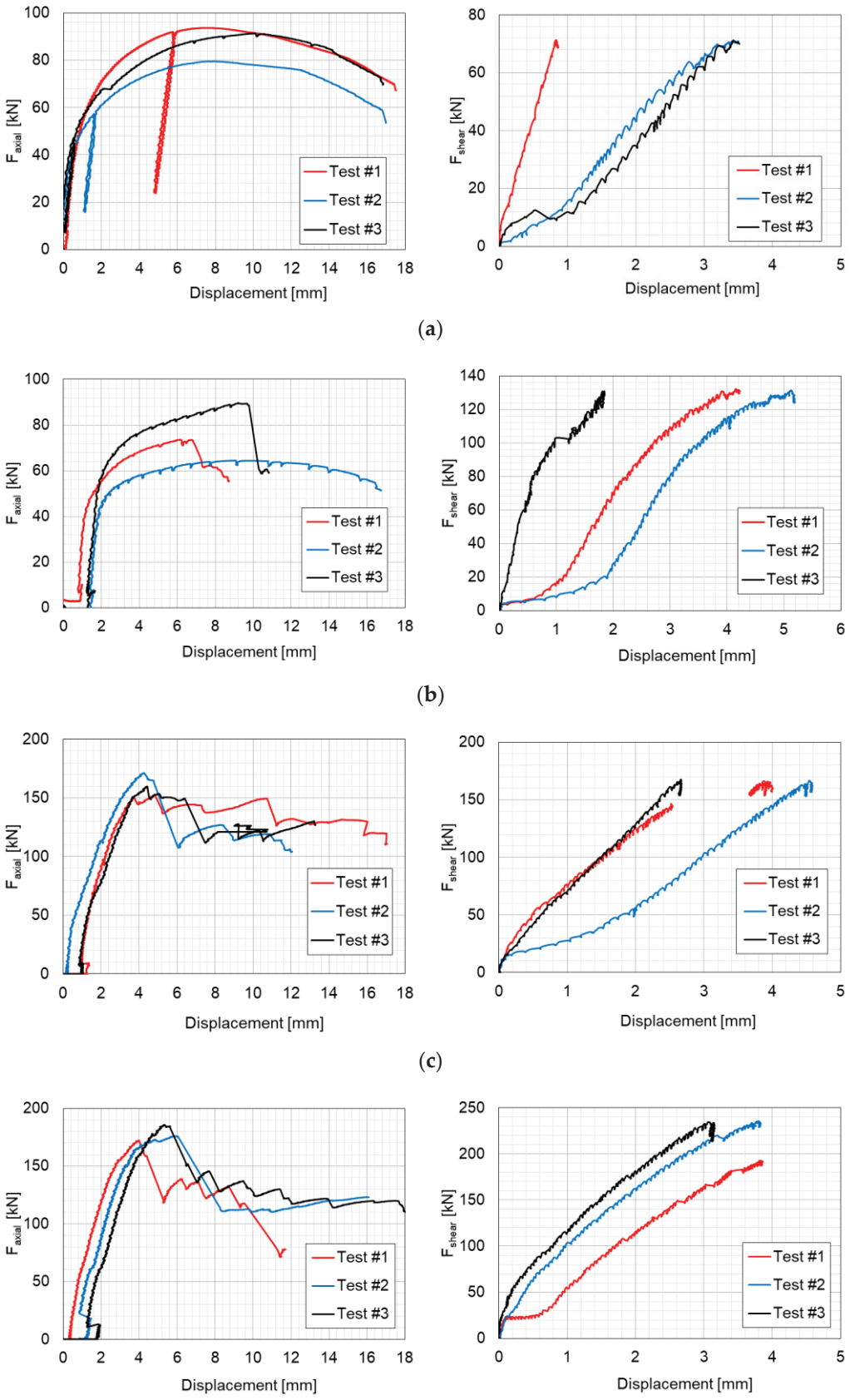

Figure 7. Axial and shear load vs. displacement: (**a**) RCN 290, (**b**) RCN 390, (**c**) MGT 430, and (**d**) MGT 550.

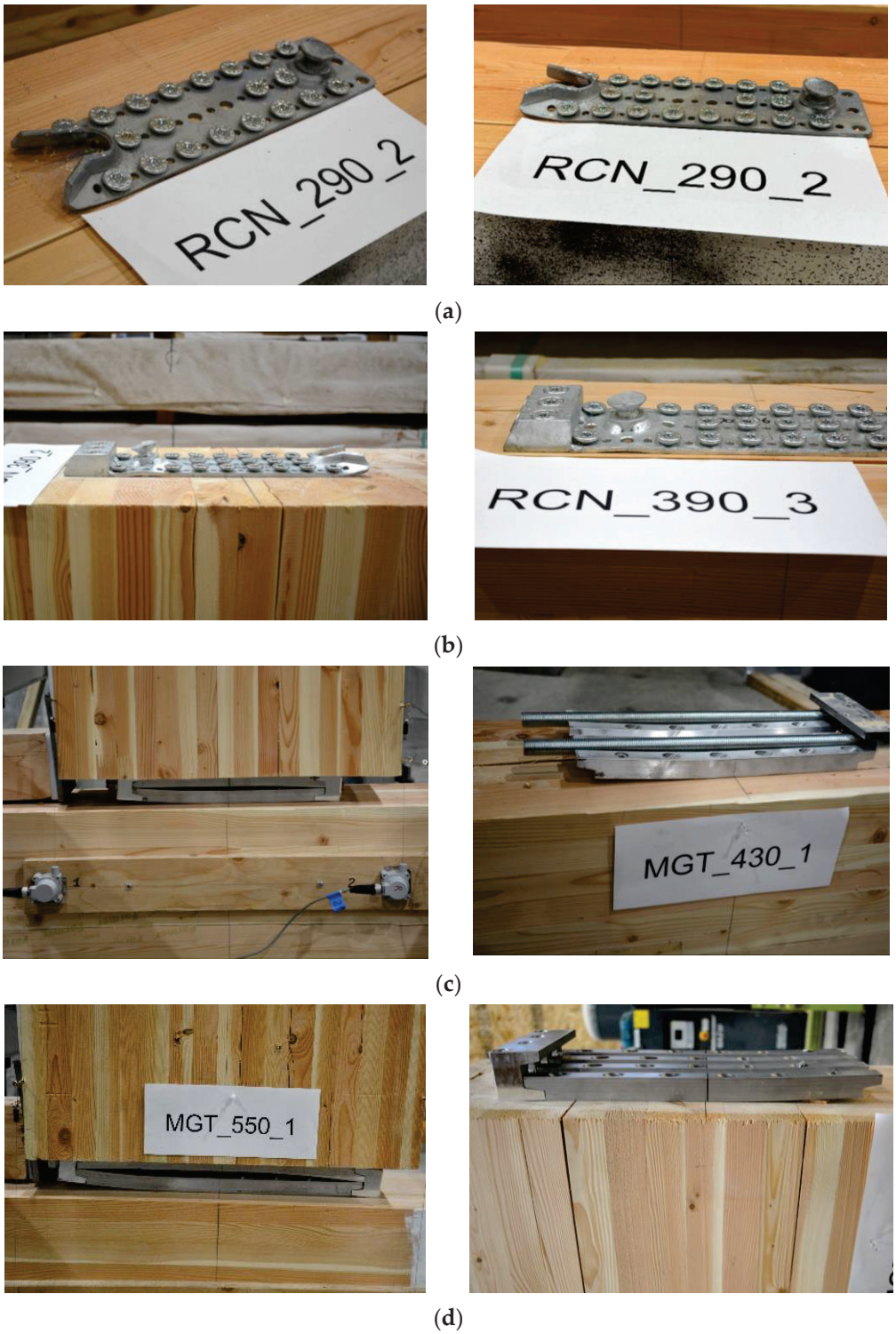

Figure 8. Failure modes: (**a**) RCN 290; (**b**) RCN 390; (**c**) MGT 43; and (**d**) MEGANT 550.

3.2. Analysis

The maximum shear force, $F_{s,max}$, and its corresponding displacement, $d_{Fs,max}$, as well as the maximum axial force, $F_{a,max}$, and its corresponding displacement, $d_{Fa,max}$, of the individual specimens and the average and coefficient of variation (CoV) values of each series are reported in Table 1. On average, RCN 290, RCN 390, MGT 430, MGT 550 took 88 kN, 76 kN, 161 kN, and 178 kN, respectively. The MEGANT connectors were on average stronger in terms of their axial load-carrying capacity, having up to 2.3 times the axial

resistance of the RICON connector, while the RICON connectors showed a higher axial deformation capacity at their peak load, averaging around 8 mm. The axial load-carrying capacity of RCN 290, RCN 390, MGT 430, MGT 550, was 124%, 58%, 97%, and 81% of their factored shear resistance respectively. The coefficient variation of the maximum axial force of Ricon connectors ranging from 7% to 14% was higher than those of MEGANT connectors, on average, falling between 3% and 14%. However, no consistent trend was observed in the CoV of the displacements corresponding to $F_{a,max}$. The CoV of the displacements corresponding to the factored shear resistance of Ricon connectors was, on average, higher compared with those of MEGANT connectors.

Table 1. Test results–maximum shear and axial forces and corresponding displacements.

Connector	Parameter	$F_{s,max}$ [kN]	$d_{Fs,max}$ [mm]	$F_{a,max}$ [kN]	$d_{Fa,max}$ [mm]
RCN 290	Test#1	70.3	0.8	93.7	7.4
	Test#2	70.9	3.5	79.5	7.6
	Test#3	71.2	3.4	91.3	10.1
	Mean	71.2	2.6	88.2	8.4
	CoV	-	48%	7%	15%
RCN 390	Test#1	133.2	4.1	73.6	6.2
	Test#2	131.4	5.1	64.4	9.0
	Test#3	130.9	1.8	89.77	9.2
	Mean	131.5	3.7	75.9	8.1
	CoV	-	37%	14%	17%
MGT 430	Test#1	166.1	3.9	152.3	4.8
	Test#2	166.8	4.5	171.2	4.3
	Test#3	167.8	2.7	159.8	4.4
	Mean	166.9	3.7	161.1	4.5
	CoV	-	21%	5%	5%
MGT 550	Test#1	192.7	3.8	172.0	4.0
	Test#2	235.5	3.8	176.0	6.0
	Test#3	234.5	3.1	185.7	5.3
	Mean	220.9	3.6	178.0	5.1
	CoV	-	10%	3%	16%

As $F_{s,max}$ was the input, determining the CoV was not applicable.

The individual test specimens and their average initial stiffnesses at 40% of the ultimate axial load (k), and at the ultimate load level (k_{ult}), as well as the ductility factors, μ, and the corresponding CoV values are reported in Table 2. At the initial stiffness level, on average, the RCN 290 connectors had a $k_{40\%}$ of 74.7 kN/mm, RCN 390 connectors had 118.7 kN/mm, MGT 430 connectors had 83.7 kN/mm, and MGT 550 connectors had 65.1 kN/mm. The CoV of the $k_{40\%}$ of the series varied between 11.6 and 27.5%, with RCN 290 having the highest CoV. Overall, at the ultimate stiffness level (k_{ult}), the MEGANT connectors had a higher residual stiffness; MGT 430 and MGT 550 had around 38.6 kN/mm of residual stiffness, while both the RICON connectors experienced a higher stiffness degradation, with RCN 290 and RCN 390 having a k_{ult} around 10 kN/mm. The CoV of the k_{ult} of the series varied between 5.3 and 20.2%.

Table 2. Test results–stiffness and ductility.

Connector	Parameter	$k_{40\%}$ [kN/mm]	k_{ult} [kN/mm]	μ [-]
RCN 290	Test#1	68.0	11.7	18
	Test#2	102.6	9.3	61
	Test#3	53.6	8.1	20
	Mean	74.7	9.7	33
	CoV	28%	15%	60%

Table 2. *Cont.*

Connector	Parameter	$k_{40\%}$ [kN/mm]	k_{ult} [kN/mm]	μ [-]
RCN 390	Test#1	114.2	12.3	7.8
	Test#2	137.3	7.4	9.7
	Test#3	104.7	10.2	5.9
	Mean	118.7	10.0	7.8
	CoV	12%	20%	20%
MGT 430	Test#1	98.4	36.0	7.7
	Test#2	78.4	39.0	3.3
	Test#3	74.2	41.0	2.9
	Mean	83.7	38.7	4.6
	CoV	13%	5%	47%
MGT 550	Test#1	77.3	43.9	2.4
	Test#2	62.5	30.8	2.6
	Test#3	55.4	41.4	1.9
	Mean	65.1	38.7	2.3
	CoV	14%	15%	13%

The RICON connectors exhibited a higher ductility; the mean μ of the RCN 290 connectors was 33.2, RCN 390 connectors was 7.8, MGT 430 connectors was 4.6, and MGT 550 connectors was 2.3. According to the criteria from Smith et al. [34], both RICON series had "high ductility", the MGT 430 series had "moderate ductility", and the MGT 550 series had "low ductility". The main reasons for the higher ductility in the RICON connectors were that, on average, they had a higher initial stiffness and the fact that the RICON connectors are made of mild steel, which resulted in the plastic deformation of the "collar bolt" of the connectors as well as the bending of the connector plates.

4. Discussion and Conclusions

Pre-engineered beam hangers are the parts of the gravity load system of a building that are designed to carry shear forces. However, under lateral displacements, such as during an earthquake event or extreme winds, the gravity load system should be able to go along with the ride, meaning the beam-to-column connections should be able to maintain their load-carrying capacity while experiencing lateral deformation and its resulting axial force. In this study, the biaxial load-carrying capacity of four beam hangers, RICON S vs. 290 × 80; RICON S vs. XL 390 × 80; MEGANT 430 × 150; and MEGANT 550 × 150, was investigated. The results demonstrated that all connectors were able to withstand 5% of the factored shear resistance of the connectors applied in an axial direction while also applying a shear load equal to 100% of the factored connector's capacity without experiencing any reduction in either load carrying or structural loss. Both the RICON and MEGANT connectors had a higher axial load-carrying capacity than their factored shear resistance. The failure of the RICON connectors was in connector yielding. The failure in the MEGANT connectors was accompanied by connector yielding as well as column splitting, However, the global axial failure under the biaxial loading showed ductility and residual deformation capacity. RCN 390 had the highest initial stiffness and, on average, both RICON series showed a higher degree of ductility compared with the MEGANT connectors.

Although both connectors showed satisfactory behavior under a biaxial force state, since beam hanger systems do not form a perfect pin, further numerical and experimental studies should aim to determine the rotational stiffness of Glulam gravity load-bearing frames with beam hanger connectors to assess the effects of the transferred moment on the load-carrying capacity of the columns when designing such frames.

Author Contributions: Conceptualization, T.T.; methodology, T.T. and F.T.; validation, H.G. and T.T.; formal analysis, H.G., T.T., and F.T.; investigation, H.G.; data curation, H.G.; writing—original draft preparation, H.G.; writing—review and editing, T.T. and F.T.; funding acquisition, T.T. and F.T. All authors have read and agreed to the published version of the manuscript.

Funding: This project was funded by the government of British Columbia through a Forest Innovation Investment (FII) grant (24/25-UNBC-SRB-W25-043) and by the Natural Sciences and Engineering Research Council of Canada (NSERC) through an Alliance grant (ALLRP 583429–23) in collaboration with MTC Solutions.

Data Availability Statement: The raw data supporting the conclusions in this article will be made available by the authors upon request.

Acknowledgments: MTC Solutions and Kalesnikoff Lumber Co., Ltd. provided in-kind contributions in the form of connectors and screws, and CLT supplied materials at a reduced price. MTC Solutions, Aspect Structural Engineers, and FPInnovations supported the funding application. The support in developing and conducting the tests provided by Dr. Tyler A Davis (MTC Solutions), UNBC lab lead Maik Gehloff, UNBC technicians Nathan Downie, James Andal and Ryan Stern, and MASc student Hamidreza Nasiri is greatly appreciated.

Conflicts of Interest: The authors declare no conflicts of interest. The funders had no role in the design of this study; in the collection, analyses, or interpretation of data; in the writing of the manuscript; or in the decision to publish the results.

References

1. Hetzer, O. Gebogener Holz-Bauteil für Vereinigte Dach-Pfosten und-Sparren. Kaiserliches Patentamt Patent n 197773, 1906.
2. Dietsch, P.; Tannert, T. Assessing the Integrity of Glued-Laminated Timber Elements. *Constr. Build. Mater.* **2015**, *101*, 1259–1270. [CrossRef]
3. Natural Resources Canada. Available online: https://natural-resources.canada.ca/home (accessed on 17 December 2024).
4. National Research Council of Canada (NRCC), Canadian Commission on Building and Fire Codes. *National Building Code of Canada*; NRCC: Ottawa, ON, Canada, 2022.
5. International Code Council. *International Building Code (IBC)*; ICC: Falls Church, VA, USA, 2021.
6. The Wood Innovation and Design Centre. Available online: https://www.unbc.ca/engineering/wood-innovation-and-design-centre (accessed on 17 December 2024).
7. Cao, J.; Xiong, H.; Liu, Y.; Yu, D.; Chen, J. Seismic Performance of Glulam Timber Post and Beam Structures with and without Light Frame Timber Shear Wall Infill. *J. Build. Eng.* **2022**, *57*, 104965. [CrossRef]
8. Tannert, T.; Lam, F.; Vallée, T. Strength Prediction for Rounded Dovetail Connections Considering Size Effects. *J. Eng. Mech.* **2010**, *136*, 358–366. [CrossRef]
9. Dietsch, P.; Brandner, R. Self-Tapping Screws and Threaded Rods as Reinforcement for Structural Timber Elements—A State-of-the-Art Report. *Constr. Build. Mater.* **2015**, *97*, 78–89. [CrossRef]
10. Vallée, T.; Tannert, T.; Fecht, S. Adhesively bonded connections in the context of timber engineering—A Review. *J. Adhes.* **2016**, *93*, 257–287. [CrossRef]
11. Schober, K.-U.; Tannert, T. Hybrid connections for timber structures. *Eur. J. Wood Prod.* **2016**, *74*, 369–377. [CrossRef]
12. Hossain, A.; Danzig, I.; Tannert, T. Cross-Laminated Timber Shear Connections with Double-Angled Self-Tapping Screw Assemblies. *J. Struct. Eng.* **2016**, *142*, 04016099. [CrossRef]
13. Brown, J.R.; Li, M.; Tannert, T.; Moroder, D. Experimental Study on Orthogonal Joints in Cross-Laminated Timber with Self-Tapping Screws Installed with Mixed Angles. *Eng. Struct.* **2021**, *228*, 111560. [CrossRef]
14. *ASTM D7147-21*; Standard Specification for Testing and Establishing Allowable Loads of Joist Hangers. ASTM International: West Conshohocken, PA, USA, 2021.
15. Bolduc, W.T.; Ladkany, S. Effect of Support Restraint on Wood-to-Wood Joist Hanger Connection. In Proceedings of the Structures Congress 2011, Las Vegas, NV, USA, 14–16 April 2011; American Society of Civil Engineers: Las Vegas, NV, USA, 2012.
16. Popovski, M.; Prion, H.G.L.; Karacabeyli, E. Seismic Performance of Connections in Heavy Timber Construction. *Can. J. Civ. Eng.* **2002**, *29*, 389–399. [CrossRef]
17. Lam, F.; Gehloff, M.; Closen, M. Moment-Resisting Bolted Timber Connections. *Proc. Inst. Civ. Eng. Struct. Build.* **2010**, *163*, 267–274. [CrossRef]

18. Wang, M.; Song, X.; Gu, X.; Zhang, Y.; Luo, L. Rotational Behavior of Bolted Beam-to-Column Connections with Locally Cross-Laminated Glulam. *J. Struct. Eng.* **2015**, *141*, 04014121. [CrossRef]
19. Xiong, H.; Liu, Y. Experimental Study of the Lateral Resistance of Bolted Glulam Timber Post and Beam Structural Systems. *J. Struct. Eng.* **2016**, *142*, E4014002. [CrossRef]
20. Tannert, T.; Prion, H.; Lam, F. Structural Performance of Rounded Dovetail Connections under Different Loading Conditions. *Can. J. Civ. Eng.* **2007**, *34*, 1600–1605. [CrossRef]
21. Zhang, X.; Azim, M.R.; Bhat, P.; Popovski, M.; Tannert, T. Seismic Performance of Embedded Steel Beam Connection in Cross-Laminated Timber Panels for Tall-Wood Hybrid System. *Can. J. Civ. Eng.* **2017**, *44*, 611–618. [CrossRef]
22. Gohlich, R.J. Development of an Innovative Hybrid Timber-Steel Moment-Resisting Frame for Seismic-Resistant Heavy Timber Structures. Ph.D. Thesis, Carleton University, Ottawa, ON, Canada, 2016.
23. He, M.; Liu, H. Comparison of Glulam Post-to-Beam Connections Reinforced by Two Different Dowel-Type Fasteners. *Constr. Build. Mater.* **2015**, *99*, 99–108. [CrossRef]
24. Masaeli, M.; Gilbert, B.P.; Karampour, H.; Underhill, I.D.; Lyu, C.H.; Gunalan, S. Scaling Effect on the Moment and Shear Responses of Three Types of Beam-to-Column Connectors Used in Mass Timber Buildings. *Eng. Struct.* **2020**, *208*, 110329. [CrossRef]
25. Palma, P.; Frangi, A.; Hugi, E.; Cachim, P.; Cruz, H. Fire Resistance Tests on Timber Beam-to-Column Shear Connections. *J. Struct. Fire Eng.* **2016**, *7*, 41–57. [CrossRef]
26. Hubbard, C.; Salem, O. Fire Resistance of a Fully Concealed, Moment-Resisting New Timber Connection Utilizing Mechanically-Fastened Steel Rods. *Fire Saf. J.* **2022**, *129*, 103546. [CrossRef]
27. Vojtilaa, G.; MacDougallb, C. Seismic Performance of Timber Connections for Sustainable Tallwood Building. In Proceedings of the New Horizons in Green Civil Engineering (NHICE-02), Victoria, BC, Canada, 24 August 2020.
28. MTC Solutions. *Beam Hangers Design Guide*; MTC Solutions: Surrey, BC, Canada, 2020.
29. Leach, H.; MacDougall, C.; Tousignant, K. Evaluation of the Interstorey Drift Performance of Timber Beam-Hanger Connection Systems. *Can. J. Civ. Eng.* **2021**, *48*, 458–469. [CrossRef]
30. Madland, H.; Fischer, E.; Sinha, A. Monotonic Testing of Glue-Laminated Beam-to-Column Connections. *J. Struct. Eng.* **2023**, *149*, 04023039. [CrossRef]
31. *ASCE/SEI-7-22*; Minimum Design Loads and Associated Criteria for Buildings and Other Structures. American Society of Civil Engineers: Reston, VA, USA, 2022.
32. *ISO 6891-1983*; Timber Structures: Joints Made with Mechanical Fasteners: General Principles for the Determination of Strength and Deformation Characteristics. International Standards Organisation: Geneva, Switzerland, 1983.
33. *ISO/TR 21141:2022*; Timber Structures—Timber Connections and Assemblies—Determination of Yield and Ultimate Characteristics and Ductility from Test Data. The International Organization for Standardization (ISO): Geneva, Switzerland, 2022.
34. Smith, I.; Asiz, A.; Snow, M.; Chui, Y.H. Possible Canadian/ISO Approach to Deriving Design Values from Test Data. In Proceedings of the 39th CIB Working Commission W18—Timber Structures, Florence, Italy, 28–31 August 2006.

buildings

MDPI

Article

Numerical Study on In-Plane Behaviour of Light Timber-Framed Wall Elements Under a Horizontal Load Impact

Miroslav Premrov and Erika Kozem Šilih *

Faculty of Civil Engineering, Transportation Engineering and Architecture, University of Maribor, 2000 Maribor, Slovenia; miroslav.premrov@um.si
* Correspondence: erika.kozem@um.si

Abstract: This study analyses the many different parameters of the in-plane flexibility problem regarding the lateral behaviour of light timber-framed (LTF) wall elements with different types of sheathing material (FPB, OSB, or even reinforced concrete), as well as the thickness of the timber frame elements (internal or external wall elements). The analysis simultaneously considers bending, shear, and timber-to-framing connection flexibility, while assuming stiff-supported wall elements as prescribed by Eurocode 5. Particular emphasis is placed on the sliding deformation between sheathing boards and the timber frame, which can significantly reduce the overall stiffness of LTF wall elements. The influence of fastener spacing (s) on sliding deformation and overall stiffness is comprehensively analysed, as well as the different bending and shear behaviours of the various sheathing materials. The results show that reducing the fastener spacing can significantly improve the stiffness of OSB wall elements, while it is less critical for FPB elements used in mid-rise timber buildings. A comparison of external and internal wall elements revealed a minimal difference in racking stiffness (3.3%) for OSB and FPB specimens, highlighting their comparable performance. The inclusion of RC sheathing on one side of the LTF elements showed significant potential to improve torsional behaviour and in-plane racking stiffness, making it a viable solution for strengthening prefabricated multi-storey timber buildings. These findings provide valuable guidance for optimizing the design of LTF walls, ensuring improved structural performance and extended application possibilities in modern timber construction.

Keywords: timber; structures; light timber-framed element; modelling; numerical analysis

1. Introduction

Due to known environmental changes, there is an increasing tendency in building design to use structural materials that require the lowest-possible CO_2 emissions for their production. As a natural material, wood has considerable advantages, as it is carbon neutral and, consequently, has excellent environmental performance. On the other hand, it has some disadvantages compared to other structural materials, especially its relatively high deformability due to its low modulus of elasticity. This has resulted in a relatively low number of existing timber buildings with high floor spans or high buildings with an exclusively timber load-bearing structure [1–4].

Due to the structural disadvantages of timber, many countries have codes that prescribe limitations for the maximal height of timber multi-storey buildings. For instance, from 1994 to 2016, Australian building regulations placed restrictions on the use of timber in multi-storey buildings [5], while in 2016, the Australian Building Codes Board (NCC) [6]

allowed developers to construct mid-rise timber buildings with an effective height of up to 25 m. In Germany, new building regulations allow for the construction of timber buildings of up to five storeys [7], while in the North America, it is usual for timber buildings to be only four storeys high, with five or six storeys occasionally allowed by authorities with local jurisdiction [8].

According to [3], there are six main structural systems for timber buildings. In contemporary multi-storey timber construction, the CLT solid-panel wall system, skeleton system, and light timber-framed (LTF) wall system are the most widely used. The advantages and disadvantages between the different structural systems, both from a structural and architectural point of view and in terms of energy efficiency and overall living comfort, are analysed in more detail in [3] and will not be dealt with separately here.

In our research, only the LTF wall system will be comprehensively analysed. The LTF wall system is one of the most common construction systems for residential houses, especially in Middle Europe and North America [9]; however, it has many structural limitations regarding building height, and it is mostly used only for one- to three-storey buildings [9]. In comparison with CLT structural systems, the racking load-bearing capacity and especially the racking stiffness are both essentially lower; therefore, LTF buildings are usually lower than CLT buildings. Moreover, the racking stiffness of LTS structures also depends on many different parameters, such as disposition and the type of fasteners, type of sheathing boards, and the dimensions of the timber frame and sheathing panels. All these parameters will be analysed in this study.

When calculating light timber-framed (LTF) wall elements, it is particularly important to consider slip deformation between the sheathing boards and timber frame, which can essentially decrease the overall in-plane stiffness of the whole composite wall element. In the analytical approach presented in [10], this fact is considered using the Gamma method, where LTF shear walls are vertical elements subjected to the horizontal point load action at the top of the wall, and the wall elements are further considered as simple linear elastic beam elements. There are also some other analytical and FEM approaches to studying the influence of some parameters [11–14], which will be presented in Section 2.

In general, there are many different parameters that may have a significant influence on the in-plane behaviour of the LTF wall element, such as the type and thickness of the sheathing material (OSB or FPB), the type and dispositions of the mechanical fasteners in the sheathing-to-framing connection, and, last but not least, the thickness of the timber frame elements, in the sense that LTF can be used as primary in-plane load-bearing internal or external wall elements. Some have already been parametrically studied by using only the OSB sheathing material [11,12,15].

However, in this study, Section 3 outlines the influence of some further important parameters on the racking behaviour of LTF elements, such as the different types and thicknesses of the sheathing boards (OSB, fibre-plaster, or even concrete sheathing material), dimensions and the spacing between the fasteners, and, finally, the thickness of the timber frame elements (internal or external walls). Because the easiest way to reach higher in-plane load-carrying capacities in timber-framed wall elements with OSB sheathings is to provide the wall element with a smaller spacing between the fasteners in the sheathing-to-framing connection [12,15], the influence of fastener position in the sheathing-to-frame connection is especially studied. Thus, finally, the results for the in-plane racking stiffness (R) and overall racking behaviour of LTF elements are presented regarding their dependence on the spacing (s) between the fasteners, which has not been previously analysed in any other mentioned study, making this research novel. However, the previously developed semi-analytical modified γ-method [10] used in this numerical study only ensures accurate

results before the forming of any cracks in the sheathing material; therefore, only the linear elastic response of LTF elements is analytically studied in this paper.

2. In-Plane Behaviour of Light Timber-Framed (LTF) Wall Elements

2.1. Composition of LTF Wall Elements

The light timber-framed (LTF) structural system originates from Scandinavian–American construction methods, i.e., balloon-frame and platform-frame construction types with on-site assembly works. A further developed prefabricated off-site version, sometimes called a frame panel system, has many benefits such as a faster assembly process because the ready-made elements are crane-lifted to be erected onto the foundation platform, adjusted, and screw-fastened. Furthermore, the transition from the single-panel construction system (Figure 1a) to the macro-panel construction system (Figure 1b) means even greater reductions in assembly time and higher stiffness of the entire structure due to a lower number of joints [16].

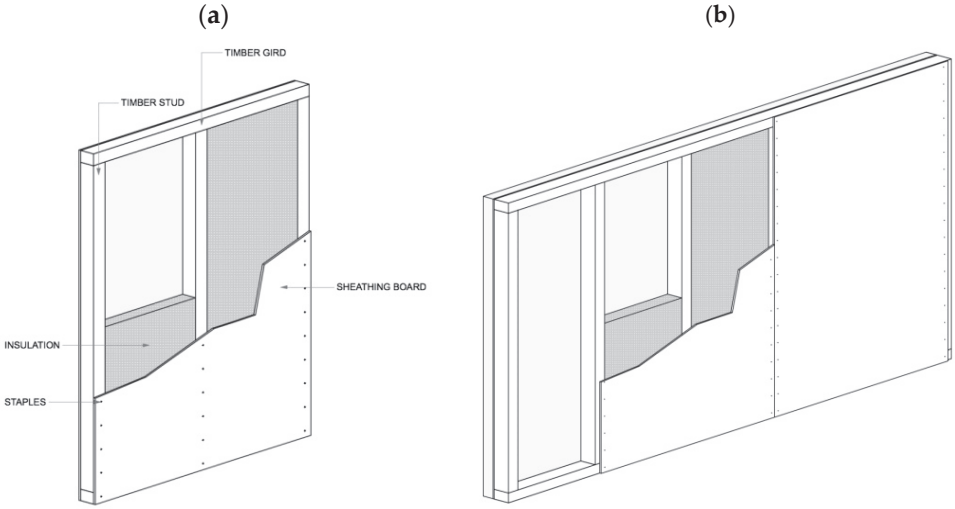

Figure 1. Single-panel construction system (**a**) and macro-panel construction system (**b**) [16].

Prefabricated timber-framed walls that function as the main vertical bearing capacity elements and also as primary bracing elements for the horizontal load impact, whose typical single-panel dimensions usually have a width of $b = 1200 - 1250$ mm and a height of $h = 2500 - 3100$ mm, are composed of a timber frame and sheets of board material fixed by mechanical fasteners to one or both sides of the timber frame, as schematically presented in Figure 1a. The timber frame elements (studs and girders) are usually made of sawn or glue-laminated timber and are typically between 80 mm (internal walls) and 200 mm (external walls) thick. The required thickness of the external walls is usually dictated by the national standards for the required thermal transmittance U-values, depending mostly on climate conditions and not so much on the specific statical requirements, which is what we will additionally aim to show in our study as well. There are many different types of available panel sheet products that may have a certain level of structural capacity, such as wood-based materials (plywood, oriented strand board, hardboard, particleboard, etc.) or fibre-plasterboard. Many different experimental and numerical [4,9–12,14,15,17–21] studies that analyse the influence of the sheathings only on the statical requirements and in-plane load-bearing capacity and stiffness have been already performed.

The sheathing boards are mechanically connected to the timber frame elements with staples, nails, or even bolts. The type of connector usually also depends on the type and thickness of the sheathing material. In comparison to OSB or fibre-plasterboard (FPB), it has been experimentally proven that LTF elements with OSB have a higher load-

bearing capacity but a significantly lower racking stiffness [19,20]. The racking capacity of LTF elements with FPB is usually increased by using double-layer sheathing panels, but the procedure is still not covered by valid Eurocode standards and is mostly based only on experimental or numerical studies, including some proposals with correction coefficients [21]. The literature [15,19,20] also shows the improved performance of using staples on smaller spacing (*s*) than in fibre-plaster sheathing boards [22], with the racking resistance of LTF elements with OSB panels significantly increased. A more in-depth numerical approach to this issue is presented in Section 3.

2.2. Numerical Treatment of LTF Wall Elements

2.2.1. Analytical or Semi-Analytical Computational Approach

The distribution of the effect of the horizontal load across the individual components of the load-bearing LTF wall element is shown schematically in Figure 2. According to the previously presented composition of the element, it is obvious that the horizontal force is transmitted first through the fasteners as a shear flow between the sheathing board and the timber frame and, after that, through the sheathing tensile diagonal with the width of b_{eff}.

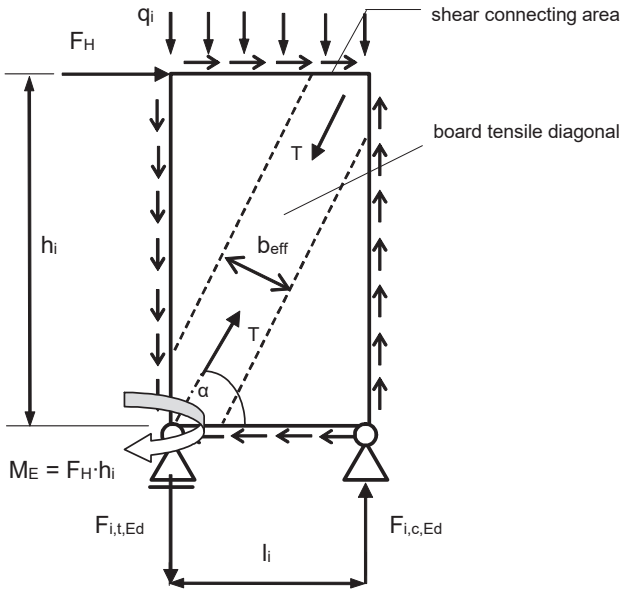

Figure 2. Scheme of the force distribution in a timber frame wall element.

Following the scheme, it is obvious that three possible failure criteria can occur in such a composite structural element:

- Shear criteria caused by yielding of the fasteners in the connecting area between the boards and the timber frame elements (a);
- Tensile stress criteria caused in the diagonal of the sheathing boards (b);
- Tensile and compressive stress criteria in the stud elements of the timber frame (c).

Many experimental and numerical studies [12,13,15,17] have shown that the first criterion (a) almost always occurs when OSB sheathing is used. In contrast, with FPB, the tensile strength of the gypsum material is very low (only about 2 to 2.5 MPa), meaning that diagonal tensile failure (b) usually occurs [11,19–21]. The third criterion (c) has not yet been proven in experimental studies.

In the past, many computational methods and models were suggested to calculate the in-plane stress distribution caused by the horizontal load impact in LTF wall assemblies. As described in [23–26] and Eurocode 5 [27], the most common way to calculate structural behaviour in the timber frame panel wall assembly under the horizontal load impact is

to assume that each floor platform is rigid, with each timber frame wall being a vertical cantilever beam fixed at the bottom and free to deflect at the top, as schematically presented in Figure 2. Both supports approximate the influence of the neighbouring panel walls and assure a boundary condition for the wall in question. The supports can be considered as rigid, such as in [24,27], or flexible, such as in [11–13], which is more realistic in addition to being more accurate.

Forty years ago, Källsner [28] and Äkerlund [29] suggested a very useful and quite simple approach to determine the in-plane load bearing capacity of the wall unit, based on two major assumptions: the behaviour of the joints between the sheet and the frame members is assumed to be linearly elastic until the point of failure; the frame members and sheets are assumed to be rigid and hinged to each other. Based on the assumption that the timber frame members and the sheets are rigid and hinged to each other, Källsner and Lam [30] developed the "Lower bound plastic method" that defines the characteristic shear resistance of the wall ($F_{v,Rk}$) as a sum of all the fasteners' shear resistance values ($F_{f,Rk}$) along the loaded edges. This procedure was further practically adopted for current Eurocode standards [27] for defining the racking resistance of LTF elements. In practice, there is often a need for simple and useful expressions to determine the racking resistance of the timber frame walls by using hand calculation only. In this way, Källsner and Girhammar [31] developed an elastic analysis model for fully anchored sheathed timber frame shear walls with timber-based sheathing boards. The authors developed a simplified expression for the horizontal load-bearing capacity ($F_{H,k}$) in a very simple form with a linear dependence with the shear capacity of the fastener ($F_{f,Rk}$):

$$F_{H,k} \approx \frac{1}{6} \cdot \sqrt{\frac{5929}{170}} \cdot \frac{b_i}{s_r} \cdot F_{f,Rk} \approx 0.984 \cdot \frac{b_i}{s_{is}/2} \cdot F_{f,Rk} \quad (1)$$

However, in valid Eurocode standards [27], there are still no prescribed expressions for the calculation of lateral deformations at the top of the LTF elements that will be used as lateral load-bearing elements in multi-storey timber buildings. The prescribed expressions are important in order to satisfy prescribed Serviceability Limit State (SLS) conditions according to Eurocode 0 [32] and Eurocode 8 [33] standards. Usually, the prescribed value of the maximal lateral displacements is $u_{max} = H/500$, where H is the height of the building. As the modulus of elasticity of timber is very low, in practice, the deformation criterion is often the most decisive in the design of timber structures, which makes it even more important to check the maximum horizontal deflections at the top of the LTF wall element. To create expressions to calculate the maximal horizontal displacements at the top of the wall element, Casagrande et al. [12] developed a simplified numerical model, called UNITN, to provide a tool to evaluate the elastic response of light timber frame shear walls [13]. Starting from the analytical developments of Källsner and Girhammar [31], they defined the horizontal displacement (Δ) of a light timber frame wall subjected to a horizontal force as a sum of different contributions and sources, as follows:

$$\Delta = \Delta_{sh} + \Delta_h + \Delta_p + \Delta_a \quad (2)$$

where Δ_{sh} is the contribution given by the sheathing-to-framing deformability of the mechanical fasteners in the sheathing–timber frame connection, Δ_h is due to the rigid-body rotation of the shear wall (in-plane bending), Δ_p is due to the shear deformation of the sheathing panel (in-plane shear), and Δ_a is due to the rigid-body translation caused by shear connectors of LTF elements to the foundation. The total horizontal displacement (Δ)

can now be rewritten to highlight the contribution of various flexibilities due to the force F_H and Equation (2) in the form of:

$$\Delta = \frac{F_H}{R} = F_H \cdot \left(D_{sh} + D_h + D_a + D_p\right) = \frac{F_H}{K_{tot}} = F_H \cdot \left(\frac{1}{K_{sh}} + \frac{1}{K_h} + \frac{1}{K_a} + \frac{1}{K_p}\right) \quad (3)$$

where K_{sh} is the sheathing-to-framing stiffness; K_h is the stiffness of the rigid-body rotation (in-plane bending) but where the influence of the fasteners and a consequent slip in the connecting area are not considered; K_a is the rigid-body translation stiffness; and K_p is the sheathing panel shear stiffness. In [12], a parametric numerical study was performed by analysing the influence of all four possible flexibilities from Equation (3); however, it was for only one selected disposition with constant spacing s between the fasteners connecting the sheathings and the timber frame elements. Additionally, the study was performed for the OSB sheathing panels only. It was demonstrated that the flexibilities of the sheathing-to-framing connection (D_{sh}) and the rigid-body rocking (D_h) are the highest (45% each), while the flexibility of the rigid-body translation (D_a) is only 6%, and the flexibility of the sheathing panel (D_p) is only 4%. The obtained numerical results were additionally validated by the experimental study performed by Gattesco et al. [34] and supported with different configurations of shear walls.

Aloisio et al. also presented a notable parametric numerical approach to study the influence of all possible flexibilities of LTF elements [11]. According to [12] and Equation (2), two additional horizontal deformations are also taken into account, namely, the rocking of the anchors (u_R) caused by the tensile reaction force $F_{i,t,Ed}$ in Figure 2 and bottom rail deformation (u_C) caused by the compressive reaction force $F_{i,c,Ed}$ perpendicular to the wood grains in the girder element. Technical Committee CEN is currently developing a new Eurocode standard proposal for timber structures [35,36], including analytical or semi-analytical expressions for all six mentioned horizontal deformations for calculating the lateral deflection for LTF elements in the forms of:

$$\text{In-planebending} : u_B = \frac{F_H \cdot h_i^3}{3 \cdot \left(EI_y\right)_{eff,LTF}} \quad (4a)$$

$$\text{In-plane shear} : u_S = \frac{F_H \cdot h_i}{\left(G_{p,1} \cdot t_{p,1} + G_{p,2} \cdot t_{p,2}\right)} \quad (5)$$

$$\text{Sheathing-to-frame deformation} : u_N = \frac{F_H / l^2}{\left(\frac{K_{ser,1}}{\alpha_{1,1} \cdot l_{per,1}} + \frac{K_{ser,2}}{\alpha_{1,2} \cdot l_{per,2}}\right)} \quad (6)$$

$$\text{Sliding} : u_A = \frac{F_H}{\left(\sum_j K_{a,x,j}\right)} \quad (7)$$

$$\text{Rocking} : u_R = \frac{M_E}{K_R} - \frac{N_E(l - l_c)}{2K_R} \quad (8)$$

$$\text{Bottom rail deformation} : u_C = w_{ser,z} \frac{h_i}{l_i} \quad (9)$$

Most of the geometrical values (h_i, l_i) and the force impacts (F_H, M_E) are schematically presented in Figure 2. The flexibility of all fasteners is approximated by the slip modulus of all fasteners: $K_{ser,1}$ and $K_{ser,2}$ by connecting both two-sided sheathing boards via mechanical fasteners (staples or nails) to the timber frame, $K_{a,x,j}$ of the shear connectors, and K_R of the anchors to prevent the uplifting of LTF elements (Figure 2). Equations (4) and (5) show that a simple beam theory respecting Bernoulli's hypothesis is used for calculation of the in-plane bending and the in-plane shear displacements of the wall element, which is a

statical design actually considered as a simple cantilever beam element with an acting horizontal force at the top. Furthermore, it is important to mention that by calculating the in-plane bending (u_B) in the bending stiffness expression ($EI_{y,eff,LTF}$) Equation (4), the sheathing-to-frame deformability is not taken into account, and only the pure bending stiffness of the timber frame elements is considered. Similarly, only the in-plane shear deformation caused by the sheathing boards (u_S) is considered. In this case, the shear deformability of the sheathing-to-framing connections is taken into account separately by Equation (6).

A huge parametric study analysing the elastic response of LTF elements was conducted in [11] by using these new Eurocode proposals [35,36], with the expressions given in Equations (4)–(9), with the aim of analysing the sensitivity of all parameters. However, similar to the study in [12], it was performed only on LTF elements with OSB sheathing, not gypsum sheathing material. Additionally, the spacings of the fasteners (s) only vary parametrically, namely, s = 75 mm, 100 mm, and 120 mm, as usually used in practice. Similar to the study in [12], the most important contribution to the overall lateral in-plane displacement is the flexibility of the sheathing-to-framing connection—50% if no vertical load influence is considered in the calculation.

However, with both calculation methods, it is not possible to analyse the analytical dependence of all deformations and the consequent in-plane racking stiffness (K_{tot}) of the fastener spacing (s). Because of the high flexibility of mechanical fasteners, the sheathing-to-framing connection is mostly the strongest sensitive parameter, influencing the overall racking stiffness of the whole LTF wall element. Therefore, it is recommended to demonstrate that this expression also has analytical dependence on parameter s and not only on the selected parametrically chosen values, such as in [11,12]. Therefore, in [10,37], a quite similar calculation analytical approach was developed for Eurocode proposals in [35,36]. The obtained numerical results demonstrated very good similarity with the previously measured ones on the real-scale test samples, with exactly the same geometrical and material properties [10,37,38].

In reality, the treated wall elements consisting of the timber frame and the sheathing boards behave as composite cantilever elements and should, thus, be analysed as such. The effective bending stiffness $(EI_y)_{eff}$ and the shear stiffness $(GA_s)_{eff}$ of mechanically jointed beams also empirically consider the flexibility of fasteners via coefficient γ_y, taken from Eurocode 5 [27]; this can, therefore, be written in the analytical form of:

$$\left(EI_y\right)_{eff} = \sum_{i=1}^{n} E_i \cdot \left(I_{yi} + \gamma_{yi} \cdot A_i \cdot a_i^2\right) = \sum_{i=1}^{n_{timber.}} \left(E_i \cdot I_{yi} + E_i \cdot \gamma_{yi} \cdot A_i \cdot a_i^2\right)_{timber} + \sum_{j=1}^{n_b} \left(E_i \cdot I_{yi}\right)_b \quad (10)$$

$$\left(GA_s\right)_{eff} = \gamma \cdot (GA_s)_{timber} + (GA_s)_{board} \quad (11)$$

where n is the total number of elements in the relevant cross-section and a_i is the spacing between the global y-axis of the entire cross-section and the local y_i-axis of the i-th element with a cross-section A_i (see scheme in Figure 3). Equation (10) shows that both stiffnesses strongly depend on the stiffness coefficient of the connecting line (γ_y), which simulates the sheathing-to-frame flexibility of the fasteners and is not directly considered in Equations (4) and (5). Regarding Eurocode 5 [27], γ_y can be defined via the fastener spacing (s) and the slip modulus per shear plane per fastener (K) in the semi-analytical form of:

$$\gamma_y = \frac{1}{1 + \left(\frac{\pi^2 \cdot A_{t1} \cdot E_t \cdot s}{{L_{eff}}^2 \cdot K}\right)} \quad (12)$$

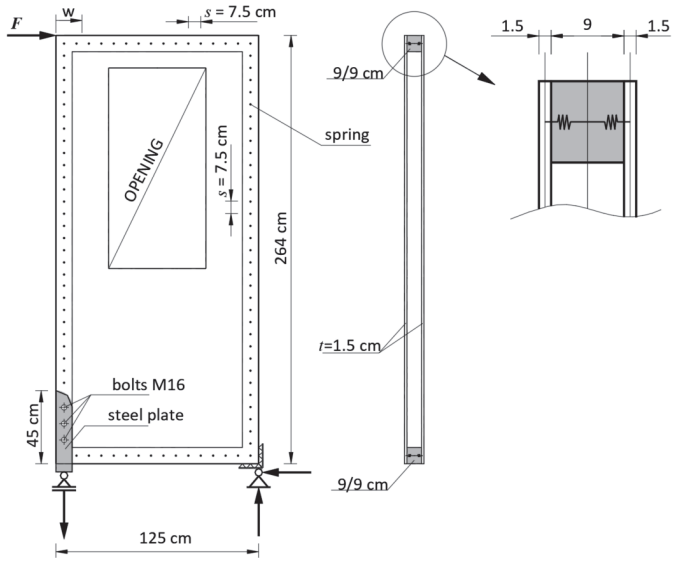

Figure 3. Schematical presentation of FEM of LTF wall elements using elastic spring elements [14].

The expression of the so-called »Modified γ-method« is based on the differential equation for the partial composite action, with the following fundamental assumptions, developed originally by Möhler [39]:

- Bernoulli's hypothesis is valid for each sub-component.
- The slip stiffness is constant along the whole connecting area in the element. This means that the fasteners must be spread at constant intervals (s).
- The material behaviour of all sub-components is considered to be linearly elastic.

Similar to the new Eurocode proposals [35,36], in a statical design, the LTF element is further considered as a vertical cantilever beam element using Bernoulli's hypothesis, and it is fixed at the bottom and free to deflect at the top, with the horizontal point force acting at the top of the element, as schematically presented in Figure 2. Using these general assumptions, the horizontal deformations due to the bending moment ($M_E = F_H \cdot h_i$) and the shear force ($V_E = F_H$) can be further calculated in the analytical form of:

$$u_{M+V} = u_M + u_V = \int_S \frac{M_E \cdot \overline{M}}{(EI)_{eff}} dx + \int_S \frac{V_E \cdot \overline{V}}{(GA_S)_{eff}} dx = \frac{F_H \cdot h_i^3}{(EI_y)_{eff}} + \frac{F_H \cdot h_i}{(GA_S)_{eff}} \quad (13)$$

It is important to point out that in this expression of Equation (13), the flexibility of the sheathing-to-frame connection is directly considered in the reduced effective bending stiffness $(EI)_{eff}$ and also in the reduced shear stiffness $(GA_S)_{eff}$, which is not the case for expressions in Equations (4)–(9). Consequently, there is no need to take Equation (6) into account regarding simulating the deformability of the sheathing-to-frame behaviour of the fasteners when calculating the total lateral displacement at the top of the wall element. In addition, by using Equation (13), it is also possible to study the influence of the flexibility of the sheathing-to-frame connection almost completely in an analytical form in dependence of the spacing between the fasteners (s). Therefore, we perform a numerical analysis in Section 3 for all possible different types of sheathing boards.

Of course, it is also possible to consider the contribution of the rigid-body translation caused by shear connectors of LTF elements to the bottom rail deformation (u_C, Equation (9)), rocking of the anchors (u_R, Equation (8)), and the sliding of the shear

connectors (u_A, Equation (7)). Therefore, finally, the total horizontal displacement (u) at the top of the LTF element is then expressed in the form of:

$$u = u_{M+V} + u_A + u_R + u_c \tag{14}$$

With the proposed method, it is also possible to calculate the force forming the first crack ($F_{H,cr}$) in FPB, in addition to analysing the non-linear post-cracking behaviour of the elements defining the ultimate load-bearing horizontal force ($F_{H,max}$). It is also possible to model such LTF wall elements by considering strengthening LTF elements. All these concepts and calculation procedures are presented, analysed, and compared with the experimental results in [37,38].

Finally, if all supports in this procedure are considered as completely rigid and the consequent displacements u_A, u_R, and u_c are set to zero, the racking stiffness (R) of the analysed LTF wall element can be calculated in the form of:

$$R = \frac{F_H}{u_{M+V}} = \frac{h_i^3}{(EI_y)_{eff}} + \frac{h_i}{(GA_S)_{eff}} \tag{15}$$

As the tensile strength of FPB sheathing material is very low (Table 1; f_{bt} = 2.5 MPa), tensile cracking of the brittle material occurs very early in this case [10,19]. The horizontal force forming the first tensile crack in the sheathing board ($F_{H,cr,k}$) can be defined according to the normal stress criteria and the tensile strength of the sheathing material ($f_{bt,k}$) in the form of:

$$F_{H,cr,k} = \frac{M_{y,cr}}{h_d} = \frac{2 \cdot f_{bt,k} \cdot \left(EI_y\right)_{eff}}{E_b \cdot b \cdot h_d} \tag{16}$$

Knowing the value of this force is important because the behaviour of the LTF wall element with FPB sheathing is purely linearly elastic up to this value. Consequently, the value of the flexural stiffness of the cross-section $(EI_y)_{eff}$, the shear stiffness $(GA_s)_{eff}$ and, as a final result, the value of the racking stiffness of the wall element (R) are consequently constant. After this value of F_H, the LTF elements demonstrate non-linear post-cracking behaviour, and the stiffness $(EI_y)_{eff}$ and $(GA_s)_{eff}$ should be adequately reduced by using only the uncracked area of FPB. When using the OSB sheathing, the tensile strength of the material is essentially higher than the FPB (Table 1; f_{bt} = 20 MPa), and, consequently, the mechanical fasteners almost always yield before the formation of any cracks in the boards. In this case, the horizontal force (F_H) at which the fasteners yield ($F_H = F_{v,k}$) can be very simply calculated by Equation (1). Consequently, in this case, the $(EI_y)_{eff}$ and $(GA_s)_{eff}$ should be decreased in another way according to the decreased value of the fasteners slip modulus (K) in Equation (12). A detailed numerical study about all given facts in a case of both sheathing types (FPB and OSB) is already presented in [10]; therefore, we will not discuss it further here. Instead, only the in-plane elastic behaviours of LTF elements and their influence on the racking stiffness (R) of the whole LTF element will be analysed in detail.

2.2.2. Finite Element Modelling (FEM) of LTF Elements

In particular, to determine the horizontal stiffness of LTF wall elements, it is useful to additionally model them using the FE method, as has been previously used and presented in slightly different ways in [11,12,14]. This modelling approach additionally provides very clear insight into the analysis of the influence of the individual parameters described above on the in-plane behaviour of such wall elements. When using this approach, it is also very important to avoid using some of the essential computational theoretical assumptions described in previous analytical or semi-analytical approaches, in particular, Bernoulli's

hypothesis of straight sections, which we used as one of the essential assumptions in Section 2.2.1, and the consequent calculation of a cantilevered linear beam with a horizontal force acting at the top of the element. The reason for this is that the FEM calculation can treat the wall element as an in-plane two-dimensional composite structure, which is the only fully correct assumption. As the connection between the sheathing boards and the timber frame elements is flexible, resulting in some slip in the plane of connection, this flexibility of the fasteners in the connecting plane is simulated by a system of elastic springs (ESS), and they shall be placed at the same spacing (s) as the actual longitudinal spacing between the fasteners. This study analyses the behaviour of the structures in a linearly elastic range; therefore, all springs are assumed to be linearly elastic. Considering the highly orthotropic properties of wood, the elements of the timber frame are modelled in the FEM approach as orthotropic linearly elastic elements, with the different sheathing panels as isotropic two-dimensional shell elements.

With the presented ESS model, the force forming the first tensile crack in the sheathing panel ($F_{H,cr}$) can be calculated when the maximal tensile stress in the sheathing board reaches the tensile strength ($f_{t,k}$) of the sheathing material (Table 1). By using the value of the corresponding horizontal displacement (u_{cr}) at the top of the wall element, at this force, the racking stiffness ($R = F_{H,cr}/u_{cr}$) of the wall can be finally calculated for the element's completely linearly elastic behaviour.

On the other hand, the disadvantage of this FEM approach compared to the analytical or semi-analytical approach previously described in Section 2.2.1. is that only a parametric computational approach can be used, where individual calculations can only be performed for a specific or selected set-up or layout. As in the previous subsection, the dependence of the horizontal stiffness cannot be specified through an analytical functional dependence on the spacing of the fasteners (s) in the connection plane between the sheathing panel and the timber frame. The calculation method is also very time consuming.

3. Numerical Study

3.1. Test Specimens

Only single-panel LTF elements will be analysed according to the presented scheme and boundary conditions in Figure 2, with the total length l = 1250 mm and the total height h = 2635 mm. As the first aim of this study is to analyse the influence of the timber frame thickness, the LTF elements are separately analysed as follows:

- Internal wall elements with a strength grade C22 according to [40] and with a thickness of 90 mm and width of 90 mm (A_{t1} = 90 × 90 mm) for all timber frame elements (with l_i = 1160 mm and h_i = 2545 mm in Figure 2).
- External wall elements with a strength grade C22 according to [40] and with a thickness of 160 mm and width of 80 mm (A_{t1} = 80 × 160 mm) for all timber frame elements (l_i = 1160 mm and h_i = 2545 mm).

The sheathing boards are also separately analysed as follows:

- Symmetrical two-sided fibre-plaster boards (FPBs) with a thickness of 15 mm.
- Symmetrical two-sided OSBs with a thickness of 15 mm.
- Asymmetrical one-sided reinforced-concrete (RC) panel with a thickness of 50 mm on the external side, and an OSB sheathing of a thickness of 15 mm on internal side, as proposed in the study conducted by Destro at al. [41], as an optional strengthening timber–concrete composite (TCC) load-bearing external LTF element in multi-storey timber-framed buildings.

All material properties of all sub-components are listed in Table 1.

The FPB and OSB sheathings are fastened to the timber frame using staples with a diameter of d_s = 1.53 mm and length of l_s = 35 mm. Using the Eurocode 5 [27] expressions, the slip modulus of the staples is, therefore, $K_{ser,FPB}$ = 295.218 N/mm for the wall elements with FPB and $K_{ser,OSB}$ = 194.028 N/mm for OSB LTF elements. The RC board in the case of [41] is more stiffly fastened to the timber frame elements, using bolts with a diameter of d_{RC} = 10 mm and a consequently higher slip modulus of $K_{ser,RC}$ = 2464.09 N/mm. For the connection of the OSB sheathing to the timber frame on the internal side, the same value $K_{ser,OSB}$ = 194.028 N/mm is used because the OSBs are stapled to the timber frame, as with the LTF OSB elements.

All supports, as shown schematically in Figure 2, are assumed to be fully rigid in the further static design. This statical design is also prescribed by Eurocode 5 [27]. Consequently, the displacements u_A, u_R, and u_C in Equation (14) are set to be zero and only the bending, shear, and sheathing-to-framing flexibility in the sense of calculated u_M and u_V displacements are further considered and analysed. Compared with the numeric parametrical study in [11], where two alternatives with the vertical load impact are analysed, no vertical load impact is considered in this research.

3.2. Analysis of Results

The obtained numerical results are first presented separately for the internal and external walls. To study the influence of fasteners and different types of sheathing material on the calculated displacements, the shear stiffness coefficient (γ_y) in the sheathing-to-frame connection is first analysed. Following expressions in Equations (10)–(13), the effective bending ($EI_{y,eff}$) and effective shear stiffness ($GA_{s,eff}$) of the composite cantilever element are further calculated regarding their analytical dependence on the spacing between the fasteners (s). Using these values in Equation (13), both displacements (u_M and u_V) can be further calculated under a fictive horizontal force F_H = 10 kN applied at the top of the wall element (Figure 2). Additionally, the total horizontal displacement ($u = u_{M+V}$) is also calculated separately in Section 2.2.2., describing the FEM approach to validate the obtained results. However, with the FEM approach, it is not possible to consider the spacing between the fasteners (s) in any analytical form; therefore, the calculating procedure is performed only for the most typical value used in a practical design with s = 75 mm, which was also previously experimentally tested. Finally, the racking stiffness (R) can be analytically determined regarding s to judge the analytical influence of sheathing-to-framing flexibility.

3.2.1. Internal Wall Elements

To analyse the internal LTF wall elements, the stiffness coefficient of the connecting line (γ_y) regarding the dependence of the spacing s will be first presented for the case with FPB and OSB sheathing (Figure 4). When the γ_y coefficient is known, it is further possible to calculate both stiffnesses of the cross-section ($EI_{y,eff}$ and $GA_{s,eff}$) using Equation (10), and both are also presented in Figure 4.

It is obvious from the plotted results that the γ_y is slightly higher for FPB than for the OSB elements. The slip modulus (K_{ser}) of the staples is mainly due to the higher density of the sheathing material, which is larger in the case of FPB. The difference in the γ_y value is the biggest for s values between 30 and 75 mm, which is also the most commonly used space in practice. By analysing only the dependence of $EI_{y,eff}$ and $GA_{s,eff}$, it is obvious that there is a much bigger difference between the sheathings for the shear stiffness $GA_{s,\mathrm{eff}}$, and it also rapidly converges at a value of s for 50 mm. For $EI_{y,eff}$, this dependence on s is much more sensitive and converges by a value of s for 150 mm only. The reason is, in fact, that the shear modulus (G_{mean}) of OSB is very low compared with FPB (see Table 1). On the other hand, there is no essential difference in $EI_{y,eff}$ value between both types of sheathings.

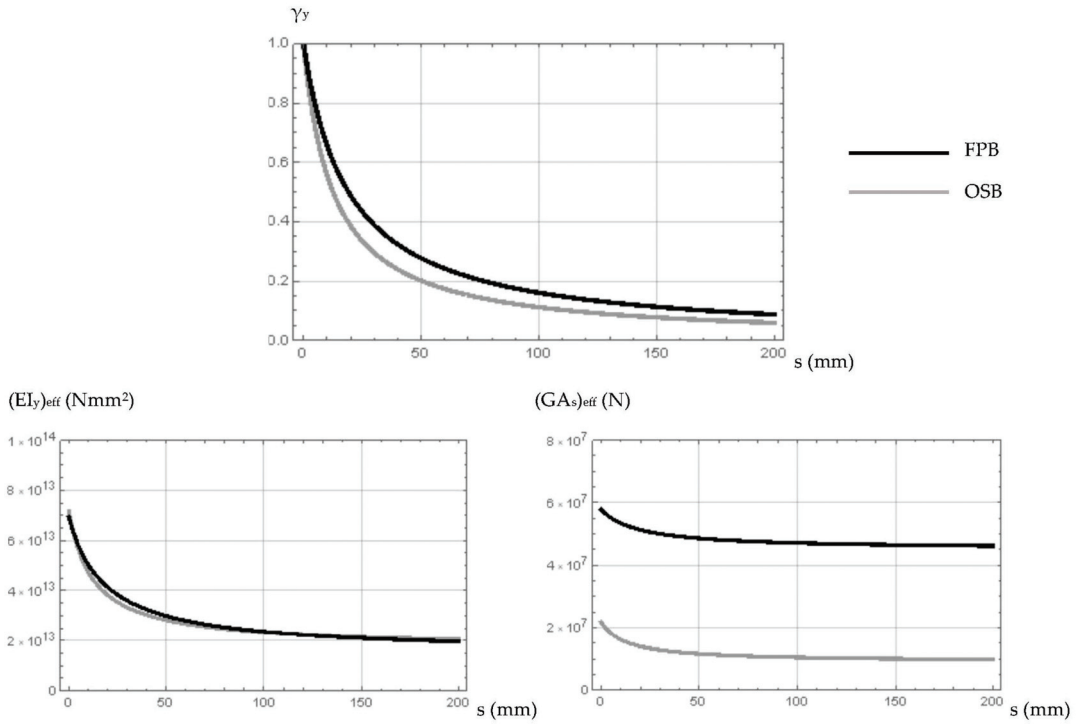

Figure 4. Stiffness coefficient (γ_y) and stiffness $(EI_y)_{eff}$ and $(GA_s)_{eff}$ in dependence of spacing *s*.

Using these values with Equation (13), horizontal displacements u_M and u_V can now be obtained. They are all plotted in analytical dependence of *s* in Figure 5 for OSB and FPB sheathings separately.

Table 1. Properties of the used materials.

	$E_{0,mean}$ [N/mm²]	G_{mean} [N/mm²]	$f_{m,k}$ [N/mm²]	$f_{t,k}$ [N/mm²]	$f_{c,k}$ [N/mm²]	$f_{v,k}$ [N/mm²]	ρ_{mean} [kg/m³]
Timber C22	10,000	630	22	13	20	2.4	410
Fibre-plaster board	3000	1200	4.0	2.5	20	5.0	1050
OSB 3	3500	240	20	20	20	/	600
Reinforced concrete [41]	30,960	12,900	2.5	2.5	30	2.5	2500

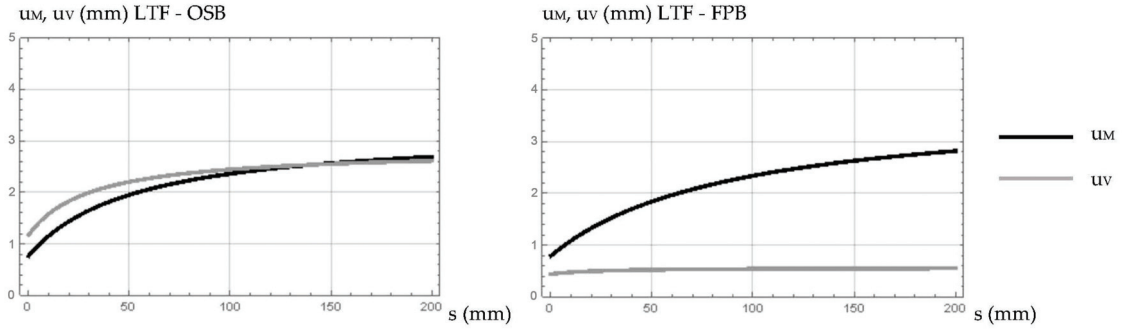

Figure 5. Displacements u_M and u_V in analytical dependence of spacing *s*.

Consequently, the in-plane bending displacement (u_M) for FPB is significantly greater than the in-plane shear deformation (u_V), which is contradictory to u_M, which is almost independent of the spacing (*s*). Conversely, through OSB LTF elements, we can observe a quite high dependence of in-plane shear deformation (u_V) on the spacing between the fasteners (*s*). For a small *s* value (below 100 mm), which is the most commonly used

in practice, it is even greater than the in-plane bending (u_M), and after that, it is almost completely in a comparable range with the in-plane bending displacement. The relation between both displacements for OSB is also in quite good agreement with the results presented in the parametric studies in [11,12]; however, these were performed on the OSB test samples only.

Because our final goal is to calculate the racking stiffness (R) in the linearly elastic range, let us first calculate the value of the horizontal force up to which the behaviour of the sheathing material and the connecting fasteners is purely linearly elastic; therefore, a fully linearly elastic methodology and model can be further used for the calculation of the racking stiffness. For the case with the FPB sheathing material, Equation (16) is relevant for $F_{H,cr,k}$, which is essentially lower than the force resulting in the yielding of the fasteners ($F_{v,k}$). The reason is because the tensile strength of the sheathing material is very low in this case (Table 1), and, consequently, the cracks in the tensile board diagonal appear first. In the case of OSB sheathing material, where the tensile strength is up to eight-times higher than that of FPB (Table 1) and, as a consequence, the fasteners always yield before the formation of any cracks in the sheathing boards, the simplified Equation (1) is, thus, the only relevant calculation of the characteristic horizontal force ($F_{v,k}$). All obtained curves depending on the spacing (s) between the fasteners are plotted in Figure 6. It is obvious from the presented results that the behaviour of the LTF element with FPB can be treated as fully linearly elastic in all wall subcomponents (timber frame elements, mechanical fasteners, and sheathing boards) until the horizontal point load reaches the value of $F_{H,cr}$. On the other hand, the behaviour of the LTF OSB elements is linearly elastic up to the value of $F_{v,k}$, which represents a full yielding of the fasteners that always appears before the formation of any cracks.

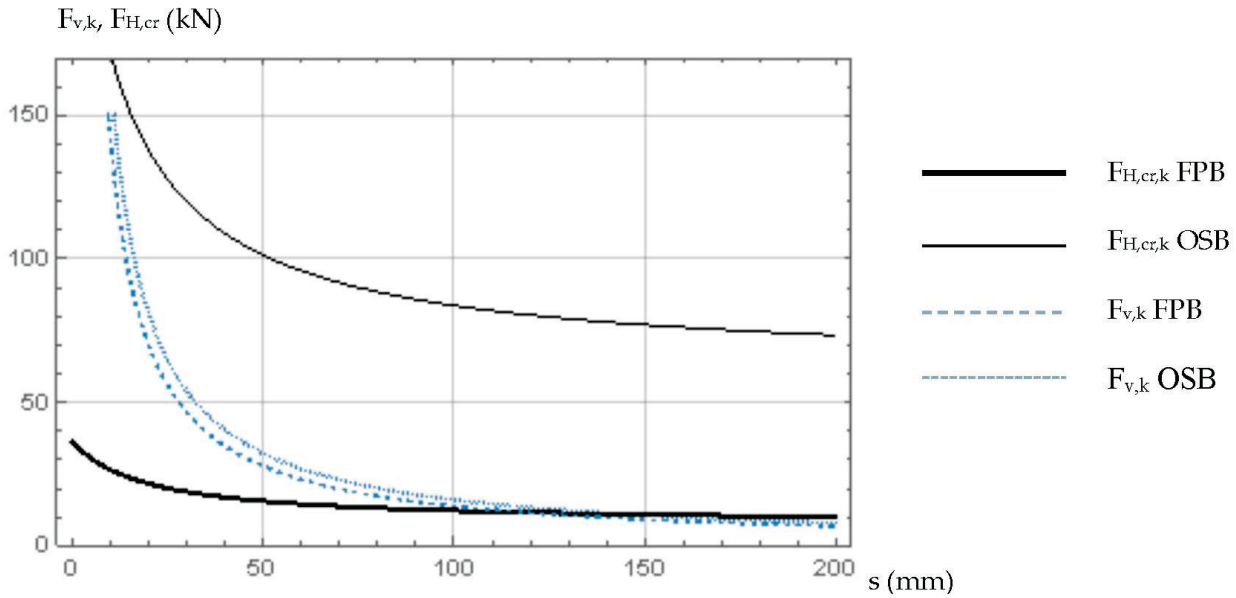

Figure 6. Force forming the first crack in FPB ($F_{H,cr,k}$) and the yielding of fasteners in OSB ($F_{v,k}$) in dependence of spacings.

Finally, it is possible to calculate Equation (15) for the elastic racking stiffness (R) for both analysed types of LTF wall elements, which is of primary interest for any further application of LTF elements in a multi-storey prefabricated timber structure, especially considering the Serviceability Limit State criteria. The results for the analytical dependence regarding spacing (s) between the fasteners are plotted in Figure 7.

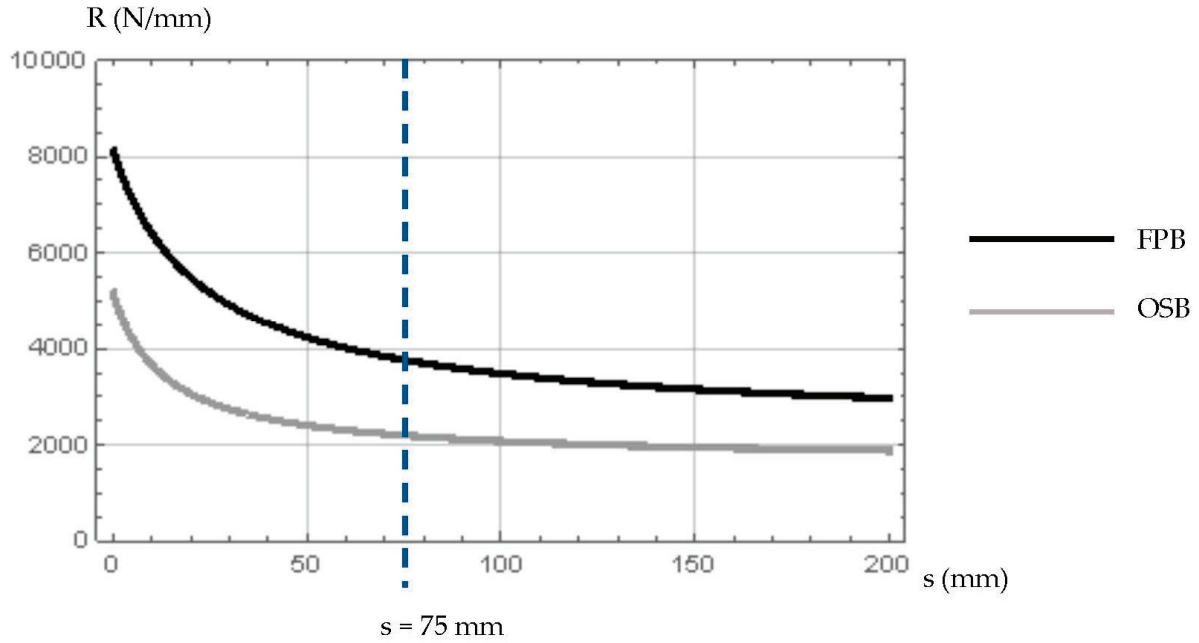

Figure 7. Elastic racking stiffness in dependence of spacing *s*.

The results show that the racking stiffness of the FPB LTF elements is generally higher than the OSB elements. In practice, there is a notable difference regarding the most frequently used space between the staples, namely, *s* = 75 mm, on which previous experimental tests [19,20] and an FEM analysis [14] were performed, using exactly the same dimensions and types of structural components. The exact calculated *R* values for *s* = 0 and *s* = 75 mm are also listed in Table 2. Additionally, by comparing the *R* values for *s* = 75 mm and *s* = 0 mm, it is possible to judge the influence of the sheathing-to-framing connection, which was regarded as the most sensitive parameter by both similar parametrical studies in [11,12], which used OSB panels only. In the case of FPB, a decrease in racking stiffness (*R*) from 8.105 N/mm to 3.760 N/mm (53.6%) is observed, whereas in the case of OSB, a decrease of 5.165 N/mm to 2.201 N/mm (57.4%) is also seen, both of which are in accordance with studies performed on OSB LTF elements in [11,12], with no vertical load impact alternatives.

Table 2. Results for $F_{H,cr}$ for disposition of the fasteners for s = 37.5, 75, 150, and 300 mm.

Group	F_{cr} (Exp.) [kN], [22,42]	F_{cr} (FEM ESS) [kN]	F_{cr} (Modified γ-Method) [kN]	Ratio Modified γ-Method/Exp.	Ratio Modified γ-Method/FEM ESS
G1: s = 37.5 mm	18.94	17.316	17.392	0.918	1.004
G2: s = 75.0 mm	17.29	13.639	13.550	0.784	0.993
G3: s = 150.0 mm	11.36	10.819	10.976	0.966	1.015
G4: s = 300.0 mm	/	9.466	9.458	/	0.999

To validate the obtained analytical results, FEM analysis using the FEM Elastic Spring System (ESS) was additionally performed on FPB elements, on which previous experiments were also performed in [14,22,42]. However, this FEM approach can be performed only for the selected spacing *s* value between the fasteners and not for any further semi-analytical or analytical method performed previously. As the most used value in practice and in previous experiments (such as in [14,20,22]), the value of *s* = 75 mm was first selected. The results for the total displacement u_{M+V} caused by a horizontal force F_H are plotted in Figure 8a. The calculation with the analytical Modified γ-Method was performed only in the

elastic range before the first crack in the FPB appeared, using $F_{H,cr}$ = 13.55 kN, as calculated by using Equation (16) and presented in analytical dependence in Figure 6. It is important that a good match with this value is obtained by using the FEM ESS approach with the value of $F_{H,cr}$ = 13.64 kN, as presented in Figure 8a. By comparing both numerical methods with the previously performed experiments [22,42], we suppose that the difference for $F_{H,cr}$ in the case of s = 75 mm appeared because the first crack in fibre-plaster boards (FPBs) was caused by a lower force in the region of the steel tensile support anchors (see Figure 2), with the crack initially not visible [14,22]. However, the agreement for specimens with s = 37.5 mm and s = 150 mm, which were also experimentally tested ([22,42]), is essentially better.

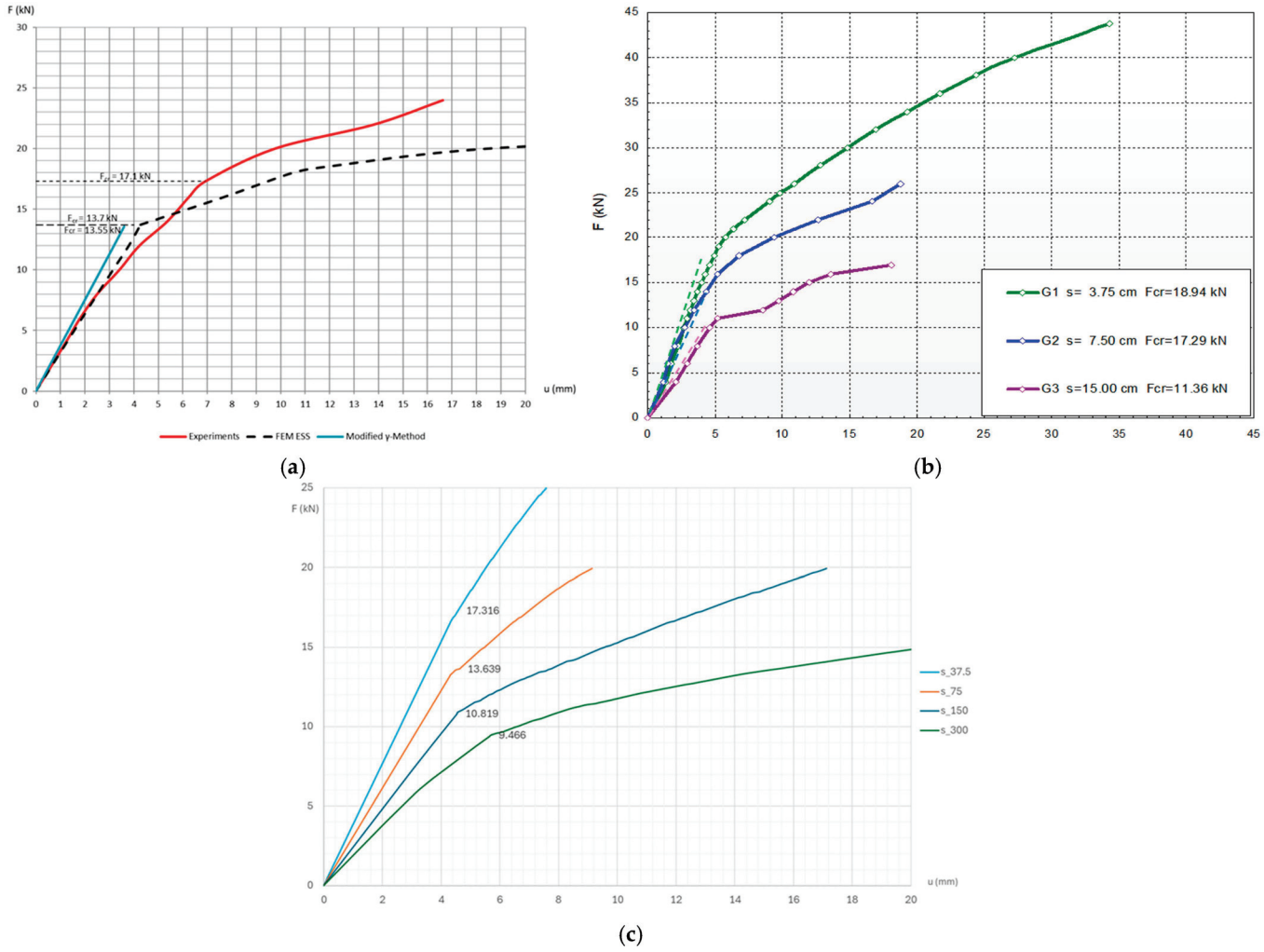

Figure 8. (**a**) Comparison of the results for u_{M+V} for FEM, analytical, and experimental case by using s = 75 mm; (**b**) comparison between experimental results [42] and numerical results for Modified γ-Method (in dotted line); (**c**) F-u behaviour of test samples performed by FEM ESS model for parametrically chosen values of s.

Additionally, we also numerically analysed the test samples with s = 300 mm. All results for $F_{H,cr}$ regarding the selected and previously experimentally tested samples are listed in Table 2, with the compared values performed using both numerical methods.

It is obvious from the listed and compared results in last two columns that both numerical methods prove satisfactory, with good agreement with the experimental results, except for the case of G2. On the other hand, matching between the results obtained by the Modified γ-Method and the FEM ESS approach is very good and never exceeds a range of 1.5%.

The results comparing only the experimental analysis and the Modified γ-Method for the values of s = 37.5 mm and s = 150 mm, which were the only ones apart from those previously experimentally tested in [22,42], are plotted in Figure 8b. It is important to point out that only a linearly elastic stage is analysed for the Modified γ-Method.

Additionally, to validate the results between both numerical methods, a parametrical analysis on the selected spacing of the fasteners for s = 37.5, 75, 150, and 300 mm using the FEM ESS approach was also performed. The calculated results are plotted in Figure 8c. First, it should be pointed out that such an FEM procedure is very accurate but also very time consuming; therefore, it is not applicable for any practical use in engineering design.

Figure 8a shows that the correlation between the analytical and FEM calculation approach and experimental test results regarding the linearly elastic behaviour for the wall elements is satisfactory for s = 75 mm. In the case of FPB sheathing, the elastic racking stiffness of the LTF element (R) is calculated by using the FEM ESS modelling R_{FEM} = 3429 N/mm, and in the case of the analytical approach with the Modified γ-Method, it is R_{analy} = 3760 N/mm. The previously measured experimental value for the elastic stiffness in the completely linearly elastic range is R_{exp} = 3333 N/mm [14,42]. Consequently, the values from Table 2 show that the analytical approach with the Modified γ-Method and the FEM ESS approach provide very similar and useful results for any selected value of s. Furthermore, the FEM ESS can be performed only on the parametrically selected s values, and the calculation procedure is also quite time consuming.

The plotted results in Figure 8a also further demonstrate that the agreement of the results is significantly worse regarding post-cracking behaviour. The reasons for this were explained and analysed in more detail in [14]. Similar conclusions were found for the Modified γ-Method in [10] regarding the Ultimate Limit State design, although comparatively with the same experiments. These findings further confirm the initial thesis of this study, namely, that LTF wall elements will be further treated with a semi-analytical approach using the Modified γ-Method exclusively in the linearly elastic range, as also proposed for the calculation of lateral displacements by new Eurocode proposals [35,36].

3.2.2. External LTF Wall Elements

For the analysis of external LTF wall elements, the wall element developed by Destro et al. [41] is additionally numerically tested using the Modified γ-Method. A second aim of this numerical study on external structural wall elements is also to demonstrate that this developed TCC wall element can strengthen the LTF element in multi-storey timber buildings, providing greater in-plane stiffness compared with classical solutions using FPB or OSB sheathing. The stiffness coefficient of the connecting line (γ_y) in dependence of the spacing s is presented in Figure 9. When the γ_y coefficient is known, it is further possible to calculate both stiffnesses of the cross-section ($EI_{y,eff}$ and $GA_{s,eff}$) using Equations (10) and (11).

It is evident from the function for γ_y that connection with the 10 mm thick bolts in the case of Destro [41] demonstrates a much stiffer shear connection compared with staples used for FPB or OSB sheathings. The bending stiffness $(EI_y)_{eff}$ and the shear stiffness $(GA_s)_{eff}$ in the case of Destro with the RC sheathing panel are considerably higher than in the case of the classic and most frequently used wall elements with FPB or OSB sheathing panels due to the significantly higher modulus of elasticity (E), shear modulus (G), and γ_y, which naturally leads to significantly lower u_M and u_V displacements. They are all plotted using the Modified γ-Method in analytical dependence of s in Figure 10. Because the values for LTF RC [41], LTF OSB, and FPB are in completely different ranges, they are plotted separately in two figures.

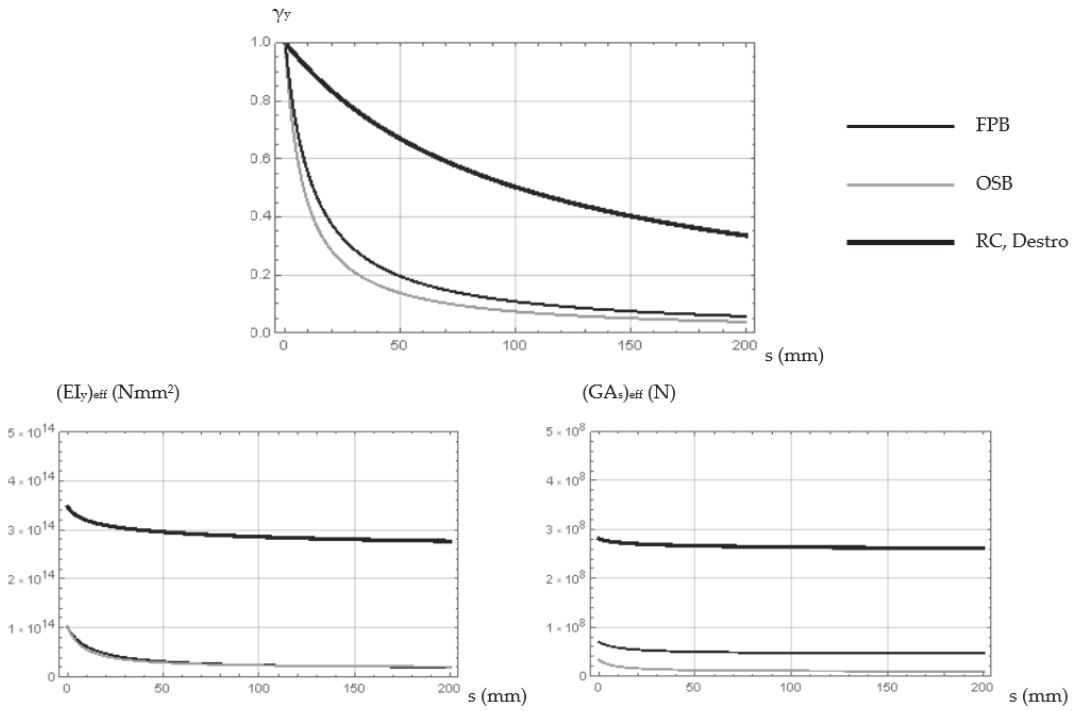

Figure 9. Stiffness coefficient of the connecting line (γ_y) and stiffness $(EI_y)_{eff}$ and $(GA_s)_{eff}$ in dependence of spacing *s* for FPB, OSB, and Destro type of LTF external wall elements.

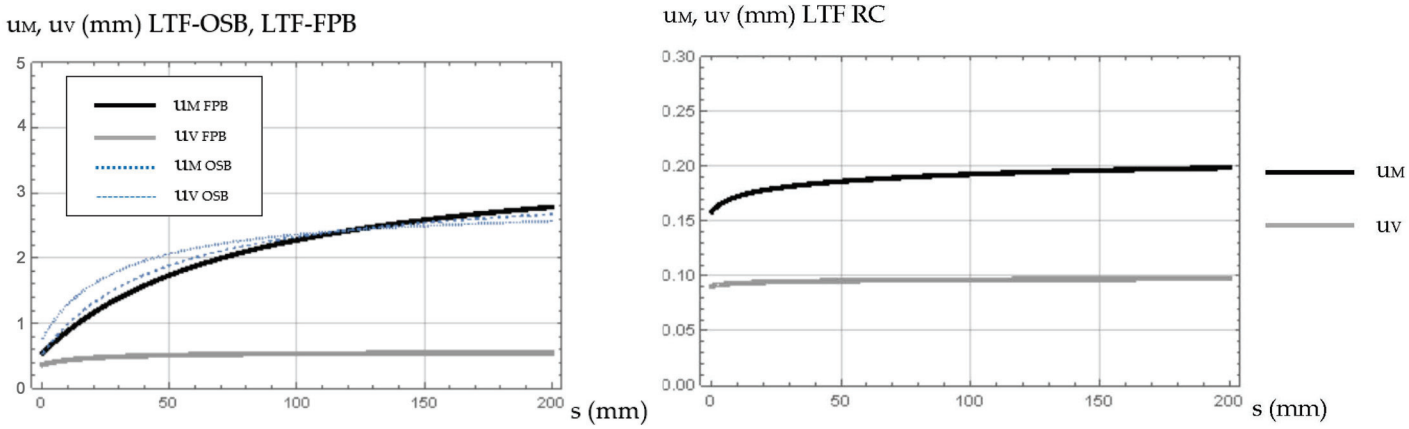

Figure 10. Displacements u_M and u_V in analytical dependence of spacing *s*.

It is evident that the results for OSB and FPB sheathing are very similar to the results for the internal walls, with exactly the same sheathings plotted in Figure 5. This influence of the timber-framed components and their thicknesses will be presented and further analysed in Figure 11. When analysing the results for the LTF RC element only, it is obvious that similar to FPB, the shear component (u_V) is essentially lower than the bending component (u_M). Otherwise, the difference between both considered displacements is somehow lower for LTF RC [41] compared to the FPB case, where the wall elements prove almost exclusively the bending behaviour, especially by increasing *s* values. Using Equation (15), it is now possible to calculate the racking stiffness *R* for all analysed sheathing types. They are plotted together in Figure 12.

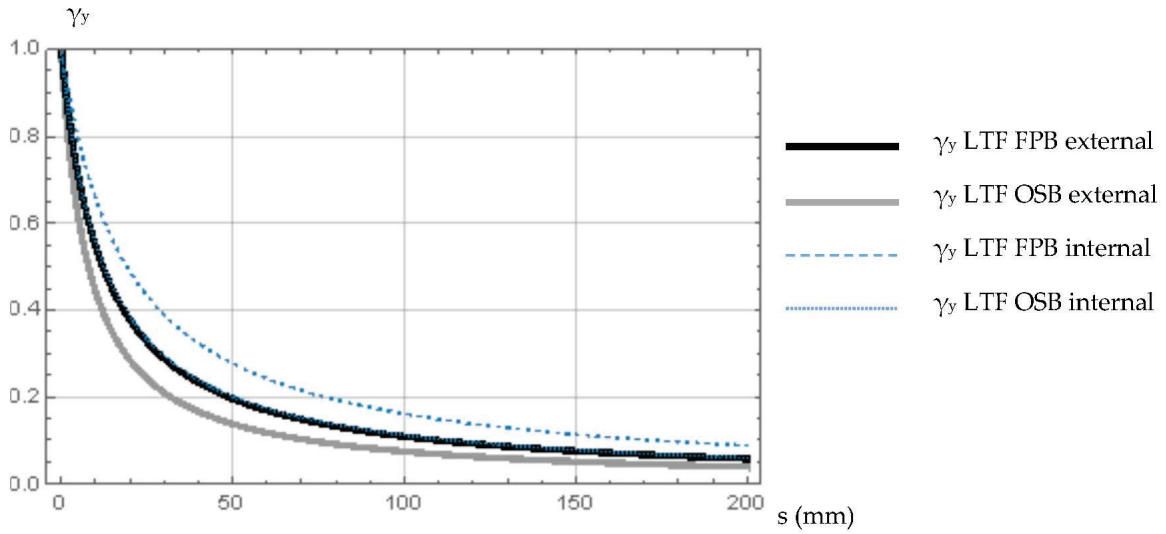

Figure 11. Stiffness coefficient of the connecting line (γ_y) for internal and external LTF elements in analytical dependence of *s*.

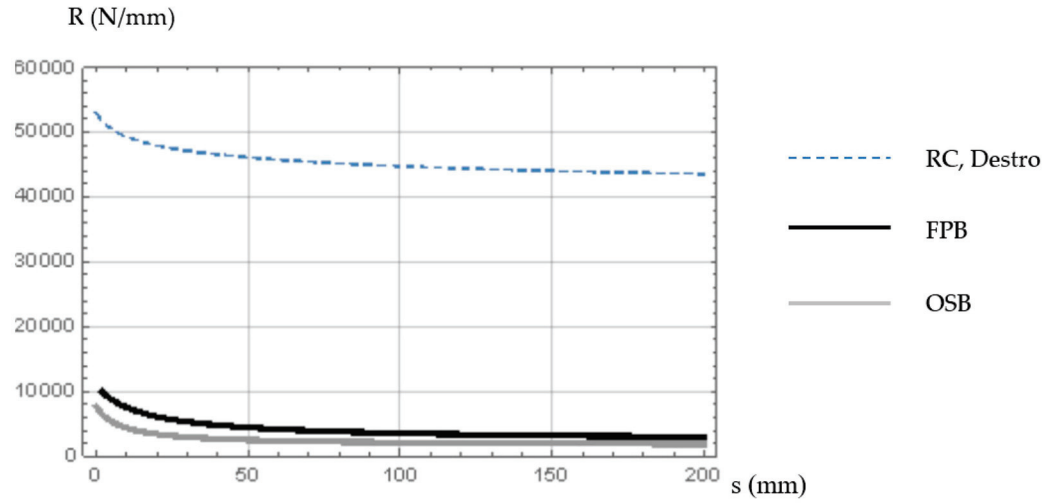

Figure 12. Racking stiffness *R* in dependence of spacing *s* for all three treated LTF elements.

The stiffness results show that the stiffness of the LTF RC wall element is significantly higher than that of other LTF elements with conventional sheathings. The results for two specifically selected parametric values of *s* are additionally presented in more detail in Table 2. From this, it can be concluded that the developed LTF RC wall element can certainly be a good load-carrying strengthening wall element to increase the horizontal stiffness of the whole multi-storey timber building, where a significant increase in loads may occur due to the action of horizontal actions (wind or earthquake).

As mentioned in the Introduction, one of the objectives of this study is to analyse the differences between external and internal LTF wall elements. Therefore, let us conclude by analysing the comparison in overall in-plane behaviour between LTF elements with OSB and FPB sheathings, which of course have substantially different dimensions of timber frame elements. First, it is recommended to analyse the behaviour of the stiffness coefficient of the connection (γ_y), which will further influence the in-plane stiffness. The results are shown in Figure 11.

The curve for γ_y LTF OSB internal is not visible in the figure because it practically fully coincides with the γ_y LTF FPB external function. A comparison between internal FPB and OSB walls was already performed by analysing the results from Figure 4. Therefore, we are now only interested in comparing the differences between external and internal

walls with the same sheathing material. It can be seen that the values for external walls are slightly lower than for internal walls in both sheathing cases, with the difference slightly larger in the case of FPB sheathing. This is due to the fact that in the case of internal walls, the sheathing board is fixed with a smaller timber stud (A_{t1}) surface area, while the slip modulus (K) and the spacing between the fastener means (s) remain the same (Equation (12)). The in-plane racking stiffness (R) for all four types of external and internal walls is plotted in Figure 13.

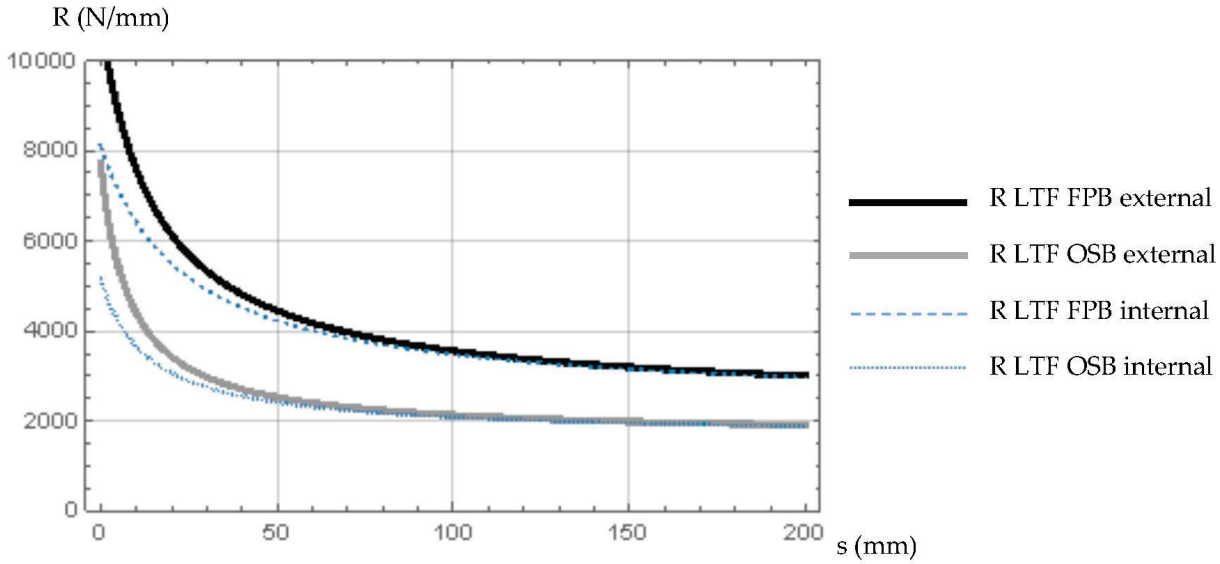

Figure 13. Racking stiffness R in dependence of spacing s for all four LTF elements.

All calculated results for the γ_y coefficient and the in-plane racking stiffness (R) obtained with the Modified γ-Method are listed in Table 3. Additionally, the ratio between the racking stiffness for the external and internal wall elements with exactly the same OSB or FPB sheathings is also presented to show the influence of the selected LTF element type. Of course, there are no results for this issue for the Destro test sample because it is used exclusively as an external wall element. Finally, the last column shows the difference in R between the completely stiff connection between the sheathings and the timber frame (s = 0.0) and the most commonly used value in the praxis (s = 75 mm). By using these data, we will be able to analyse the influence of the sheathing-to-frame connection, as performed in the numerical studies of [11,12] but for the LTF elements with the OSB sheathings only.

Table 3. Results for γ_y coefficient and the racking stiffness (R) by parametrically selecting two values for the spacing (s).

	γ_y	R (N/mm)	R_{ext} / R_{int}	Ratio R s = 75/s = 0
s = 75 mm				
Internal wall—OSB	0.1436	2201.29	1.000	0.4261
Internal wall—FPB	0.2031	3760.39	1.000	0.4639
External wall—OSB	0.1061	2273.70	1.033	0.2951
External wall—FPB	0.1390	3884.06	1.033	0.3542
External wall—RC	0.5740	45,280.50	/	0.8550
s = 0.0				
Internal wall—OSB	1.00	5165.81	1.000	/
Internal wall—FPB	1.00	8105.54	1.000	/
External wall—OSB	1.00	7703.66	1.492	/
External wall—FPB	1.00	10,964.90	1.353	/
External wall—RC	1.00	52,935.01	/	/

The following can be observed from the data in the table:

- The external/internal wall ratio (R_{ext}/R_{int}) is significantly higher for OSB and FPB sheathing at spacing s = 0.0 than at s = 75 mm and is higher for OSB, which is expected. Therefore, the spacing between the fasteners can be a very convenient strengthening approach in the case of OSB but absolutely not for FPB.
- For a spacing of s = 75 mm, the stiffness of the external walls in both cases with OSB and FPB is still only 3.3% higher than that of the internal walls with the same type of sheathing material. Thus, there are practically no significant differences.
- The impact of the sheathing-to-framing connection (ratio $s = 0/s = 75$ mm) is much greater in the case of external than internal walls. The influence of the fasteners is also greater for OSB than for FPB sheathings, where the relationship is even more pronounced for external than for internal walls. This again supports the conclusion that reducing the spacing between the fasteners in the case of OSB sheathing can be a very practical way to increase the in-plane stiffness and load-bearing capacity of LTF elements with OSB sheathing, which cannot be said in the case of FPB types.
- With similar numerical parametric studies in [11,12], only the influence of fastener flexibility for OSB interior wall specimens can be compared in our case, as there are no similar studies for FPB specimens. However, we obtained quite similar results for the value of s = 75 mm regarding the influence of the fastener flexibility in the sheathing-to-framing connection compared with the study performed by Casagrande et al. [12] (about 45%) and Aloisio et al. [11] (50%), considering at the same time that, in all cases, there was no vertical load impact.
- The racking stiffness (R) of the Destro RC wall element [41] is much higher than that of the other two LTF specimens and, in contrast to the behaviour of both OSB and FPB specimens, is much less dependent on the flexibility of the sheathing-to-framing connection.

4. Conclusions

As discussed in the first two sections, in the case of light timber-framed (LTF) wall elements, there are many different factors that can have a decisive influence on the in-plane load-bearing capacity and stiffness. Numerical treatment of the in-plane behaviour of such elements is, thus, usually very complex and time consuming. The most accurate computational approach is FEM analysis with elastic spring elements that simulate the flexibility of the fasteners in the connection plane, using a two-dimensional approach for the sheathing boards and a one-dimensional orthotropic model for all timber frame elements. However, this approach is very time consuming and practically useless for implementation in the design practice of multi-storey prefabricated timber buildings and also only allows for parametric treatment depending on the different positions of the fasteners in the connection plane. The position of the fasteners and the influence of their consequent flexibility on the sheathing-to-framing connection emerged as the most important parameters in many previous studies. Therefore, in our analysis, we express the stiffness of the connection plane (γ_y), the horizontal displacements due to bending (u_M) and the shear (u_V), and, finally, the racking stiffness of the LTF element in some analytical form depending on the spacing (s) between the fasteners, thereby showing the influence of the connection flexibility in greater detail. Thus, the Modified γ-Method was used, which provided similar results to the discrete FEM model and previous experimental studies for parametrically chosen spacings for the fasteners.

From the numerical results, we obtained the following important conclusions, which can be used for the design of multi-storey low-rise and mid-rise prefabricated LTF buildings:

- There is a significant difference in behaviour between LTF elements with FPB and OSB sheathings. On the one hand, LTF elements with OSB sheathings are significantly more effective for in-plane load bearing (Figure 6), but, on the other hand, they also exhibit a significantly lower in-plane stiffness (Figure 13, Table 2). This is due to the fact that the shear modulus of OSB material is very low; therefore, OSB wall elements also exhibit a very significant shear deformation (u_V), whereas in the case of FPB elements, the in-plane bending deformation (u_M) is clearly dominant. Consequently, it is of the utmost importance for the selection of the appropriate sheathing material, no matter whether the Ultimate Limit State (ULS) condition at the first floor or the maximum calculated displacement (SLS criteria) at the upper floor is the decisive parameter for the static calculation of a given timber building.
- The flexibility of the fasteners in the sheathing-to-framing shear connection was found to be an especially important parameter, as it had a primary influence on the in-plane behaviour of the analysed LTF wall elements. This influence turned out to be significantly higher in the case of OSB than in FPB elements, agreeing with the previous parametric numerical studies in [11,12], but which were only performed for OSB wall elements and the chosen spacing of the bonding means (s). However, this finding may be an indication that decreasing the fastener spacing (s) may be an important strengthening criterion in the case of LTF OSB elements used in mid-rise timber buildings but significantly less important in the case of FPB.
- In the comparative analysis of the external and internal wall specimens, it is notable that the thickness of the timber frame is a rather insignificant parameter, especially when using the most typified spacing fasteners s = 75 mm. The difference in racking stiffness was only 3.3% for both OSB and FPB specimens (Table 2). However, this effect increases quite significantly as the spacing (s) decreases. This finding may also have considerable practical relevance, as the external elements are usually expected to be strengthening elements around the building envelope due to the increased thickness of the frame, especially in the case of increased torsional actions due to floor plan asymmetry. In this case, it has been shown that it is better to use other strengthening LTF wall elements that can significantly increase the horizontal load-bearing capacity of the building envelope and also the in-plane racking stiffness of the whole building.
- For this very purpose, we also additionally analysed the LTF reinforcement element with 50 mm reinforced-concrete (RC) sheathing board on one side and conventional and commonly used 15 mm OSB sheathing on the other side, as presented originally in the study by Destro et al. [41]. From the results of the performed numerical analysis, it has been shown that such a prefabricated LTF RC wall element can be important for strengthening, which, when positioned on the building envelope, can contribute significantly to the torsional response and, in general, increase the in-plane racking stiffness of the whole building.

Author Contributions: Conceptualization, M.P. and E.K.Š.; methodology, M.P. and E.K.Š.; validation, M.P. and E.K.Š.; formal analysis, M.P. and E.K.Š.; investigation, M.P. and E.K.Š.; resources, M.P. and E.K.Š.; writing—original draft preparation, M.P. and E.K.Š.; writing—review and editing, M.P. and E.K.Š.; visualization, M.P. and E.K.Š.; funding acquisition, M.P. All authors have read and agreed to the published version of the manuscript.

Funding: Funding for this research was partly provided by the Slovenian Research Agency, National research programme P2-0129.

Data Availability Statement: Data available on request.

Conflicts of Interest: The authors declare no conflict of interest.

References

1. Salvadori, V. Multi-Storey Timber-Based Buildings: International Trends and Geographical Nuances. Ph.D. Thesis, Fakultät für Architektur und Raumplanung, Technische Universität Wien, Vienna, Austria, 2021.
2. Žegarac Leskovar, V.; Premrov, M. Architectural and Structural Design Typologies of Multi-Storey Timber Buildings. *Forests* **2021**, *12*, 757. [CrossRef]
3. Premrov, M.; Žegarac Leskovar, V. Innovative structural systems for timber buildings: A comprehensive review of contemporary solutions. *Buildings* **2023**, *13*, 1820. [CrossRef]
4. Alinoori, F.; Sharafi, P.; Moshiri, F.; Samali, B. Experimental investigation on load bearing capacity of full scaled light timber framed wall for mid-rise buildings. *Constr. Build. Mater.* **2020**, *231*, 117069. [CrossRef]
5. Xia, B.; O'Neill, T.; Zuo, J.; Skitmore, M.; Chen, Q. Perceived obstacles to multi-storey timber-frame construction: An Australian study. *Arch. Sci. Rev.* **2014**, *57*, 169–176. [CrossRef]
6. Australian Government Forest and Wood Products Research Department and Development Corporation. *Build in Timber*; Australian Government Forest and Wood Products Research Department and Development Corporation: Melbourne, Australia, 2016.
7. Lattke, F.; Lehmann, S. Multi-storey residential timber construction: Current developments in Europe. *J. Green Build.* **2007**, *2*, 119–129. [CrossRef]
8. John, S.; Nebel, B.; Perez, N.; Buchanan, A.H. *Environmental Impacts of Multi-Storey Buildings Using Different Construction Materials*; University of Canterbury: Christchurch, New Zealand, 2009.
9. Grossi, P.; Sartori, T.; Tomasi, R. Tests on timber frame walls under in-plane forces: Part 2. *Proc. Inst. Civ. Eng.-Struct. Build.* **2015**, *168*, 840–852. [CrossRef]
10. Premrov, M.; Dobrila, P. Numerical analysis of sheathing boards influence on racking resistance of timber-frame walls. *Adv. Eng. Softw.* **2011**, *45*, 21–27. [CrossRef]
11. Aloisio, A.; Boggian, F.; Østraat Sævareid, H.; Bjørkedal, J. Analysis and enhancement of the new Eurocode 5 formulations for the lateral elastic deformation of LTF and CLT walls. *Structures* **2023**, *47*, 1940–1956. [CrossRef]
12. Casagrande, D.; Rossi, S.; Sartori, T.; Tomasi, R. Proposal of an analytical procedure and a simplified numerical model for elastic response of single-storey timber shear walls. *Constr. Build. Mater.* **2016**, *102*, 1101–1112. [CrossRef]
13. Di Gangi, G.; Demartino, C.; Monti, G. Timber Shear Walls: Numerical Assessment of Damping of Sheathing-To-Framing Connections. In Proceedings of the OpenSees Days Europe 2017, 1st European Conference on OpenSees, Porto, Portugal, 19–20 June 2017.
14. Kozem Šilih, E.; Premrov, M.; Šilih, S. Numerical analysis of timber-framed wall elements coated with single fibre-plaster boards. *Eng. Struct.* **2012**, *41*, 118–125. [CrossRef]
15. Manser, N.; Steiger, R.; Geiser, M.; Otti, M.; Frangi, A. Shear resistance of Oriented Strand Board panel sheathings in timber-framed shear walls. *Eng. Struct.* **2024**, *316*, 118461. [CrossRef]
16. Žegarac Leskovar, V.; Premrov, M. *Energy-Efficient Timber-Glass Houses*; Springer: Berlin/Heidelberg, Germany, 2013. [CrossRef]
17. Dhonju, R.; D'Amico, B.; Kermani, A.; Porteous, J.; Zhang, B. Parametric evaluation of racking performance of Platform timber framed walls. *Structures* **2017**, *12*, 75–87. [CrossRef]
18. *CEN/TC 250/SC 8*; prEN 1998-1-2_for ENQ (Working Draft to CIB). European Committee for Standardization CEN: Brussels, Belgium, 2023.
19. Premrov, M.; Kuhta, M. *Experimental Analysis on Behaviour of Timber-Framed Walls with Different Types of Sheathing Boards*; Construction Materials and Engineering; Nova Science Publishers: Hauppauge, NY, USA, 2010.
20. Dobrila, P.; Premrov, M. Reinforcing methods for composite timber frame-fiberboard wall panels. *Eng. Struct.* **2003**, *25*, 1369–1376. [CrossRef]
21. Byloos, D.; Vandoren, B. Experimental and analytical assessment of the racking behavior of timber frame walls with single-sided double-layered sheathing panels. *Eng. Struct.* **2024**, *316*, 118592. [CrossRef]
22. Premrov, M.; Kuhta, M. Influence of fasteners disposition on behavior of timber-framed walls with single fibre-plaster sheathing boards. *Constr. Build. Mater.* **2009**, *23*, 2688–2693. [CrossRef]
23. Breyer, E.D.; Fridley, J.K.; Cobeen, E.K.; Pollock, G.D. *Design of Wood Structures—ASD/LRFD*, 6th ed.; McGraw-Hill Publishing Company: New York, NY, USA, 2007.
24. Faherty, K.F.; Williamson, T.G. *Wood Engineering and Construction Handbook*; Mc Graw-Hill Publishing Company: New York, NY, USA, 1989.
25. Thelandersson, S.; Larsen, J.S. *Timber Engineering*; John Wiley & Sons Ltd.: Hoboken, NJ, USA, 2003.
26. Schulze, H. *Wände–Decken–Bauproducte–Dächer–Konstruktionen–Bauphysik–Holzschutz*; 3. Auflage; B.G. Teuber Verlag: Wiesbaden, Germany, 2005; 552p, ISBN 10-3-519-25258-9.
27. *EN 1995-1-1:2005*; European Committe for Standardization CEN/TC 250/SC5 N173 (2005). Eurocode 5: Design of Timber Structures, Part 1-1 General Rules and Rules for Buildings. European Committe for Standardization: Brussels, Belgium, 2005.

28. Källsner, B. *Panels as Wind-Bracing Elements in Timber-Framed Walls*; Report 56; Swedish Institute for Wood Technology Research: Stockholm, Sweden, 1984.
29. Äkerlund, S. *Enkel Beräkningsmodell för Skivor på Regelstomme (Simple Calculation Model for Sheets on a Timber Frame)*; No.1; Bygg & Teknik: Stockholm, Sweden, 1984.
30. Källsner, B.; Lam, F. *Diaphragms and Shear Walls. Design/Construction Guide*; Holzbauwerke: Grundlagen, Entwicklungen, Ergänzungen nach Eurocode 5, Step 3; Fachverlag Holz: Düsseldorf, Germany, 1995; pp. 15/1–15/19.
31. Källsner, B.; Girhammar, U.A. Analysis of fully anchored light-frame timber shear walls-elastic model. *Mater. Struct.* **2009**, *42*, 301–320. [CrossRef]
32. *EN 1990:2002*; European Committe for Standardization CEN/TC 250. Eurocode: Basis of Structural Design. European Committe for Standardization: Brussels, Belgium, 2002.
33. *EN 1998-1:2005*; European Committe for Standardization CEN/TC 250. Eurocode 8: Design of Structures for Earthquake Resistance, Part 1 General Rules, Seismic Actions and Rules for Buildings. European Committe for Standardization: Brussels, Belgium, 2005.
34. Gattesco, N.; Boem, I. Stress distribution among sheathing-to-frame nails of timber shear walls related to different base connections: Experimental tests and numerical modelling. *Constr. Build. Mater.* **2016**, *122*, 149–162. [CrossRef]
35. *European Committee for Standardization CEN/TC 250/SC 5 N 1546 CEN/TC–13.7. Lateral Displacement of Multi Storey Timber Shear Walls*; Technical Report; Technical Committee CEN: Brussels, Belgium, 2022.
36. European Committee for Standardization Technical Committee CEN. *Eurocode 5: Design of Timber Structures—Common Rules and Rules for Buildings Part 1-1: General*; Tech. Rep.: Brussels, Belgium, 2021.
37. Premrov, M.; Dobrila, P.; Bedenik, B. Approximate analytical solutions for diagonal reinforced timber-framed walls with fibre-plaster coating material. *Constr. Build. Mater.* **2004**, *18*, 727–735. [CrossRef]
38. Premrov, M.; Dobrila, P. Modelling of fastener flexibility in CFRP strengthened timber-framed walls using modified γ-method. *Eng. Struct.* **2008**, *30*, 368–375. [CrossRef]
39. Möhler, K. Über das Tragverhalten von Biegeträgern und Druckstäben mit Zusammengesetztem Querrshnitt und Nachgiebigen Verbindungsmitteln. Ph.D. Thesis, TH Karlsruhe, Karlsruhe, Germany, 1956.
40. *EN 338:2003 E*; Structural Timber—Strength Classes. European Committee for Standardization CEN TC 124–Timber Structures: Brussels, Belgium, 2003.
41. Destro, R.; Boscato, G.; Mazzali, U.; Russo, S.; Peron, F.; Romagnoni, P. Structural and thermal behaviour of a timber-concrete prefabricated composite wall system. In Proceedings of the 6th International Building Physics Conference (IBPC), Torino, Italy, 14–17 June 2015.
42. Kuhta, M. Numerical Modelling of the Fasteners Influence on Horizontal Resistance of Timber-Framed Wall Elements. Ph.D. Thesis, Ilustr. Digitalna Knjižnica Univerze v Mariboru–DKUM, Digitalna Knjižnica Slovenije–dLib.si. [COBISS.SI-ID 14409750]. University of Maribor, Maribor, Slovenia, 2010; 132p. (In Slovenian).

buildings

MDPI

Article

Research on the Thermal Performance and Dimensional Compatibility of Insulation Panels with Chinese Fir Facings: Insights from Field Investigations in Qiandongnan

Sixian Dai [1], Jingkang Lin [2], Panpan Ma [3], Qiuyun Chen [3], Xiangyu Chen [1], Feibin Wang [4] and Zeli Que [3,*]

[1] Faculty of Humanities and Social Sciences, Nanjing Forestry University, Nanjing 210037, China
[2] Fujian Provincial Institute of Architectural Design and Research Co., Ltd., Fuzhou 350001, China
[3] College of Material Science and Engineering, Nanjing Forestry University, Nanjing 210037, China
[4] College of Landscape Architecture, Nanjing Forestry University, Nanjing 210037, China
* Correspondence: zelique@njfu.edu.cn

Abstract: The traditional timber architecture of Qiandongnan represents a rich cultural heritage. However, urbanization has led to the replacement of these structures with concrete and brick buildings, resulting in the loss of both functionality and cultural identity. To bridge the gap between traditional architecture and modern building needs, this study conducted field surveys to extract key design parameters from local structures, enabling the development of a modular framework for Structural Insulated Panels (SIPs) based on the dimensions of traditional dwellings. Four types of SIPs were developed using Chinese fir, OSB, EPS, and XPS, and their thermal performance and heat stability were evaluated through theoretical analysis and hot box testing. The results show that all specimens met the required heat transfer coefficient. The combination of OSB and XPS showed a slightly lower heat transfer coefficient of 0.60 compared to Chinese fir, which had a coefficient of 0.62. However, the Chinese fir–XPS combination provided the longest time lag of 6.34 h, indicating superior thermal stability. Due to the widespread use of Chinese fir in local construction and its compatibility with the landscape, this combination is ideal for both energy efficiency and cultural preservation.

Keywords: sandwich wall panels; thermal performance; modularization; traditional timber buildings; Chinese fir

1. Introduction

Qiandongnan Miao and Dong Autonomous Prefecture, located in the southeastern part of Guizhou Province, China, is home to some of the most densely concentrated traditional villages in the country, with over 400 villages [1]. The region is characterized by a typical Karst Plateau landform, featuring complex topography with rolling mountains and undulating peaks. In response to the challenging hilly and mountainous terrain, the local population has developed a unique column-and-tie beam timber structure, which is central to the residential form of stilt dwellings and allows for a flexible and diverse approach to housing construction [2]. Figure 1 illustrates a traditional Dong Dwelling in Bapa Village, alongside its signature timber structure. These timber constructions are not merely shelters, but represent an enduring cultural identity, a historical legacy, and a way of life passed down through generations [3]. As such, preserving these architectural forms is essential for maintaining the region's cultural and environmental sustainability.

Furthermore, the conservation of these traditional timber buildings can act as a significant attraction for tourism, thus promoting economic growth [4]. However, the rapid urbanization sweeping across China has significantly undermined these traditional building practices [5]. With the influx of modern construction technologies and standards from urban areas into rural regions, many villagers have opted to replace their traditional timber homes with concrete or brick structures. This shift threatens the survival of timber construction, leading to ecological degradation, the homogenization of rural landscapes, and the loss of the region's distinctive cultural and architectural heritage [6].

(**a**) (**b**)

Figure 1. Traditional Dong dwellings in Bapa Village and their characteristic column-and-tie beam timber structure. (**a**) Traditional Dong Dwelling in Bapa Village. (**b**) Column-and-tie beam timber structure.

The reasons for this shift are complex and multifaceted, involving cultural, economic, political, and functional considerations. Among these factors, the most pressing issue is the growing gap between the living demands of contemporary villagers and the performance capabilities of traditional timber buildings [7]. The construction industry in these regions is still in a state of underdevelopment, with building techniques primarily relying on traditional knowledge, rather than adopting more advanced, systematic, and standardized methods [8]. This approach inevitably results in a lack of construction precision, which in turn affects the airtightness and thermal insulation of the building envelope, leading to poor performance in resisting external environmental changes and maintaining internal comfort. Ultimately, this limits the ability of the buildings to meet modern living standards, making it difficult for local architecture to satisfy contemporary demands for high-quality living spaces [9].

To address these challenges, there is growing interest in integrating modern construction materials with traditional timber structures. Structural Insulated Panels (SIPs) are prefabricated building components that consist of an insulating foam core sandwiched between two structural facings, typically made from materials such as oriented strand board (OSB), plywood, metal sheets, or wood–cement boards [10]. SIPs offer several advantages, including lightweight construction, high strength, and excellent thermal and acoustic performance [11], which align well with the needs of timber buildings in Qiandongnan. However, a mismatch exists between the standard dimensions of SIPs and the specific structural requirements of traditional timber buildings in the region.

Traditional timber buildings in Qiandongnan adhere to dimensional rules based on a traditional Chinese measurement system that uses the units of Chi (尺) and Cun (寸) to ensure uniformity in construction. These measurements differ significantly from the standard units used in modern building practices. Additionally, the size and layout of timber buildings in this region are deeply influenced by cultural practices, with specific dimensions symbolizing values such as happiness and harmony within the local culture. In contrast, standardized SIP wall dimensions, which are typically based on building prac-

tices prevalent in regions like North America and Europe, specify panel widths of 4 feet (1.22 m), lengths up to 24 feet (7.32 m), and thicknesses ranging from 4.5 inches (114 mm) to 6.5 inches (165 mm) [12]. These standard dimensions, however, do not align with the culturally significant measurement systems of Qiandongnan. Consequently, the current SIP dimensions may not be suitable for use in this region, highlighting the need for further research to determine panel sizes that not only meet modern modular construction standards, but also respect the cultural and structural requirements of traditional timber buildings in Qiandongnan.

Chinese fir, a vital softwood species widely distributed in Guizhou Province, plays a crucial role in the construction of traditional timber buildings in Qiandongnan, shaping the distinctive rural landscape of this region [13–15]. To preserve the harmonious visual esthetics of the area while addressing rising construction costs, there is a growing interest in using Chinese fir as the facing material for SIPs, as an alternative to more commonly used materials like OSB. This shift not only supports the use of locally sourced materials, but also helps to preserve the architectural identity of this region. However, the suitability of this alternative is still in question, due to inherent differences between Chinese fir and OSB in terms of physical properties, such as structural composition, surface roughness, density, and moisture content. These variations result in distinct differences in thermal conductivity and capacity, which significantly influence the thermal performance of SIPs by affecting heat conduction, convection, and radiation. Despite these concerns, there is a lack of studies comparing the thermal insulation and stability performance of insulation panels with Chinese fir facings. Consequently, the effectiveness of Chinese fir as a facing material for SIPs has not been thoroughly examined in terms of its impact on thermal performance. Therefore, it is crucial to investigate how the unique properties of Chinese fir influence the thermal characteristics of SIPs, particularly to assess its suitability for building applications in Qiandongnan before wider adoption.

The primary goal of this research is to bridge the gap between the modern living demands of residents and the functional limitations of traditional timber buildings in Qiandongnan. While these buildings have long been integral to the region's cultural identity, their thermal properties often fail to meet contemporary standards of comfort. To address this, the study focuses on two key questions: (1) What are the optimal dimensions for SIPs that ensure compatibility with local building structures, meet modern standards, and respect cultural significance? (2) How does replacing OSB with Chinese fir as the facing material for SIPs affect thermal insulation performance and stability?

By exploring the use of locally available Chinese fir in the construction of SIPs, this study aims to enhance the functional performance of buildings while preserving the region's unique architectural and visual landscape.

2. Materials and Methods

2.1. Field Investigations

Field observations, along with photographic documentation, mapping, and on-site sketching, were conducted in six representative Miao and Dong ethnic villages—Xiaohuang, Bapa, Tang'an, Zhaoxing Dazhai, Wudong, and Langde Shangzhai—to assess the current state of timber buildings in Qiandongnan. These villages were selected for their representation of Guizhou's two major ethnic minorities: the Dong (Xiaohuang, Bapa, Tang'an, Zhaoxing Dazhai) and the Miao (Wudong and Langde Shangzhai). The villages feature distinct timber architectural traditions and span diverse topographies, including mountainous landscapes, river valleys, and terraced landscapes, providing valuable insights into how traditional timber structures adapt to varying environments. Data on climate conditions, construction methods, building component dimensions, and spatial layouts were

systematically collected. Additionally, interviews with local residents were conducted during the field research to gather insights into their living requirements and needs.

2.2. Preparation of Structural Insulation Panels

2.2.1. Raw Materials

Chinese fir finger-joint panels and oriented strand board were used as facing materials. The density and moisture content of the panels were determined according to GB/T 17657 [16].

The thermal conductivity coefficient of the panel materials was measured using a quasi-steady-state heat conductometer (FWDR-II, Harbin Hongrun Teaching Test Equipment Factory, Harbin, China). Prior to measurement, calibration was performed using two reference materials under controlled conditions of 20 °C and 60% relative humidity to ensure accuracy. The calibration process adhered to the requirements outlined in JJF 98-2024 [17]. The heat storage coefficient was calculated based on the values specified in Appendix 2 of GB50176 [16]. Expanded polystyrene (EPS) and extruded polystyrene (XPS) were used as core materials, with density, thermal conductivity, and heat capacity values provided by the suppliers. The dimensions and material properties are summarized in Table 1.

Table 1. Dimensions and material properties of raw materials.

Properties	Chinese Fir	OSB	EPS	XPS
Origin	Fujian	America	Suzhou	Suzhou
Density (kg/m^3)	367 ± 6.4 *	635 ± 2.2 *	32	38
Moisture content (%)	15.17 ± 0.63 *	9.08 ± 0.12 *	—	—
Thermal conductivity [W/(m·K)]	0.230	0.110	0.037	0.032
Coefficient of heat accumulation [W/(m^{2}K)]	3.92	3.57	0.432	0.621
Label thickness (mm)	12.00	12.00	50.00	50.00
Measured thickness (mm)	13.40	11.48	50.00	46.00

Note: Values with * represent the standard deviation.

2.2.2. Fabrication of Structural Insulation Panels

Two types of Structural Insulated Panels (SIPs) were fabricated, using Chinese fir finger-joint panels as the facing material, and either expanded polystyrene (EPS) or extruded polystyrene (XPS) as the core material. These panels are labeled as CE (with EPS core) and CX (with XPS core), respectively. The dimensions of the panels were standardized at 1100 mm in length (L), 900 mm in width (W), and 74 mm in thickness (T). The length and width were determined based on the maximum specimen size compatible with hot box testing. The thickness was selected considering both field survey findings and economic factors. Field investigations revealed that local wooden residential columns typically use mortise and tenon joints with a tenon width of 50 mm, while 12 mm thick timber panels are a common yet costly choice. Based on these factors, a total thickness of 74 mm was established. For comparison purposes, two types of SIPs with the same dimensions were fabricated, using oriented strand board (OSB) as the facing material, labeled as OE (with EPS core) and OX (with XPS core), respectively. Bisphenol A epoxy resin adhesive (6101, DONGFU, Shanghai Ranghan Industry & Trade Co., Ltd., Shanghai, China) was used. The adhesive-to-hardener ratio was maintained at 4:1. The adhesive was manually applied to the facing material at a coverage rate of 300 g per square meter. Following application, the panels were manually assembled and compressed under a pressure of 50 kPa, at a temperature of 20 °C, for 24 h, using a press. The fabrication process is outlined in Figure 2.

(**a**) (**b**) (**c**) (**d**)

Figure 2. Production process for sandwich wall panels. (**a**) Even spreading of adhesive layer. (**b**) Surface of panel with adhesive layer applied. (**c**) Cold pressing. (**d**) Specimens.

2.3. Thermal Performance Evaluation

2.3.1. Calculation of Heat Transfer Coefficient

The heat transfer resistance of a wall is a key physical property that characterizes the ability of a building envelope to resist heat flow. Its reciprocal is the heat transfer coefficient, which is an important parameter for evaluating the energy efficiency of the building envelope. The heat transfer coefficient, defined as the amount of heat transferred through a unit area of the building envelope per unit time, is inversely proportional to the energy-saving performance. In other words, a higher heat transfer coefficient leads to greater energy loss, while a lower coefficient corresponds to reduced energy loss. The calculation of heat transfer resistance is mainly based on GB 50176 [18]. In calculating the thermal resistance for XPS and EPS, the thermal conductivity was multiplied by adjustment factors of 1.10 and 1.05, respectively, to meet the requirements for thermal insulation materials used in the "Hot Summer and Cold Winter" region. The thermal resistance for a single material is calculated using Equation (1):

$$R = \frac{\delta}{\lambda} \tag{1}$$

where R is the thermal resistance, in m^2·K/W; δ is the thickness of the material, in m; and λ is the thermal conductivity of the material, in W/(m·K).

For multi-layer enclosure structures, such as SIPs, the total thermal resistance is calculated by summing the individual resistances of each layer. This is given by Equation (2):

$$R = R_1 + R_2 + \cdots + R_n \tag{2}$$

where $R_1, R_2, \cdots R_n$ is the thermal resistance of each layer, in m^2·K/W.

The overall heat transfer resistance of the building envelope, including both surface resistances and material resistances, is calculated using Equation (3):

$$R_0 = R + R_i + R_e \tag{3}$$

where R_0 is the heat transfer resistance, in m^2·K/W; R_i is the inner surface resistance of heat transfer, in m^2·K/W; and R_e is the outer surface resistance of heat transfer, in m^2·K/W.

The heat transfer coefficient of the building envelope is calculated using Equation (4):

$$K_{cal} = \frac{1}{R_0} \tag{4}$$

where K_{cal} is the heat transfer coefficient calculated theoretically, in W/(m^2·K).

2.3.2. Measurement Setup and Procedure

To validate the theoretical calculations, thermal performance tests were conducted on the walls of the SIPs using a heat flow thermal testing system (JTRG-B, Jinhua Julong Computer Experimental Machine Co., Ltd., Jinhua, China). The hot box of this system has a temperature control range of 0–100 °C, with air temperature fluctuations limited to ±0.5 °C and a heat transfer coefficient of less than 5%. The cold box, which is non-adjustable, isolates external air temperature fluctuations and maintains an initial temperature equal to room temperature. The system features a 20-channel thermocouple array with a measurement range of −50–100 °C, an accuracy of ±0.5 °C, and a resolution of 0.1 °C. The thermocouples are arranged into two sets of 10 channels, with nine measurement points on both the hot and cold surfaces. These points are spaced 300 mm apart and grouped into three sets (top, middle, and bottom). Additional environmental temperature measurement points are located 10 cm away from the specimen in both the hot and cold boxes. Two heat flow meters are installed on the hot surface for heat transfer analysis.

The test specimen was placed in the hot box and insulated on the sides with fiberglass to minimize edge heat loss. Data were collected every 20 min, with the hot box temperature maintained at 40 °C and the room temperature controlled at 15 °C via air conditioning. Relative humidity was kept between 50% and 60% throughout the experiment. The testing system and the layout of the temperature and heat flow meters are shown in Figures 3 and 4, respectively.

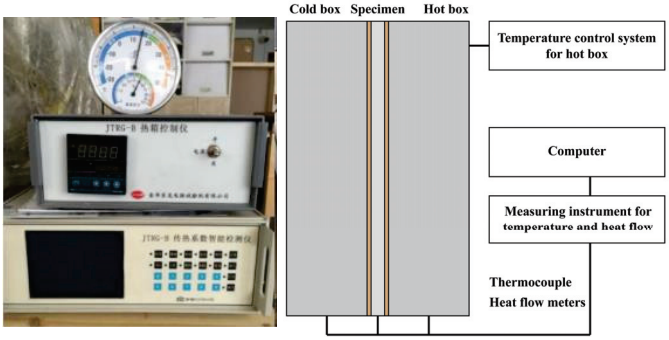

Figure 3. Hot box–cold box system for SIP wall thermal testing: 20-channel thermocouples (±0.5 °C) and dual heat flow meters under controlled conditions. (**a**) JTRG-B testing system. (**b**) Schematic of experimental setup.

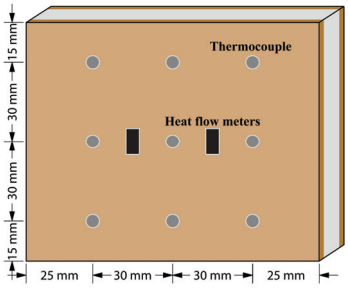

Figure 4. Thermocouple and heat flow meter arrangement: 9 points per surface (300 mm spacing), with environmental sensors.

2.3.3. Calculation of Heat Transfer Coefficient from Test Results

The heat transfer coefficient K of the specimen was calculated following the guidelines established in GB/T 13475 [19] for thermal performance evaluation. The calculation

involves considering both convective and radiative heat transfer contributions. The heat balance equation at either surface of the specimens is given by Equation (5):

$$\frac{\Phi}{\mathrm{A}} = \varepsilon h_r \left(T'_r - T_s\right) + h_c (T_a - T_s) \tag{5}$$

where Φ/A is the heat flow per unit area into the surface, in W/m^2; T'_r is the average radiant temperature seen by the specimen, in K or °C; T_a is the temperature adjacent to the specimen, in K or °C; T_s is the surface temperature of the specimen, in K or °C; ε is the emissivity factor; h_r is the radiation coefficient, in W/(m^2·K); and h_c is the convection coefficient, in W/(m^2·K).

To simplify the analysis, the air and radiant temperatures are combined into the environmental temperature, T_n, which represents the proper weighting of the two temperature components. The heat flow can then be expressed in terms of the surface thermal resistance, as shown in Equation (6):

$$\frac{\Phi}{\mathrm{A}} = \frac{1}{R_s}(T_n - T_s) \tag{6}$$

where R_s is the surface thermal resistance.

The environment temperature is calculated using Equation (7):

$$T_n = \frac{\varepsilon h_r}{\varepsilon h_r + h_c} T'_r + \frac{h_c}{\varepsilon h_r + h_c} T_a \tag{7}$$

In cases where the convection coefficient, h_c, is unknown, T_n can be determined using a rearranged form of the heat balance equations, as shown in Equation (8):

$$T_n = \frac{T_a \frac{\Phi}{\mathrm{A}} + \varepsilon h_r \left(T_a - T_r'\right) T_s}{\frac{\Phi}{\mathrm{A}} + \varepsilon h_r \left(T_a - T_r'\right)} \tag{8}$$

In practice, the average radiation temperature T_r and the temperature adjacent to the specimen T_a in the hot and cold boxes are very close, especially when the thermal resistance of the specimen is much greater than the surface thermal resistance, or when forced convection is used such that the convection coefficient h_c is significantly greater than εh_r. In such cases, the heat transfer coefficient can be determined based on the temperature difference between the two environmental temperatures across the specimen, as given by Equation (9):

$$K = \frac{\Phi}{\mathrm{A}(T_{n1} - T_{n2})} \tag{9}$$

where K is the heat transfer coefficient, in W/ (m^2·K); and T_{n1} and T_{n2} are the environment temperatures on the hot and cold sides of the specimen, respectively, in K.

2.3.4. Evaluation of Thermal Stability

The thermal inertia, damping factor, and time lag were calculated according to standard 50176 to evaluate the thermal stability of specimens [18]. The thermal inertia can be calculated using Equation (10):

$$D = R \times S \tag{10}$$

where D is the thermal inertia, without dimension; and S is the coefficient of heat accumulation, in W/ (m^2·K).

For multi-layer enclosures, the total thermal inertia is calculated by Equation (11):

$$D = D_1 + D_2 + \cdots + D_n \tag{11}$$

where $D_1, D_2, \cdots D_n$ is the thermal inertia of each layer, in W/ (m^2·K).

The damping factor is calculated using Equation (12):

$$v = \frac{A_e}{A_i} \tag{12}$$

where v is the damping factor, without dimension; A_e is the amplitude of outdoor temperature fluctuation, in K; and A_i is the amplitude of indoor surface temperature fluctuation, in K.

The time lag is calculated using Equation (13):

$$\xi = \xi_i - \xi_e \tag{13}$$

where ξ is the time lag, in h; ξ_i is the time when the indoor surface temperature reaches its maximum, in h; and ξ_e is the time when the outdoor temperature reaches its maximum, in h.

3. Results and Discussions

3.1. Filed Investigation Results

3.1.1. Construction Methods and Thermal Performance of Traditional Timber Dwellings in Qiandongnan

Qiandongnan, located in the southeastern part of Guizhou, is a typical Karst Plateau region, with 92.5% of the land being mountainous and hilly [3]. The climate in Qiandongnan is mild throughout the year, with minimal temperature fluctuations across the four seasons [2]. The traditional timber-framed houses of the Miao and Dong ethnic groups in this region have evolved over thousands of years to adapt to local climate conditions and available resources [9,20]. Field investigations indicate that the main types of traditional houses in the region are the Dong ethnic group's dry-platform houses and the Miao ethnic group's semi-dry-platform stilt houses. The construction of these dwellings involves an extensive preparation and material processing phase, followed by a relatively short erection period. Figure 5 reveals that the construction process utilizes traditional tools, such as axes, chisels, planes, and saws, alongside modern machinery. Despite the use of modern tools, the design and construction methods remain relatively simplified, relying largely on the experiential knowledge of local artisans, known as "Zhang Mo Shi" (掌墨师), and their practical understanding of the terrain [21]. Notably, the construction process lacks formal planning, empirical data, and theoretical design principles [22]. Consequently, the structural stability of these houses depends heavily on the individual skill and experience of the craftsmen, often leading to insufficient overall reliability and stability. The construction is also guided more by subjective expertise and esthetic preferences than by formal design documentation [23].

In terms of materials, the traditional dwellings feature lightweight structures, with floors and walls typically constructed from Chinese fir boards, usually 20 mm or 30 mm thick, as shown in Figure 6. While this material choice fills the frame, it compromises the thermal performance of the building envelope, resulting in low thermal efficiency [24]. Despite the mild climate in Qiandongnan, maintaining a stable indoor temperature remains a challenge [25]. Interviews with local residents revealed concerns regarding the thermal insulation performance of their homes, with many expressing dissatisfaction over the lack of year-round comfort. This issue is not limited to the Qiandongnan area; similar thermal insulation challenges have been observed in traditional timber buildings across various provinces in China, including Zhejiang [7]. These findings highlight the urgent need for improved thermal performance in the envelopes of traditional timber buildings.

(**a**)

(**b**)

Figure 5. Traditional dwelling construction in Qiandongnan Xiaohuang Village. (**a**) Construction of traditional dwellings involves use of various woodworking tools, such as axes, chisels, planes and saws. (**b**) Simplified construction methods rely on direct carving and experiential knowledge of local artisans.

(**a**) (**b**)

Figure 6. Lightweight construction of traditional dwellings. (**a**) Chinese fir veneer panels used for walls. (**b**) Thin floors (20–30 mm) contributing to poor thermal performance.

3.1.2. Structural Dimensions of Traditional Wooden Houses in Qiandongnan

The construction scale and craftsmanship within the Dong nationality are deeply influenced by traditional tools, such as the Luban ruler [26], which plays a key role in marking specific measurements for architectural work. The Luban ruler is divided into two sets of four segments, totaling eight parts. One set, marked in red, is associated with auspicious meanings, while the other, marked in black, signifies less favorable outcomes.

In traditional Chinese architecture, measurements are based on three primary units: Chi (尺), Cun (寸), and Fen (分). The Luban ruler is primarily used to determine the unit of Chi (尺), which is the basic measurement unit. For finer divisions, such as Cun (寸) and

Fen (分), carpenters typically rely on the carpenter's square (曲尺), a tool that provides greater precision for smaller measurements.

Within the carpenter's square, certain numbers, such as 6 and 8, hold special significance. According to the Nine Palaces (九宫) numerology, the numbers 1, 6, and 8 are considered auspicious, often represented by the color white, which signifies good fortune. These symbolic numbers are believed to bring positive outcomes, and are consciously used in construction to align with these cultural beliefs. As a result, the number 8 is commonly used as the final digit in architectural measurements, while 6 is frequently incorporated into the design of furniture and interiors. This practice, known as "Ya Bai" (压白), involves ensuring that the dimensions of components end in these lucky numbers to promote favorable outcomes and avoid misfortune.

As depicted in Figure 7, this cultural influence is evident in the architectural dimensions of traditional timber houses in the region. The first-floor heights typically range from 2000 mm to 2200 mm, and the second-floor heights from 2200 mm to 2400 mm—both multiples of 8. Similarly, the width and depth of these structures, such as 1860 mm, 2040 mm, 3810 mm, and 4140 mm, often correspond to values divisible by 3, with some also divisible by 8.

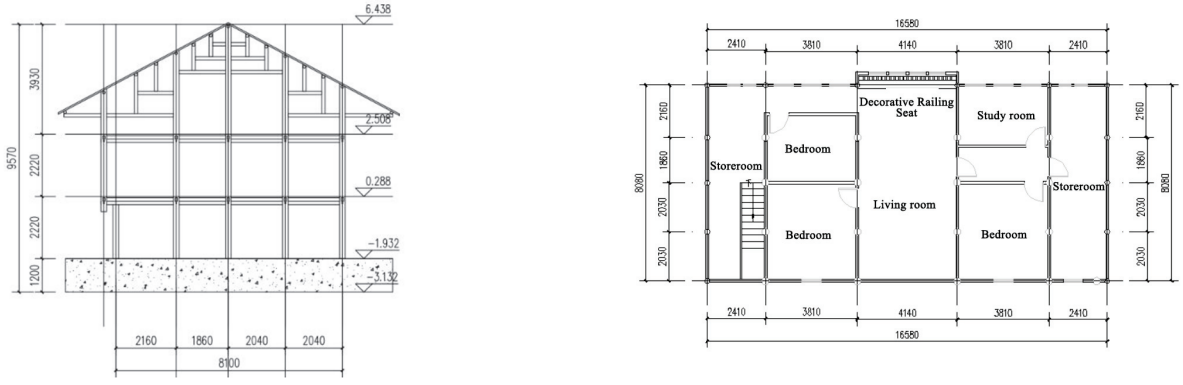

(**a**) (**b**)

Figure 7. Traditional timber houses in Wu-Dong Miao Ethnic Village. (**a**) Sectional view showing floor heights (2000–2400 mm) designed as multiples of 8. (**b**) Second-floor plan with dimensions (e.g., 1860 mm, 2040 mm) reflecting cultural numerology and "Ya Bai" practices.

In terms of structural measurements, the width of Chinese fir wall panels is generally 300 mm, while the column diameter is also around 300 mm. The columns are equipped with through-beam tenons, each approximately 50 mm wide. Additionally, floorboards are typically 25 mm thick, and the openings and tenons measure about 5 mm.

To facilitate the industrialization of housing construction in China, the Chinese Standard for Modular Coordination of Building defines a basic modular unit, M, which is 100 mm [27]. Based on field investigations in Qiandongnan, a modular system has been developed to meet the height requirements of traditional dwellings while improving coordination with modern construction components. A multi-modular system of 3 M and an infra-modular size of 1/20 M (300 mm and 5 mm, respectively) have been selected for the wall modules. Based on this modular framework, the dimensions of each SIP unit are set at 2400 mm in length and 300 mm in width, with adjacent units seamlessly connected via a tongue-and-groove joint, featuring a 25 mm depth. This system ensures smooth integration with the traditional timber framework, while also allowing compatibility with modern, market-ready construction materials.

3.2. Thermal Performance Evaluation Results

3.2.1. Evaluation of Heat Transfer Coefficient

The heat transfer coefficient was initially calculated using Equation (3) to determine the heat transfer resistance, followed by Equation (4) to calculate the heat transfer coefficient. Based on field investigation results, the values of R_i and R_e used in Equation (3) were sourced from GB 50176 [16], and were determined to be 0.11 m^2·K/W and 0.04 m^2·K/W, respectively. The thermal inertia was calculated using Equation (11). The results are summarized in Table 2.

Table 2. Results of heat transfer coefficient calculation.

Specimen Code	Heat Resistance (R)/m^2·K/W	Heat Transfer Resistance (R_0)/m^2·K/W	Heat Transfer Coefficient (K_{cal})/W/(m^2·K)	Thermal Inertia (D)
OX	1.518	1.668	0.600	1.56
CX	1.426	1.576	0.635	1.27
OE	1.498	1.648	0.607	1.30
CE	1.406	1.556	0.643	1.01

To further verify the accuracy of the theoretical calculations, the heat transfer coefficient of all specimens was also determined using Equation (9), based on data obtained from hot box testing. The comparison between the test results and theoretical calculations is presented in Figure 8. As shown in the figure, the test outcomes closely align with the theoretical predictions, with differences within 5%, confirming the reliability of the calculated data.

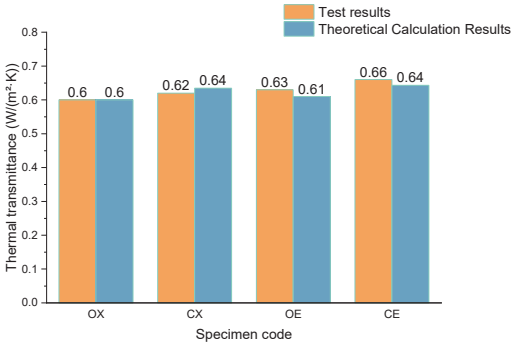

Figure 8. Heat transfer coefficient of each specimen.

Among the specimens tested, the OX specimen, featuring OSB facings and an XPS core, exhibited the lowest heat transfer coefficient, indicating the most efficient thermal performance. In contrast, the CE specimen showed the highest thermal conductivity under steady-state conditions, resulting in the greatest heat loss. For specimens with the same core material thickness, using OSB facings reduced the heat transfer coefficient slightly, highlighting the critical role of facing materials in enhancing thermal efficiency. Furthermore, when the same facing materials were used, the incorporation of XPS as the core material significantly lowered the heat transfer coefficient, effectively minimizing heat loss. When utilizing the same core materials, a primary factor contributing to the observed variation in the heat transfer coefficient is the difference in thermal conductivity between Chinese fir and OSB. Chinese fir is characterized by a continuous cellular structure, whereas OSB is composed of smaller wood particles bonded with adhesive. As a result, heat is more readily transmitted through the wood than through the OSB [28,29]. Furthermore, the continuous cellular structure of Chinese fir promotes greater moisture absorption, resulting

in a higher moisture content compared to OSB [30]. Because increased moisture content elevates thermal conductivity, this further contributes to a higher heat transfer coefficient in Chinese fir.

Figure 9 presents the heat flux density over time for each specimen. As observed during the experiment, the rapid temperature increase in the heat box from 15 °C to 40 °C initially caused a sharp rise in heat flux through the specimens, followed by a gradual stabilization. For specimens with EPS cores, the heat flux exhibited significant fluctuations in response to the sudden temperature change. In contrast, specimens with XPS cores displayed approximately 75% less fluctuation. After these fluctuations, the EPS-core specimens reached steady-state conditions relatively quickly, stabilizing in about 2 h, whereas the XPS-core specimens took approximately 3 h to achieve thermal equilibrium. The substantial difference between core materials, coupled with the relatively minor variation between face materials, underscores the crucial influence of core material properties on heat flux. Therefore, the observed discrepancies in specimens with different core materials can primarily be attributed to variations in the heat accumulation coefficient between EPS and XPS. Materials with a higher heat accumulation capacity, such as XPS, are able to store more heat, leading to a slower rate of temperature change and introducing a time lag in achieving steady-state conditions [31].

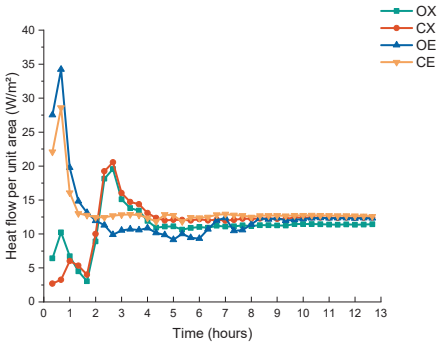

Figure 9. Time-dependent heat flux changes of specimens.

In addition, the disparity in thermal conductivity further contributes to these differences, stemming from the distinct structural characteristics of the materials. The manufacturing process, particularly the extrusion method used for both EPS and XPS, results in XPS having a denser particle arrangement. This tightly bonded structure enhances its ability to impede heat transfer more effectively than EPS, thereby leading to a lower thermal conductivity [32]. As a consequence of these differences in heat accumulation and thermal conductivity, EPS-core specimens experienced a more rapid initial temperature rise and a quicker response to fluctuations in thermal conditions. This resulted in EPS-core specimens reaching steady-state conditions more rapidly than XPS-core specimens.

According to the Design Standard for Energy Efficiency of Residential Buildings in Guizhou, the Qiandongnan region is classified as a "Hot Summer and Cold Winter" zone [33]. For residential buildings with up to three stories, the required heat transfer coefficient for the building envelope must be less than 1.0 when the thermal inertia index is lower than 2.5, or less than 1.5 when the thermal inertia index exceeds 2.5 [34]. All specimens tested in this study meet these criteria, indicating their suitability for use in residential buildings in the Qiandongnan area. Considering the reduced temperature fluctuations in XPS compared to EPS, due to its lower thermal conductivity and superior thermal insulation properties, XPS helps to maintain more stable interior temperatures and improves energy efficiency. This makes it a more suitable choice for wall systems, particularly in maintaining consistent thermal comfort and minimizing energy loss. Referring to the se-

lection of facing materials, from a practical perspective, although the OX specimen demonstrated the lowest heat transfer coefficient, the CX wall—composed of Chinese fir panels as facings and XPS cores—emerged as the optimal choice. This solution strikes a balance, offering superior energy efficiency while preserving esthetic harmony. This combination makes the CX wall the most suitable option for timber residential buildings in the Qiandongnan area, ensuring both thermal performance and visual integration with the local architectural style.

3.2.2. Thermal Stability Assessment

The heat transfer coefficient typically evaluates the thermal performance of walls under steady-state conditions. However, in practical applications, external temperatures fluctuate continuously, leading to potential discrepancies between the heat transfer behavior predicted by steady-state analysis and real-world conditions. Therefore, analyzing the temperature variations before the specimens reach a steady state provides valuable insight into the dynamic heat transfer characteristics of the wall during actual use. This approach helps to provide a better understanding of how temperature changes impact the thermal performance of the building envelope over time. Figure 10a,b illustrate the variation in temperature over time for the cold-side and hot-side surfaces of each specimen, respectively, from the initial measurement taken 20 min after the experiment began, to the steady-state temperature at 12 h.

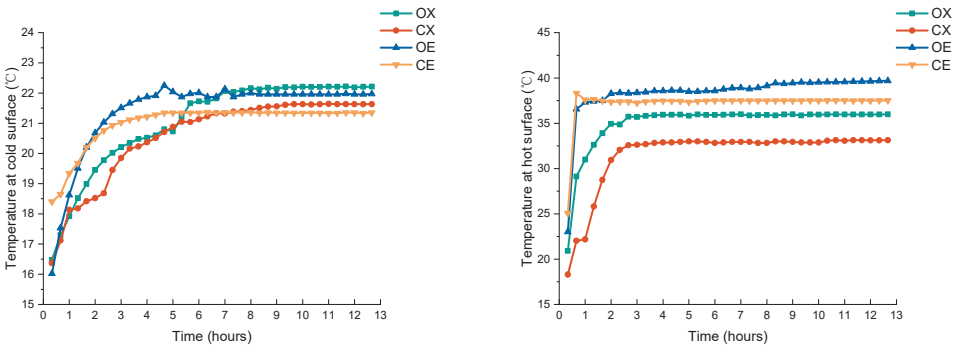

Figure 10. Time-dependent temperature changes at cold-side surface (**a**) and hot-side surface (**b**) of specimens.

For the cold-side surface, the specimen with EPS as the core material exhibited the highest initial temperature increase within the first 20 min compared to the other specimens. This rapid temperature rise indicates a quick thermal response, which is consistent with the lower thermal resistance of EPS relative to XPS. The lower thermal resistance and coefficient of heat accumulation in EPS allowed the EPS-core specimens to reach a thermal steady state faster, in approximately 4 h, the shortest stabilization time among all specimens. Once the steady state was reached, the temperature of the EPS-core specimen was slightly lower than that of the XPS-core specimen. The CE specimen exhibited the lowest steady-state temperature, recorded at 21.35 °C. This can be attributed to the most efficient heat dissipation to the environment, resulting from the highest thermal transfer coefficient among all specimens, which lowered the cold-side surface temperature when steady-state conditions were achieved [35]. This observation suggests that the XPS-core specimens demonstrated superior thermal stability performance over time.

A similar trend was observed on the hot-side surface, where EPS-core specimens exhibited a higher initial temperature and a faster temperature rise compared to the XPS-core specimens. The XPS-core specimens reached thermal steady-state conditions after approximately 2 h, while the EPS-core specimens stabilized after about 1 h. Upon reaching a

steady state, the CX specimen displayed the lowest temperature on the hot side, further highlighting its superior thermal stability. This can be attributed to the higher moisture content in Chinese fir compared to OSB. While higher moisture content generally increases thermal conductivity and may negatively affect thermal insulation, a moderate increase in moisture content, when used as a facing material, can enhance heat absorption, due to the larger thermal capacity of water [36]. This results in a lower surface temperature on the hot side, contributing to better thermal stability. Moreover, this finding suggests that the superior moisture absorption capability of solid wood boards as facings may not always be detrimental to the building envelope; in some cases, it can be beneficial. This highlights the importance of considering moisture content variation when using wood boards, such as Chinese fir, as an alternative to OSB in real-world applications.

When comparing the temperature variation on both the cold-side and hot-side surfaces, it is evident that heat loss differs depending on the core material through which heat is transferred. This difference can be evaluated using the damping factor and time lag indices, which provide valuable insight into the material's ability to store and release heat. These parameters are essential for evaluating the thermal performance of building envelopes. A higher damping factor and longer time lag indicate better resistance to temperature fluctuations, reflecting superior thermal stability. The damping factor and time lag were calculated using Equations (12) and (13), respectively, and the results are presented in Table 3.

Table 3. Results of damping factor and time lag calculations.

Specimen Code	Damping Factor	Time Lag (h)
OX	1.70	5.67
CX	1.85	6.34
OE	1.94	3.34
CE	1.87	3.67

The results reveal distinct thermal behaviors across the specimens, marked by subtle yet significant differences in thermal wave attenuation and propagation. The damping factors ranged from 1.70 to 1.94, with a narrow variation of 0.24, indicating relatively consistent heat dissipation characteristics. In contrast, the time lag values ranged from 3.34 to 6.34 h, highlighting more pronounced variations in heat transfer dynamics. The OE specimen exhibited the highest damping factor of 1.94 and the shortest time lag of 3.34 h, signifying the most rapid thermal response and efficient heat dissipation. On the other hand, the CX specimen, with the longest time lag of 6.34 h, exhibited thermal behavior similar to the envelope constructed from earth brick stabilized with cement, which had a time lag of 6 h [37]. Considering the significantly thinner profile of the CX specimen compared to the 140 mm thickness of the brick envelope, this further emphasizes its suitability for applications requiring long-term thermal stability and minimal heat transfer fluctuations.

Figure 11 illustrates the environmental temperature on the cold side. It shows that, although the fluctuations in environmental temperature align with the surface temperature changes, the environmental temperature adjusts more gradually. It takes approximately 8 h for the environmental temperature to reach equilibrium. The environmental temperature on the cold side is about 1 °C lower than the surface temperature, indicating that the heat on the surface is attenuated while radiating to the surrounding environment. The CE specimens exhibit the smallest temperature difference, at 0.59 °C, which aligns with the observation from the variation in cold-side surface temperature. This can be attributed to the higher thermal transfer coefficient of the CE specimens, which facilitates more efficient

heat dissipation to the environment. As a result, the surface temperature is lowered, while the environmental temperature increases [35].

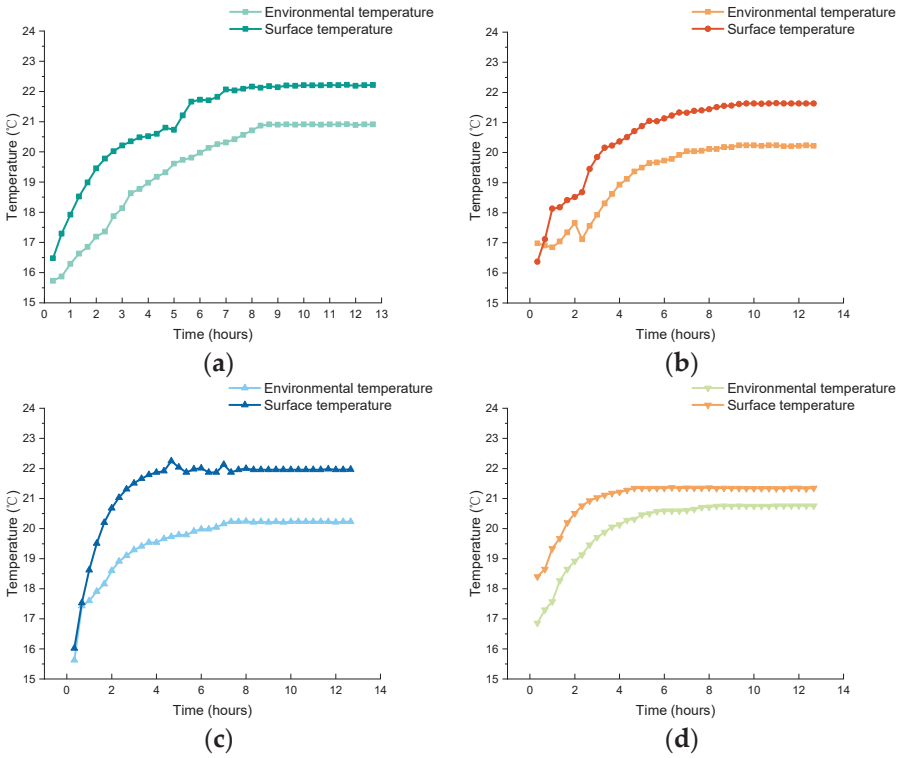

Figure 11. Time-dependent changes in environmental and surface temperatures at cold side for specimens (**a**) OX, (**b**) CX, (**c**) OE, and (**d**) CE.

4. Conclusions

This study investigated the potential for modular wall design in traditional wooden dwellings in Qiandongnan. By evaluating SIPs made with Chinese fir, OSB, XPS, and EPS materials, the feasibility of using Chinese fir as a facing material for SIPs was assessed. The key findings are as follows:

(1) Field investigation reveals that traditional timber dwellings in Qiandongnan rely on the Chinese measurement system, using units of Chi and Cun, and emphasize the "Ya Bai" (压白) concept, with dimensions typically ending in 6 or 8. Consequently, modular wall components were designed using a 3 m module for overall dimensions and a 1/20 m module for structural details, ensuring compatibility with traditional architectural frameworks while meeting modern factory production standards.

(2) Thermal performance analysis showed that all specimens met the required standards, with XPS-core specimens having a lower heat transfer coefficient than EPS-core specimens. The analysis of heat flux revealed that XPS responded more slowly to temperature changes and exhibited smaller fluctuations. However, once steady-state conditions were reached, the differences between the two were minimal.

(3) Thermal stability analysis indicated that the CX specimen, which had the longest time lag, displayed the best thermal stability, suggesting superior resistance to temperature fluctuations. Using locally sourced Chinese fir as a facing material for SIPs not only meets contemporary thermal performance standards, but also supports environmental sustainability and cultural preservation in the region. The use of SIPs fabricated from Chinese fir and EPS is anticipated to better meet the modern living needs of residents, potentially slowing the replacement of traditional timber buildings with concrete structures. This approach not only enhances living comfort,

but also supports the preservation of Qiandongnan's unique architectural heritage and landscape.

Author Contributions: Conceptualization, Z.Q.; methodology, S.D. and J.L.; software, P.M.; validation, S.D., Q.C. and P.M.; formal analysis, S.D. and P.M.; investigation, Q.C., S.D. and P.M.; resources, J.L., Z.Q., F.W. and X.C.; data curation, Q.C.; writing—original draft preparation, S.D.; writing—review and editing, P.M.; visualization, S.D. and P.M.; supervision, Z.Q; project administration, J.L. All authors have read and agreed to the published version of the manuscript.

Funding: This research was funded by the Fujian Provincial Department of Housing and Urban-Rural Development Science and Technology Plan Project, grant number 2023-K-14.

Data Availability Statement: Some or all of the data, models, or code that support the findings of this study are available from the corresponding author upon reasonable request.

Conflicts of Interest: Author Jingkang Lin was employed by the company Fujian Provincial Institute of Architectural Design and Research Co., Ltd. The remaining authors declare that the research was conducted in the absence of any commercial or financial relationships that could be construed as a potential conflict of interest.

References

1. Mao, L.; Zhang, X.; Ma, J.; Jia, Y. Cultural relationship between rural soundscape and space in Hmong villages in Guizhou. *Heliyon* **2022**, *8*, e11641. [CrossRef]
2. Xue, L.; Pan, X.; Wang, X.; Zhou, H. Stilt Houses on Top of Leigong Mountain, Ancient Miao Villages in Southeastern Guizhou Province. In *Traditional Chinese Villages*; Springer: Singapore, 2021. [CrossRef]
3. Gong, L.; Yang, J.; Wu, C.; Zhou, H. Fractal Characteristics of the Spatial Texture in Traditional Miao Villages in Qiandongnan, Guizhou, China. *Sustainability* **2023**, *15*, 13218. [CrossRef]
4. Bottino-Leone, D.; Exner, D.E.; Adami, J.; Troi, A.; Balest, J. An Energy Self-Sufficient Alpine Hut: The Refurbishment of an Ex-Tobacco Farm Using Building Integrated Photovoltaics. *Buildings* **2024**, *14*, 518. [CrossRef]
5. Wei, D.; Yani, Y.; Yu, D. Village morphology and the construction of place identity in the Aihui area along the Heilongjiang River, China. *River Res. Appl.* **2022**, *39*, 1328–1341. [CrossRef]
6. Yi, Z.; Qu, H.; Guo, L. Protection and Design of Miao Traditional Village in Qiandongnan Region in China During Rapid Urbanization. In Proceedings of the 2024 5th International Conference on Urban Construction and Management Engineering (ICUCME 2024), Xi'an, China, 19–21 July 2024.
7. Rao, X.; Qi, F.; Zhang, X.; Mao, Z. Evaluation Method on Energy-Efficient Retrofitting of Wooden Walls of Chinese Traditional Dwelling—A Case Study of Rendetang in Jinhua. *Buildings* **2022**, *12*, 1017. [CrossRef]
8. Gonzalez-Longo, C. Authenticity in architectural heritage conservation: Discourses, opinions, experiences in Europe, South and East Asia. *Conserv. Manag. Archaeol. Sites* **2019**, *21*, 136–140. [CrossRef]
9. Huang, Y.; Zhang, C.; Xiang, H.; Xiang, X.; Liu, X.; Chen, J. Development types and design guidelines for the conservation and utilization of spatial environment in traditional villages in Southern China. *J. Asian Archit. Build. Eng.* **2023**, *23*, 1699–1716. [CrossRef]
10. Thongcharoen, N.; Khongtong, S.; Srivaro, S.; Wisadsatorn, S.; Chub-Uppakarn, T.; Chaowana, P. Development of Structural Insulated Panels Made from Wood-Composite Boards and Natural Rubber Foam. *Polymers* **2021**, *13*, 2497. [CrossRef]
11. Ryoo, J.; Nah, H.; Choi, S. Performance of structural insulation panels under eccentric axial and racking loads with varying opening ratios. *Structures* **2024**, *67*, 106969. [CrossRef]
12. *ANSI/APA PRS 610.1-2013*; Standard for Performance-Rated Structural Insulated Panels in Wall Applications. American Wood Council: Washington, DC, USA, 2013.
13. Wang, H.; Sun, J.; Duan, A.; Zhu, A.; Wu, H.; Zhang, J. Dendroclimatological Analysis of Chinese Fir Using a Long-Term Provenance Trial in Southern China. *Forests* **2022**, *13*, 1348. [CrossRef]
14. Kong, F.; Zhou, B.; An, X.; Wang, F.; Wang, S.; Ma, P.; Que, Z. Experimental investigation on mechanical properties of Chinese fir composites as cross-laminated timber. *Ind. Crop. Prod.* **2024**, *213*, 118411. [CrossRef]
15. Zhou, B.; Peng, D.; Zhao, Q.; Yangnan, S.; Yang, S.; Yang, F.; Qu, G.; Tang, W.; Ou, J.; Xiang, W.; et al. Improvements in timber production of Chinese fir (*Cunninghamia lanceolata*) per unit forest area in China via tree breeding: Status and challenges. *Dendrobiology* **2020**, *83*, 43–51. [CrossRef]
16. *GB/T 17657-2013*; Test Methods of Evaluating the Properties of Wood-Based Panels and Surface Decorated Wood-Based Panels. China Architecture & Building Press: Beijing, China, 2013.

17. *JJF 98-2024*; Calibration Specification for Thermal Conductivity Testers. Jiangsu Metrology Association: Nanjing, China, 2024.
18. *GB 50176-2016*; Code for Thermal Design of Civil Building. China Architecture & Building Press: Beijing, China, 2016.
19. *GB/T 13475-2008*; Thermal Insulation-Determination of Steady-State Thermal Transmission Properties-Calibrated and Guard Hot Box. China Architecture & Building Press: Beijing, China, 2008.
20. Xie, S.; Huang, M.; Zhan, L.; Wang, Z. *Technical Strategies for Low-Cost Adaptive Renovation of Traditional Dong Ethnic Group Residences in Southeast Guizhou*; Springer Nature: Singapore, 2025; pp. 199–222.
21. Congcong, R.; Ruchen, B.; Simiao, L. Construction of Chuandou Timber Houses in Southwest china: Technology and Community. In Proceedings of the ARCHTHEO '17/XI. International Conference on Theory and History of Architecture, Istanbul, Turkey, 3–4 November 2017.
22. Xu, G.; Han, H. *Investigation, Development and Application of Wood Structure Dwellings in Qiannan*; Springer: Singapore, 2021; pp. 1185–1193.
23. Liu, S.; Gong, L.; Zhou, L.; Liu, C. *Research on the Construction System of Traditional Wooden Dwellings of Miao Nationality in Southeast Guizhou Based on BIM Technology*; Springer: Singapore, 2024; pp. 926–936.
24. Ma, H.; Zhuang, Z.; Ye, H.; Cheng, J.; Chen, J.; Qin, B. Physical Environment of Stilted Buildings in Rural Area of Southwest China. *Procedia Eng.* **2015**, *121*, 341–348. [CrossRef]
25. Lin, L.; Gui, Y. Traditional culture of settlements associated with the natural environment: The case of Yi minority Southwest China. *J. Asian Archit. Build. Eng.* **2024**, 1–19. [CrossRef]
26. Jones, P.B.; Kong, D. The case for an oral architecture: Carpentry and communal assembly among the Dong of Southwest China. *Archit. Res. Q.* **2016**, *20*, 145–158. [CrossRef]
27. *GB/T 50002-2013*; Standard for Modular Coordination of Building. China Architecture & Building Press: Beijing, China, 2013.
28. Kawasaki, T.; Kawai, S. Thermal insulation properties of wood-based sandwich panel for use as structural insulated walls and floors. *J. Wood Sci.* **2006**, *52*, 75–83. [CrossRef]
29. Sonderegger, W.; Niemz, P. Thermal conductivity and water vapour transmission properties of wood-based materials. *Eur. J. Wood Wood Prod.* **2009**, *67*, 313–321. [CrossRef]
30. Park, H.-J.; Jo, S.-U. Moisture Absorption and Desorption Properties of Douglas Fir, Hinoki, Larch, Plywood, and WML Board® in Response to Humidity Variation. *J. Korean Wood Sci. Technol.* **2020**, *48*, 488–502. [CrossRef]
31. Jin, X.; Zhang, X.; Cao, Y.; Wang, G. Thermal performance evaluation of the wall using heat flux time lag and decrement factor. *Energy Build.* **2012**, *47*, 369–374. [CrossRef]
32. Amir, A.H. Comparison between Heat Conductivity of EPS (Expanded Polystyrene) and XPS (Extruded Polystyrene). *Int. J. Recent Res. Civ. Mech. Eng.* **2018**, *4*, 24–31.
33. *DBJ52/49-2008*; Design Standard for Energy Efficiency of Residential Buildings of Guizhou. Guizhou Provincial Department of Housing and Urban-Rural Development: Guiyang, China, 2008.
34. *JGJ 134-2010*; Design Standard for Energy Efficiency of Residential Buildings in Hot Summer and Cold Winter Zone. China Architecture & Building Press: Beijing, China, 2010.
35. Ghandouri, I.E.; Maakoul, A.E.; Saadeddine, S.; Meziane, M. Thermal performance of a corrugated heat dissipation fin design: A natural convection numerical analysis. *Int. J. Heat Mass Transfer* **2021**, *180*, 121763. [CrossRef]
36. Kočí, V.; Vejmelková, E.; Čáchová, M.; Koňáková, D.; Keppert, M.; Maděra, J.; Černý, R. Effect of Moisture Content on Thermal Properties of Porous Building Materials. *Int. J. Thermophys.* **2016**, *38*, 28. [CrossRef]
37. Toure, P.M.; Dieye, Y.; Gueye, P.M.; Sambou, V.; Bodian, S.; Tiguampo, S. Experimental determination of time lag and decrement factor. *Case Stud. Constr. Mater.* **2019**, *11*, e00298. [CrossRef]

buildings

MDPI

Article

An Analytical Model for Predicting the Axial Stress Distribution of Self-Tapping Screws Due to Axial Load and Moisture Swelling of Mass Timber Products

Mehsam Tanzim Khan [1,*], Sara Keypoursangsari [2], Chun Ni [3], Ying Hei Chui [4] and Zengtao Chen [2]

[1] Department of Civil and Environmental Engineering, Northwestern University, Evanston, IL 60208, USA
[2] Department of Mechanical Engineering, University of Alberta, Edmonton, AB T6G 2E1, Canada; keypours@ualberta.ca (S.K.)
[3] Building Systems, FPInnovations, Vancouver, BC V6T 1Z4, Canada
[4] Department of Civil and Environmental Engineering, University of Alberta, Edmonton, AB T6G 2E1, Canada
* Correspondence: mehsam@u.northwestern.edu

Abstract: Self-tapping screws are becoming increasingly popular for use in modern timber structures. The axial stress distribution of self-tapping screws due to a mechanical load has been previously studied. However, the stress distribution of self-tapping screws due to moisture swelling-induced load from wood has not been explored so far. This research presents an analytical model to predict the axial stress distribution in self-tapping screws embedded in mass timber products under the combined effects of axial mechanical loading and wood moisture-induced swelling. The analytical model has been validated with numerical simulation. The input properties of the analytical model can be determined from withdrawal tests of self-tapping screws and the manufacturer's guide of screw and mass timber products. A simple program has been developed to predict the stress distribution and maximum axial stress in self-tapping screws for a range of effective penetration lengths under a pre-load and moisture content change. Correctly predicting the maximum axial stress in self-tapping screws under the simultaneous action of a pre-load and wood moisture swelling-induced load can help design safer timber structures. This research provides a practical method for practicing engineers to predict the maximum axial stress in self-tapping screws due to pre-load and wood moisture swelling.

Keywords: mass timber products; moisture swelling; self-tapping screw; CLT; glulam

1. Introduction

Mass timber construction has gained significant traction in North America as a structural component in constructing tall, complex structures [1]. Self-tapping screws (STSs) are commonly used in mass timber construction for their ease of installation, high connection stiffness, and availability in a wide range of lengths and diameters [2]. Mass timber products such as glulam and cross-laminated timber (CLT) undergo hygroscopic deformation as the wood absorbs or desorbs moisture due to changes in the surrounding moisture conditions. For example, numerical simulations of moisture movement in post-tensioned CLT panels suggest that increasing the relative humidity from 50% to 70% results in an axial strain of around 2% [3]. Moisture swelling of the wood might adversely affect the axial performance of STSs by inducing additional tensile stress before the structural loads come into action. On the other hand, moisture shrinkage of wood does not cause additional tensile stress, as the moisture shrinkage has an overall effect of tensile stress relaxation on STSs.

During construction, exceeding the manufacturer-recommended installation torque for STSs can induce additional axial stress in the screws, similar to post-tensioning in pre-stressed concrete. This stress, combined with moisture-induced swelling of the surrounding wood, may lead to premature tensile failure if it exceeds the screw's tensile strength, even before full structural loads are applied. Such failure can occur when over-torquing during installation is followed by fluctuations in the wood's moisture content over its service life.

The axial stress distribution in dowels [4] and threaded rods installed in predrilled holes [5,6] under only mechanical axial load has been previously studied. The mechanical load might stem from any external source, such as structural loads or over-torquing of the screw. Understanding and quantifying the axial stress distribution in an STS under the simultaneous action of an axial load and moisture swelling of wood is critical to addressing some critical conditions, such as the potential problem of premature tensile failure of STSs installed in an over-torqued condition under increasing moisture conditions. The axial stress distribution of STSs under the simultaneous action of a pre-load and moisture swelling of glulam and CLT was numerically modeled in previous research using the finite element method by the authors of this study [7]. The current study continues the previous study by aiming to develop an analytical model to predict the axial stress distribution of STSs under the same combined loading condition.

The overall stress distribution of the analytical model proposed in this study results from the superposition of the stress distribution from two separate mechanisms: mechanical load (called Mechanism 1 here) and moisture swelling of the wood of mass timber (called Mechanism 2). The analytical model can predict the stress distribution along the longitudinal axis of STSs under the simultaneous action of mechanical load and glulam or CLT moisture swelling. From this stress distribution, the maximum axial stress in a self-tapping screw under a given moisture content changes and the axial load from an external source can be predicted. For simplicity, the proposed analytical model assumes no moisture content gradient in the glulam or CLT.

2. Theoretical Basis of the Analytical Model

The analytical model is inspired by the works presented in [4,6,8], which are based on applying the classical Volkerson theory [9] to axially loaded fasteners. In the analytical model, under the action of an axial load on the screw, it is assumed that pure axial stress arises in the screw and the wood surrounding the screw in the x-direction (Figure 1). Force transfer between the screw and the wood occurs through a shear layer situated at the interface between the wood [4,6,8] and the outer threaded part of the screw [4]. The shear layer is assumed to be in a state of pure shear, while the screw and the wood surrounding the screw are considered to be under pure axial stress. Considering the wood and the screw being under pure axial stress implies that they are more rigid to deformation than reality, which will result in the calculated value of the shear stress of the shear layer being higher than the actual value. Thus, this simplification gives an upper-bound solution to the stresses, and basing the design on these stresses will lead to a conservative design.

The stress–strain relationship of STSs is usually linear elastic up to the yield point, and the post-elastic region is marked by an almost horizontal yield plateau with limited strain hardening [10]. Thus, the material of STSs can be assumed to be elastic-perfectly plastic, and the yield point is taken as the failure point of the STS in the analytical model. As a result, the proposed analytical model falls under the domain of linear elastic stress analysis, which justifies the application of the linear superposition principle of stress presented in the following sections.

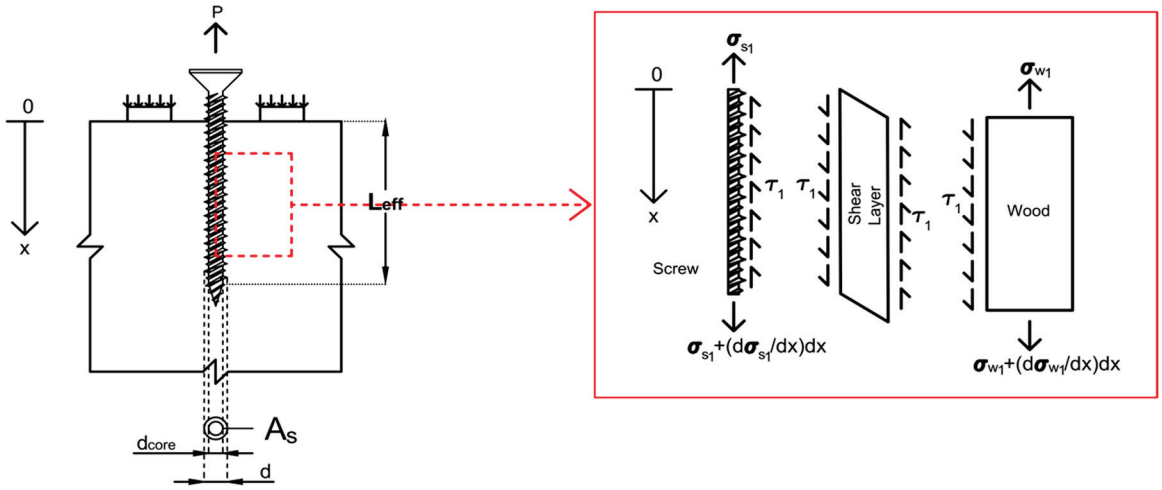

Figure 1. Wood–screw system (**left**) and wood–screw interaction zone with one axisymmetric section (**right**).

2.1. Stress Distribution Due to Mechanical Load

An axially loaded STS embedded in wood under pull–push loading conditions, similar to axially loaded threaded rods [5], is presented on the left of Figure 1. The top of the wood is held down in this loading condition while the screw is pulled in axial tension. The pull–push loading condition is similar to a two-member wood-to-steel connection with an axially loaded self-tapping screw, where the side member is assumed to be sufficiently rigid to support the top surface of the main wood member (Figure 2). Thus, if the stress distribution under the pull–push loading condition is known, the axial stress distribution of the screw in a wood-to-steel connection can be determined under the action of a mechanical load.

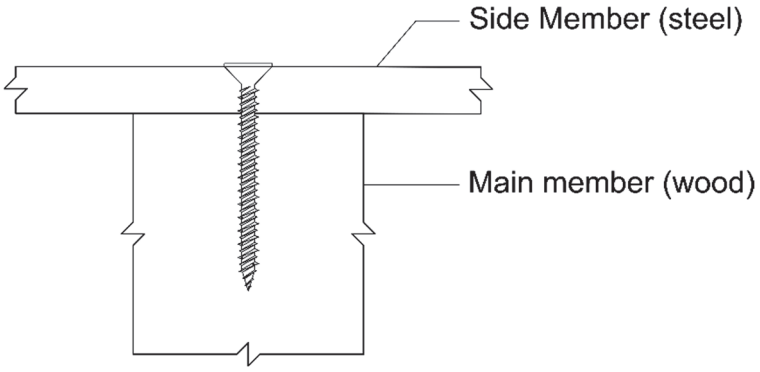

Figure 2. Two-member STS connection.

A differential section of length dx of the wood–screw interaction zone is considered on the right of Figure 1. The differential section is axisymmetric to the longitudinal axis of the screw. The origin of the coordinate system for the model is taken at the entrant side of the screw in the wood.

When the screw is pulled in axial tension from the wood member, the whole length of the screw is ineffective in imparting withdrawal resistance to the screw due to the tapering geometry of the screw at the tip. The effective penetration length, L_{eff}, (Figure 1) of the screw excludes the tip of the screw. Only the effective screw length is effective in imparting withdrawal resistance to the screw. The effective penetration length of the screw can be determined following the screw manufacturer's guide.

The shear layer displacement due to an axial load (P) is given by

$$\delta_1(x) = \delta_{s_1}(x) - \delta_{w_1}(x) \quad (1)$$

Here, $\delta_1(x)$ is the displacement of the shear layer, $\delta_{s_1}(x)$ is the displacement of the screw, and $\delta_{w_1}(x)$ is the displacement of the wood surrounding the screw.

The thickness of the shear layer is assumed to be infinitesimally small, and a linear model describing the constitutive relation of the shear layer is shown in Equation (2):

$$\tau_1(x) = \Gamma_e \delta_1(x) \tag{2}$$

Here, $\tau_1(x)$ is the shear stress, and Γ_e is the equivalent shear stiffness parameter of the shear layer. Subscript "e" in the equivalent shear stiffness parameter signifies that the linear elastic domain of the model is considered.

The static equilibrium conditions lead to the following differential equations for the screw and the wood, respectively:

$$\frac{\mathrm{d}\sigma_{s_1}(x)}{dx} = \frac{\pi d_{core}\tau_1(x)}{\frac{\pi {d_{core}}^2}{4}} = \frac{4}{d_{core}}\tau_1(x) \tag{3}$$

$$\frac{\mathrm{d}\sigma_{w_1}(x)}{dx} = -\frac{\pi d_{core}}{A_{w,eff}}\tau_1(x) \tag{4}$$

Here, $\sigma_{s_1}(x)$ is the stress in the screw, $\sigma_{w_1}(x)$ is the stress in the wood, d_{core} is the inner core diameter of the screw (excluding screw thread), and $A_{w,eff}$ is the effective area of wood under pure axial stress. The effective area of wood is given by [6], assuming a 3:1 stress dispersion from the support at the top surface of the wood.

$$A_{w,eff} = 2b\left\{s_s + min\left(e, \frac{L_{eff}}{6}\right) + min\left(\frac{s}{2}, \frac{L_{eff}}{6}\right)\right\} \tag{5}$$

Here, b is the width of the wood member, s_s is the length of the support at the top surface of the wood member, e is the edge distance from the end of the support, and s is the internal distance between the supports (Figure 3). For a wood-to-steel or wood-to-wood connection, as shown in Figure 2, $A_{w,eff}$ is the area of the whole top surface of the main wood member.

Successive differentiation of Equation (1) leads to the following equations:

$$\frac{d\delta_1(x)}{dx} = \frac{d\delta_{s_1}(x)}{dx} - \frac{d\delta_{w_1}(x)}{dx} = \varepsilon_{s_1}(x) - \varepsilon_{w_1}(x) \tag{6}$$

$$\frac{d^2\delta_1(x)}{dx^2} = \frac{d\varepsilon_{s_1}(x)}{dx} - \frac{d\varepsilon_{w_1}(x)}{dx} \tag{7}$$

Here, $\varepsilon_{s_1}(x)$ and $\varepsilon_{w_1}(x)$ are the respective strains in the screw and wood, which are related to the stresses by the one-dimension Hooke's law:

$$\varepsilon_{s_1}(x) = \frac{\sigma_{s_1}(x)}{E_s} \tag{8}$$

$$\varepsilon_{w_1}(x) = \frac{\sigma_{w_1}(x)}{E_w} \tag{9}$$

where E_s and E_w are the Young's modulii of the screw and the wood in the x-direction, respectively. By proper substitutions and manipulations of Equations (1)–(9), the following governing differential equation can be derived:

$$\frac{d^2\delta_1(x)}{dx^2} - \left(\frac{\omega}{L_{eff}}\right)^2\delta_1(x) = 0 \tag{10}$$

where the parameters ω is defined as [6]

$$\omega = \sqrt{\pi d_{core}\Gamma_e\beta {L_{eff}}^2} \tag{11}$$

in which

$$\beta = \frac{1}{A_s E_s} + \frac{1}{A_{w,eff} E_w} \tag{12}$$

where $A_s = \left(\frac{\pi}{4} \times {d_{core}}^2\right)$ is the inner core area of the screw.

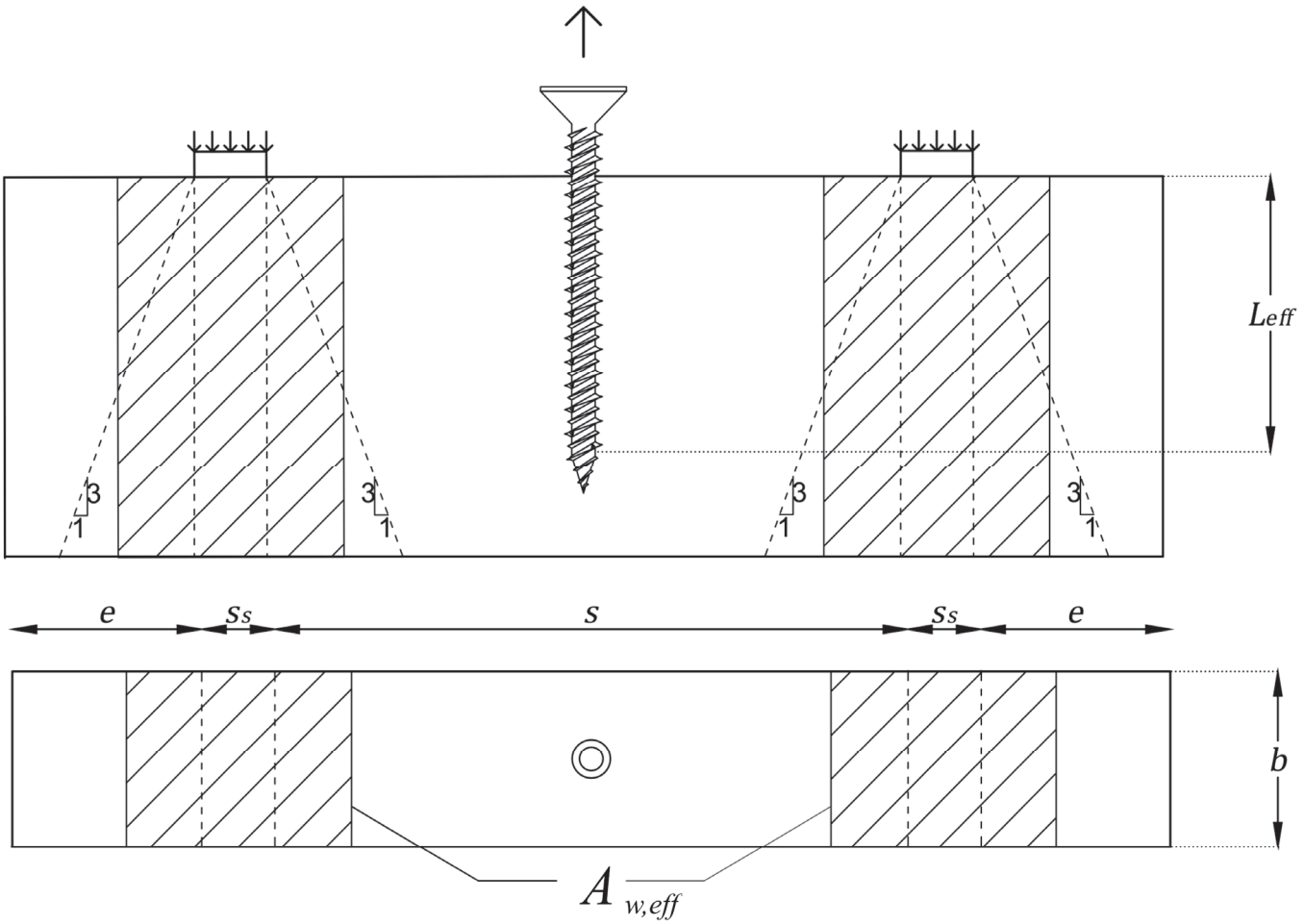

Figure 3. Determination of $A_{w,eff}$ (**top**) side view and (**bottom**) plan view.

Now, the general solution of Equation (10) is given by

$$\delta_1(x) = c_1 e^{\frac{\omega x}{L_{eff}}} + c_2 e^{-\frac{\omega x}{L_{eff}}} \tag{13}$$

Differentiation of Equation (13) and substitution from Equation (6) leads to

$$\frac{d\delta_1(x)}{dx} = \frac{\omega}{L_{eff}}\left(c_1 e^{\frac{\omega x}{L_{eff}}} - c_2 e^{-\frac{\omega x}{L_{eff}}}\right) = \varepsilon_{s_1}(x) - \varepsilon_{w_1}(x) \tag{14}$$

where c_1 and c_2 are constants in Equation (14), which can be determined by the proper boundary conditions.

According to Figure 4, boundary conditions for the pull–push loading configuration can be written as

$$\text{At x} = 0, \varepsilon_{s_1}(0) = \frac{P}{E_s A_s}\ (\text{Tension}), \varepsilon_{w_1}(0) = -\frac{P}{E_w A_{w,eff}}\ (\text{Compression}) \tag{15}$$

$$\text{At x} = L_{eff}, \varepsilon_{s_1}\left(L_{eff}\right) = 0, \varepsilon_{w_1}\left(L_{eff}\right) = 0 \tag{16}$$

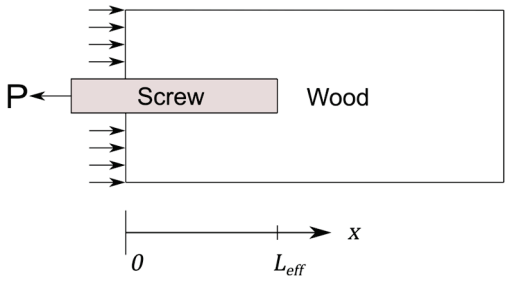

Figure 4. Pull–push boundary conditions.

Using boundary conditions (15) and (16) in Equation (14), the values of the constants c_1 and c_2 are determined as

$$c_1 = \frac{P\beta L_{eff} e^{-\omega}}{\omega(e^{-\omega} - e^{\omega})}, c_2 = \frac{P\beta L_{eff} e^{\omega}}{\omega(e^{-\omega} - e^{\omega})} \tag{17}$$

Substituting Equation (17) into Equation (13) gives the displacement function of the shear layer, $\delta_1(x)$:

$$\delta_1(x) = \frac{-P}{\pi d_{core} L_{eff} \Gamma_e} \frac{\omega}{\sinh\omega} \cosh\left(\omega\left(1 - \frac{x}{L_{eff}}\right)\right) \tag{18}$$

The shear stress of the shear layer, $\tau_1(x)$ is given by

$$\tau_1(x) = \Gamma_e \delta_1(x) = \frac{-P}{\pi d_{core} L_{eff}} \frac{\omega}{\sinh\omega} \cosh\left(\omega\left(1 - \frac{x}{L_{eff}}\right)\right) \tag{19}$$

The differential equation for screw stress distribution is given by Equation (3). The stress distribution in the screw at any point x is given by rearrangement and integration of Equation (3):

$$\sigma_{s_1}(x) = \int_0^x \frac{4}{d_{core}} \tau_1(x) dx = \frac{4P}{\pi {d_{core}}^2} \frac{\sinh\left(\omega\left(1 - \frac{x}{L_{eff}}\right)\right)}{\sinh\omega} \tag{20}$$

Equation (20) gives the stress distribution model inside the screw due to applying a mechanical load P on the screw under the pull–push loading condition. Subscript "1" in the equations signifies the load mechanism under only mechanical load, which is referred to as "Mechanism 1" in this study. Equation (20) is a hyperbolic monotonic function whose maximum value occurs at x = 0. The stress distribution model under a mechanical load presented in this section is based on the work of Stamatopoulos [5], who extended the model initially proposed by Jensen [4] for threaded rods.

2.2. Stress Distribution Due to Wood Swelling

The stress distribution of the STS due to a change in moisture content inside the wood of mass timber members is proposed in this section. The load and stress distribution due to moisture content change is referred to as "Mechanism 2" in this study to maintain consistency with "Mechanism 1" introduced in the previous section. As mentioned before, moisture swelling of the wood in mass timber products might adversely affect the axial performance of STSs by inducing additional axial tensile stress. On the other hand, when wood loses moisture, it shrinks and reduces the confinement around the STS. The loss of confinement leads to a relaxation of any pre-existing tensile stress in the screw, as the surrounding wood contracts away from the screw rather than pressing against it. This loss of confinement has an overall effect of tensile stress relaxation on the STS. Thus, the increased moisture content will lead to wood swelling and contribute to the STS's total axial tensile stress.

The material of the screw, steel, does not undergo any dimensional changes due to moisture content changes in the wood. Though steel expands/contracts significantly due to temperature changes, the effect of temperature change is not a focus of this research.

Wood can deform freely in unrestrained conditions due to changes in moisture content. However, an STS inserted into a wood member acts as a restraint due to the composite action between the wood material and the thread of the screw, which creates a restrained swelling condition in the wood member. The screw provides the restraint and acts throughout its effective length. In the restrained swelling state, the swelling tendency of wood will lead to additional stress distribution in the screw due to the composite action of the wood and the screw thread.

Chen and Nelson [11] conducted a study to determine the stress distribution in bonded materials induced by thermal expansion, which is analogous to the wood–screw composite system under moisture swelling. Consequently, the shear stress distribution in the shear layer along the length of the screw will be symmetric about the mid-point along the length of the screw, as was found in [11]. The coordinate system of Figure 5 will be considered for the analytical treatment of the screw stress distribution due to wood swelling. The coordinate system is based on the findings of [11], where the shear stress distribution at the junction of two dissimilar materials under thermal expansion was symmetric about the center of the joint. Two independent variables define the coordinate system, x_1 and x_2, to leverage the symmetric shear stress distribution and form simplified stress distribution expressions. The effective screw length (L_{eff}) is the total screw length inside the wood member, excluding the screw tip (L_{tip}). Each of the variables x_1 and x_2 span half of the effective screw length.

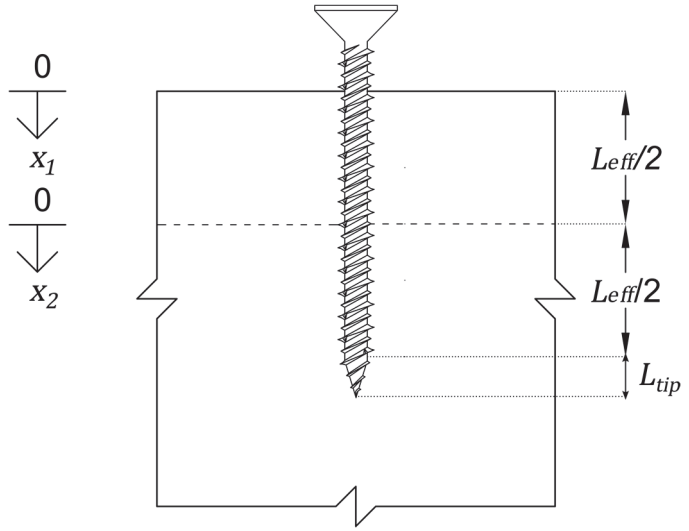

Figure 5. Coordinate system for wood swelling.

The same assumption of pure axial stress in the screw and the wood surrounding the screw in the x-direction is considered as before. The moisture content change (Δu) is considered uniform throughout the wood member and along the length of the screw. If the swelling coefficient of wood in the x-direction is α, under the uniform moisture content change, the strain of the shear layer is given by the following equation:

$$\frac{d\delta_2(x)}{dx} = \varepsilon_{s_2}(x) - \varepsilon_{w_2}(x) - \alpha\Delta u \tag{21}$$

All the symbols used in this section have similar meanings to the same symbols used in the previous section, the only difference being the subscript "2" instead of "1" to

emphasize Mechanism 2. Differentiation of Equation (21), assuming a constant value of Young's modulus along x-direction, leads to

$$\frac{d^2\delta_2(x)}{dx^2} = \frac{d\varepsilon_{s_2}(x)}{dx} - \frac{d\varepsilon_{w_2}(x)}{dx} = \frac{1}{E_s}\frac{d\sigma_{s_2}(x)}{dx} - \frac{1}{E_w}\frac{d\sigma_{w_2}(x)}{dx} \tag{22}$$

The stress–strain relationship of the shear layer and the equilibrium conditions given by Equations (2)–(4) for Mechanism 1 apply to Mechanism 2 as well and are given as

$$\tau_2(x) = \Gamma_e \delta_2(x) \tag{23}$$

$$\frac{\mathrm{d}\sigma_{s_2}(x)}{dx} = \frac{\pi d_{core}\tau_2(x)}{\frac{\pi {d_{core}}^2}{4}} = \frac{4}{d_{core}}\tau_2(x) \tag{24}$$

$$\frac{\mathrm{d}\sigma_{w_2}(x)}{dx} = -\frac{\pi d_{core}}{A_{w,eff}}\tau_2(x) \tag{25}$$

Now utilizing Equations (23)–(25), Equation (22) can be rewritten as

$$\frac{1}{\Gamma_e}\frac{d^2\tau_2(x)}{dx^2} = \left(\frac{4}{d_{core}E_s} + \frac{\pi d_{core}}{A_{w,eff2}E_w}\right)\tau_2(x) \tag{26}$$

$$\frac{d^2\tau_2(x)}{dx^2} - \left(\frac{4}{d_{core}E_s} + \frac{\pi d_{core}}{A_{w,eff2}E_w}\right)\Gamma_e\tau_2(x) = 0 \tag{27}$$

Here, $A_{w,eff2}$ is the effective area of the wood under pure axial stress due to wood swelling, which is different from the effective area of wood under pure axial stress under the pull–push loading conditions ($A_{w,eff}$) described in the previous section. The effective area $A_{w,eff2}$ represents the wood area that interacts with the screw thread during wood swelling. The additional stress induced in the screw due to moisture swelling of wood is assumed to be caused by the swelling of the wood in this effective area. This area is given by assuming the same 3:1 stress dispersion from the two ends of the screw (the screw entrant side and the screw tip), as assumed for the pull–push loading conditions in [6]. We do not know the exact stress dispersion angle yet, and in the absence of any better estimates, the 3:1 stress dispersion, similar to the previous case, is assumed. Further research will be conducted to verify the stress dispersion angle in the future. The effective area $A_{w,eff2}$ is given by Equation (28), where d is the outer nominal diameter of the STS, as shown in Figure 6.

$$A_{w,eff2} = \frac{\pi}{2}\left(\left(\frac{L_{eff}}{6} + \frac{d}{2}\right)^2 - \left(\frac{d}{2}\right)^2\right) \tag{28}$$

Equation (27) is a second-order linear differential equation that can be simplified to

$$\frac{d^2\tau_2(x)}{dx^2} - {K_s}^2\tau_2(x) = 0;\ \left[{K_s}^2 = \left(\frac{4}{d_{core}E_s} + \frac{\pi d_{core}}{A_{w,eff2}E_w}\right)\Gamma_e\right] \tag{29}$$

The highest shear stress will occur at the screw entrant side and near the end of the screw and will decrease exponentially to zero at the center of the screw inside the wood member. The general solution to Equation (29), which describes this behavior, is given by [8]

$$\tau_{1,swelling}(x_1) = c_3 e^{-K_s x_1};\ 0 \le x_1 \le \frac{L_{eff}}{2} \tag{30}$$

$$\tau_{2,swelling}(x_2) = c_4 e^{K_s(x_2 - L_{eff})};\ \frac{L_{eff}}{2} < x_2 \le L_{eff} \tag{31}$$

It was mentioned in the previous section that subscript "1" in the equations signifies the load mechanism under only mechanical load. In Equations (30) and (31) and onwards, the subscripts "1" and "2" signify the top half and bottom half of the screw, respectively. The term "swelling" is added to the subscripts to differentiate them from the mechanical

load mechanism. Hence, the shear stress in the shear layer from Equations (30) and (31) is compactly given as

$$\tau_2 = \begin{cases} \tau_{1,swelling}(x_1)\ if\ 0 \le x_1 \le \frac{L_{eff}}{2} \\ \tau_{2,swelling}(x_2)\ if\ \frac{L_{eff}}{2} < x_2 \le L_{eff} \end{cases}$$

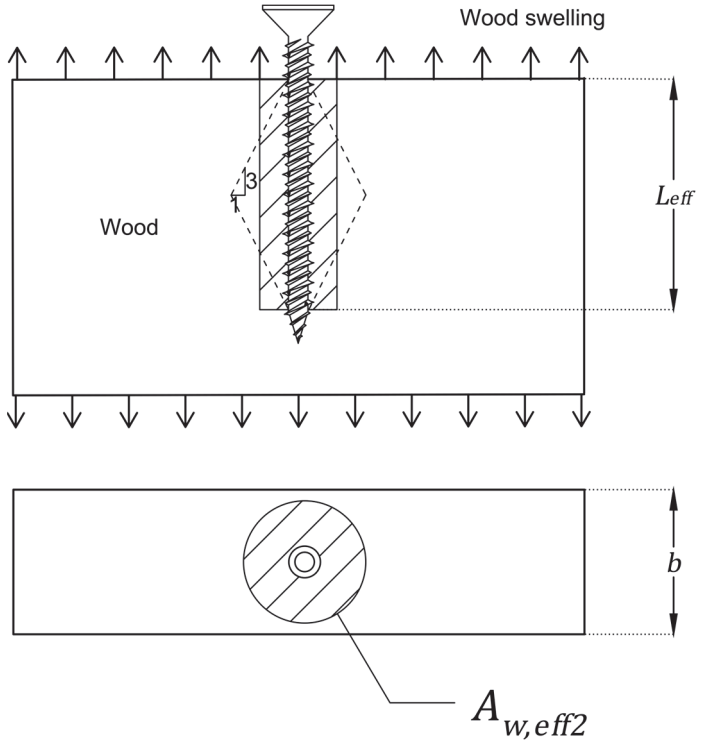

Figure 6. Determination of $A_{w,eff2}$: (**top**) side view and (**bottom**) plan view.

In Equations (30) and (31), c_3 and c_4 are constants that can be determined from the boundary conditions. Differentiation of Equations (30) and (31) leads to

$$\frac{d\tau_{1,swelling}(x_1)}{dx_1} = -K_s c_3 e^{-K_s x_1} \tag{32}$$

$$\frac{d\tau_{2,swelling}(x_2)}{dx_2} = K_s c_4 e^{K_s(x_2 - L_{eff})} \tag{33}$$

The boundary condition for the restrained wood swelling case can be written as

$$\begin{gathered} \text{At } x_1 = 0,\ \frac{d\tau_{1,swelling}(0)}{dx_1} = \Gamma_e \frac{d\delta_{1,swelling}(0)}{dx_1} \\ \Gamma_e \frac{d\delta_{1,swelling}(0)}{dx_1} = \Gamma_e(\varepsilon_{s_2} - \varepsilon_{w_2} - \alpha\Delta u) = \Gamma_e(0 - 0 - \alpha\Delta u) = -\alpha\Delta u\Gamma_e \end{gathered} \tag{34}$$

$$\begin{gathered} \text{At } x_2 = L_{eff},\ \frac{d\tau_{2,swelling}(L_{eff})}{dx_2} = \Gamma_e \frac{d\delta_{2,swelling}(L_{eff})}{dx_2} \\ \Gamma_e \frac{d\delta_{2,swelling}(L_{eff})}{dx_2} = \Gamma_e(\varepsilon_{s_2} - \varepsilon_{w_2} - \alpha\Delta u) = \Gamma_e(0 - 0 - \alpha\Delta u) = -\alpha\Delta u\Gamma_e \end{gathered} \tag{35}$$

where ε_{s_2} and ε_{w_2} are the strains in the screw and the wood, respectively, which are zero at the extremities.

Applying boundary conditions (34) and (35) in Equations (32) and (33), the values of the constants c_3 and c_4 are determined as

$$c_3 = \frac{\alpha\Delta u\Gamma_e}{K_s} \tag{36}$$

$$c_4 = -\frac{\alpha\Delta u\Gamma_e}{K_s} \tag{37}$$

Substituting Equations (36) and (37) into Equations (30) and (31) and using Equation (23), the displacement ($\delta_{1,swelling}$ and $\delta_{2,swelling}$) and shear stress distribution function of the shear layer due to wood swelling are

$$\delta_{1,swelling}(x_1) = \frac{\alpha\Delta u}{K_s} e^{-K_s x_1} \tag{38}$$

$$\tau_{1,swelling}(x_1) = \frac{\alpha\Delta u\Gamma_e}{K_s} e^{-K_s x_1} \tag{39}$$

$$\delta_{2,swelling}(x_2) = -\frac{\alpha\Delta u}{K_s} e^{K_s(x_2 - L_{eff})} \tag{40}$$

$$\tau_{2,swelling}(x_2) = -\frac{\alpha\Delta u\Gamma_e}{K_s} e^{K_s(x_2 - L_{eff})} \tag{41}$$

Now, the differential equation for screw stress distribution is given by

$$\frac{d\sigma_{s_2}(x)}{dx} = \frac{4}{d_{core}} \tau_2(x) \tag{42}$$

The stress distribution in the screw due to wood swelling is given by re-organization and integration of Equation (42):

$$\sigma_{s_{1,swelling}}(x_1) = \int \frac{4}{d_{core}} \tau_{1,swelling}(x_1) dx = -\frac{4\alpha\Delta u\Gamma_e}{d_{core}{K_s}^2} e^{-K_s x_1} + c_5 \tag{43}$$

$$\sigma_{s_{2,swelling}}(x_2) = \int \frac{4}{d_{core}} \tau_{2,swelling}(x_2) dx = -\frac{4\alpha\Delta u\Gamma_e}{d_{core}{K_s}^2} e^{K_s(x_2 - L_{eff})} + c_6 \tag{44}$$

Hence, the axial stress in the screw from Equations (43) and (44) is compactly given as

$$\sigma_{s_2} = \begin{cases} \sigma_{s_{1,swelling}}(x_1) \; if \; 0 \le x_1 \le \frac{L_{eff}}{2} \\ \sigma_{s_{2,swelling}}(x_2) \; if \; \frac{L_{eff}}{2} < x_2 \le L_{eff} \end{cases}$$

In Equations (43) and (44), c_5 and c_6 are constants of integration, which can be determined from the following boundary conditions:

$$\sigma_{s_{1,swelling}}(0) = 0 = -\frac{4\alpha\Delta u\Gamma_e}{d_{core}{K_s}^2} + c_5 = 0 \tag{45}$$

$$c_5 = \frac{4\alpha\Delta u\Gamma_e}{d_{core}{K_s}^2} \tag{46}$$

$$\sigma_{s_{2,swelling}}\left(L_{eff}\right) = -\frac{4\alpha\Delta u\Gamma_e}{d_{core}{K_s}^2} + c_6 = 0 \tag{47}$$

$$c_6 = \frac{4\alpha\Delta u\Gamma_e}{d_{core}{K_s}^2} \tag{48}$$

Thus, the stress distribution in the screw due to wood swelling (Mechanism 2) is given by

$$\sigma_{s_{1,swelling}}(x_1) = \frac{4\alpha\Delta u\Gamma_e}{d_{core}{K_s}^2}\left(1 - e^{-K_s x_1}\right);\; 0 \le x_1 \le \frac{L_{eff}}{2} \tag{49}$$

$$\sigma_{s_{2,swelling}}(x_2) = \frac{4\alpha\Delta u\Gamma_e}{d_{core}{K_s}^2}\left(1 - e^{K_s(x_2 - L_{eff})}\right);\; \frac{L_{eff}}{2} < x_2 \le L_{eff} \tag{50}$$

The stress distribution model under wood swelling presented in this section is derived based on the principles adopted from [8,11], which dealt with the stress distributions in dissimilar bonded materials caused by differential expansion and contraction.

2.3. Shear Stiffness Parameter Determination and Superposition of Stress Distribution

The unknown parameter in the analytical model is the constant Γ_e, which is required to determine the constant ω given by Equation (11). Setting $x = 0$ and ignoring the negative

sign in Equations (18) and (38) give the withdrawal displacements of the screw at the top surface of the wood. The withdrawal displacement under mechanical load is given by

$$\delta_{withdrawal_1} = \frac{P\omega}{\pi d_{core} L_{eff} \Gamma_e} \frac{\cosh\omega}{\sinh\omega} = \frac{P}{\pi d L_{eff} \Gamma_e} \frac{\omega}{\tanh\omega} \tag{51}$$

The withdrawal displacement due to wood swelling is given by

$$\delta_{withdrawal_{1,swelling}} = \frac{\alpha \Delta u}{K_s}(1) = \frac{\alpha \Delta u}{K_s} \tag{52}$$

The withdrawal stiffness K_w is given by

$$K_w = \frac{P}{\delta_{withdrawal_1} + \delta_{withdrawal_{1,swelling}}} \tag{53}$$

Here, P is the axial load acting in the screw at $x = 0$.

Now, $\delta_{withdrawal_1}$ is the withdrawal displacement due to the application of an external axial load and $\delta_{withdrawal_{1,swelling}}$ is the withdrawal displacement of the screw due to moisture swelling of the wood, which physically represents the gradual emergence of the screw from the wood member with moisture ingress. The withdrawal displacement due to an external "active" load acting directly on the screw should be higher than the withdrawal displacement due to moisture ingress, which is somewhat of a "passive" effect since it stems from the wood material. Thus, $\delta_{withdrawal_1} \gg \delta_{withdrawal_{1,swelling}}$, and ignoring $\delta_{withdrawal_{1,swelling}}$ in Equation (53), the withdrawal stiffness becomes

$$K_w = \frac{P}{\delta_{withdrawal_1}} = \pi d_{core} L_{eff} \Gamma_e \frac{\tanh\omega}{\omega} \tag{54}$$

The withdrawal stiffness K_w can be determined from a withdrawal test of the STS inserted into glulam or CLT, and Equation (54) can be solved to determine the value of Γ_e. A program was developed in MATLAB R2023b to determine the value of Γ_e.

Finally, the stress distribution in the screw is given by the superposition of the stress distribution from two mechanisms due to mechanical load and moisture swelling of the wood of mass timber. The superposition of Equations (20) (Mechanism 1), (49), and (50) (Mechanism 2) are given by the following equations:

$$\sigma_s(x) = \sigma_{s_1}(x) + \sigma_{s_{1,swelling}}(x_1) = \frac{4P}{\pi {d_{core}}^2} \frac{\sinh\left(\omega\left(1 - \frac{x}{L_{eff}}\right)\right)}{\sinh\omega} + \frac{4\alpha\Delta u \Gamma_e}{d_{core} {K_s}^2}\left(1 - e^{-K_s x_1}\right) \tag{55}$$

$$\sigma_s(x) = \sigma_{s_1}(x) + \sigma_{s_{2,swelling}}(x_2) = \frac{4P}{\pi {d_{core}}^2} \frac{\sinh\left(\omega\left(1 - \frac{x}{L_{eff}}\right)\right)}{\sinh\omega} + \frac{4\alpha\Delta u \Gamma_e}{d_{core} {K_s}^2}\left(1 - e^{K_s(x_2 - L_{eff})}\right) \tag{56}$$

where $0 \le x_1 \le \frac{L_{eff}}{2}$, $\frac{L_{eff}}{2} < x_2 \le L_{eff}$ and $0 \le x \le L_{eff}$.

Equations (55) and (56) give the stress distribution in an axially loaded STS under pull–push loading conditions due to moisture swelling of a wood member. The coordinate system for the analytical model is shown in Figure 5.

In a two-member wood-to-steel connection with an STS (Figure 2), if the screw is tightened with a torque more than that required to make the connection snug, an axial load will be induced in the screw. The side member is assumed to be sufficiently rigid to provide support at the top surface of the main wood member. Then, the axially loaded screw in the main wood member is similar to an axially loaded screw under pull–push loading conditions. In this over-torqued condition of the screw, if there is a change in moisture content in the main wood member, the total stress distribution in the screw is given by Equations (55) and (56).

3. Analytical Model Input Properties

It is essential to choose representative values of the input properties for the analytical model to model the screw stress distribution reliably. The equivalent shear stiffness parameter can be found by solving Equation (54) if the withdrawal stiffness is known from STS withdrawal tests. For this purpose, a withdrawal test program was conducted under varying moisture conditions. The specimens shown in Figure 7 were tested after exposure to the moisture content changes listed in the second and third columns of Table 1. As shown in Figure 7, screws with nominal outer diameters of 8 mm and 13 mm were centrally inserted into the broad face of CLT and glulam of various sizes. The glulam used in the tests was Douglas Fir–Larch, with a stress grade of 16c-E, while the CLT was Spruce–Pine–Fir (SPF) with a stress grade of V2 [12]. The initial moisture condition in Table 1 represents the wood moisture content at the time of self-tapping screw installation. In contrast, the final moisture content corresponds to the equilibrium moisture content after specimen conditioning. For simplicity, this study assumes a uniform moisture content throughout the CLT or glulam in both stages, disregarding the effects of moisture gradients [7].

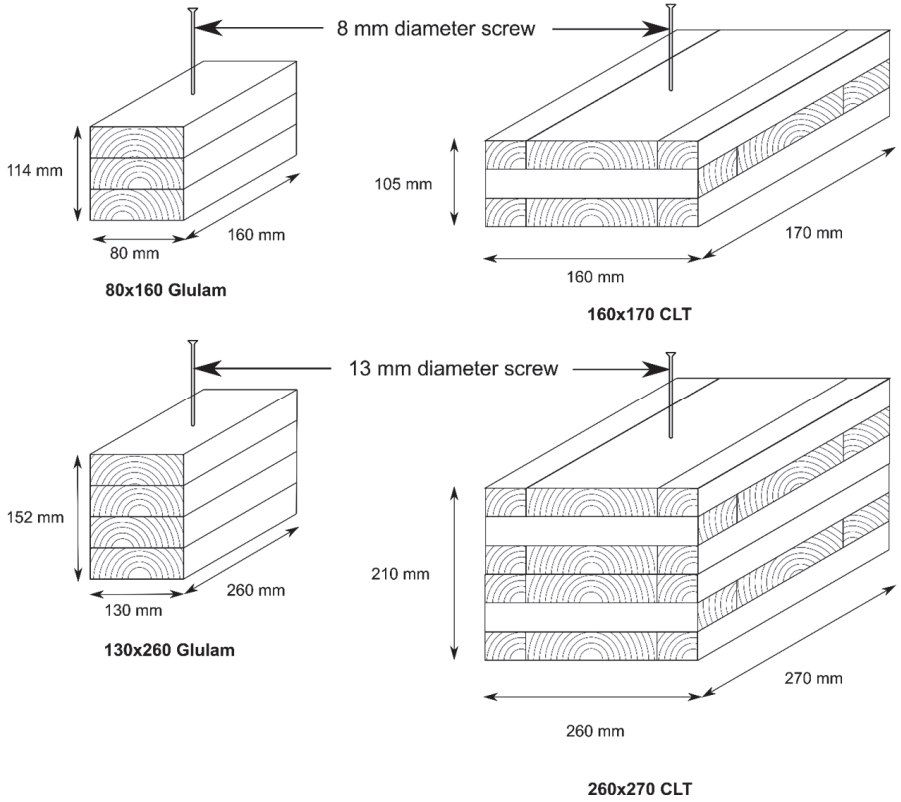

Figure 7. Withdrawal test specimens.

The specimens underwent a two-stage conditioning process to achieve the targeted moisture conditions. The first stage established the initial equilibrium moisture content (EMC) for self-tapping screw installation, while the second stage conditioned the specimens to reach the final target EMC. This approach ensured that the screw installation did not significantly disrupt the uniform moisture content within the glulam or CLT. After achieving the final target EMC, withdrawal tests were conducted on the specimens in displacement control under pull–push loading conditions. From the withdrawal tests, the withdrawal stiffness of the different specimen configurations under the different moisture conditions was determined. Details of the test program can be found in [13].

If the withdrawal stiffness values are expressed in units of force per unit length of the screw, Equation (54) can be solved by using the MATLAB program developed

by the authors to determine the equivalent shear stiffness parameter at 12%, 16%, and 21% EMC. The equivalent shear stiffness parameter (Γ_e) for the different withdrawal test specimen configurations were determined from the withdrawal stiffness (K_w) values using Equation (54) and the MATLAB program developed by the authors (shown in Table 1). Higher moisture contents are known to have a softening effect on wood [14] and are marked by lower values of the withdrawal stiffnesses, as seen in Table 1. Though the equivalent shear stiffness parameter changes with the change in the moisture content of the wood, a constant value of the shear stiffness parameter was considered in the analytical model to obtain simple forms of the analytical expressions. It is suggested that the shear stiffness parameter be taken at the initial moisture content of the wood since that gave more conservative predictions on par with the numerical analysis, as exhibited in the following section.

Table 1. Withdrawal stiffness and equivalent shear stiffness properties of different test groups.

Mass Timber Product and Self-Tapping Screw	Target Initial and Final EMC	K_w (kN/mm)	CoV (%)	Γ_e (MPa/mm)	Withdrawal Strength (MPa)
160 × 170 mm CLT, 8 mm Screw	12%	22.86	10.92	23.84	9.39
	16%	18.69	38.35	19.01	7.19
	21%	13.98	25.06	13.71	6.45
260 × 270 mm CLT, 13 mm Screw	12%	22.09	23.18	6.62	6.18
	16%	21.23	19.73	6.34	6.04
	21%	15.55	10.29	4.55	4.72
80 × 160 mm Glulam, 8 mm Screw	12%	19.41	24.67	20.21	9.31
	16%	20.32	12.52	21.64	9.13
	21%	17.41	10.82	18.03	7.71
130 × 260 mm Glulam, 13 mm Screw	12%	26.13	24.09	8.15	8.83
	16%	22.54	22.10	7.01	7.13
	21%	20.46	20.12	6.29	5.64

Young's modulus values of glulam and CLT at 12% and 21% EMC were determined from the product manufacturers' guides on the glulam and CLT and the published literature [15]. The Young's modulus values of the glulam and CLT are summarized in Table 2. Similar to the shear stiffness parameter, it is recommended to use the value of Young's modulus at the initial moisture content as the input for the analytical model, as this results in higher axial stress values in the screw. In the absence of experimental methods to validate the analytical model, we have opted for the more conservative approach, which provides higher predicted maximum stress values. The swelling coefficient values along the radial and tangential anatomic direction of the laminates of glulam and CLT were determined experimentally from swelling tests described in [13]. The average swelling coefficient values of all layers of each CLT and glulam product are given in Table 3. In verifying the analytical model with numerical analysis, Young's modulus and swelling coefficient values of glulam in the tangential direction were taken as the input values ($E_W = E_T$ and $\alpha = \alpha_T$), as the moisture swelling of wood is the highest in the tangential direction.

Table 2. Young's modulus of CLT and glulam.

Mass Timber Product	Layer Type	Wood EMC	E_R (MPa)	E_T (MPa)
160 × 170 mm CLT	Longitudinal	12%	1193.4	631.8
	Transverse		918	486
	Longitudinal	21%	918.9	486.5
	Transverse		706.9	374.2
260 × 270 mm CLT	Same property for all layers	12%	969	513
		21%	746.1	395
80 × 160 mm Glulam	Same property for all layers	12%	843.2	620
		21%	649.3	477.4
130 × 260 mm Glulam	Same property for all layers	12%	843.2	620
		21%	649.3	477.4

Table 3. Effective swelling coefficient values.

Type of Wood Product	Layer Type	$\alpha_L\left(\%^{-1}\right)$	$\alpha_R\left(\%^{-1}\right)$	$\alpha_T\left(\%^{-1}\right)$
160 × 170 mm CLT	Longitudinal	0	0.0016	0.0024
	Transverse	0.0001	0.0017	0.0028
260 × 270 mm CLT	Longitudinal	0	0.0016	0.0027
	Transverse	0.0002	0.0019	0.0029
All Glulam	-	0.0001	0.0017	0.0029

The effective area of wood under axial stress in the pull–push loading condition ($A_{w,eff}$) was calculated for the withdrawal test specimens using Equation (5), and the results are given in Table 4.

Table 4. Wood effective areas.

Wood Products and Self-Tapping Screw	$A_{w,eff}$ (mm^2)
160 × 170 mm CLT, 8 mm Screw	32,064
260 × 270 mm CLT, 13 mm Screw	60,424
80 × 160 mm Glulam, 8 mm Screw	16,032
130 × 260 mm Glulam, 13 mm Screw	30,212

The core diameter of the screws (d_{core}) and the effective penetration length (L_{eff}) were determined from the screw manufacturer's guide, according to the geometry of the withdrawal test specimens (Table 5). Young's modulus of the screws were taken from the screw tensile tests conducted by [13] and shown in Table 5. Once all the properties mentioned in Tables 1–5 are known, the flowchart in Figure 8 illustrates how the analytical model can be used to model the stress distribution and the maximum stress in the STS. The two MATLAB programs developed by the authors are identified as "gammasolver.m" and "maxstress.m" in the flowchart and can be obtained from the first author (.m is the file extension for the program script in MATLAB). The first program, "gammasolver.m" is used to solve for the equivalent shear stiffness parameter. Once the equivalent shear stiffness parameter is determined for a particular combination of screw and wood product

for the moisture content change range of interest, the value can be used to model the stress distribution of the same screw in a wood-to-wood or wood-to-steel connection in which the main member consists of the same wood product, using the second program, "maxstress.m". Further implementation of the analytical model is described in the following sections.

Table 5. Screw properties.

Screw Type	d_{core} (mm)	L_{eff} (mm)	Mean E_S (GPa)
8 mm nominal diameter screw	5	72	208.2
13 mm nominal diameter screw	9.6	120	226.6

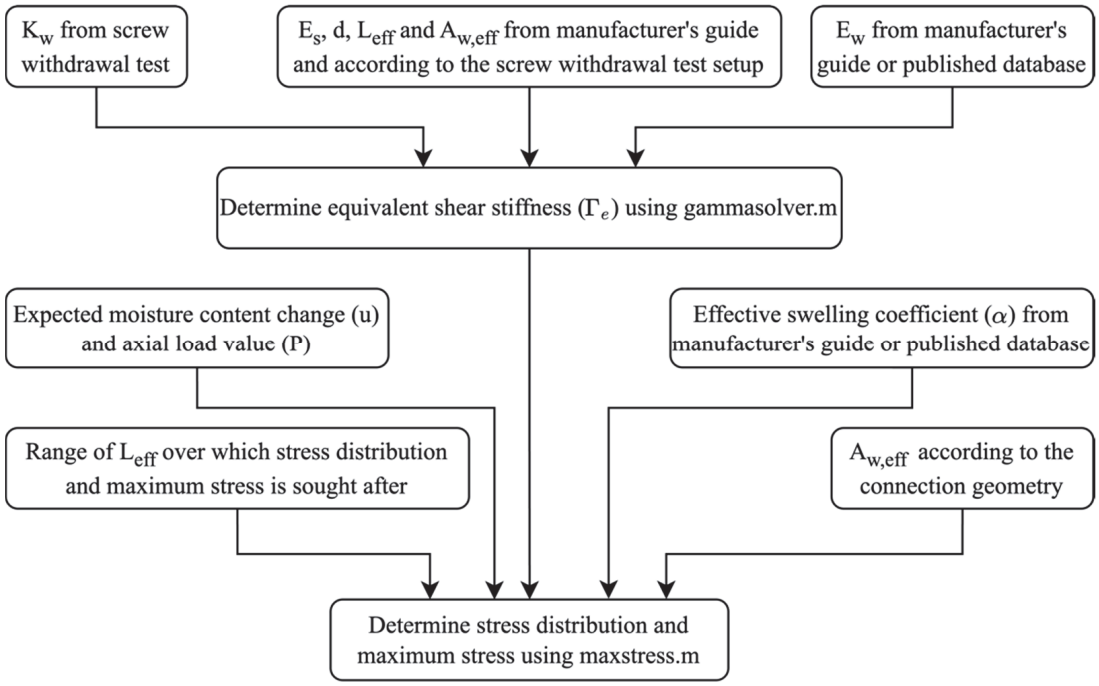

Figure 8. Flowchart describing the calculation procedure of the proposed analytical model.

4. Validation with Numerical Analysis

4.1. Finite Element Model

The proposed analytical model was validated through finite element analysis (FEA) simulations using ABAQUS/Standard Solver 2021 [16]. The theoretically predicted stress distributions in self-tapping screws were compared with FEA results for a wood-to-steel connection. The connection included a glulam timber specimen with dimensions of 80 mm × 160 mm and an 8 mm self-tapping screw with a total length of 160 mm. The screw was inserted centrally into the glulam product, perpendicular to the grain direction, with a penetration length of 10d (excluding the screw tip), as shown in Figure 9. In the wood-to-steel connection, the steel component was considered rigid. A fixed boundary condition was applied at the top of the glulam instead of explicitly modeling the steel plate to simplify the model.

Although three-dimensional (3D) finite element models can fully capture the orthotropic behavior of wood, they impose significant computational demands. A two-dimensional (2D) axisymmetric approach offers substantially reduced computational cost while maintaining solution accuracy [17]. Previous investigations have demonstrated that for axially loaded fasteners, the differences in the predicted withdrawal capacity and connection stiffness between 3D and 2D axisymmetric models are negligible [18]. Based on

these considerations and the axial symmetry of the loading configuration, a 2D axisymmetric modeling approach was implemented in the current study. The geometric configuration of the axisymmetric model is depicted in Figure 9, with the axis of symmetry coinciding with the longitudinal axis of the self-tapping screw.

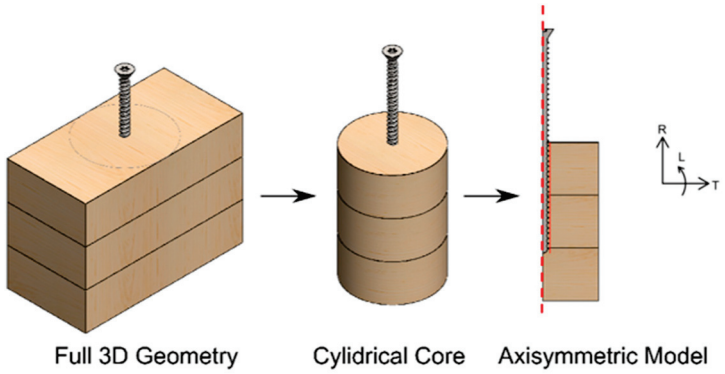

Figure 9. Axisymmetric model generation (red dotted line represents the axis of symmetry).

The self-tapping screw in a connection is typically installed as a tight fit, with the wood material filling the screw pitch and leaving no clearance between the screw thread surfaces and the wood. Under combined loading conditions—comprising external axial loads from torque and forces due to wood swelling—failure may occur in both the wood and the screw. Possible failure mechanisms in wood include the initiation and propagation of cracks at the root of the internal threads formed by the screw. These cracks may lead to the creation of a withdrawal failure surface along the screw thread path, depending on the magnitude of the moisture content (MC) change and the torque-induced load. The finite element model incorporates hard contact with a friction-type model to simulate the interaction between the screw and the wood, accounting for a tight-fit connection. A cohesive zone model was employed to capture the initiation and propagation of damage along the potential withdrawal failure path. Cohesive surfaces were defined along the screw length and around the threaded region, enabling the simulation of crack growth and development, as illustrated in Figure 10.

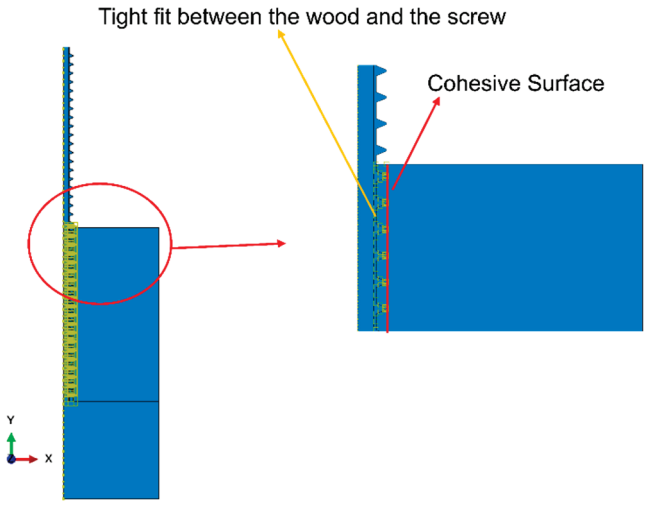

Figure 10. Contact between wood and screw and cohesive surface for crack propagation.

The finite element model is based on the foundations laid in previously established models [7,13,19]. The geometry of the connection was created using the Part and Assembly module in ABAQUS/CAE [16], with a refined meshing strategy to accurately capture stress

concentrations in the screw-threaded region. Four-node bilinear axisymmetric quadrilateral elements (CAX4R) were employed. The finite element analysis comprised approximately 10,700 elements, with the mesh density determined through a convergence study. The mesh size was gradually increased with distance from the screw–wood interface to optimize computational efficiency without compromising accuracy, as illustrated in Figure 11.

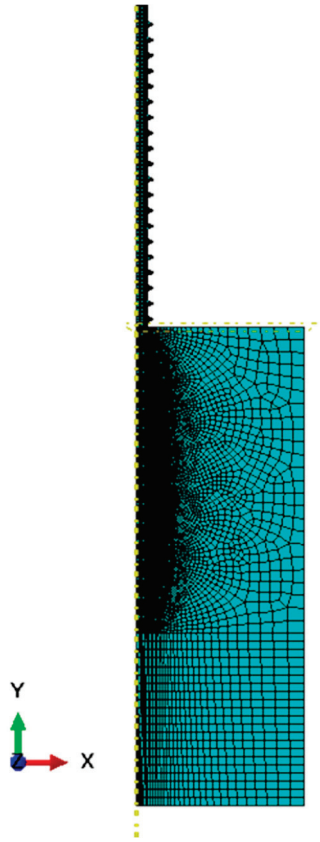

Figure 11. Mesh distribution.

4.2. Material Properties

Isotropic material properties, given in Table 6, were assigned to the STS, and the tensile strength was taken as 1100 MPa [10]. The wood of the glulam member was assigned orthotropic material properties, reflecting its varied characteristics along the local longitudinal, radial, and tangential directions. The input material properties for the glulam were determined according to the stress grade of the glulam, as shown in Table 6. Accurate stress analysis requires incorporating the moisture-dependent variations in elastic properties. Accordingly, these material properties at different moisture contents were determined from previous studies [13,15,20]. Since all layers of the glulam were of the same grade, it was modeled as a single unit without separately representing individual layers and glue lines. The results indicate this approach is appropriate for standard-sized glulams [21].

The interaction between the screw threads and the surrounding wood was defined using "Hard contact" for normal behavior and a "Penalty" approach for tangential behavior. A friction coefficient of 0.2 was used for the tangential behavior [7]. Potential cracks in the wood due to withdrawal were modeled using cohesive surfaces along the screw thread, as introduced in the previous section. The fundamentals of the constitutive behavior and the traction–separation law of the cohesive surface, called the Cohesive Zone Model [19], are provided in the following section.

Table 6. Glulam input properties for finite element analysis.

E_L (MPa)	E_T (MPa)	E_R (MPa)	v_{RL}	v_{TL}	v_{RT}	G_{RT} (MPa)	G_{LT} (MPa)	G_{LR} (MPa)	EMC (%)
12,400	620	843.2	0.036	0.029	0.39	86.8	967.2	793.6	12
11,656	558	758.88	0.036	0.029	0.39	78.99	880.15	722.18	15
11,532	551.8	750.45	0.036	0.029	0.39	78.12	870.48	714.24	16
11,160	502.2	682.99	0.036	0.029	0.39	73.78	822.12	674.56	18
10,788	477.4	649.26	0.036	0.029	0.39	69.44	773.76	634.88	21

4.3. Cohesive Surface

The Cohesive Zone Model (CZM) simulates fracture behavior in materials and their interfaces through a traction–separation law. This law characterizes the response between cohesive traction and separation across the fracture surface, capturing the progressive degradation of material properties during the fracture process [19,22].

In fracture mechanics theory, crack development in materials can follow three principal modes: Mode I (opening), Mode II (sliding), and Mode III (tearing). The CZM can handle interface failure under both pure and mixed-mode loading conditions. To define the cohesive contact interaction in ABAQUS/CAE, three essential parameters must be specified: elastic stiffness, which characterizes the initial elastic response of the interface through normal and shear stiffness components; damage initiation criteria, which determine the onset of interface degradation based on traction or separation thresholds; and damage evolution law, which governs the progressive deterioration of the interface properties after damage initiation, typically through energy-based or displacement-based approaches.

The initial linear elastic behavior of the traction–separation model, which relates the normal and shear stresses to normal and shear separation across the interface, is given by

$$\{t\} = \begin{Bmatrix} t_n \\ t_s \\ t_t \end{Bmatrix} = \begin{bmatrix} K_{nn} K_{ns} K_{nt} \\ K_{ns} K_{ss} K_{st} \\ K_{nt} K_{st} K_{tt} \end{bmatrix} \begin{Bmatrix} \delta_n \\ \delta_s \\ \delta_t \end{Bmatrix} = [K]\{\delta\} \quad (57)$$

The nominal traction stress vector t consists of t_n (normal traction) and t_s, t_t (shear tractions), with corresponding separations δ_n, δ_s, and δ_t. K is the interface stiffness matrix.

Figure 12 illustrates the cohesive constitutive law for pure mode loading conditions. The constitutive response can be expressed as

$$t = K\delta \ \delta < \delta_m^0 \quad (58)$$

$$t = (1 - D)K\delta \ \delta_m^0 \leq \ \delta < \delta_m^f \quad (59)$$

$$t = 0 \ \delta \ \geq \ \delta_m^f \quad (60)$$

where δ_m^0 is separation at the initiation of damage, and δ_m^f is the effective separation at complete failure.

A scalar damage variable, D, represents the damage at the contact point and is defined as

$$D = \frac{\delta_m^f \left(\delta_m^{max} - \delta_m^0 \right)}{\delta_m^{max} \left(\delta_m^f - \delta_m^0 \right)}; \ D \in [0, 1] \quad (61)$$

In Equation (61), δ_m^{max} refers to the maximum value of the effective separation.

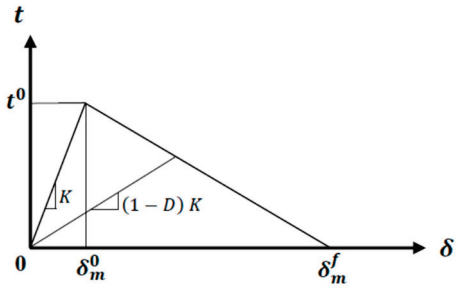

Figure 12. Linear damage evolution law for cohesive surfaces.

This study adapted material parameters for the cohesive surface model from [7]. Due to slight differences between the current model and that of [7], particularly in the modeling of the screw thread geometry, the suitability of these parameters for the current model was validated with the experimental results. Withdrawal tests were simulated with the finite element model at three distinct equilibrium moisture contents (EMC) of 12%, 16%, and 21%. The finite element results were compared with the experimental data reported by [7].

The stiffness values in the normal and the two transverse directions define the elastic regime of the bilinear traction–separation law of the cohesive layer. In this study, the focus was on axial loading conditions, making the normal stiffness perpendicular to the longitudinal axis of the screw (K_{nn}) the least significant. The two transverse stiffness values, shear stiffness (K_{ss}) and tangential stiffness (K_{tt}), are crucial since they are oriented parallel to the longitudinal axis and tangent to the cylindrical surface of the screw, respectively. The two transverse stiffness values are assumed to be equal since, for the 2D axisymmetric modeling adopted here, differentiating the stiffness values does not lead to any significant difference [18]. The shear stiffness values were then compared with experimental data from withdrawal tests, as shown in Table 7.

Table 7. Cohesive surface properties for finite element analysis.

EMC (%)	K_{nn}, K_{ss}/K_{tt} (N/mm^3)	K_{ser} from Test (N/mm^3)	K_{ser} from Finite Element Analysis (N/mm^3)	Difference in K_{ser} (%)	F_{max} from Test (kN)	F_{max} from Finite Element Analysis (kN)	Difference in F_{max} (%)
12	200, 118	19.41	19.7	1.48	16.85	17.1	1.48
16	200, 146	20.32	20.04	1.38	16.52	16.4	0.73
21	200, 57.73	17.41	17.12	1.67	13.96	14.2	1.72

Damage begins when the cohesive interaction between two interfaces starts degrading [16]. Several damage initiation criteria are available; in this simulation, it is assumed that damage initiates when a quadratic traction function involving the nominal stress (traction) ratios reaches a value of one (Equation (62)).

$$\left\{\frac{\langle t_n \rangle}{t_n^0}\right\}^2 + \left\{\frac{t_s}{t_s^0}\right\}^2 + \left\{\frac{t_t}{t_t^0}\right\}^2 = 1 \tag{62}$$

The quadratic traction damage initiation criterion requires three parameters. t_n^0 represents the maximum traction when separation occurs normally at the screw interface and t_s^0 and t_t^0 represent the maximum tractions under pure shear in the two shear directions. As the screw's axial loading makes the maximum normal traction the least critical parameter in this finite element model, it was arbitrarily set to 100 N/mm² [7]. The maximum traction in the shear directions was assigned the mean withdrawal strength value from the specimen's withdrawal test results at 12%, 16%, and 21% EMC (Table 1).

A linear energy-based softening model, excluding mode-mixing, was employed as the damage evolution model. The area under the curve in Figure 12 represents the fracture energy, also called fracture toughness. This quantity reflects the energy dissipated during the complete separation of the two initially bonded surfaces. A constant fracture energy value characterized damage evolution and ultimate failure in all three directions. The fracture energy was calculated from the area under the force–displacement curves from the withdrawal tests. The reader is referred to [7]. The details of the withdrawal tests and the determination of numerical model parameters are described here.

The suitability of the properties adopted from [7] for the threaded screw model used in this study was verified by conducting displacement control simulations and comparing the numerical results with the experimental withdrawal test results at 12%, 16%, and 21% EMC (Table 7). Two metrics were used to judge the equivalence of the numerical and experimental results: the slope of the linear fit between 10% and 40% of the maximum load in the load–displacement response (K_{ser}) and the maximum force reached (F_{max}). It can be seen from Table 7 that there was a negligible difference in K_{ser} and F_{max}, confirming the suitability of the properties adopted from [7].

4.4. Numerical Simulation Strategy and Comparison with Analytical Model

The EMC change in the glulam member was modeled using a hydro-thermal analogy in the ABAQUS Standard solver, simulating moisture content increases from 12% to 18% and 12% to 21%, as thermal stress formulations are analogous to the moisture swelling process in wood. The hydro-thermal analogy uses the mathematical similarity between Fourier's law of heat conduction and Fick's law of diffusion to simulate moisture transport in materials. In this analogy, heat flux is analogous to moisture flux, thermal conductivity is analogous to the diffusion coefficient, and temperature is analogous to moisture concentration [23,24].

Fourier's law is expressed as

$$q = -k\nabla T \tag{63}$$

which is analogous to Fick's law:

$$J = -D\nabla C \tag{64}$$

q and J are the heat and moisture fluxes, k and D are the thermal conductivity and diffusion coefficients, and T and C are the temperature and moisture concentrations, respectively.

The analogy applies to the governing equations for both transient and steady-state conditions. The equations describe how the driving variables change over time in transient conditions. For heat conduction, the transient equation is

$$\frac{\partial T}{\partial t} = \nabla(k\nabla T) \tag{65}$$

For moisture diffusion, it takes the following form:

$$\frac{\partial C}{\partial t} = \nabla(D\nabla C) \tag{66}$$

For constant density, this simplifies to

$$\frac{\partial u}{\partial t} = \nabla(D\nabla u) \tag{67}$$

Here, u is the moisture content (MC). Under steady-state conditions, and in the case of uniform moisture content or temperature changes, both Fourier's law of heat conduction and Fick's law of diffusion simplify to Laplace's equation:

$$\nabla^2 T = 0 \tag{68}$$

$$\nabla^2 u = 0 \tag{69}$$

In these conditions, the solution depends entirely on the boundary conditions applied to the system, such as fixed temperatures or moisture content.

The total strain in wood subjected to moisture content changes can be expressed as the sum of four primary components [23]:

$$\varepsilon = \varepsilon_e + \varepsilon_s + \varepsilon_{ms} + \varepsilon_c \tag{70}$$

The elastic strain (ε_e) represents the material's mechanical response and is determined through the compliance matrix, incorporating the moduli of elasticity, shear moduli, and Poisson's ratios. The shrinkage/swelling strain (ε_s) accounts for dimensional changes caused by variations in moisture content and is defined as

$$\varepsilon_s = \alpha \Delta u \tag{71}$$

Here, α is the hygro-expansion coefficient (moisture swelling coefficient), and Δu represents the change in moisture content. Mechano-sorptive creep (ε_{ms}) describes the deformation resulting from the interaction of mechanical loads and moisture changes, while creep (ε_c) accounts for deformation under sustained loads over time. Given that this study considers loading within a few days of installation of the screw, the effects of mechano-sorptive creep and normal creep were not included in the analysis due to their minimal impact.

An analogy with thermal expansion is employed to model moisture-induced strain. In thermal analysis, the strain caused by temperature changes is expressed as

$$\varepsilon_s = \beta \Delta \mathrm{T} \tag{72}$$

where β is the thermal expansion coefficient, and ΔT is the temperature change [16].

A comparison between Equations (69) and (70) highlights the analogy between the two phenomena. Both types of strain are governed by a material-dependent coefficient (β and α). They are directly proportional to temperature change (ΔT) in the case of thermal strain and moisture content change (Δu) for shrinkage/swelling strain. Therefore, the thermal-moisture analogy was used to simulate the MC change in ABAQUS. In this analogy, temperature corresponds to the wood's moisture content, while the coefficient of thermal expansion represents the swelling coefficient. The wood moisture swelling coefficient along the three orthotropic directions (Table 3) was defined in the finite element model with material orientation per the specimen's orthotropic directions.

To simulate the effect of moisture and torque on screws in steel-to-wood connections, the numerical analysis was conducted in two steps. A constant predefined temperature field was applied throughout the glulam in the initial step. In the first step, following the initial step, an axial load was introduced to simulate the torque effect. The second step involved modifying the predefined temperature field to represent moisture content variations and simulate wood swelling. Two moisture changes were analyzed, from 12% to 18% and 12% to 21%. The moisture content was assumed to be uniform inside the glulam member.

Typically, glulam members are connected to thick side members using self-tapping screws, where the thick side member can be considered rigid. A fixed boundary condition was applied to the top surface of the glulam member to represent its rigid support. The bottom surface was constrained against vertical movement in the initial analysis step. After the initial step, this boundary condition was deactivated, primarily to ensure convergence of the finite element model during the moisture swelling and shrinkage phase. The finite element model and boundary conditions are illustrated in Figure 13. A concentrated load of 5 kN was applied to simulate the axial force generated by the screw torque. This load was implemented through a reference point (RP) located at the top of the screw core, which was kinematically coupled to the screw's upper surface to ensure proper load distribution.

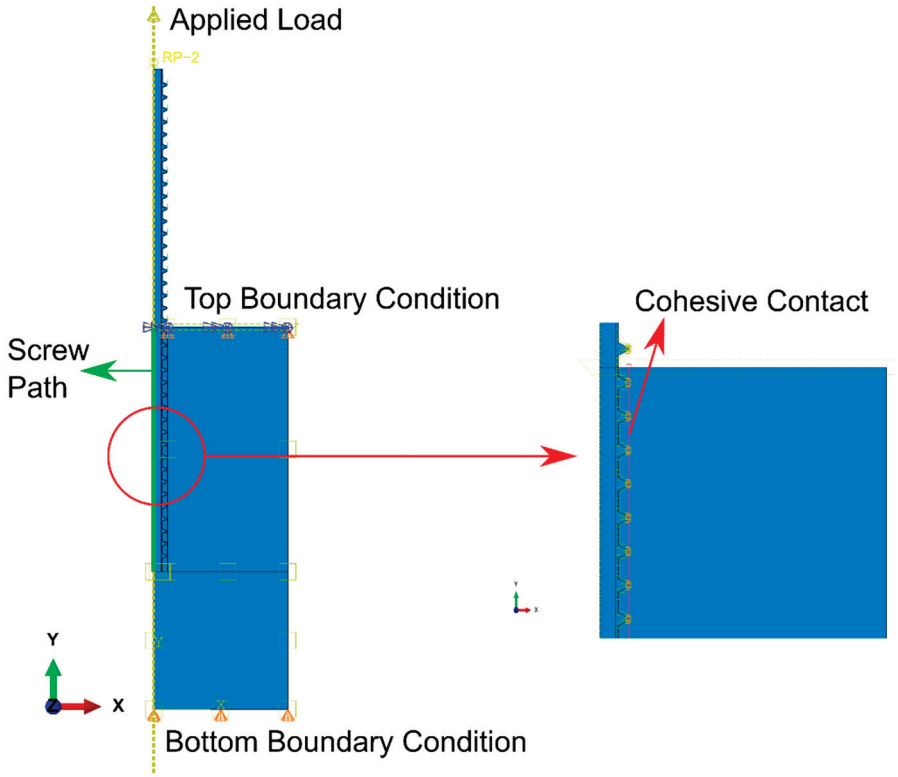

Figure 13. Finite element model along with boundary conditions (top and bottom are fixed against rotations).

In the finite element model, the vertical (y) direction, aligned with the screw's longitudinal axis, was considered as the tangential direction of the glulam. Young's modulus and swelling coefficient values of glulam in the tangential direction were taken as the input values (E_W and α) in the analytical model to maintain consistency with the numerical model. The reader is referred to [7] for further details on the finite element model.

The contour plots of the stress distribution from the numerical simulations, shown in Figure 14, illustrate the effects of different axial loads and moisture content (EMC) changes. Figure 15 compares the analytical and numerical stress distributions along the length of the screw, starting from the screw entrant side in the glulam. It is important to note that the stress distribution shown in Figure 15 follows the screw path marked in Figure 13, which represents the center of the screw. This path was defined using the ABAQUS/CAE visualization module.

The contour plots in Figure 14 reveal that higher stresses occur at the screw threads, as these areas experience stress concentrations compared to the stresses along the screw center. Both the analytical and numerical stress distributions follow similar trends. The undulations in the numerical stress distribution are attributed to the inclusion of screw

thread geometry, which creates a stress concentration that propagates across the screw length. This phenomenon cannot be captured in the analytical model.

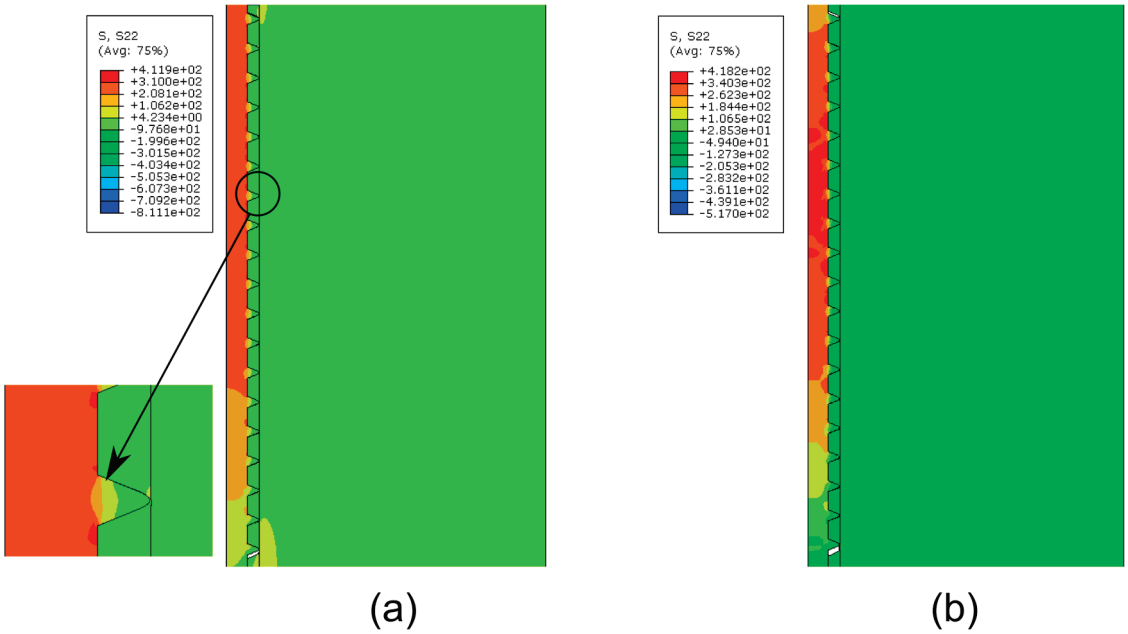

Figure 14. Contour plot of stress distribution obtained from finite element analysis under 5 kN: (**a**) 12–18% EMC; (**b**) 12–21% EMC.

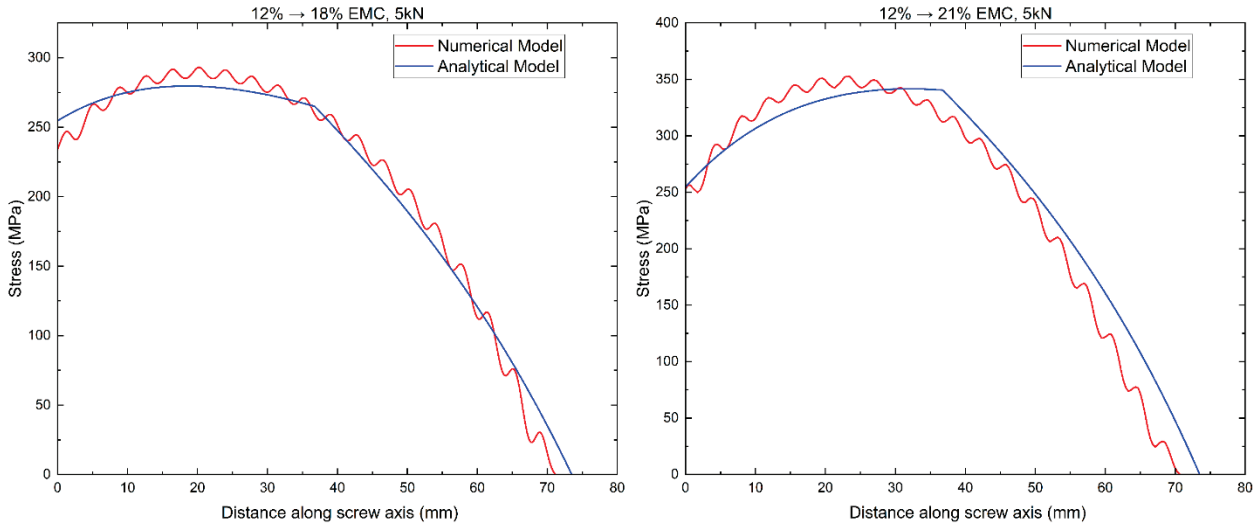

Figure 15. Numerical and analytical model stress distribution comparison under 5 kN: (**left**) 12–18% EMC; (**right**) 12–21% EMC.

The differences between the maximum stresses predicted by the numerical and analytical models were 4.6% for EMC changes from 12% to 18% and 3.1% for EMC changes from 12% to 21%. The critical conditions of the screw are the higher moisture content changes and, to that end, the difference in the predicted maximum stresses from the numerical and analytical model are minimal.

5. Analytical Model Implementation and Discussion

For the withdrawal test specimen comprising 130 × 260 mm glulam and a 13 mm screw (Figure 7), the total average stress distribution in the screw was decomposed into the stress distributions from the two separate mechanisms of mechanical loading and moisture swelling

of the wood. The total stress distribution was decomposed using Equations (20), (49) and (50) and illustrated in Figure 16. The mechanical axial load considered for the illustration of stress decomposition was 15 kN. The 15 kN load was arbitrarily chosen for illustration purposes only. The moisture content change considered for the stress decomposition in Figure 16 is 9% (for example, a change in EMC of wood from 12% to 21%). Although the screw stress distribution in Mechanism 1 is non-linear, as given by Equation (20), the non-linearity is not reflected if the effective length of the screw is relatively small. Thus, for the effective length of the screw of 120 mm, as shown in Figure 16, although the stress distribution in Mechanism 1 appears to be linear, it is not. With a larger effective penetration length of the screw, the shape of the stress distribution curve in Mechanism 1 will appear convex.

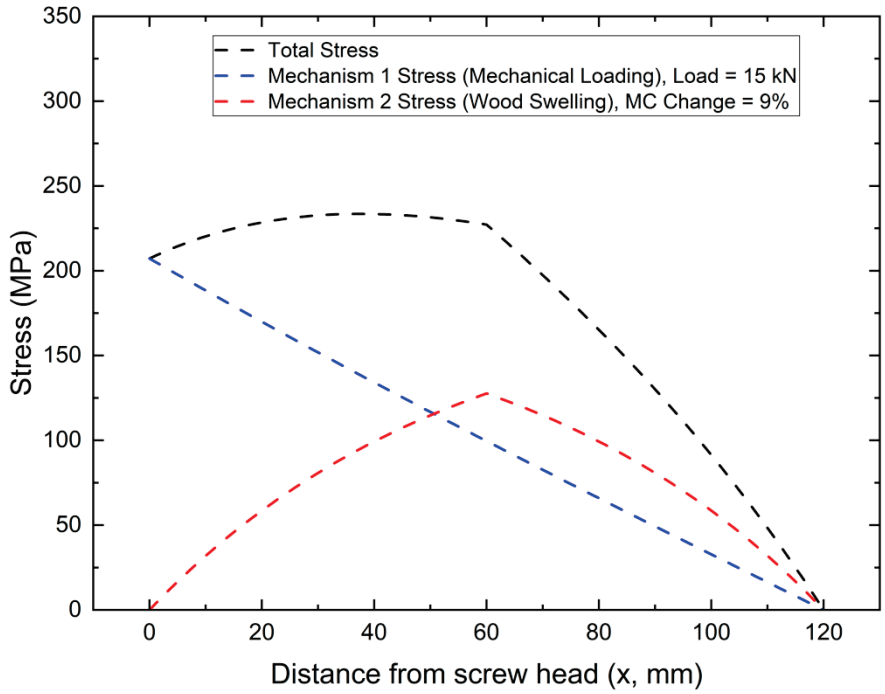

Figure 16. Total stress distribution decomposition for 130 × 260 mm glulam with a 13 mm screw.

The axial load alone induces a maximum stress of approximately 210 MPa in the screw, while moisture-induced swelling of the wood increases this value to about 250 MPa. The typical tensile strength of 13 mm self-tapping screws used in this study is about 1200 MPa [13]. Therefore, by comparing the axial stress in the screw from Figure 16 to the tensile strength, it can be inferred that moisture swelling alone is unlikely to generate axial stress values high enough to cause axial tensile failure in screws since the moisture content change considered is already greater than typical moisture content variations in wood structures in Canadian climates [12]. According to Table 12.2.1.6 of CSA O86 [12], a moisture content greater than 19% is considered a green condition, which the interior of wood structures rarely experiences. The initial moisture content in this study is 12% and a moisture content change close to 7% is generally not expected. In summary, a sufficiently high mechanical load combined with moisture-induced wood swelling can cause tensile failure in long self-tapping screws.

In two-member connections, such as the one shown in Figure 17, an axial load can develop if the screw is tightened beyond the necessary torque to secure the connection. If the side member is rigid enough to support the upper surface of the primary member, this situation becomes analogous to screw withdrawal under pull–push loading. If the primary wood member swells due to moisture while in this over-torqued state, the analytical model presented in this study can be used to predict the axial stress distribution in the

screw within the primary wood member, provided the induced axial load is known. The axial load resulting from over-torquing can be estimated by correlating it with the screw installation torque, which the second author of this study is currently investigating. Nevertheless, the mechanical axial load in the analytical model might stem from any external source, like the over-torquing of the screw or load transfer between two or more structural member connections.

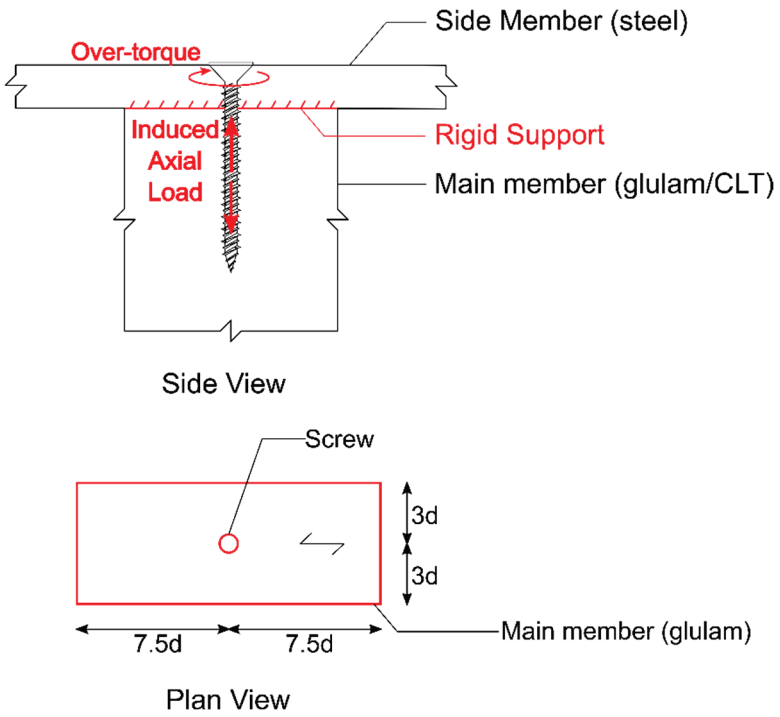

Figure 17. Model application in a two-member connection.

From the screw stress distribution provided by the analytical model, the maximum axial stress in screws with different effective penetration lengths (L_{eff}) under the combined effects of axial load and moisture swelling of the wood can be determined. This maximum axial stress corresponds to the peak point in the "Total Stress" curve shown in Figure 16. The maximum axial stresses in screws with 8 mm and 13 mm outer nominal diameters at various penetration lengths inserted into the glulam main member, as shown in Figure 17 (where d is the outer nominal diameter of the screw), were calculated. The induced nominal stresses in an STS at different penetration lengths, subjected to axial loads of 5 kN and 7 kN and three moisture content changes in the main glulam member, are plotted in Figures 18–21. These plots were generated using the method outlined in the flowchart of Figure 8. The axial load values of 5 kN and 7 kN were based on reasonable estimates from an ongoing test program conducted by the second author, which investigates the relationship between screw over-torque and the induced axial load.

In Figures 18–21, the tensile strengths of the screws [13] are shown as horizontal lines. For the 8 mm screw, a 9% change in EMC results in the maximum axial stress exceeding the tensile strength when the effective penetration length exceeds approximately 225 mm for a 5 kN axial load and 200 mm for a 7 kN load. In contrast, for the 13 mm self-tapping screw, the maximum axial stress exceeds the tensile strength at an effective penetration length of about 425 mm for a 5 kN load and 400 mm for a 7 kN load. A 9% EMC change is unlikely in timber connections unless they are exposed to outdoor conditions, and the same holds for a 6% EMC change. For a 6% EMC change, the critical screw lengths for the 8 mm screw are approximately 325 mm and 300 mm for 5 kN and 7 kN loads, respectively.

For the 13 mm screw, the critical lengths are around 600 mm and 575 mm for 5 kN and 7 kN loads, respectively.

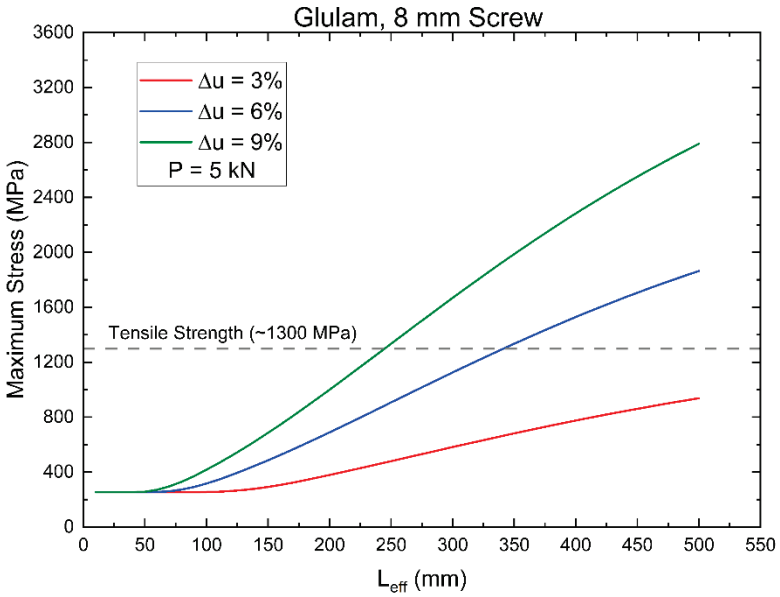

Figure 18. Maximum axial stress in 8 mm self-tapping screw at different penetration lengths and equilibrium moisture content changes (Δu) for an induced axial load of 5 kN.

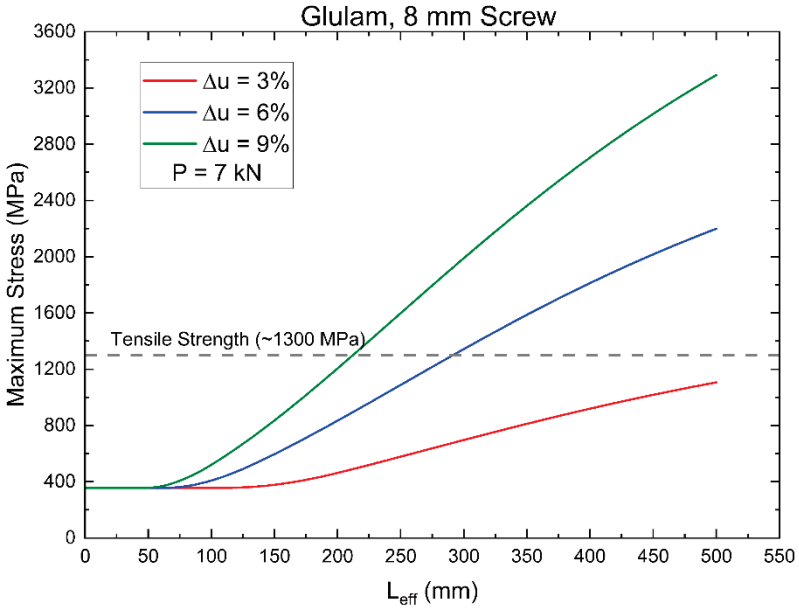

Figure 19. Maximum axial stress in 8 mm self-tapping screw at different penetration lengths and equilibrium moisture content changes (Δu) for an induced axial load of 7 kN.

The curves shown in Figures 18–21 can be interpolated for intermediate values of EMC changes. However, new plots must be made for different axial load values. Curves similar to Figures 18–21 can be produced for self-tapping screws of different nominal outer diameters (d), moisture content changes (u), axial load values (P), and effective penetration lengths (L_{eff}) from the analytical model. As shown in Figure 8, the input parameters of the analytical model are the withdrawal stiffness (K_w) from a screw withdrawal test, the screw geometry (d, d_{core} and L_{eff}), the screw's modulus of elasticity (E_s), the connection geometry ($A_{w,eff}$), the main wood member's modulus of elasticity (E_w), and the shrinkage/swelling coefficient (α) parallel to the screw axis. The two MATLAB programs developed by the first

author can generate these curves and provide an easy implementation of the analytical model, which is available on the first author's GitHub page. These curves can form the basis of design guidelines for STSs in terms of the induced axial load stemming from initial screw installation torque or any other sources and the maximum expected moisture content change in the wood member from the time of screw installation.

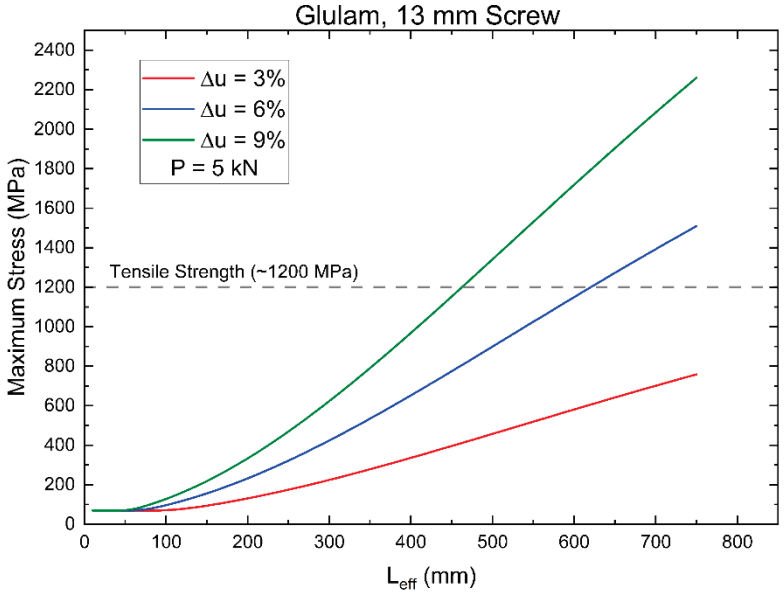

Figure 20. Maximum axial stress in 13 mm self-tapping screw at different penetration lengths and equilibrium moisture content changes (Δu) for an induced axial load of 5 kN.

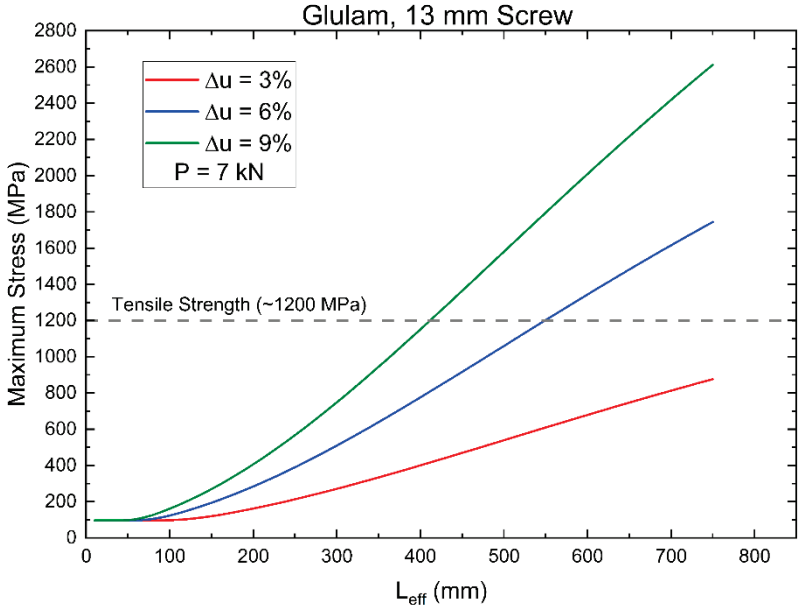

Figure 21. Maximum axial stress in 13 mm self-tapping screw at different penetration lengths and equilibrium moisture content changes (Δu) for an induced axial load of 7 kN.

6. Conclusions

This research presents an analytical model for predicting the axial stress distribution in self-tapping screws embedded in a wood member. The model accounts for externally applied axial mechanical loads and additional loads induced by wood moisture swelling. Validation was performed through numerical analysis using the finite element method. The analytical model could not be validated with experimental data, as we currently do

not have a method available to measure the stress distribution of the screw within the wood member.

This study primarily focuses on screws embedded in mass timber products such as glulam and CLT, but the proposed model can be applied to any wood member. For simplicity, the model assumes a uniform moisture content change throughout the wood member. Future research could extend this approach to incorporate non-uniform moisture variations. Additionally, the effective area of the wood in swelling, a key parameter in the analytical model, would benefit from further exploration.

Despite the limitations, this study establishes a foundation for analyzing the critical stress state in wood screws under the combined effects of axial loads and moisture swelling of the wood. The proposed model is mechanics-based and does not rely on empirical coefficients or experimental calibration. The input properties for the model can be determined from simple screw withdrawal tests. A computational tool has been developed to predict the stress distribution and maximum axial stress in self-tapping screws across various penetration lengths, given a specific axial load and a range of moisture content changes. By integrating moisture-induced axial loads into the stress analysis of axially loaded self-tapping screws, this research can contribute to safer design practices and the development of standards for the structural use of self-tapping screws in timber structures.

Author Contributions: Conceptualization: C.N. and Y.H.C.; Data curation: M.T.K. and S.K.; Formal analysis: M.T.K. and S.K.; Funding acquisition: C.N. and Y.H.C.; Investigation: M.T.K. and S.K.; Methodology: C.N. and M.T.K.; Project administration: C.N., Y.H.C. and Z.C.; Resources: C.N. and Y.H.C.; Software: M.T.K. and S.K.; Supervision: C.N., Y.H.C. and Z.C.; Validation: M.T.K. and S.K.; Visualization: M.T.K. and S.K.; Writing—original draft: M.T.K.; Writing—review and editing: S.K., Y.H.C. and Z.C. All authors have read and agreed to the published version of the manuscript.

Funding: This research received no external funding.

Data Availability Statement: All the data and MATLAB codes used in this study can be obtained from https://github.com/MehsamKhan/Analytical-model---STS.git. Accessed on 30 January 2025.

Conflicts of Interest: Author Chun Ni was employed by the company FPInnovations. The remaining authors declare that the research was conducted in the absence of any commercial or financial relationships that could be construed as a potential conflict of interest.

References

1. Svatoš-Ražnjević, H.; Orozco, L.; Menges, A. Advanced Timber Construction Industry: A Review of 350 Multi-Storey Timber Projects from 2000–2021. *Buildings* **2022**, *12*, 404. [CrossRef]
2. Dietsch, P.; Brandner, R. Self-tapping screws and threaded rods as reinforcement for structural timber elements—A state-of-the-art report. *Constr. Build. Mater.* **2015**, *97*, 78–89. [CrossRef]
3. Nguyen, T.T.; Dao, T.N.; Aaleti, S.; Hossain, K.; Fridley, K.J. Numerical Model for Creep Behavior of Axially Loaded CLT Panels. *J. Struct. Eng.* **2019**, *145*, 4018224. [CrossRef]
4. Jensen, J.L.; Koizumi, A.; Sasaki, T.; Tamura, Y.; Iijima, Y. Axially loaded glued-in hardwood dowels. *Wood Sci. Technol.* **2001**, *35*, 73–83. [CrossRef]
5. Stamatopoulos, H.; Malo, K.A. Withdrawal capacity of threaded rods embedded in timber elements. *Constr. Build. Mater.* **2015**, *94*, 387–397. [CrossRef]
6. Stamatopoulos, H.; Malo, K.A. Withdrawal stiffness of threaded rods embedded in timber elements. *Constr. Build. Mater.* **2016**, *116*, 263–272. [CrossRef]
7. Khan, M.T.; Ni, C.; Wang, J.; Chui, Y.H. Numerical Investigation of the Axial Stress Distribution of Self-Tapping Screws in Mass Timber Products during Wetting or Drying. *Buildings* **2023**, *13*, 623. [CrossRef]
8. Taylor, T.C.; Yuan, F.L. Thermal stress and fracture in shear-constrained semiconductor device structures. *IRE Trans. Electron Devices* **1962**, *9*, 303–308. [CrossRef]
9. Volkerson, O. Die Niektraftverteiling in Zugbeanspruchten mit Konstanten Laschquershritten. *Luftfahrforschung* **1938**, *48*.

10. Khan, M.T.; Ni, C. Expanding Wood Use Towards 2025. Developing Design Guidelines to Prevent Failure of Self-Tapping Screw Due to Wetting, Year 2. Vancouver, Mar. 2022. Available online: https://library.fpinnovations.ca/link/fpipub8691 (accessed on 30 January 2025).
11. Chen, W.T.; Nelson, C.W. Thermal Stress in Bonded Joints. *IBM J. Res. Dev.* **1979**, *23*, 179–188. [CrossRef]
12. Canadian Standards Association CSA O86:19 Engineering Design in Wood. 2019. Available online: https://www.csagroup.org/store/product/CSA%20O86:19/?srsltid=AfmBOor3OXCdqzyC8WTClbcB0R8Tb_-bXKWQtse3qXsW0CxHieS7n2Np (accessed on 30 January 2025).
13. Khan, M.T. Axial Performance of Self-tapping Screws in Mass Timber Products Under Moisture Content Variation. Master's Thesis, University of Alberta, Edmonton, AB, Canada, 2022.
14. Tiemann, H.D. *Effect of Moisture Upon the Strength and Stiffness of Wood*; US Department of Agriculture, Forest Service: Washington, DC, USA, 1906.
15. Gerhards, C.C. Effect of Moisture Content and Temperature on the Mechanical Properties of Wood: An Analysis of Immediate Effects. *Wood Fiber Sci.* **1982**, *14*, 4–36.
16. *Simulia ABAQUS Software Version 2021*; Dassault Systèmes: Providence, RI, USA, 2021.
17. Redondo, R.; Mehmanparast, A. Numerical analysis of stress distribution in offshore wind turbine M72 bolted connections. *Metals* **2020**, *10*, 689. [CrossRef]
18. Thelin, A.; Feldt, P. *Glued-in Rods in Timber Structures-Finite Element Analyses of Adhesive Failure*; Chalmers University of Technology: Gothenburg, Sweden, 2018.
19. Fang, L.; Qu, W.; Zhang, S. Numerical Simulation for Parallel-To-Grain Withdrawal Failure of Self-tapping Screws in Glulam. In Proceedings of the 17th East Asian-Pacific Conference on Structural Engineering and Construction, 2022: EASEC-17, Singapore, 27–30 June 2022; Springer: Berlin/Heidelberg, Germany, 2023; pp. 929–939.
20. Ross, R.J. *Wood Handbook: Wood as an Engineering Material*; Forest Products Laboratory: Madison, WI, USA, 2010. [CrossRef]
21. O'Ceallaigh, C.; Sikora, K.; McPolin, D.; Harte, A.M. An experimental and numerical study of moisture transport and moisture-induced strain in fast-grown sitka spruce. *Maderas Cienc. Y Tecnol.* **2019**, *21*, 45–64. Available online: https://revistas.ubiobio.cl/index.php/MCT/article/view/3294 (accessed on 10 November 2024). [CrossRef]
22. Nikrad, S.F.; Keypoursangsari, S.; Asadi, H.; Akbarzadeh, A.H.; Chen, Z.T. Computational study on compressive instability of composite plates with off-center delaminations. *Comput. Methods Appl. Mech. Eng.* **2016**, *310*, 429–459. [CrossRef]
23. Hassani, M.M.; Wittel, F.K.; Hering, S.; Herrmann, H.J. Rheological model for wood. *Comput. Methods Appl. Mech. Eng.* **2015**, *283*, 1032–1060. [CrossRef]
24. Afshari, Z.; Malek, S. Moisture transport in laminated wood and bamboo composites bonded with thin adhesive layers—A numerical study. *Constr. Build. Mater.* **2022**, *340*, 127597. [CrossRef]

buildings

MDPI

Article

Experimental Study on the Shear Performance of Epoxy Resin-Bolted Steel-Cross Laminated Timber (CLT) Connections

Qing Lyu [1], Jinxun Ye [1], Huake Wang [2], Jiale Xu [2], Yunfeng Xiao [1], Bo Fu [3,*], Xianlei Li [1] and Zhaoyang Zhang [1]

[1] School of Civil and Transportation Engineering, Ningbo University of Technology, Ningbo 315211, China; lvqing@nbut.edu.cn (Q.L.); 18758325639@163.com (J.Y.); yunfengxiao@nbut.edu.cn (Y.X.); lixianlei001@163.com (X.L.); 15853729511@163.com (Z.Z.)

[2] Huaxing Steel Structure Co., Ltd., Ningbo 315336, China; wanghuake@cnnhsc.com (H.W.); xujiale@cnnhsc.com (J.X.)

[3] School of Civil Engineering, Chang'an University, Xi'an 710061, China

* Correspondence: 90_bofu@chd.edu.cn

Abstract: Steel–timber composite (STC) structures offer a sustainable and low-carbon structural solution. Steel–timber interface behavior is critical for the mechanical performance of STC structures. This paper introduces a novel connection for steel–timber composites (STC) that combines mechanical interlocking with adhesive bonding through an epoxy-bonded bolted design. Epoxy resin is injected into the timber dowel slots, followed by pre-tightening of the bolts, forming a composite dowel system where the 'bolt–epoxy resin–timber' components work in synergy. The load–displacement characteristics and failure modes of nine specimen groups were investigated through a series of double-shear push-out tests. The influence of a wide range of connector parameters on the stiffness, shear bearing capacity, and ductility of STC joints was systematically investigated. The parameters included fastener strength grade, thread configuration, diameter, number, and the use of epoxy resin reinforcement. The experimental results demonstrated that high-strength partially threaded bolts were crucial for achieving a synergy of high load-bearing capacity and commendable ductility, while full-threaded bolts exhibited vulnerability to brittle shear failure, a consequence of stress concentration at the root of the threads. Although screw connections provided enhanced initial stiffness through timber anchorage, ordinary bolt connections exhibited superior ultimate load-bearing capacity. In comparison with conventional bolt connections, epoxy resin–bolt connections exhibited enhanced mechanical properties, with an augmentation in ultimate load and initial stiffness of 12% and 11.8%, respectively, without sacrificing ductility.

Keywords: cross laminated timber; steel–timber composite structure; epoxy resin connection; bolt; shear performance

1. Introduction

Compared to traditional concrete structures, which are energy-intensive and have high self-weight, wood has emerged as an ideal green prefabricated building material due to its energy-saving, environmentally friendly, lightweight, high-strength, and easy-to-process properties [1–3]. Progress in wood engineering technology has led to a significant improvement in the mechanical performance of engineered wood products. Modern engineered wood products, represented by Glue laminated timber (GLT) and Cross laminated timber (CLT), effectively overcome the limitations of natural wood, such as constraints in size, strength, and

anisotropy [4]. This progress has greatly expanded the application potential of timber structures in multi-story and large-span buildings [5,6], and has also provided a critical material foundation for achieving a green transformation in the construction industry.

To optimize the performance of its materials, the steel–timber composite (STC) structure has emerged as an efficient composite system. By combining the high strength of steel with wood's lightweight and environmentally friendly properties, this system achieves dual improvements in both structural performance and sustainability [7,8]. In STC structures, shear connections at the steel–timber interface are critical for ensuring the synergistic performance of the two materials [9,10]. The mechanical behavior of the connection joints, including strength, stiffness, and ductility, directly determines the overall performance of the composite member and the structure as a whole. Consequently, the development and performance evaluation of high-performance steel–timber shear connectors has remained a key research focus in this field. However, in most mechanical connection methods (especially bolt connections), to ensure the feasibility of on-site construction, the dimensions of the mortise slots reserved on timber components are typically 1–2 mm larger than the diameter of the connecting components. This directly compromises the initial stiffness of STC joints, leading to a significant reduction.

To provide a valuable reference for high-performance shear connections, it is instructive to draw parallels with the well-established field of steel-concrete composite structures. For performance, welded shear studs are the most prevalent and effective means of achieving composite action, renowned for their high shear strength [11,12]. Specially, due to the direct welding and mechanical interlocking, they have high initial stiffness. For design philosophy, the frontier has moved towards damage-control systems that enhance seismic resilience. As demonstrated by He et al. [13,14], this is achieved by designing specific components, such as steel angles, as replaceable "fuse elements". These fuses concentrate inelastic deformation, protecting the primary structure and enabling rapid post-earthquake repair. The pursuit of a high-performance, ductile, and slip-free connection, informed by these advanced concepts, provides a crucial reference for innovation in the STC field.

In recent years, scholars have explored various connections. Traditional mechanical fasteners like bolts and screws are widely used due to their simplicity [15–19]. However, they often fail to resolve the issue of initial slip. To address this, composite connection forms have been investigated. One prominent approach involves combining epoxy resin with fasteners. For example, extensive studies by Hassanieh et al. [20–24] demonstrated that epoxy-screw combinations achieve excellent compo-site efficiency and ductility. However, while self-tapping screws inherently provide a better initial stiffness, their shear strength and stiffness are generally inferior to those of bolts of a similar diameter. This may limit their application in structures demanding high shear resistance Another advanced solution is the perfobond rib or perforated steel plate connector, often combined with epoxy resin or grout [25,26]. These connectors exhibit exceptional stiffness and load-bearing capacity. Nevertheless, their fabrication is often complex, requiring precise manufacturing of the steel plates and meticulous on-site assembly, which can increase construction complexity and cost. Other techniques such as applying prestress [27,28] or using grouting materials [29–32], have also proven effective but come with their own complicated procedural demands. Therefore, a new connection method is urgently needed. It must not only enhance the joint's initial stiffness but also retain the structural simplicity of traditional mechanical fasteners.

Therefore, this paper proposes a novel steel–timber connection construction—epoxy resin–bolt connection. Figure 1 illustrates the construction method of this joint: first, epoxy resin is uniformly injected into the pre-drilled holes of the CLT panel, after which bolts are inserted to securely fasten the H-steel to the CLT panel. This design allows the epoxy

resin to tightly encase the bolts, forming a 'bolt–epoxy resin–timber' composite dowel system that works synergistically after curing. This construction method effectively fills the gaps between the bolts and the timber, fundamentally eliminating the initial slip of the connection. It transfers shear forces more uniformly to a larger area of the timber, thereby enhancing the connection's initial stiffness and ultimate shear bearing capacity. At the same time, this connection method retains the structural simplicity and ease of fabrication of traditional mechanical fasteners.

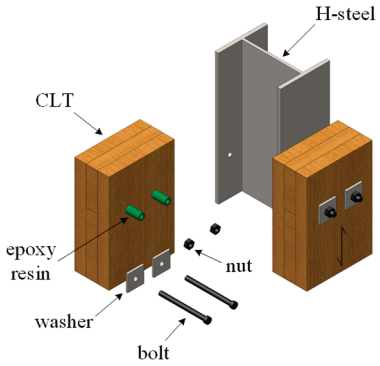

Figure 1. Epoxy resin–bolt connection schematics.

Nine groups of monotonic double-shear push-out tests were conducted to evaluate the performance of this new connector. The influence of fastener strength grade, bolt configuration, type, diameter, number, and epoxy resin reinforcement measures on the stiffness, shear bearing capacity, and ductility of the STC joints was analyzed in the tests. The results of these tests were then used to provide preliminary design suggestions for epoxy resin–bolt connections.

2. Materials and Methods

2.1. Specimen Details

The experimental program involved a total of nine groups of push-out tests, comprising six bolted and three screwed connection configurations, with each group consisting of four replicate specimens. The design and configuration of the test specimens are detailed in Figure 2. To ensure uniform force distribution during loading, each specimen consisted of a central hot-rolled H-steel beam with two CLT panels attached symmetrically to its flanges by shear connectors. The H-steel section was model HN194 × 150 × 6 × 9. It had a section height of 194 mm, a web thickness of 6 mm, and flanges that were 150 mm wide and 9 mm thick. The washer size is 50 mm × 50 mm, thickness of 3 mm. The CLT panels were fabricated from spruce-pine-fir. Each panel consisted of three 35 mm thick layers of timber lamellas, which were arranged orthogonally to one another. The primary design parameters for all specimens are summarized in Table 1, where D and L denote the connector diameter and length, respectively.

The preparation process of the test specimens primarily consisted of two stages: pre-treatment of components and overall assembly. First, holes were pre-drilled in the flanges of the H-steel. To ensure proper connection clearance, the holes were designed with a diameter 2 mm larger than that of the connecting fasteners(bolts or screws). Subsequently, holes were pre-drilled in the CLT panels, and the specific sizes of the drill holes were determined according to the connection method: (1) For bolted connection joints without an epoxy resin adhesive layer, the diameter of the dowel slots in the CLT panels was the same as the bolt diameter; (2) For bolted connection joints with an epoxy resin adhesive layer, to accommodate the epoxy resin and ensure it fully encapsulated the bolt, the dowel slots in the CLT panels were designed with a diameter 4 mm larger than that of the bolts;

(3) For test specimens with screws, the guide hole diameter and depth were set to 0.75 *D* and 0.75 *L*, respectively. Finally, the pre-treated H-steel was positioned and assembled with the CLT panels.

During the connection process, except for the screws with a diameter of 8 mm, which were tightened with a torque of 10 N·m, all other test specimens were subjected to a preload torque of 30 N·m when connecting the H-steel flange to the side of the CLT panel to ensure the initial tightening state of the connection. For bolted connection specimens containing epoxy resin adhesive layer, the assembly procedure was as follows: firstly, epoxy resin was evenly injected into the dowel slots of the CLT panel, then the bolts were inserted and the H-steel was securely fastened to the CLT panel. After curing at room temperature for 24 h, an epoxy resin–bolt composite connection was formed.

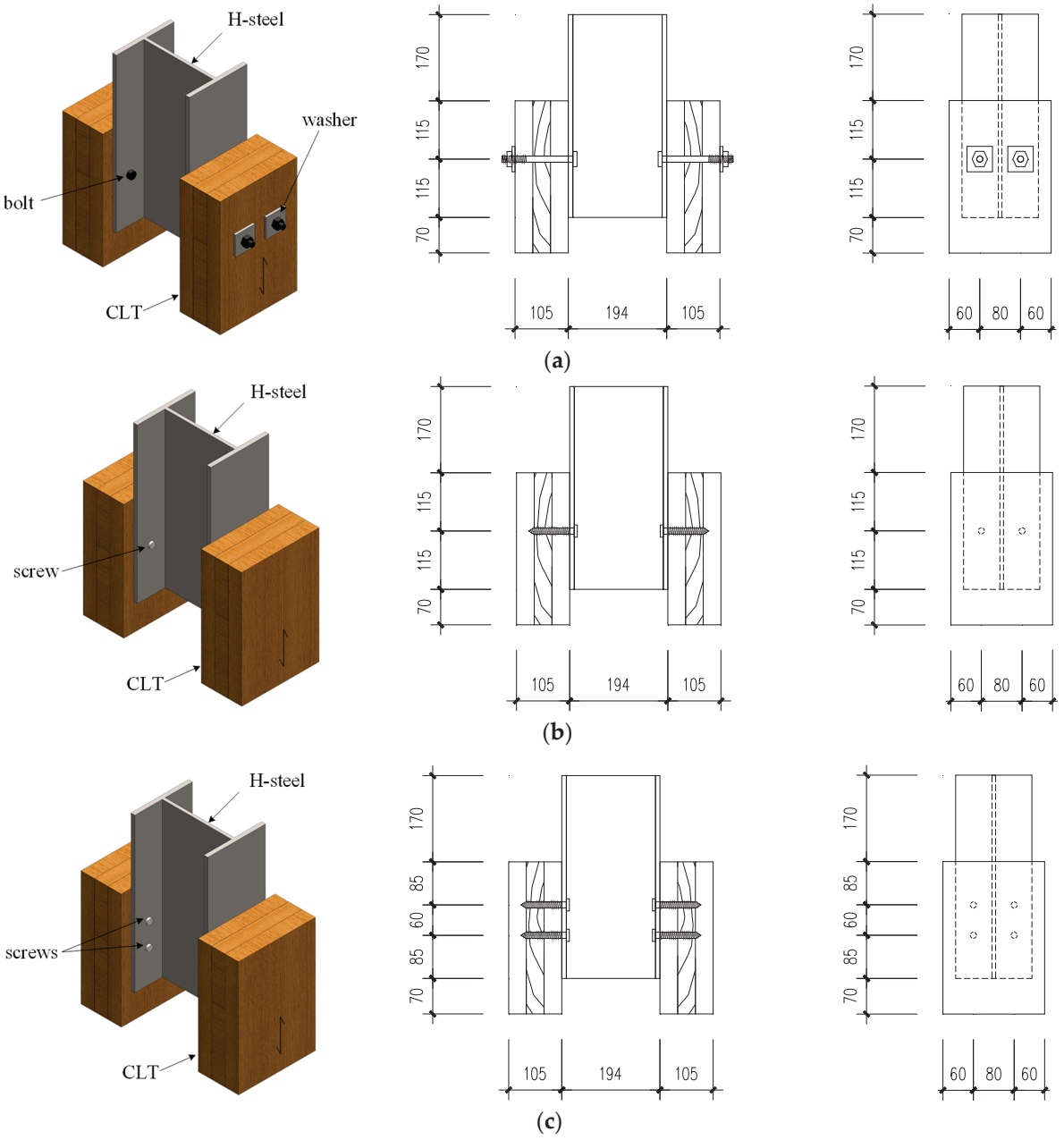

Figure 2. Diagram of push-out test specimens: (**a**) Specimen with bolts; (**b**) Specimen with a single-row of screws; (**c**) Specimen with double-row of screws.

To ensure consistency across specimens and to investigate the primary shear transfer mechanisms, a controlled preload was applied to all bolted connections. The target preload was based on a Grade 8.8 M12 bolt, with a preload (P) of $0.15 \cdot f_y \cdot A_s$ (where f_y is the yield strength and A_s is the tensile stress area), resulting in approximately 10.85 kN. Using the empirical formula $T = K \cdot d \cdot P$, with a torque coefficient (K) of 0.24 for non-lubricated bolts in steel-to-wood contact, the required torque (T) was calculated to be 31.27 N·m. Considering the scale interval of the torque wrench used in the laboratory, a practical and consistent torque of 30 N·m was applied to all bolted specimens. This consistent application ensures that the influence of preload is a controlled variable across the relevant test groups. For the self-tapping screw specimens, the applied torque was not intended to achieve a specific load-bearing preload. Instead, its primary function was to ensure the components were snugly fastened.

Table 1. Primary design parameters of the push-out specimens.

Group	Shear Connector						Epoxy Resin
	Number of Rows	Number of Columns	D (mm)	L (mm)	Type	Strength Grade	
1B-12	1	2	12	140	Partially threaded bolt	8.8	Without
1BF-12	1	2	12	140	Fully threaded bolt	8.8	Without
1B#-12	1	2	12	140	Partially threaded bolt	4.8	Without
1BE-8	1	2	8	140	Partially threaded bolt	8.8	With
1BE-12	1	2	12	140	Partially threaded bolt	8.8	With
1BE-16	1	2	16	140	Partially threaded bolt	8.8	With
1S#-8	1	2	8	80	Screw	4.8	Without
1S#-12	1	2	12	80	Screw	4.8	Without
2S#-12	2	2	12	80	Screw	4.8	Without

Note: The thickness of the epoxy resin adhesive layer is 2 mm; B represents bolted connection; S represents screw connection; E represents epoxy-reinforced connection; F represents fully threaded bolt; # represents 4.8-grade connection.

2.2. Material Properties

The test specimens in this experiment primarily consisted of three materials: CLT, metal connectors and epoxy resin. For the CLT panels, their basic mechanical properties were determined following the procedures in GB/T 50329-2012 [33] and GB/T 26899-2011 [34], with the results summarized in Table 2. The metal connectors were subjected to tensile strength tests in accordance with GB/T 228.1-2021 [35], and the corresponding results are presented in Table 3. Figure 3 illustrates the testing process for the mechanical properties of CLT panels and metal connectors. The epoxy resin used in the test was MT-500 anchor adhesive produced by Nanjing Mankate Science and Technology Co., Ltd. (Nanjing, China). The mechanical and durability properties of the MT-500 anchor adhesive are presented in Tables 4 and 5, respectively. For the steel components, hot-rolled H-sections were used, which were made of Q235B grade steel conforming to the requirements of GB 50017-2017 [36] and GB 50011-2010 [37].

Table 2. Mechanical properties of CLT.

$F_{c,\,max}$ (kN)	E_c (GPa)	f_c (MPa)	τ_c (MPa)	ρ (kg/m^3)	ω (%)	μ
362.11	8.48	28.74	1.19	464.88	11.6	0.43

Note: The values presented in the table are the averages from the tested CLT specimens. $F_{c,\,max}$ represents the peak compressive load; E_c represents the modulus of elasticity; f_c represents the compressive strength; τ_c represents the rolling shear strength; ρ represents the specimen density; ω represents the moisture content and μ represents the Poisson's ratio.

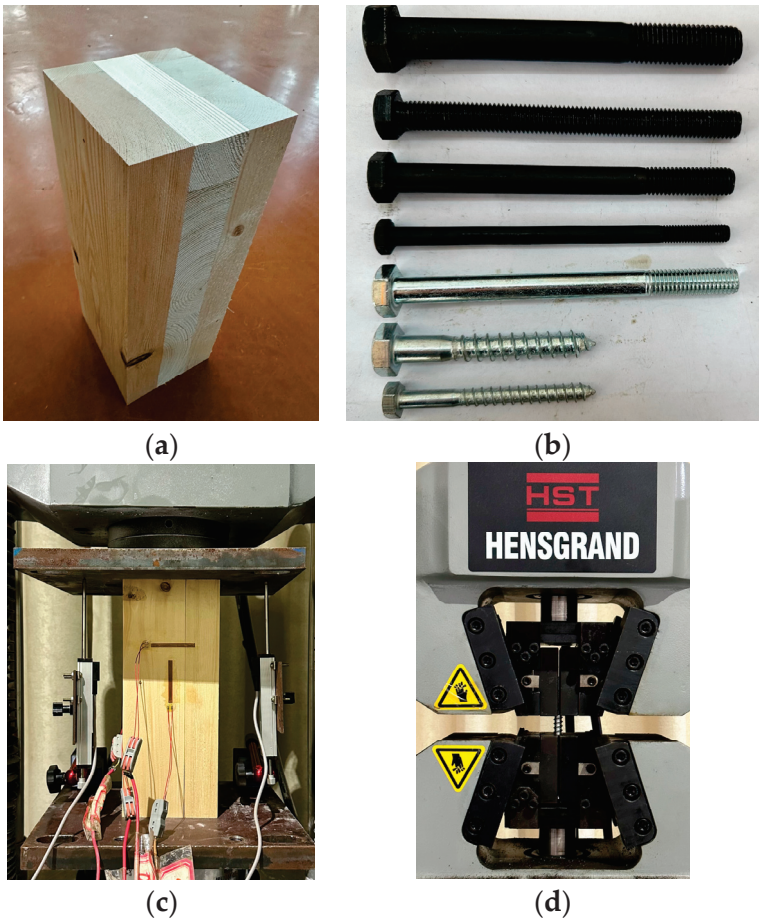

Figure 3. Material property experiment: (**a**) CLT; (**b**) Connection type; (**c**) CLT compression test; (**d**) Tensile test of connectors.

Table 3. Test results of tensile strength of connectors.

Strength Grade	Type	Nominal Diameter (mm)	Maximum Load (kN)			Average Value (kN)	Tensile Strength (MPa)
			Specimen 1	Specimen 2	Specimen 3		
4.8	Screw	8	17.24	18.23	18.42	17.96	357.48
	Screw	12	40.25	40.06	37.93	39.41	348.63
	Partially threaded bolt	12	48.14	48.83	49.61	48.86	432.01
8.8	Partially threaded bolt	8	43.43	41.48	41.01	41.97	835.39
	Partially threaded bolt	12	103.06	101.03	105.04	103.04	911.53
	Partially threaded bolt	16	185.85	181.36	176.52	181.24	901.87
	Fully threaded bolt	12	70.93	79.54	73.46	74.64	660.29

Table 4. Mechanical properties of the epoxy adhesive at room temperature.

Tensile Strength (MPa)	Bending Strength (MPa)	Compressive Strength (MPa)	Steel-to-Steel Tensile Shear Strength (MPa)	Complete Curing Time (h)
19.57	77.5	107.6	21.3	24

Note: The data in this table are sourced from the test report provided by the Nanjing Mankate Science and Technology Co., Ltd. All test results were obtained under controlled conditions of (23 ± 2) °C and (50 ± 5)% RH. Tensile strength: the maximum tensile stress a standard specimen can withstand before fracture during a tensile test. Bending strength: the maximum bending stress of a standard specimen can withstand before failure during a bending test. Compressive strength: the maximum compressive stress a standard specimen can withstand before failure during a compression test. Steel-to-steel tensile shear strength: the maximum shear stress of the bonded interface can withstand when two lap-jointed steel plates are pulled apart.

Table 5. Durability properties of the epoxy adhesive.

Environmental Resistance			Stress Resistance		Resistance to Medium Corrosion			
Damp-Heat Aging Resistance (%)	Heat Aging Resistance (%)	Freeze–Thaw Resistance (%)	Long-Term Stress Resistance	Fatigue Stress Resistance	Salt Spray Resistance (%)	Seawater Immersion Resistance (%)	Resistance to Alkaline Medium	Resistance to Acidic Medium
−4.4	−2.9	−3.4	Specimen does not fail	Specimen does not fail	−3.7	−3.5	Strength did not decrease, failure in concrete	Failure in concrete

Note: The data in this table are sourced from the test report provided by the Nanjing Mankate Science and Technology Co., Ltd. Damp-heat aging resistance: Reduction rate of steel-to-steel tensile shear strength after aging for 90 days at 50 °C, 95% RH. Heat aging resistance: Reduction rate of steel-to-steel tensile shear strength after aging for 30 days at (80 ± 2) °C. Freeze–thaw resistance: Reduction rate of steel-to-steel tensile shear strength after 50 freeze–thaw cycles (−25 °C to +35 °C). Long-term stress resistance: Under 4.0 MPa sustained shear stress for 210 days at (23 ± 2) °C, (50 ± 5)%RH. Fatigue stress resistance: With-stand 2 × 10^6 cycles of sine wave shear load (20 Hz, max stress 4.0 MPa) at room temp. Salt spray resistance: Reduction rate of steel-to-steel tensile shear strength after 90 days in a 5% NaCl salt spray environment. Sea-water immersion resistance: Reduction rate of steel-to-steel tensile shear strength after immersion in artificial seawater for 30 days. Resistance to alkaline medium: After immersion in saturated $Ca(OH)_2$ solution for 60 days, conduct a concrete bond strength test. Resistance to acidic medium: After immersion in 3% H_2SO_4 solution for 30 days, conduct a concrete bond strength test.

2.3. Loading Method

The loading regimen used in the test was based on the relevant provisions of BS EN 26891:1991 [38], with the loading apparatus shown in Figure 4. The loading procedure involved two main phases: an initial force-controlled phase followed by a displacement-controlled phase to failure. A typical loading path is shown in Figure 5. To establish the estimated ultimate load F_{est} for each group, one specimen from each group was randomly selected and subjected to a preliminary loading test. A constant loading rate of 4 mm/min was applied to the specimen until it failed. The maximum load recorded during this process was defined as F_{est} for that group of specimens. The remaining three replicate specimens in each group were then subjected to a formal graded loading protocol, which consisted of the following steps: (1) The specimen was loaded under force control at a rate of 0.2 F_{est}/min up to a load of 0.4 F_{est}. This load was then held for 30 s; (2) The load was reduced to 0.1 F_{est} at the same rate and held for another 30 s; (3) The specimen was reloaded to 0.7 F_{est} at a rate of 0.2 F_{est}/min. At this point, the control method was switched to displacement control. Loading then proceeded under displacement control at a constant rate of 4 mm/min. The test was terminated when either the specimen failed or the relative slip reached a limit of 50 mm.

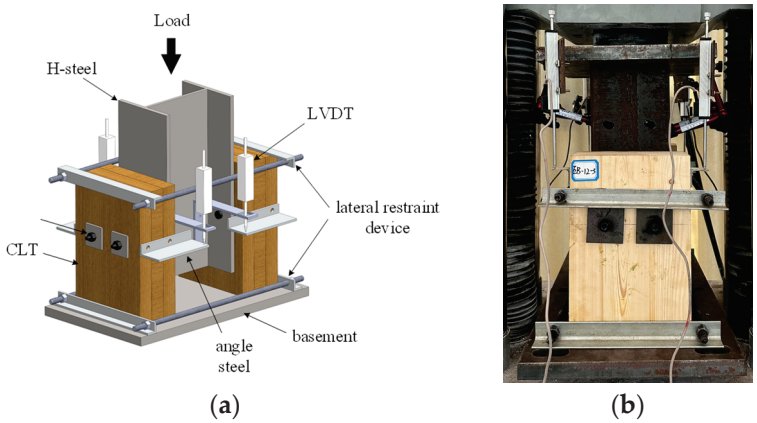

(**a**) (**b**)

Figure 4. Experimental specimens and instruments: (**a**) Schematic of the test setup; (**b**) Photograph of the test setup.

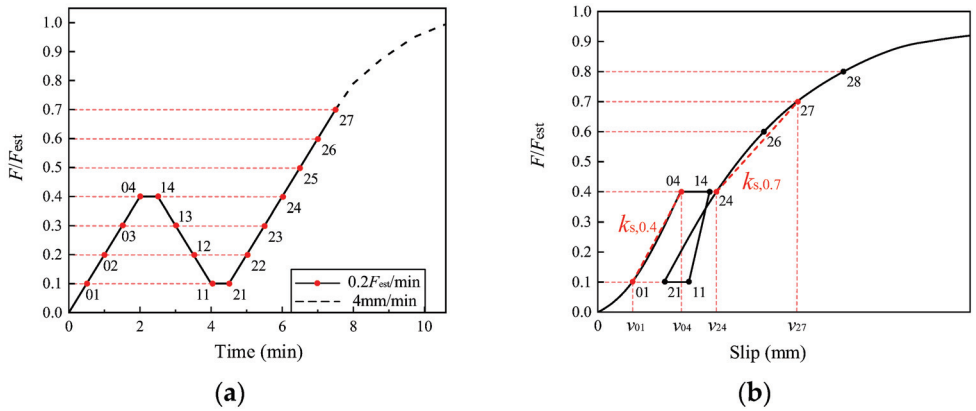

(**a**) (**b**)

Figure 5. Loading procedure for push-out test: (**a**) Loading procedure; (**b**) Corresponding slip.

3. Experimental Results

3.1. Load–Displacement Curves

Figure 6 displays the complete set of load–displacement curves obtained from the experimental program. The load of the double-row screw specimens was normalized by dividing it by the number of rows to facilitate a comparative analysis of the mechanical properties of single-row and double-row screw specimens. A set of three identical specimens is tested for each group to ensure repeatability. As some specimens contained initial fabrication defects, only two effective specimens were available in the 1B-12 and 1BE-8 groups. The defective specimens were excluded from the statistical analysis. However, to facilitate a comprehensive analysis of the macroscopic mechanical performance, the load–displacement curve of the third specimen is still presented, designated with the suffix "−3". The thick solid red lines represent the average response of the effective specimens in the same group. As shown in the figure, the load–displacement curves of the specimens in each group exhibit small variability, and the average response effectively characterizes the overall mechanical performance of the connection joints in that group.

A clear distinction in failure modes was observed from the curves. As shown in Figure 6b–d, the specimens in the 1BF-12, 1B#-12, and 1BE-8 groups failed abruptly due to bolt shear fracture, leading to a sudden loss of capacity. Conversely, the specimens in the 1B-12, 1BE-12, and 1BE-16 groups were governed by progressive wood crushing, which caused only minor load fluctuations at large displacements. The load–displacement curves for all specimen groups exhibited a remarkably consistent progression, which can be characterized by four distinct stages: elastic, elasto-plastic, plastic development, and failure. Taking specimen 1B#-12 as an example, the typical development process of its load–displacement curve is described as follows:

(1) Elastic stage: In the initial loading stage, the connection exhibited a linear load–displacement relationship, indicating that both the bolt and timber were deforming elastically. With increasing load, the specimen gradually yields, and the joints stiffness begins to exhibit non-linear degradation, subsequently entering the elastic-plastic stage.

(2) Elasto-plastic stage: This stage is characterized by the non-linear smooth degradation of joint stiffness. Wood fibers are compressed by the bolt, gradually undergoing plastic deformation, causing the joint's tangential stiffness to continuously decrease. However, the load-bearing capacity of the joint continued to increase due to the compaction of the wood. This resulted in the curve exhibiting a distinct convex non-linear characteristic.

(3) Plastic development stage: As deformation accumulates, the joint enters a stage dominated by material plasticity, characterized by strengthening and increased ductility.

The bolts exhibit significant bending deformation and gradually form one or more plastic hinges. The compressed wood areas below the pin slots or washers become denser, and the load-bearing capacity continues to increase, eventually reaching the peak load, with the specimen exhibiting some ductility. During the continued loading process, the wood fibers experience sustained and non-uniform fracture, which manifests as slight fluctuations in the load displacement curve.

(4) Failure stage: When the displacement exceeds the peak load point, the curve enters the load-bearing capacity decline segment, marking the beginning of the loss of structural integrity at the joint. Due to the compressive failure of the pin slot wall, shear fracture of the bolt, or local compressive failure of the wood beneath the washer, the bearing capacity of the joint significantly decreases and the specimen fails.

However, some high-performance bolt specimens exhibited significant plastic deformation capacity. No obvious failure stage was observed within the displacement range set for the test, and their response remained in the plastic development stage at the end of the test. Therefore, for these specimens, the recorded load-slip curves did not fully reflect the load-bearing capacity degradation after the peak and the final failure process.

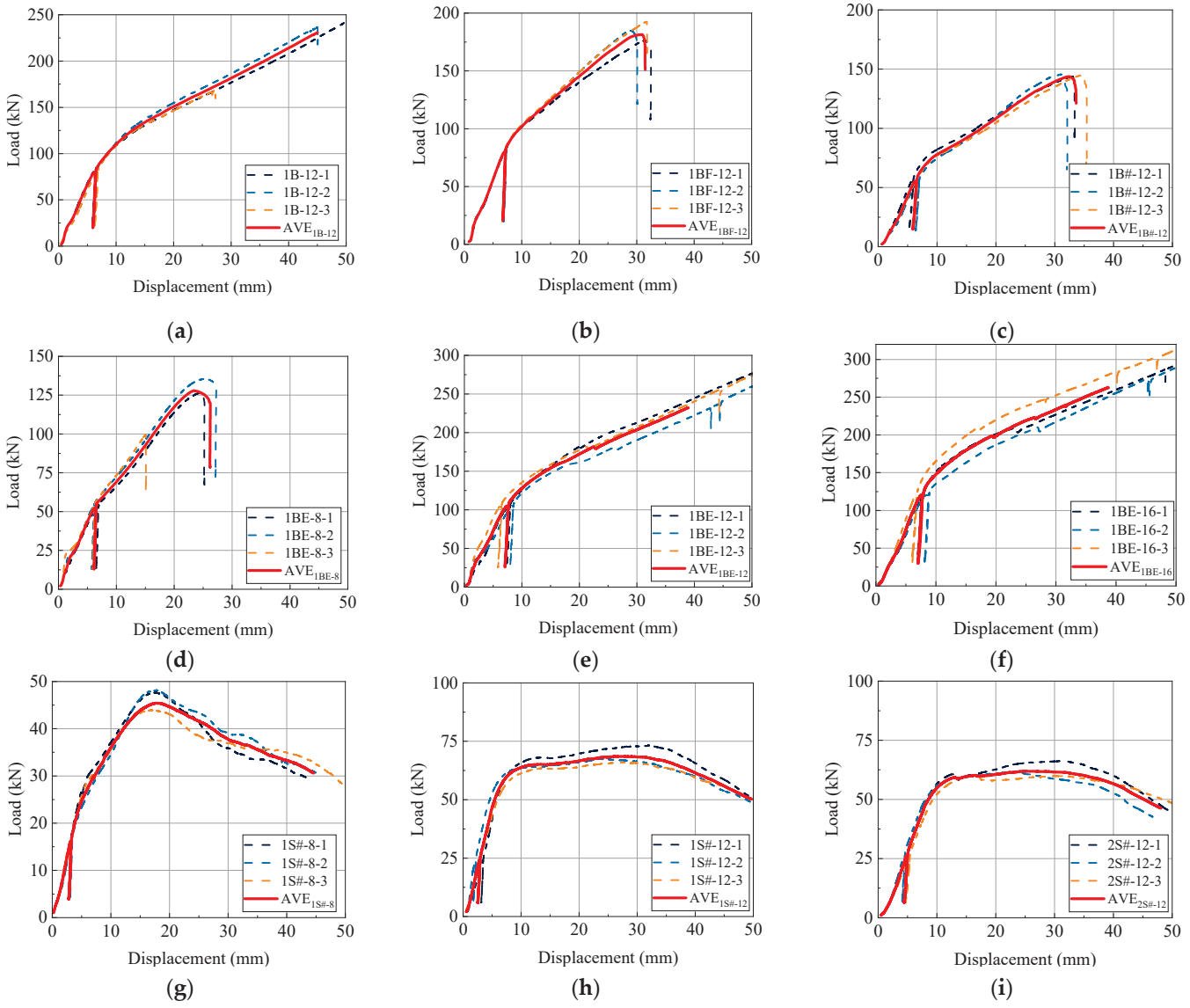

Figure 6. Test load–displacement curve: (**a**) 1B-12; (**b**) 1BF-12; (**c**) 1B#-12; (**d**) 1BE-8; (**e**) 1BE-12; (**f**) 1BE-16; (**g**) 1S#-8; (**h**) 1S#-12; (**i**) 2S#-12.

3.2. Failure Modes

After the test, the nut head was removed to facilitate the complete extraction of the connection components. The failure modes for each specimen group are summarized in Table 6, with typical failure patterns illustrated in Figure 7.

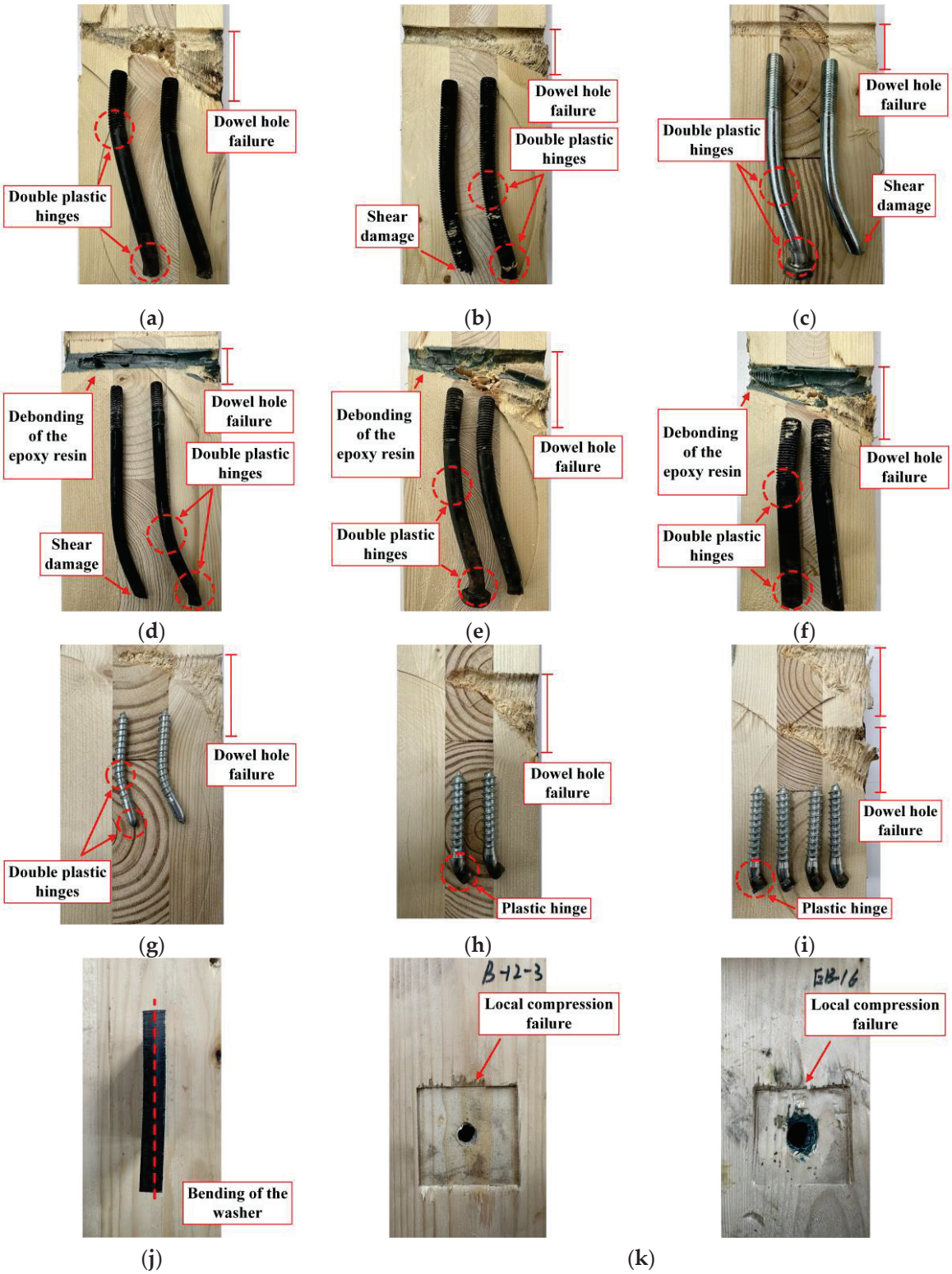

Figure 7. Experimental failure phenomenon: (**a**) 1B-12; (**b**) 1BF-12; (**c**) 1B#-12; (**d**) 1BE-8; (**e**) 1BE-12; (**f**) 1BE-16; (**g**) 1S#-8; (**h**) 1S#-12; (**i**) 2S#-12; (**j**) Washer; (**k**) CLT.

All connection components exhibited plastic hinging after the test. Based on the number of plastic hinges, the failure mechanism can be categorized into two typical failure modes. Failure mode I: single plastic hinge yielding, similar to yielding mode III_m in GB 50005—2017 'Standard for design of timber structures' [39]; failure mode II: double plastic hinge yielding, similar to yielding mode IV in the same standard. Additionally, in groups with lower connection member strength or higher aspect ratios, failure mode III was observed: shear failure occurred at the location of the plastic hinge formed at the CLT to steel interface.

In addition to the yielding and fracture of the connectors themselves, a series of accompanying damages were widely observed in the tests: under the squeezing action of the connectors, significant compressive failure occurred in the timber dowel slot regions of all specimens, accompanied by the generation of squeezing debris; In bolted connection specimens, clear local compression indentations formed beneath the washers; for epoxy resin–bolt connections, the failure process was also accompanied by delamination of the epoxy resin layer from the bolt and wood bonding interface. These composite damage phenomena collectively constituted the complete failure mechanism of the connection joints.

4. Discussion

4.1. Mechanical Properties

Table 7 summarizes the key mechanical properties for the nine groups of test specimens, including the average values and their corresponding coefficients of variation. In accordance with the standards BS EN26891:1991 [38] and BS EN 12512:2001 [40], the parameters are defined as follows:

(1) The maximum load observed throughout the test is denoted as the peak load F_{max}. A peak load is deemed valid only when the load–displacement curve shows a clear maximum, followed by a period of sustained load decay. For specimens where the load continues to increase until the end of loading, the peak load is not defined.

(2) As illustrated in Figure 8, two distinct methods are employed to determine the yield point (v_y, F_y), corresponding to the different types of load–displacement curves observed for the various connectors.

(3) The ultimate displacement v_u is defined as the smallest of the following three criteria: (a) the displacement corresponding to a significant decrease in load due to shear failure of the connector; (b) the displacement corresponding to a load equal to 0.8 F_{max} of the load on the descending segment of the curve; (c) a maximum displacement limit of 30 mm.

(4) The ultimate load F_u is identified as the load value on the curve corresponding to the ultimate displacement v_u.

(5) The joint's initial stiffness $K_{s,0.4}$ and secondary stiffness $K_{s,0.7}$ are calculated according to Equations (1) and (2), respectively.

$$K_{s,0.4} = \frac{0.3F_{est}}{v_{04} - v_{01}} \quad (1)$$

$$K_{s,0.7} = \frac{0.3F_{est}}{v_{27} - v_{24}} \quad (2)$$

In the formula: F_{est} is the estimated ultimate load; v_{01} and v_{04} are the joint displacements corresponding to the first stage of loading when the load reached 0.1 F_{est} and 0.4 F_{est}, respectively; v_{24} and v_{27} are the joint displacements corresponding to the third stage of loading when the load reached 0.4 F_{est} and 0.7 F_{est}, respectively, as shown in Figure 5b.

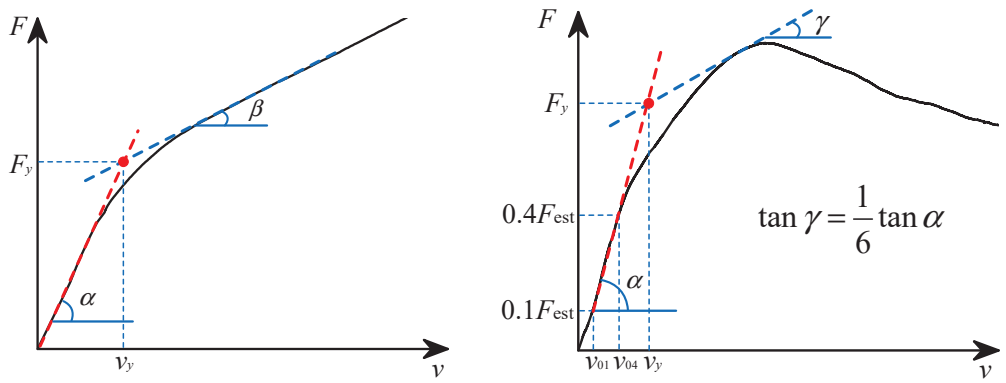

Figure 8. Definition method of yield point for load–displacement curve: (**a**) Bolted connection; (**b**) Screwed connection.

Table 6. Test failure mode.

Group	Shear Connector			CLT Local Compression Failure	Failure Mode
	Single Plastic Hinge	Double Plastic Hinges	Shear Damage		
1B-12		√		Severe	II
1BF-12		√	√	Moderate	II + III
1B#-12		√	√	Moderate	II + III
1BE-8		√	√	Slight	II + III
1BE-12		√		Severe	II
1BE-16		√		Severe	II
1S#-8		√			II
1S#-12	√				I
2S#-12	√				I

(6) The ratio of the ultimate displacement to the yield displacement is used to define the ductility coefficient Δ. Table 8 presents the method for determining the minimum required ductility and corresponding ductility classes for Cross-Laminated Timber (CLT) structures, as specified in prEN 1998-1-2:2023 [41].

Table 7. Mechanical properties of specimens.

Group	F_{max} (kN)	F_y (kN)	F_u (kN)	v_y (mm)	v_u (mm)	$K_{s,0.4}$ (kN/mm)	$K_{s,0.7}$ (kN/mm)	Δ
1B-12	/	113.43 [6.04]	181.47 [3.75]	8.45 [9.04]	30 [0.00]	12.76 [3.46]	5.78 [15.86]	3.56 [9.04]
1BF-12	184.46 [4.44]	93.17 [1.27]	181.84 [4.13]	7.83 [3.70]	29.62 [2.22]	11.97 [0.90]	5.21 [8.90]	3.79 [5.77]
1B#-12	144.85 [0.60]	69.55 [6.47]	139.15 [3.31]	7.39 [1.64]	30 [0.00]	10.32 [9.10]	3.98 [6.44]	4.06 [1.62]
1BE-8	131.01 [4.79]	54.12 [3.44]	131.01 [4.79]	6.33 [3.24]	24.98 [1.05]	8.12 [4.41]	4.78 [4.76]	3.95 [4.29]
1BE-12	/	137.18 [8.56]	203.37 [5.82]	9.03 [10.89]	30 [0.00]	14.27 [16.54]	5.14 [17.78]	3.35 [11.61]
1BE-16	/	143.52 [10.76]	232.24 [7.84]	8.45 [3.60]	30 [0.00]	18.23 [17.81]	6.00 [31.50]	3.55 [3.57]
1S#-8	46.58 [4.94]	41.39 [6.45]	37.29 [4.34]	7.17 [10.56]	30 [0.00]	5.74 [8.60]	4.38 [18.49]	4.22 [11.22]
1S#-12	68.91 [5.56]	57.83 [6.79]	68.29 [5.79]	5.71 [33.81]	30 [0.00]	11.75 [37.44]	10.84 [10.59]	5.75 [38.47]
2S#-12	62.53 [5.25]	54.09 [2.73]	61.55 [6.42]	8.58 [9.19]	30 [0.00]	7.04 [13.04]	7.15 [7.10]	3.52 [9.10]

Note: Values in [ ] denote the coefficient of variation (%).

Table 8. Minimum required ductility Δ as defined of dissipative zones tested accordingly.

Structural Type	Dissipative Sub-Assembly/Joint/2D-or 3D Connector/Connection	Type of Ductility	Δ DC2	Δ DC3
Cross laminated timber structures	Shear wall	Displacement	1.5	2.5
	Hold-downs, tie-downs, foundation tie-downs, angle brackets, shear plates	Displacement	1.5	1.5
	Screwed wall panel-to-panel joints	Displacement	-	5.5

Note: DC2: Ductility Class 2, which represents a medium energy dissipation capacity. DC3: Ductility Class 3, which represents a high energy dissipation capacity.

4.2. Comparison of Test Results with Eurocode 5 Predictions

In Eurocode 5 [42], the bearing capacity Z_d of connections using multiple bolts may be calculated according to Equations (3) and (4):

$$Z_d = n_{ef} Z \tag{3}$$

$$n_{ef} = n^{kd} \tag{4a}$$

$$n_{ef} = n^{0.9} \sqrt[4]{\frac{a_1}{13d}} \tag{4b}$$

where Z is the characteristic load-carrying capacity of a single fastener; n_{ef} is the effective number of fasteners in a row parallel to the grain(calculated according to Equations (4a) and (4b) for screw and bolted connections, respectively); and Z_d is the resulting effective characteristic capacity of that entire row.

The theoretical capacity of each fastener was predicted based on the Eurocode 5 provisions for a steel plate as the central member in a double shear connection. The code provides distinct equations to account for different ductile failure modes: Equation (5) corresponds to failure with two plastic hinges, while Equation (6) applies to failure with a single plastic hinge. A noteworthy feature of Eurocode 5 is its explicit inclusion of the "rope effect", which adds a capacity contribution from the fastener's axial resistance $F_{ax,Rk}/4$ to the primary Johansen yield theory component. For bolted connections, the code limits this rope effect contribution to 25% of the Johansen capacity. The specific calculation content is shown in Table 9.

$$Z = f_{em} t_1 d \left[\sqrt{2 + \frac{4 M_{y,Rk}}{f_{em} d {t_1}^2}} - 1 \right] + \frac{F_{ax,Rk}}{4} \tag{5}$$

$$Z = 2.3 \sqrt{M_{y,Rk} f_{em} d} + \frac{F_{ax,Rk}}{4} \tag{6}$$

where $M_{y,Rk}$ is the characteristic fastener yield moment (N·mm); and $F_{ax,Rk}$ is the characteristic withdrawal capacity of the fastener (N), which for a bolt is taken as the lesser of either its tensile capacity or the bearing capacity provided by the washer or steel plate; f_{em} denotes the characteristic embedment strength in the timber member, set as 5.7 MPa ($f_c/5$); d denotes the fastener diameter; t_1 is the smaller value between the side timber thickness and the penetration depth.

Eurocode 5, as a classic design standard, demonstrates good accuracy in predicting the yield strength of connections with conventional screws and high-strength bolts, with prediction errors generally within 20% of the experimental values. However, the code significantly overestimates the capacity of low-strength bolts by a non-conservative margin of 33.8%. On the other hand, it severely underestimates the performance of the epoxy

resin–bolt connections proposed in this study, proving overly conservative by neglecting the composite strengthening effect of the epoxy grout.

Table 9. Evaluation of design code predictions for connection bearing capacity.

Group	F_y (kN)	Eurocode 5 (kN)	Error (%)	Group	F_y (kN)	Eurocode 5 (kN)	Error (%)	Group	F_y (kN)	Eurocode 5 (kN)	Error (%)
1B-12	113.43	99.09	−12.6	1BE-8	54.12	64.76	+19.6	1S#-8	41.39	45.27	+9.4
1BF-12	93.17	95.96	+2.9	1BE-12	137.18	99.09	−27.7	1S#-12	57.83	57.29	−0.9
1B#-12	69.55	93.08	+33.8	1BE-16	143.52	135.29	−5.7	2S#-12	54.09	44.63	−17.5

Note: The error was calculated as [(Predicted − Experimental) / Experimental] × 100%.

4.3. Comparison of the Performance of Ordinary Bolt Joints

Under the same nominal diameter, the load–displacement curves of ordinary bolted joint specimens with different construction types are shown in Figure 9, clearly revealing the effect of bolt strength grade and thread construction on the joint's mechanical properties.

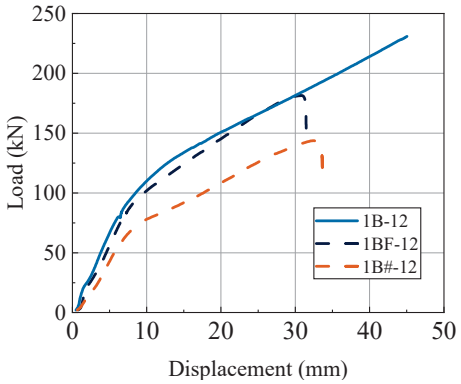

Figure 9. Load–displacement curve of ordinary bolt specimens.

During the initial loading phase, all specimens exhibited near-linear elastic behavior. Among them, the specimen groups using 8.8-grade bolts (1B-12 and 1BF-12) showed similar and relatively high initial stiffness. However, the initial stiffness of the specimen group using 4.8-grade bolts (1B#-12) was relatively low, which may be attributed to the lower-strength steel exhibiting microplastic deformation at local high-stress points earlier. As shown in Table 7, specimen group 1B#-12 exhibited a significant reduction in mechanical properties compared to group 1B-12. The initial stiffness, secondary stiffness, and ultimate load decreased by 19.1%, 31.1%, and 23.3%, respectively. This directly demonstrates that using high-strength bolts is an effective means of enhancing the ultimate load-bearing capacity of connections.

Although both are high-strength bolts, the fully threaded specimen group 1BF-12 experienced shear failure at the ultimate load due to the reduction in the net cross-sectional area at the bolt root and stress concentration effects, exhibiting typical brittle failure characteristics. Similarly, although the specimen group 1B#-12 avoided stress concentration issues in the threads, its insufficient material strength caused the bolts to reach their shear limit before the timber reached its bearing capacity, leading to premature failure of the connection and failing to fully utilize the wood's plastic deformation capacity to develop ductility. This specimen group experienced bolt fracture immediately after reaching a peak load of 144.85 kN, also exhibiting brittle failure. In contrast, specimen group 1B-12 demonstrated the optimal mechanical performance, maintaining a high level of load-bearing capacity within a large deformation range even after reaching the ultimate load, and its final failure mode was characterized by bolt yielding.

4.4. Comparison of Bolt and Screw Joint Performance

In STC beams, screws or groups of screws are commonly used in conjunction with each other. Therefore, based on single-row bolt joint tests, this study investigated the differences in mechanical performance between single- and double-row screw joints and single-row bolt joints.

Figure 10 compares the load–displacement curves of 4.8-grade bolts and screw specimens. Due to the anchoring effect of washers and nuts, bolt specimen group 1B#-12 had a high peak load, but its failure mode is brittle failure. The screw specimen groups (1S#-8, 1S#-12, and 2S#-12) had lower peak loads but demonstrated excellent ductility. Their load–displacement curves exhibit a prolonged plastic platform, with a very gradual post-peak degradation in load-bearing capacity, while also demonstrating a large ultimate deformation capacity. This ideal ductile failure mode is primarily due to the inherent ductility of screws. In the later stages of loading, the screws undergo significant bending deformation, which synergistically deforms with the surrounding wood, accompanied by the extraction of the screws, thereby forming an energy dissipation mechanism. Notably, when the specifications of the screws are similar to those of bolts, the initial stiffness of the screw connection test specimens group 1S#-12 was 13.8% higher than that of the bolt connection test specimens group 1B#-12. This phenomenon is attributed to the fundamental difference in installation methods: screws are screwed into a 0.75 D diameter slot via self-tapping, forming a tight thread-wood engagement interface that effectively utilizes the wood's anchoring effect, thereby achieving excellent initial embedment performance.

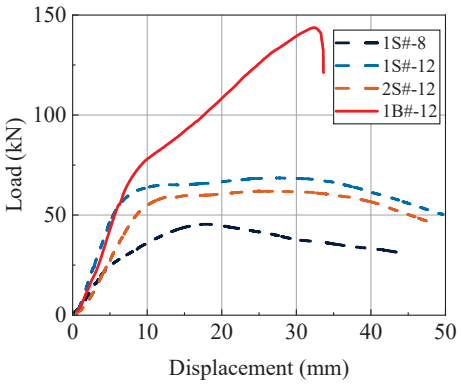

Figure 10. Load–displacement curve of 4.8-grade bolt and screw specimens.

Within the screw test specimen group, the normalized peak load of the double-row screw test specimen group 2S#-12 was slightly lower than that of the single-row screw test specimen group 1S#-12, with initial stiffness and secondary stiffness decreasing by 40% and 34%, respectively. The phenomenon that the total capacity of the connection is not equal to the simple linear sum of the contributions from individual fasteners clearly reveals the 'group nail effect' in double-row screw connections. This effect stems from the load transfer is intrinsically coupled with material strain. In a multi-row screw arrangement, the load is first transferred to the leading row of screws—those closest to the point of application. The load is then conveyed to subsequent rows through the combined deformation of the interconnecting materials, including both the steel and timber. In this process, the load is attenuated on the transfer path as the wood around the row of screws is subjected to pressure deformation. During this transfer, the load is attenuated on the transfer path as the wood around the row of screws is subjected to pressure deformation. The screw load distribution shows a gradient characteristic, that is, the closer the screw is to the load application point, the greater the load it bears. As a result, the total load-bearing capacity of the connection fails to reach the simple linear superposition of individual screw capacities.

This phenomenon is referred to as the 'group nail effect' and it significantly reduces the overall efficiency of the connection.

By increasing the diameter of the screw from 8 mm (specimen group 1S#-8) to 12 mm (specimen group 1S#-12), the strength and stiffness of the specimens were significantly improved. This is in line with the expected scenario, as a larger diameter provides a greater timber bearing area and higher shear resistance of the screws, thereby comprehensively enhancing the mechanical performance of the connection joint. This demonstrates that increasing the diameter is an effective method for strengthening connection performance.

4.5. Comparison of the Performance of Ordinary Bolts and Epoxy Resin-Bolted Joints

Figure 11 compares the load–displacement curves of 8.8-grade ordinary bolts and epoxy resin-bolted specimens. By comparing the 12 mm diameter ordinary bolt specimen group 1B-12 with the epoxy resin-bolted specimen group 1BE-12, it was confirmed that the introduction of an epoxy resin adhesive layer moderately improved the mechanical performance of the connection joints.

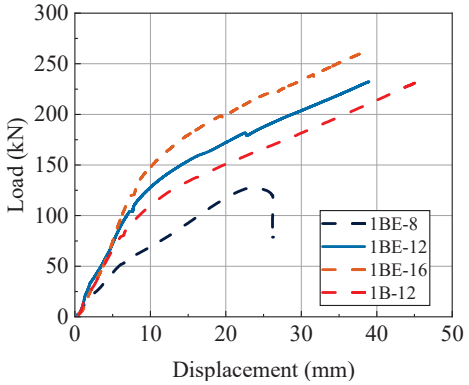

Figure 11. Load–displacement curve of ordinary bolt and epoxy resin–bolt specimens.

At any given displacement level, the load of the specimen group 1BE-12 was higher than that of the specimen group 1B-12. The ultimate load and initial stiffness were increased by 12% and 11.8%, respectively. The underlying mechanism behind this performance improvement lies in the high-strength epoxy resin forming a 'rigid sleeve' between the bolt hole wall and the timber dowel slot. In a conventional bolted connection, load is transferred directly from the bolt shank to the timber hole wall through a localized, high-stress region. This process inevitably causes stress concentration and can lead to the premature crushing of wood fibers. In the epoxy resin–bolt connection, however, the load is first transferred from the bolt to the epoxy sleeve, and then from the sleeve to the timber over a much larger contact area. The high compressive strength and stiffness of the epoxy allow it to effectively convert a line load from the bolt into a distributed surface load on the timber, thereby significantly reducing stress concentration at the hole wall and suppressing localized brittle failure of the wood. This effectively increases the load-bearing area, homogenizes the stress distribution transmitted from the bolt to the wood, significantly reduces stress concentration at the hole walls, and suppresses premature crushing of wood fibers, thereby forming a composite dowel system where the bolt, epoxy resin, and wood work synergistically. This enhancement is made possible by the excellent mechanical properties of the epoxy resin itself (as shown in Table 4). Its high compressive strength of 107.6 MPa, which is substantially greater than the transverse compressive strength of the wood (f_c = 28.74 MPa), ensures that the sleeve is not crushed under the high bearing pressure from the bolt. Concurrently, its bending strength of 77.5 MPa allows the sleeve to maintain its integrity and deform synergistically as the bolt bends.

This reinforcement method significantly enhances strength and stiffness without sacrificing the ductility of the connection joints. As shown in Table 7, the unreinforced specimen group 1B-12 exhibited a ductility ratio (Δ) of 3.56, while the epoxy-reinforced specimen group 1BE-12 showed a slightly lower ratio of 3.35. According to Table 8, common dissipative connectors in CLT structures, like hold-downs and shear plates, are required to have a minimum ductility ratio of Δ = 1.5 to qualify for the medium ductility class (DC2). Both the ductility ratios of the reinforced specimen group 1BE-12 and the unreinforced specimen group 1B-12 are more than double this minimum requirement, demonstrating a positive plastic deformation capacity.

Comparing the epoxy resin–bolt specimen groups (1BE-8, 1BE-12, and 1BE-16), it was found that the bolt diameter was significantly positively correlated with the mechanical properties of the epoxy resin–bolt connection joints. Increasing the bolt diameter from 8 mm to 16 mm resulted in a significant improvement in the connection's strength and stiffness. When displacement reached 20 mm, the load-bearing capacity of the specimen group 1BE-16 was approximately 20% and 80% higher than that of the specimen group 1BE-12 and 1BE-8, respectively. This directly reflects the higher shear stiffness and strength of bolts with larger diameters. The most critical finding is that bolt diameter directly determines the final failure mode of the epoxy resin–bolt connection specimens. The smallest diameter specimen group 1BE-8 experienced a sharp decline in load-bearing capacity after reaching a peak load of approximately 131.01 kN, exhibiting failure mode III with typical brittle fracture characteristics. This indicates that, for 8 mm bolts, their inherent strength became the weakest link in the composite connection system: after wood reinforcement, failure is controlled by the shear fracture of the bolts themselves. In contrast, specimens with diameters of 12 mm and 16 mm exhibited good ductility, with failure modes dominated by the plastic yielding of the bolts and the progressive crushing of the wood.

5. Conclusions and Design Recommendations

5.1. Conclusions

The interface performance between timber and H-steel is critical for designing STC joints. This study involved nine groups of double shear tests on STC joints. The investigation focused on the effects of connection component strength grades, screw construction, type, diameter, quantity, and epoxy resin reinforcement measures on the stiffness, shear bearing capacity, and ductility of STC joints. The specific conclusions are as follows:

(1) Using high-strength bolts was found to be a direct way to enhance the ultimate load-bearing capacity of connection joints. Additionally, compared to fully threaded bolts, partially threaded bolts had a larger effective cross-sectional area, resulting in higher shear load-bearing capacity. Furthermore, by forming a plastic hinge at the root of the bolt, the failure mode of partially threaded bolts transitioned from brittle shear failure to the desired ductile failure.

(2) Ordinary bolt specimens exhibited significantly higher ultimate load-bearing capacity than screw specimens of the same diameter due to the anchoring effect at the nut end. However, screw specimens effectively utilized the wood's anchoring capacity through the close thread-wood engagement interface, thereby demonstrating superior initial stiffness. Regarding the number of screw rows, increasing the number of connection elements enhanced load-bearing capacity and stiffness. However, due to the 'cluster nail effect,' performance improvements were not linearly increased, and the efficiency reduction of group nails needs to be considered in the design.

(3) Compared with ordinary bolts, the epoxy resin–bolt joint formed by injecting epoxy resin into the bolt slot increased the initial stiffness and ultimate load of the connection by 12% and 11.8%, respectively, without sacrificing ductility. However, when the

wood end is sufficiently reinforced, smaller-diameter bolts became the weak link in the connection system, which caused the failure mode to shift from the ideal ductile yielding to unexpected bolt brittle fracture.

5.2. Design Recommendations

The epoxy resin–bolt connection method proposed in this paper has significant advantages and can effectively enhance the mechanical performance of connection joints. Based on the findings above, the following preliminary design recommendations are proposed to guide the application of this novel connection in engineering practice:

(1) This study demonstrated that 12 mm and 16 mm diameter bolts can establish a good synergistic mechanism with the epoxy-reinforced timber, leading to ductile failure. To ensure the connection possesses adequate ductility and reliability by avoiding brittle failure of the bolt itself, it is recommended to use high-strength bolts with a diameter of no less than 12 mm.

(2) The 2 mm epoxy layer thickness used in this study performed well experimentally. This thickness represents an effective balance between constructability and mechanical performance. In the absence of further parametric studies, a 2 mm thickness is recommended as a reference. Designers should ensure that the oversized hole is large enough for uniform epoxy filling but avoid excessive thickness that could increase material consumption and potential issues related to volumetric shrinkage.

(3) To mitigate the group nail effect, proper spacing is essential. In this composite system, the load is transferred by the 'epoxy resin-bolt' composite dowel, which has a diameter of the hole (D). This is different from the bare bolt diameter. Therefore, all spacing calculations should be based on this composite diameter D. With reference to the provisions for dowel-type fasteners in Eurocode 5, we suggest: Spacing parallel to the load direction of no less than $4D$ and spacing perpendicular to the load direction of no less than $4D$. This recommendation is a rational inference but requires validation through future dedicated experimental studies. Until more precise reduction factors for this specific composite connection are developed, a conservative approach should be taken in design by applying the capacity reduction factors for conventional multi-row bolted connections to ensure structural safety.

(4) For the epoxy resin-bolted connections, which exhibited a ductile failure mode governed by bolt yielding and progressive wood crushing, Eurocode 5 provided a reasonable prediction of the bearing capacity, making it suitable for design applications.

Author Contributions: Conceptualization, Q.L. and B.F.; methodology, Q.L. and H.W.; software, J.X.; validation, Q.L. and B.F.; formal analysis, J.Y.; investigation, Q.L. and B.F.; resources, Y.X.; data curation, X.L.; writing—original draft preparation, J.Y.; writing—review and editing, Q.L. and B.F.; visualization, Z.Z.; supervision, Q.L.; project administration, Q.L. and H.W.; funding acquisition, J.X. All authors have read and agreed to the published version of the manuscript.

Funding: This research was funded by the Ningbo Science and Technology Bureau through the Public Welfare Research Plan Project of Ningbo, grant number 2024S080; the Department of Housing and Urban-Rural Development of Zhejiang Province through the Zhejiang Provincial Construction Science and Technology Research Project, grant number 2024K161; and the Ningbo University of Technology through the General Research Project (Postgraduate Special), grant number 2024NGYA001.

Data Availability Statement: The data presented in this study are available from the first author upon reasonable request.

Acknowledgments: Thanks are due to Xiaoai Fang and Renliang Fang for assistance with the experiments.

Conflicts of Interest: Authors Huake Wang and Jiale Xu were employed by the company Huaxing Steel Structure Co., Ltd. The remaining authors declare that the research was conducted in the absence of any commercial or financial relationships that could be construed as a potential conflict of interest.

Abbreviations

The following abbreviations are used in this manuscript:

CLT	Cross laminated timber
STC	Steel–timber composite
GLT	Glue laminated timber

References

1. Quintana Gallo, P.; Carradine, D.M.; Bazaez, R. State of the art and practice of seismic-resistant hybrid timber structures. *Eur. J. Wood Wood Prod.* **2021**, *79*, 5–28. [CrossRef]
2. Chiniforush, A.A.; Akbarnezhad, A.; Valipour, H.; Xiao, J. Energy implications of using steel-timber composite (STC) elements in buildings. *Energy Build.* **2018**, *176*, 203–215. [CrossRef]
3. Liu, W.; Yang, H. Research progress on modern timber structures. *J. Build. Struct.* **2019**, *40*, 16–43.
4. Brandner, R.; Flatscher, G.; Ringhofer, A.; Schickhofer, G.; Thiel, A. Cross laminated timber (CLT): Overview and development. *Eur. J. Wood Wood Prod.* **2016**, *74*, 331–351. [CrossRef]
5. Fan, Y.; Zhang, L.; Chen, S.; Yamahiro, S. Technological Iteration and Design Evolution of Medium and Large Timber Architecture in Japan. *Archit. J.* **2023**, *9*, 24–31. [CrossRef]
6. Svatoš-Ražnjević, H.; Orozco, L.; Menges, A. Advanced timber construction industry: A review of 350 multi-storey timber projects from 2000–2021. *Buildings* **2022**, *12*, 404. [CrossRef]
7. Ataei, A.; Valipour, H.R.; Bradford, M.A.; Chiniforush, A.A. Experimental study of steel-timber composite beam-to-column joints with extended end plates. *Constr. Build. Mater.* **2019**, *226*, 636–650. [CrossRef]
8. Ascione, F.; Esposito, F.; Iovane, G.; Faiella, D.; Faggiano, B.; Mele, E. Sustainable and efficient structural systems for tall buildings: Exploring timber and steel–timber hybrids through a case study. *Buildings* **2024**, *14*, 524. [CrossRef]
9. Ataei, A.; Bradford, M.A.; Valipour, H.R. Sustainable high strength steel flush and plate beam-to-column composite joints with deconstructable bolted shear connectors. In Proceedings of the Second International Conference on Performance-Based and Lifecycle Structural Engineering, Brisbane, QLD, Australia, 9–11 December 2015; pp. 749–757.
10. Wang, X.; He, Q.; An, Z.; Liu, G.; Wen, X.; Wang, Y.; Zhong, Z. Experimental study of perfobond rib shear connector under lateral force. *Appl. Sci.* **2021**, *11*, 9088. [CrossRef]
11. Xu, X.; Liu, Y.; He, J. Study on mechanical behavior of rubber-sleeved studs for steel and concrete composite structures. *Constr. Build. Mater.* **2014**, *53*, 533–546. [CrossRef]
12. Zhuang, B.; Liu, Y.; Yang, F. Experimental and numerical study on deformation performance of Rubber-Sleeved Stud connector under cyclic load. *Constr. Build. Mater.* **2018**, *192*, 179–193. [CrossRef]
13. He, X.; Yam, M.C.; Ke, K.; Zhou, X.; Zhang, H.; Gu, Z. Behaviour insights on damage-control composite beam-to-beam connections with replaceable elements. *Steel Compos. Struct.* **2023**, *46*, 773–791.
14. He, X.; Ke, K.; Chen, Y.; Yam, M.C.; Shao, T. An experimental study of steel-concrete composite connections equipped with fuse angles. *J. Constr. Steel Res.* **2022**, *195*, 107357. [CrossRef]
15. Wang, C.-L.; Lyu, J.; Zhao, J.; Yang, H. Experimental investigation of the shear characteristics of steel-to-timber composite joints with inclined self-tapping screws. *Eng. Struct.* **2020**, *215*, 110683. [CrossRef]
16. Ataei, A.; Chiniforush, A.; Bradford, M.; Valipour, H. Cyclic behaviour of bolt and screw shear connectors in steel-timber composite (STC) beams. *J. Constr. Steel Res.* **2019**, *161*, 328–340. [CrossRef]
17. Yang, R.; Li, H.; Lorenzo, R.; Ashraf, M.; Sun, Y.; Yuan, Q. Mechanical behaviour of steel timber composite shear connections. *Constr. Build. Mater.* **2020**, *258*, 119605. [CrossRef]
18. Chiniforush, A.A.; Valipour, H.R.; Bradford, M.A.; Akbarnezhad, A. Long-term behaviour of steel-timber composite (STC) shear connections. *Eng. Struct.* **2019**, *196*, 109356. [CrossRef]
19. Li, Z.; Wang, X.; He, M.; Dong, W. Experimental investigation of timber-steel hybrid walls and seismic design method for timber-steel hybrid structural system. *J. Build. Struct.* **2018**, *39*, 191–197.
20. Hassanieh, A.; Valipour, H.R.; Bradford, M.A. Experimental and numerical study of steel-timber composite (STC) beams. *J. Constr. Steel Res.* **2016**, *122*, 367–378. [CrossRef]
21. Hassanieh, A.; Valipour, H.R.; Bradford, M.A. Load-slip behaviour of steel-cross laminated timber (CLT) composite connections. *J. Constr. Steel Res.* **2016**, *122*, 110–121. [CrossRef]

22. Hassanieh, A.; Valipour, H.R.; Bradford, M.A. Experimental and analytical behaviour of steel-timber composite connections. *Constr. Build. Mater.* **2016**, *118*, 63–75. [CrossRef]
23. Hassanieh, A.; Valipour, H.; Bradford, M.; Sandhaas, C. Modelling of steel-timber composite connections: Validation of finite element model and parametric study. *Eng. Struct.* **2017**, *138*, 35–49. [CrossRef]
24. Hassanieh, A.; Valipour, H.R.; Bradford, M.A. Experimental and numerical investigation of short-term behaviour of CLT-steel composite beams. *Eng. Struct.* **2017**, *144*, 43–57. [CrossRef]
25. Loss, C.; Piazza, M.; Zandonini, R. Connections for steel–timber hybrid prefabricated buildings. Part I: Experimental tests. *Constr. Build. Mater.* **2016**, *122*, 781–795. [CrossRef]
26. Loss, C.; Piazza, M.; Zandonini, R. Connections for steel–timber hybrid prefabricated buildings. Part II: Innovative modular structures. *Constr. Build. Mater.* **2016**, *122*, 796–808. [CrossRef]
27. He, M.; Ni, S.; Ma, R.; Bai, X. Loading Tests of Prestressed Tube Bolted Joint with Slotted-in Steel Plate. *J. Tongji Univ. (Nat. Sci.)* **2013**, *41*, 1353–1358.
28. He, M.; Zhao, Y.; Ma, R. Experimental investigation on lateral performance of pre-stressed tube bolted connection with high initial stiffness. *Adv. Struct. Eng.* **2016**, *19*, 762–776. [CrossRef]
29. Ling, Z.; Liu, C.; Zhang, H. Shear performance of grouted stud connections for steel-cross laminated timber composite beams. *J. Build. Struct.* **2024**, *45*, 232–242.
30. Hassanieh, A.; Valipour, H.R.; Bradford, M.A. Composite connections between CLT slab and steel beam: Experiments and empirical models. *J. Constr. Steel Res.* **2017**, *138*, 823–836. [CrossRef]
31. Hassanieh, A.; Valipour, H.R.; Bradford, M.A. Bolt shear connectors in grout pockets: Finite element modelling and parametric study. *Constr. Build. Mater.* **2018**, *176*, 179–192. [CrossRef]
32. Zhao, Y.; Yuan, Y.; Wang, C.-L.; Zheng, J.; Zhou, Y. Experimental study on shear performance of steel-timber screw connectors with grout pockets. *Eng. Struct.* **2022**, *266*, 114535. [CrossRef]
33. *GB/T 50329-2012*; Standard for Methods Testing of Timber Structures. China Architecture & Building Press: Beijing, China, 2012.
34. *GB/T 26899-2011*; Structural Glued Laminated Timber. Standards Press of China: Beijing, China, 2011.
35. *GB/T 228.1-2021*; Metallic Materials: Tensile Testing: Part 1, Method of Test at Room Temperature. Standards Press of China: Beijing, China, 2021.
36. *GB 50017-2017*; Standard for Design of Steel Structures. China Architecture & Building Press: Beijing, China, 2017.
37. *GB 50011-2010*; Code for Seismic Design of Buildings. China Architecture & Building Press: Beijing, China, 2016.
38. *BS EN 26891:1991*; Timber Structures-Joints Made with Mechanical Fasteners-General Principles for the Determination of Strength and Deformation Characteristics. CEN: Brussels, Belgium, 1991.
39. *GB 50005-2017*; Standard for Design of Timber Structures. China Architecture & Building Press: Beijing, China, 2017.
40. *BS EN 12512-2001*; Timber Structures-Test Methods-Cyclic Testing of Joints Made with Mechanical Fasteners. CEN: Brussels, Belgium, 2001.
41. *prEN 1998-1-2:2023*; Design of Structures for Earthquake Resistance—Part 1-2, Buildings. CEN: Brussels, Belgium, 2023.
42. *EN 1995-1-1*; Eurocode 5, Design of Timber Structures—Part 1-1, General Common Rules and Rules for Buildings. European Committee for Standardization: Brussels, Belgium, 2004.

buildings

MDPI

Article

Experimental Study of the Actual Structural Behaviour of CLT and CLT–Concrete Composite Panels with Embedded Moment-Resisting Joint

Matúš Farbák *, Jozef Gocál and Peter Koteš

Department of Structures and Bridges, Faculty of Civil Engineering, University of Žilina, Univerzitná 8215/1, 010 26 Žilina, Slovakia; jozef.gocal@uniza.sk (J.G.); peter.kotes@uniza.sk (P.K.)
* Correspondence: matus.farbak@uniza.sk

Abstract: Timber structures and structural members have undergone rapid development in recent decades and are now fully competitive with traditional structures made of reinforced concrete or structural steel in many areas. Low self-weight, high durability, rapid construction assembly, and a favourable environmental footprint predispose timber structures for wider future use. A persisting drawback is the often-complicated joining of individual elements, especially when moment resistance is required. For CLT panels, this issue is more urgent due to their relatively small thickness and cross-laminated lay-up. This paper presents experimental research investigating parameters related to the actual behaviour of a moment-resisting embedded joint of CLT panels. The test programme consisted of four series (12 specimens) loaded in four-point bending to failure. The proposed and tested joint consists of high-strength steel rods glued into the two connected parts of the CLT panel. In addition to a detailed investigation of the resistance and stiffness of the joint, this research evaluates the effect of composite action with a reinforced-concrete slab on the performance of this type of joint. The experimental results and their detailed analysis are also extended to propose a framework concept for creating a theoretical (mechanical) model based on the component method.

Keywords: moment-resisting joint; epoxy embedded joint; CLT panel; CLT–concrete composite panel; experimental study; component-method model

1. Introduction

Cross-laminated timber, also named CLT, crosslam, or X-Lam, can be defined as a prefabricated engineered wood product made of an odd number (usually, three to seven) of orthogonal layers of graded sawn lumber or structural composite lumber that are laminated by gluing with structural adhesives. CLT is manufactured under controlled factory conditions by gluing laminations in layers, which are stacked crosswise, i.e., at 90 degrees, in a generally alternating manner. In typical CLT products, direction from the outer layers corresponds to the panel's major strength direction, while those arranged perpendicular to the outer layers correspond to the panel's minor strength direction. CLT panels vary in size depending on the manufacturer, although they can be made up to 18 m long by 5 m wide with a thickness of up to 500 mm, making them ideal for floors, walls, and roofs.

CLT is a relatively new and innovative mass timber product that is gaining popularity within the construction industry. Its development only dates to the early 1990s in Austria and Germany [1], with commercial production in Europe starting in the early 2000s. The

use of CLT has subsequently spread throughout Europe, with particular growth in the UK [2] and Scandinavia [3], but also worldwide, particularly in North America [4], Australia, and New Zealand [5]. The use of CLT in buildings has increased remarkably in the second decade of the 21st century. Hundreds of impressive buildings and other structures built around the world using CLT [2] show the many advantages this product can offer to the construction sector. The worldwide experience shows that CLT construction can be competitive, particularly in mid-rise and high-rise buildings. Modern manufacturing techniques combined with good strength properties make CLT a useful construction material with unique properties [3]:

- High strength in relation to the self-weight of the material.
- Small manufacturing tolerances and good dimensional stability.
- Good load-bearing capacity in fire.
- Good thermal insulation capacity.
- Low self-weight, which means lower transport and assembly costs, as well as lower foundation costs.
- Good capacity to tolerate chemically aggressive environments.
- Flexible production that even allows the manufacture of curved surfaces.

In connection with the advantages, it is also necessary to mention the environmental aspect of using cross-laminated timber or mass timber in general [6]. As a natural and renewable building material, timber has excellent ecological attributes. It acts as a carbon sink and has low embodied energy. The energy required to convert trees into wood, and subsequently into structural timber, is significantly lower than that needed for other structural materials, such as steel and concrete [6,7]. Whereas these conventional materials are responsible for vast amounts of CO_2 during production, trees naturally remove around two tonnes of CO_2 from the atmosphere to create one tonne of their own dry mass [8]. Hence, when mass timber products are used in buildings, the carbon sequestered during production is stored over their lifespan. As such, the use of mass timber to replace concrete and steel will drastically reduce the emissions embodied in buildings [9–13]. With the progressive mandatory implementation of standards for the environmental assessment of construction products and entire buildings (e.g., EN 15804:2012+A2:2019 [14]; EN 15978 [15]; ASTM E2921 [16]; ISO 14044:2006 [17]; ISO 21930:2017 [18]), the potential for wider use of CLT panels in the construction industry is significantly increasing.

CLT structures are characterised by fast and simple assembly of prefabricated surface and box units. The components can be joined using simple and traditional methods such as nailing and screwing. For more demanding structures, there are more advanced fixing methods. A CLT structure has full load-bearing capacity even before assembly and, as with other timber structures, minor changes can be made on site using simple hand tools. Wood has been used in buildings for centuries and is a material with excellent durability when used correctly.

The expansion of the use of CLT since the beginning of the 21st century has been supported by intensive global research and development in the field of production and construction of CLT panels. Research activities reflect a very wide range of related issues, from the design of CLT cross-sections and connections [3,4,19–23] through its combination with other building materials [24–27], global analysis [28], consideration of seismic effects [29], assembly procedures, development of structural details, fire resistance [30–32], acoustics in CLT structures [33], etc. The results of theoretical and applied research are gradually reflected in various recommendations, manuals, and national standards, serving as an aid for the design of structures from CLT panels. Currently, the final phase of preparation of the second generation of European timber design standards, known as Eurocode 5, is underway,

the availability of which is scheduled for August 2025 [34]. One of the changes or extensions of the design procedures concerns the issue of designing structures from CLT panels.

Connections in mass timber structures, including those built with CLT, play an essential role in ensuring strength, stiffness, stability, and ductility to the structure [3,4]. A wide variety of fasteners and types of joints can be used for floor-to-floor, wall-to-wall, roof-to-wall, wall-to-floor, and inter-storey connections in CLT and mixed structures. While CLT manufacturers typically recommend long self-tapping screws, which are commonly used for connecting floor panels and walls to floors, standard dowel-type fasteners, such as wood screws, nails, bolts, and dowels, have also been effectively used in connecting panel elements together in many projects. Other traditional fasteners, including timber connectors, such as split rings, shear plates, spikes, and tooth plates, may have some potential; however, their use is expected to be limited to applications where high loads are involved. There are also several more innovative solutions, such as glued-in rods [35], and advanced package solutions that cover all corner solutions, including assembly fixings and systems for invisible load-transferring joints. The new systems often rely on a high degree of prefabrication of CLT panels and the fact that CNC machines are used to design fixings.

This article deals with a possible solution for a floor-to-floor moment-resisting connection of two CLT panels in their major strength direction. Due to dimensional restrictions, connections are required to establish continuity between adjacent CLT panels. Amongst metal dowel-type fasteners, self-tapping screws (STSs) have become the preferred choice because they can be installed without predrilling, making STSs a cost-efficient solution. These types of connections are typically assumed to be effective in transmitting primarily shear forces [36,37]. Flexural performance of splice connections in CLT panels is investigated in [38], where the moment capacity, rotational rigidity, and ductility of half-lap and single-spline CLT connections using STSs and bolts are compared. Similarly, the authors in [39] investigated the out-of-plane performance of edge-to-edge connections employing STSs in half-laps and single splines, when the direction of the applied moment is especially observed. In [40], the authors tested edge-connected CLT panels using screwed LVL splines under out-of-plane bending and used various diameters, lengths and angles of STSs.

For a moment-resisting connection of two CLT panels, glued-in rods are used, which provide an efficient and, at the same time, aesthetically very favourable method of connecting two wooden elements. This type of connection is well researched and used mainly in the field of glued laminated timber structures [41]. Its use in CLT panels is still less common. However, several authors have also addressed this issue [42–45]. In the mentioned works, the emphasis is placed on the resistance and/or stiffness of the glued rod under uniaxial stress (in tension or compression), considering the specifics of the CLT panel, especially the alternation of longitudinal and transverse lamellas [35]. The bending action of this type of connection has not yet been sufficiently investigated, which is an undeniable contribution of this paper.

The presented moment-resisting connection is usable both in areas of sagging bending moments and in areas of hogging bending moments (above internal supports). This article also deals with the use of such a moment-resistant connection in composite CLT-reinforced concrete panels, where primary use is expected in areas of sagging moments.

2. Experimental Investigation

2.1. Description of Specimens and Material

The experimental programme focused on investigating the actual performance and behaviour of moment-resisting, embedded, bonded joints in CLT panels (or CLT–concrete composite panels). The joint itself consisted of high-strength steel rods that were glued into

prepared horizontal holes in two separate pieces of CLT panels using epoxy thixotropic adhesive, and these parts were then joined together.

In total, one CLT panel joint consisted of seven steel rods, with five rods installed at the bottom surface and two rods installed at the top surface of the panel. The geometry of the joint is shown in Figure 1. The primary reasons for such a structural joint design were the requirements to ensure sufficient moment resistance while using a minimum number of different components, and the architectural requirement that the joint should not be visible in exposed ceilings (i.e., be embedded), which also provides the additional benefit of increased fire resistance.

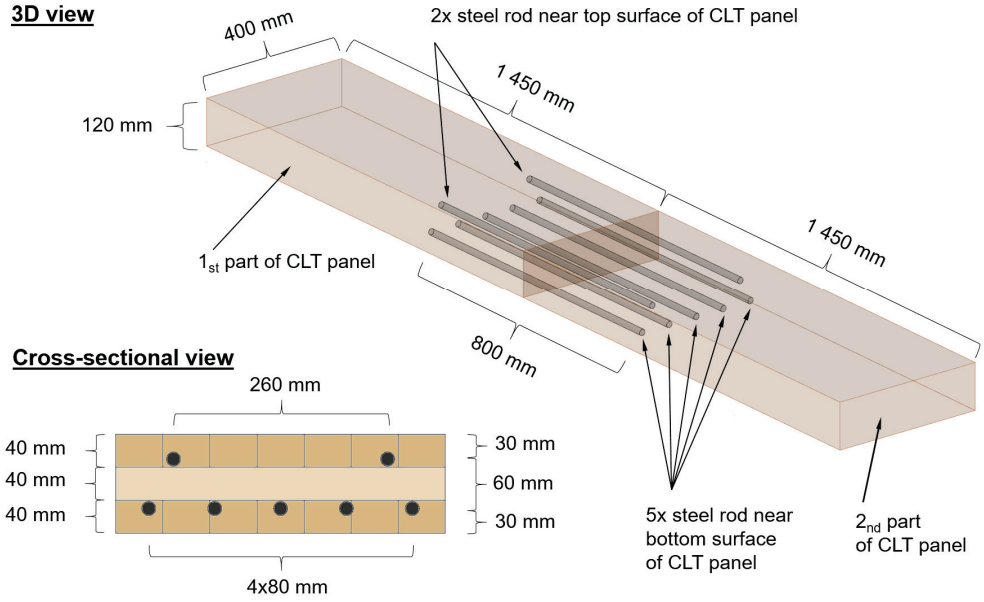

Figure 1. Embedded moment-resisting joint of CLT panels.

A total of 12 specimens were tested as part of the experimental programme, divided into four series, each containing three identical specimens:

- Series *A* (CLT panel without joints and without a concrete slab);
- Series *AC* (CLT panel without joints and with a concrete slab);
- Series *B* (CLT panel with joints and without a concrete slab);
- Series *BC* (CLT panel with joints and with a concrete slab).

The specimens were 2.9 m long and 0.4 m wide with a thickness of 120 mm (CLT panel) or 180 mm (CLT panel and concrete slab) and are shown together with their dimensions in Figure 2. Each CLT panel consisted of three layers of timber lamellae (L–T–L lay-up).

The epoxy adhesive consisted of two components: one was a dispersion of inorganic fillers and pigments in a mixture of modified epoxy resins and specialised additives, and the other was a mixture of amine hardeners. Based on experience from practical application, it is generally advisable to use adhesives with lower viscosity. The compressive strength of the used adhesive after 14 days is 85 MPa, and the compressive modulus of elasticity is 7800 MPa.

In the case of CLT panels with a 60 mm thick concrete slab, flat-head wood screws with a diameter of Ø8 mm and a length of 140 mm were used as shear connectors. The screws were installed in the CLT panels at a 45° angle, with a timber penetration of 80 mm. A total of 144 screws were used per panel. Their placement is shown in Figure 3. The primary purpose of using inclined screws is to ensure the transfer of shear flow at the concrete–timber interface. The anti-delamination effect of using these screws is limited due to the insufficient screw penetration into the middle (transverse) layer of the CLT panel, and

the screws do not penetrate the bottom (longitudinal) layer at all. The number and layout of shear connectors were determined using a standard procedure according to Eurocode 5 [46] to ensure that shear connection failure would not occur during the experimental testing. The 45° screw angle was chosen to achieve the highest possible resistance and especially the stiffness of the composite CLT–concrete cross-section [47,48].

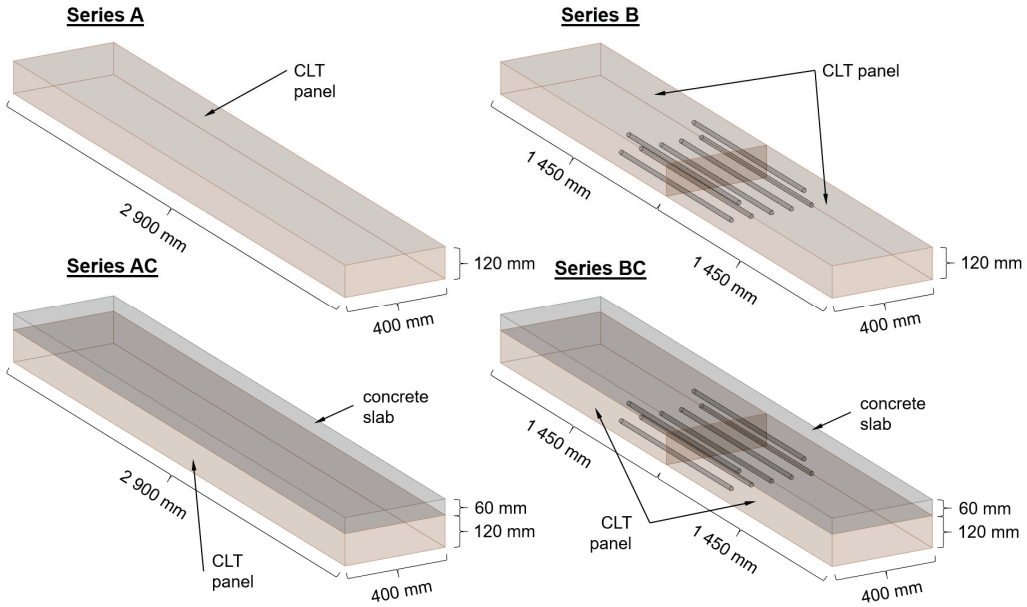

Figure 2. Four series of tested specimens.

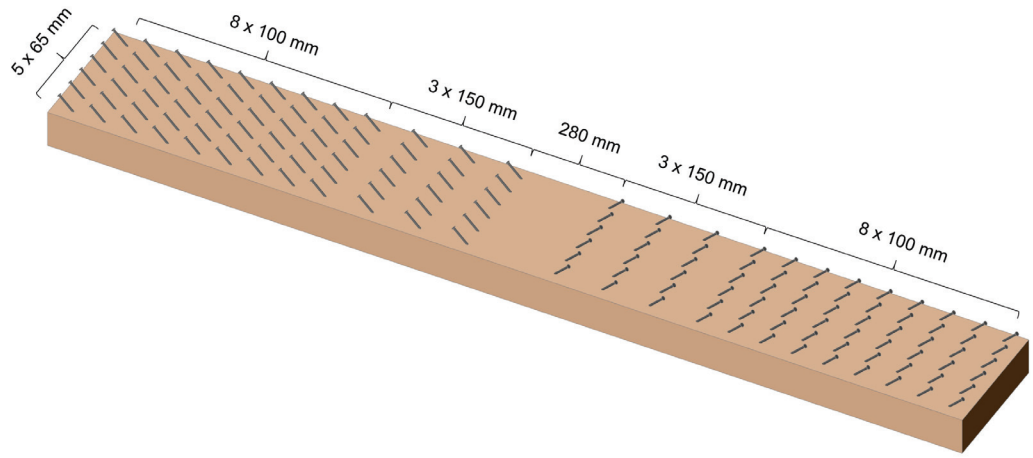

Figure 3. Layout of shear connectors.

During the casting of the concrete slab, samples of concrete and reinforcement steel were taken for further laboratory testing of materials. Concrete cubes with dimensions 150 × 150 × 150 mm were properly measured, weighed, and subjected to destructive compressive testing. The average cube compressive strength of concrete at the time of testing the AC and BC series specimens was $f_{cm,cube}$ = 35.7 MPa. B500B concrete reinforcement was also used in the concrete composite slab, with four Ø8 mm reinforcement bars used in the longitudinal direction. According to the material tests preformation, the average yield strength of the reinforcement was f_y = 560.0 MPa.

2.2. Test Set-Up and Loading Procedure

Individual specimens were tested in separate series. Each specimen was supported on a pair of steel bearings to ensure the most accurate static configuration of a simple supported beam with a span of 2.50 m. Two steel plates and rollers were placed on the upper surface of the specimens, on which a load-bearing crossbeam made of a pair of *IPE 160* rolled profiles was placed. The specimens were thus subjected to four-point bending. A distribution plate with a modified hemispherical surface was placed at the mid-span on the upper surface of the crossbeam, against which the piston of the hydraulic cylinder rested during the test. The hydraulic cylinder, with a maximum capacity of 400 kN and its aggregate and electronic system, ensured controlled loading of the specimens by incremental deformation. The loading speed rate was 0.05 mm/s for all specimens. A photograph of the specimen under test is given in Figure 4. During the loading of the specimens, the load and its corresponding displacement were recorded for the specimens at the midpoint of the span and above the supports. In the case of selected specimens with joints, the opening of the joint-gap was also recorded. In addition to recording displacements, strains were also measured near the middle of the panel span, on both the upper and lower surfaces. Monitoring the strains was an important part of the experiment, primarily for the accurate control of the testing process and the prediction of the maximum load acting on the specimens. All displacement transducers and strain gauges, together with the output from the force sensor, were connected to a single data acquisition bus. The schematic arrangement of the test and the positions of the sensors for each series of tests are shown in Figure 5. The displacement transducers (marked as *DS*) record the vertical displacements and gap openings (in specimens with joints), while the strain gauges (labelled as *SG*) measure the strains on the top and bottom surfaces of the specimens.

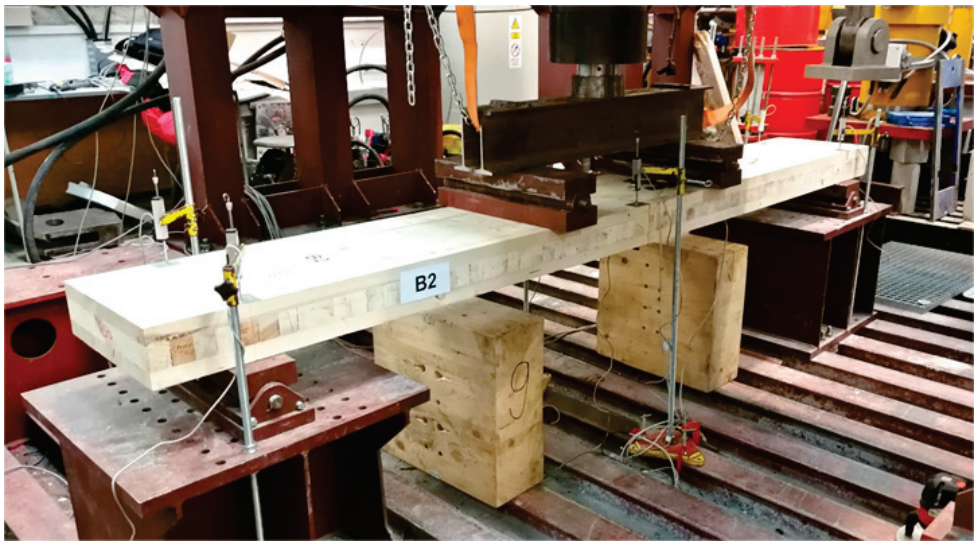

Figure 4. Photograph of the specimen under test.

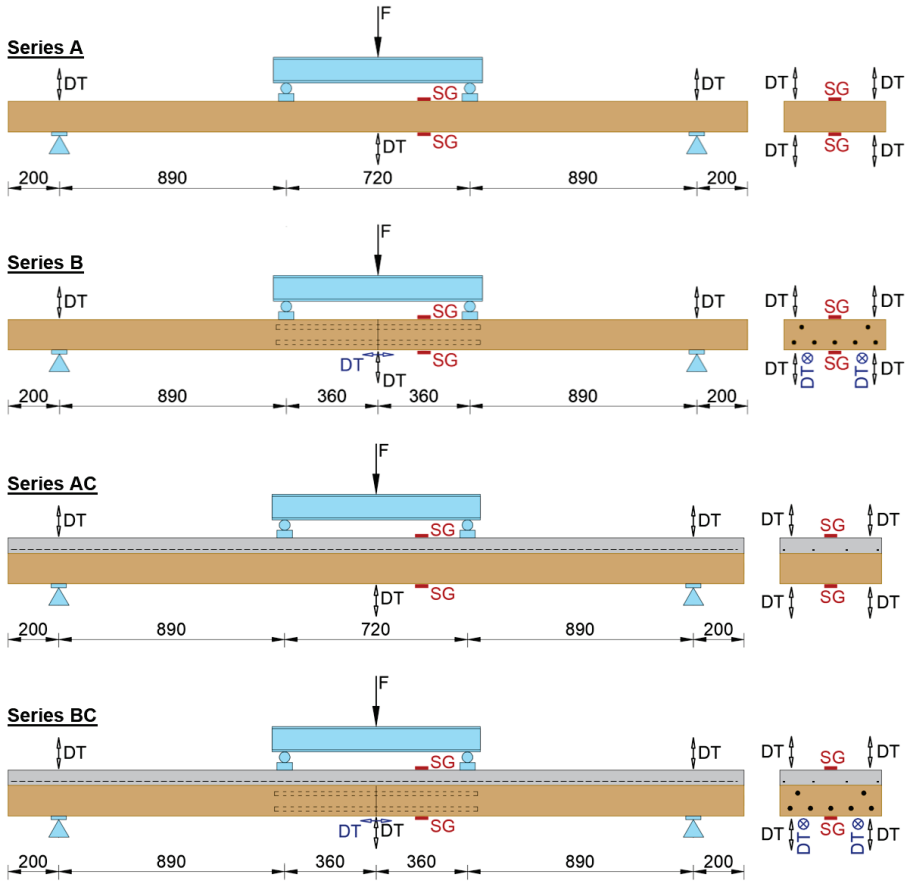

Figure 5. Geometric scheme of test set-up for each series.

3. Experimental Results

During the experimental programme, the applied load, strains on the surface, and displacements were recorded; for series *B* and *BC*, the opening of the joint-gap was also monitored, as described in Section 2. The experimental results are summarised in the figures below. The most important outcome is the set of load–displacement relationships, which—for clarity—are presented across multiple graphs in Figure 6. Based on the plots, the stiffness effect of individual specimens and significant differences in resistance between individual series (depending on structural design) are clearly visible.

In the case of specimens with a moment-resisting joint in the middle of their span, the joint-gap opening (*s*) was also recorded. Due to technical issues during the experimental testing of specimen *B1*, this piece of data (*s*) was not recorded for this specimen. For the purposes of this study, the missing values were reconstructed using second-degree polynomial regression with an interaction term. The model was calibrated on the complete datasets of specimens *B2* and *B3* (load *F*, mid-span displacement *w*, and joint-gap opening *s*) and then evaluated with the measured data of *B1*, consistent with its load–displacement curve. The regression model used to estimate the probable joint-gap opening was

$$S_{gap} = \beta_0 + \beta_1 \cdot F + \beta_2 \cdot w + \beta_3 \cdot F^2 + \beta_4 \cdot w^2 + \beta_5 \cdot F \cdot w \quad (1)$$

where

S_{gap}: reconstructed joint-gap opening (estimated from the regression model);

F: load;

W: mid-span displacement;

β_0–β_5: model coefficients determined by the least-squares method based on complex datasets of specimens *B2* and *B3*.

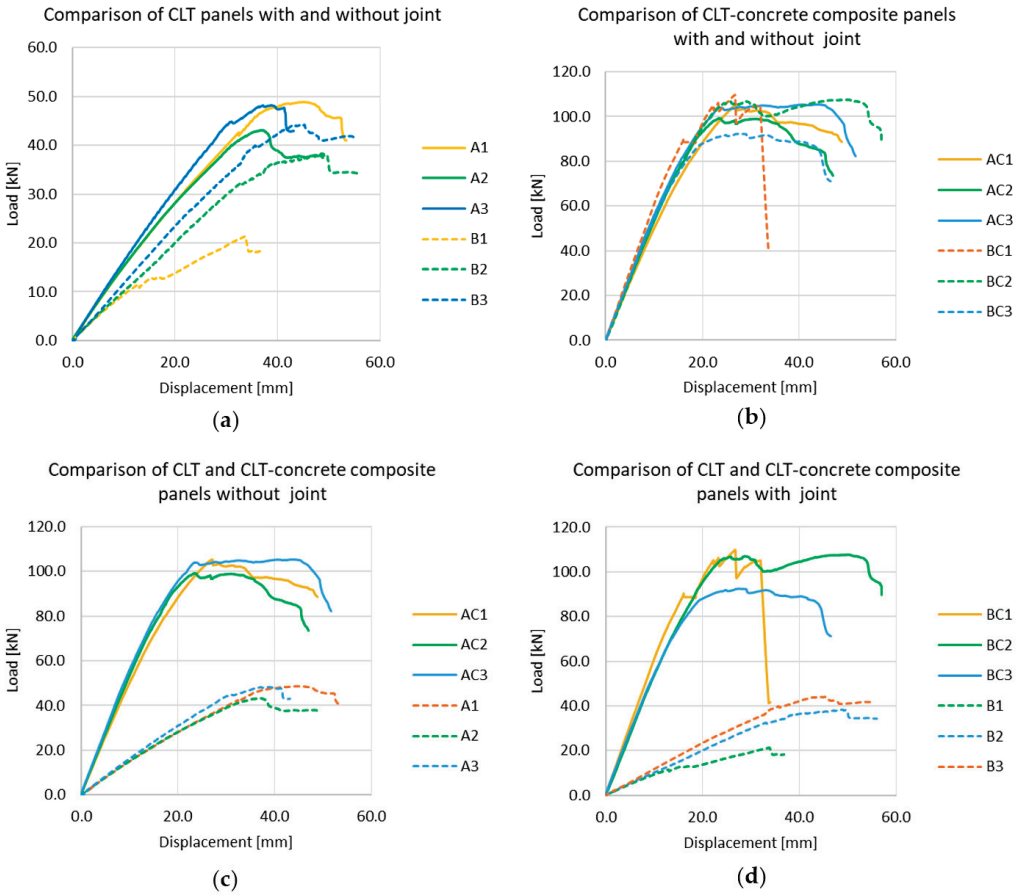

Figure 6. Load–displacement behaviour: (**a**) CLT panels with and without joint; (**b**) CLT–concrete composite panels with and without joint; (**c**) CLT panels and CLT–concrete composite panels without joint; (**d**) CLT panels and CLT–concrete composite panels with joint.

The model was validated by comparing its outputs with the measured data of specimens *B2* and *B3* and achieved very good agreement (coefficient of determination $R^2 > 0.98$). In all figures in this paper, the reconstructed (estimated) joint-gap opening data are clearly distinguished as *B1** from the directly measured data. Figure 7 presents the load vs. joint-gap opening response, while Figure 8 illustrates the relationship between mid-span displacement and joint-gap opening.

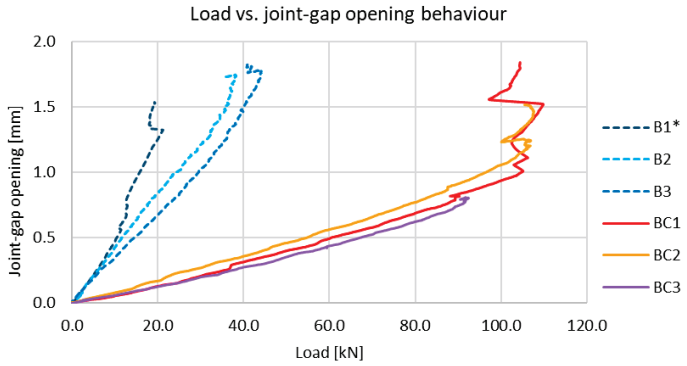

Figure 7. Relationship between load and joint-gap opening (*B1**—estimated data).

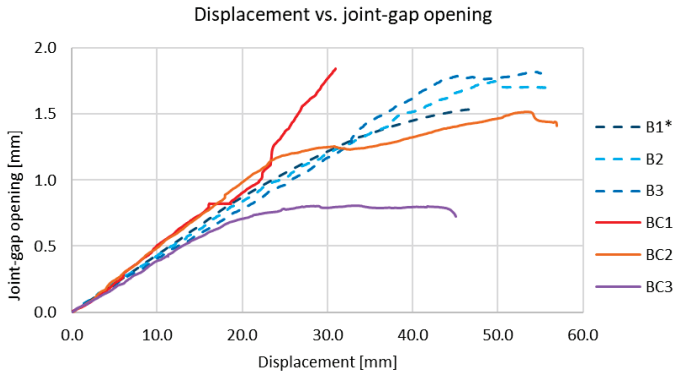

Figure 8. Relationship between min-span displacement and joint-gap opening (*B1**—estimated data).

The outputs from the strain-gauge measurements (strains) were transformed into stress and, for better clarity, they are presented as surface stress on the top (compression, σ−) and bottom (tension, σ+) faces of the panels during the testing (Figure 9).

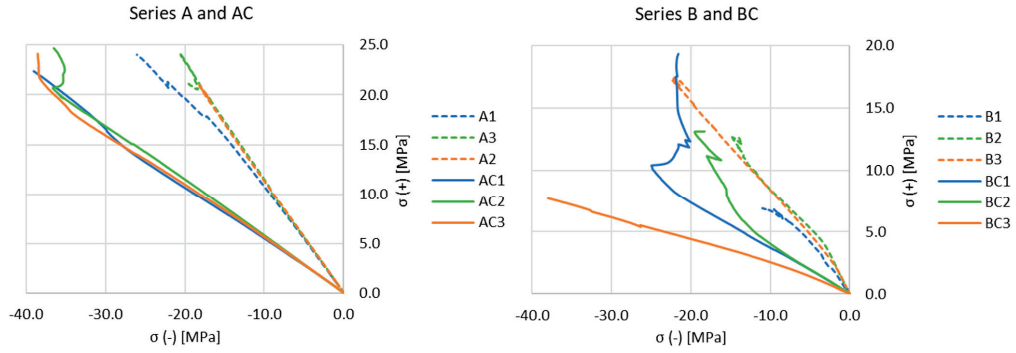

(**a**) (**b**)

Figure 9. Surface stress pairs from strain-gauge measurements during four-point bending. (**a**) Series *A* and *AC*. (**b**) Series *B* and *BC*.

The curves were obtained by pairing synchronous σ− and σ+ readings throughout the test, so the trajectories directly reflect the relationship between the two surface stresses at the same load level. The primary purpose of the strain-gauge measurements was to indicate the stress levels during the experiments to enable proper test control.

For each test, the failure mechanism of the specimen was documented. The specimens failed by rolling shear, delamination, joint failure, or a combination of flexural and joint failure. Table 1 summarises the ultimate load recorded during the test, the corresponding mid-span deflection, and the observed failure mode (documented in Figure 10).

Table 1. Ultimate load with corresponding mid-span deflection and failure mode for all specimens.

Specimen	Ultimate Load F_{max}	Deflection at F_{max}	Failure Mode
-	[kN]	[mm]	-
A1	48.80	45.21	shear
A2	43.12	37.26	delamination and shear
A3	48.24	37.16	partial delamination and shear
B1	21.31	33.71	joint
B2	38.29	48.97	shear
B3	44.14	45.26	partial delamination and shear

Table 1. *Cont.*

Specimen	Ultimate Load F_{max}	Deflection at F_{max}	Failure Mode
-	[kN]	[mm]	-
AC1	105.43	27.16	shear
AC2	99.12	23.40	shear
AC3	105.40	24.14	partial delamination and shear
BC1	109.71	26.70	joint and bending
BC2	107.65	28.91	shear
BC3	92.49	27.44	delamination and shear

Figure 10. Failure of specimens during experimental testing.

It has been reaffirmed that rolling shear in the perpendicular layers of CLT panels is often a limiting factor in terms of the resistance of CLT panels subjected to out-of-plane loading [49–51]. This is related to the very low strength of wood under the shear stress acting on the radial–tangential plane perpendicular to the grain. The connection to the concrete slab appears to have no significant effect on this phenomenon.

4. Discussion

4.1. Observed Behaviour

The performed experimental measurements demonstrated a number of interesting dependencies related to both the action of the joint and its stiffness, as well as to the composite action between the CLT panel and the reinforced-concrete slab.

In each series, three specimens were tested, which represents the necessary minimum for a basic statistical assessment of the experimental programme. The ultimate load achieved during the test is analysed as the first and most important parameter. The graph in Figure 11

clearly presents the ultimate force value (F_{max}) for each specimen, the average ultimate force value achieved within the individual series, as well as the standard deviation (SD).

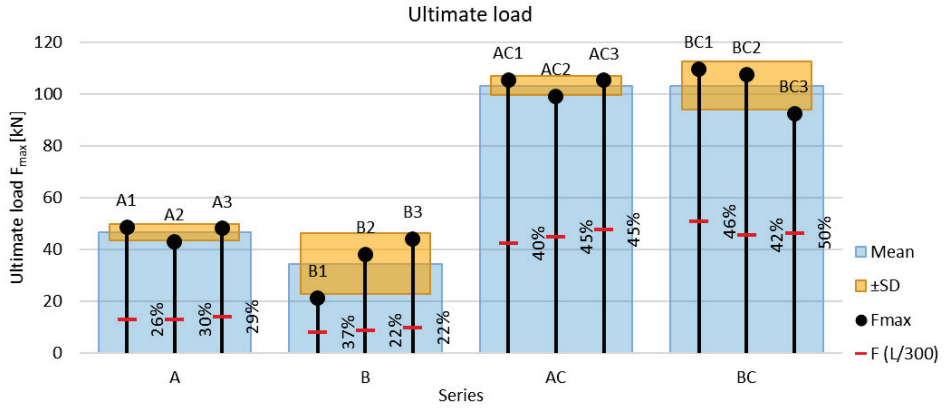

Figure 11. Ultimate load by series (Mean ± SD) with SLS Marker at $L/300$.

In general, the series containing a moment-resisting joint exhibits a markedly higher SD, indicating greater variability in the ultimate load and failure mechanism. Since the failure modes included rolling shear, delamination, and joint failure (including flexural and joint failure combination), the larger SD indicates that some specimens with moment-resisting joints were probably close to joint failure. If there were no failure due to shear or due to delamination, probably even with a relatively small increase in the load, joint failure could occur.

In addition to the ultimate resistance of the system, a comparison from the point of view of limit deflections is also crucial. In the context of serviceability limit states, the limit value $L/300$, as specified in EN 1995 and its national annexe [46,52], is used as the criterion for deflection. The value of the load at the limit deflection level is shown in the graph in Figure 11 as a percentage of the ultimate load.

Another important investigated parameter is the determination of the initial stiffness and the comparison between individual specimens. Initial stiffness K_0 was evaluated as the least-squares slope of the load–displacement (F-w) response within the linear range 10–40% of ultimate load (F_{max}), following EN 408 [53] procedures for bending tests (and, by analogy, EN 26891 [54] for joints). For CLT panels, EN 16351 [55] refers to EN 408 for stiffness evaluation. The graph in Figure 12 documents the initial stiffness of individual specimens, the mean value within each series, and also the standard deviation.

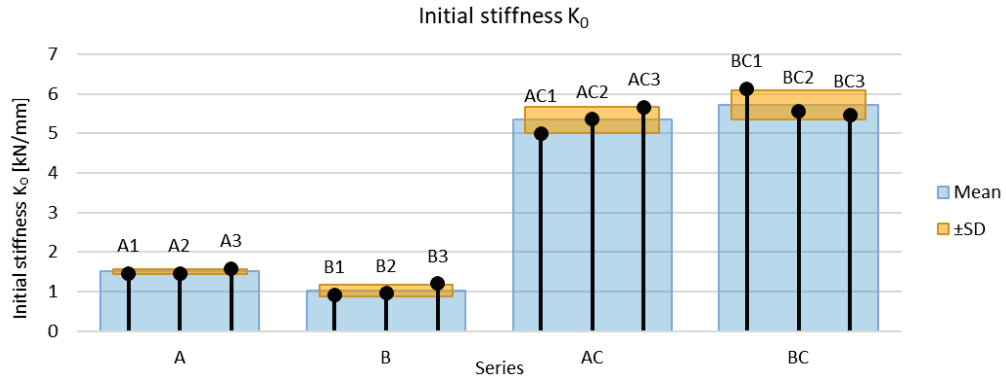

Figure 12. Initial stiffness by series (Mean ± SD).

In the case of CLT panels without a reinforced concrete slab (series *A* and *B*), the mean initial stiffness of the specimens with a joint is approximately 32% lower than that of the CLT panels without a joint. In the case of CLT panels with a reinforced concrete slab (series *AC* vs. *BC*), the average initial stiffness of the specimens with and without a joint is approximately the same (the difference is roughly at the level of the standard deviation).

The presence of the reinforced-concrete slab causes an average increase in initial stiffness of more than ~3.5 times for CLT panels without a joint and more than ~5.5 times for CLT panels with a joint.

Another view of the stiffness of individual CLT panels is provided in Figure 13, which shows the normalised stiffness K_{sec}/K_0 versus the normalised load F/F_{max}. For specimens with a joint (series *B* and series *BC*), significant differences in the development of K_{sec}/K_0 can be clearly observed between specimens within the same series, indicating considerable inter-specimen variability in the shape of the curves. In contrast, for the series without a joint (series *A* and *AC*), the inter-specimen variability is relatively small.

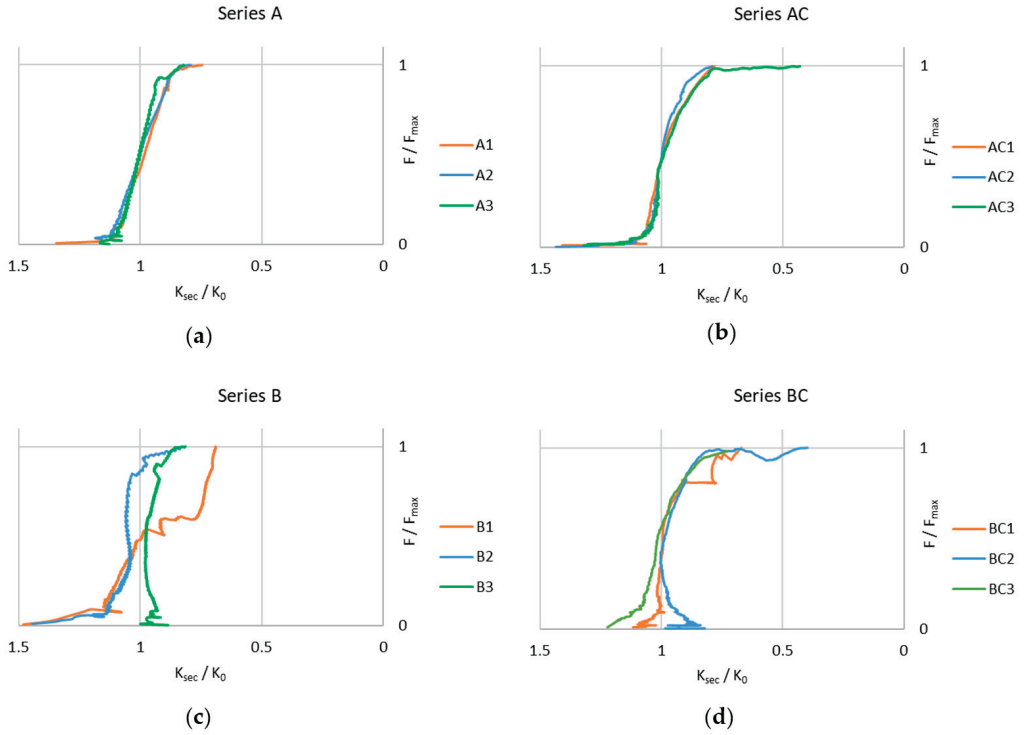

Figure 13. Normalised stiffness K_{sec}/K_0 versus normalised load F/F_{max}: (**a**) CLT panel without joint; (**b**) CLT–concrete composite panel without joint; (**c**) CLT panel with joint; (**d**) CLT–concrete composite panel with joint.

For completeness, Figures 14 and 15 illustrate the gradual decrease in stiffness of the specimens from series *A* and *B* as well as series *AC* and *BC*, as a function of the increasing bending moment at midspan ($M = (F/2 \cdot a)$). Pronounced differences in stiffness and its reduction are again particularly evident between specimens of series *A* and *B*.

Based on the normalised stiffness graphs ($K_{sec}/K_0 - F/F_{max}$) and the relationship between bending moment and secant stiffness ($M - K_{sec}$), the global stiffness was transformed into the apparent bending stiffness EI_{app}. As the deflection w is proportional to the ratio F/EI, for a given test arrangement geometry (L—distance between supports; a—distance from the support to the point of load application), the following expression can be written:

$$EI_{app} = \Delta_{geom}(L;a)\frac{F}{w(F)} = \Delta_{geom}K_{sec}(F) \tag{2}$$

where

EI_{app}: apparent bending stiffness;

Δ_{geom}: geometric coefficient taking into account the position of the load and the boundary conditions;

F: load;

w: displacement;

K_{sec}: secant stiffness.

From the above, the specific EI_{app} for a specimen subjected to four-point bending can be determined, assuming the applied load F and displacement w are known, as follows:

$$EI_{app} = \frac{F \cdot a \cdot (3L^2 - 4a^2)}{48w} \tag{3}$$

EI_{app} includes not only the standard bending stiffness of the cross-section but also all system compliances (shear deformations of the CLT panel, slip at the CLT–concrete interface, joint behaviour, etc.). The EI_{app} values were subsequently compared directly with the joint-gap opening—see Figure 16 (note: the joint-gap opening of specimen B1, designated as B1*, was estimated using a regression model; see Section 3). For the specimens with a composite reinforced-concrete slab, a more significant decrease in EI_{app} stiffness can be observed with increasing joint-gap opening (s).

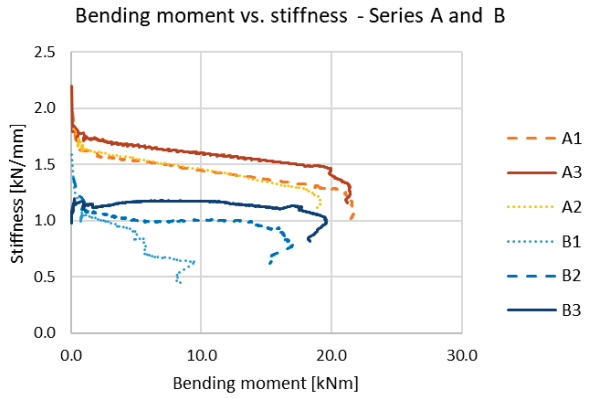

Figure 14. Bending moment versus stiffness for CLT panels without concrete slab without (series *A*) and with joint (series *B*).

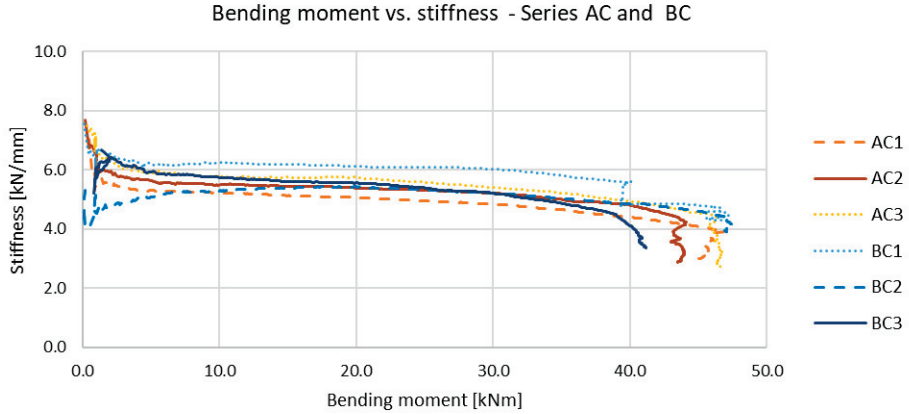

Figure 15. Bending moment versus stiffness for CLT–concrete composite panels without (series *AC*) and with joint (series *BC*).

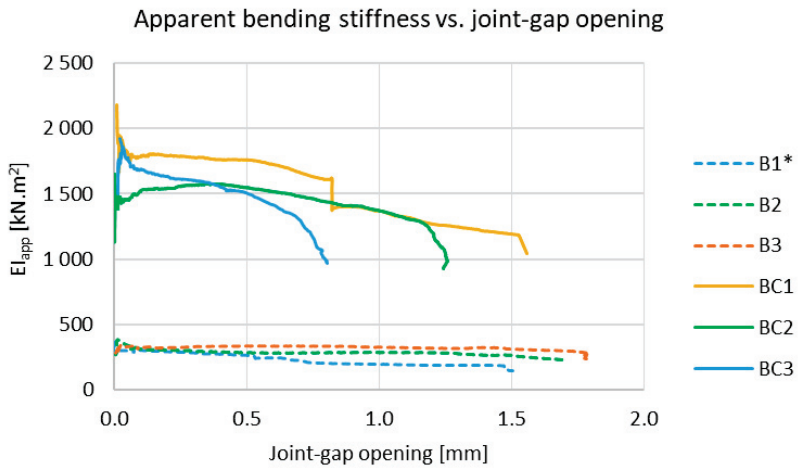

Figure 16. Joint-gap opening versus apparent bending stiffness EI_{app} (*B1**—estimated data).

For a comprehensive assessment of the actual behaviour of the investigated specimens, it is not entirely sufficient to evaluate only the load capacity and stiffness of the system. A suitable integrated indicator is the energy U, i.e., the work performed by the load during the deformation of the specimen. While the dependencies $K_{sec}/K_0 - F/F_{max}$; $M - K_{sec}$; and $EI_{app} - s$ (joint-gap opening) describe the changes in the stiffness of the element and the mechanical behaviour of the joint, the energy provides another comparable metric across the series of specimens and summarises the total work of the system (in this case, until F_{max} is reached). This allows for a comparison of the usable deformation capacity and the total toughness of the system. The energy was determined as the area under the load–displacement curve (see Figure 17) for each specimen:

$$U = \int F dw \approx \sum \frac{1}{2}(F_{i+1} + F_i)(w_{i+1} - w_i) \tag{4}$$

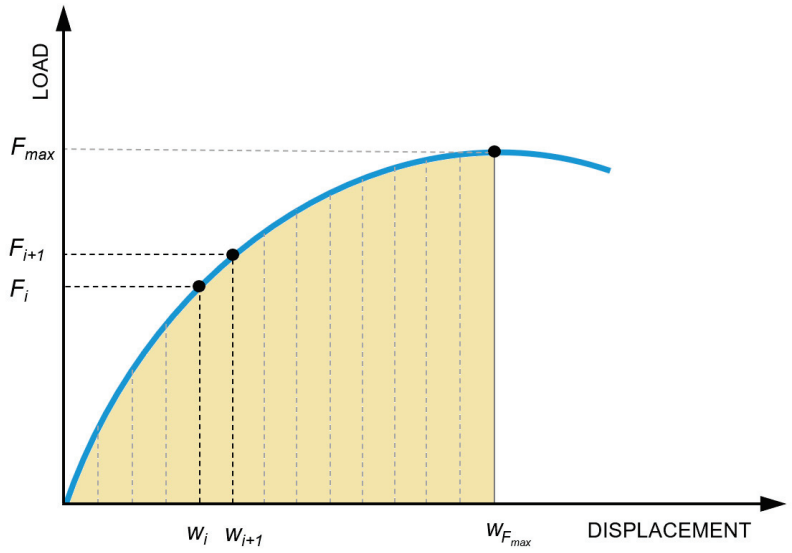

Figure 17. Energy as area under load–displacement curve.

The calculations were performed by interpolating the load–displacement data at the target load levels {0, 25, 50, 75, 100% F_{max}} for each specimen and subsequently computing the partial increments of ΔU over the corresponding intervals. The graphs in Figure 18 present the cumulative energy as a function of load level for each series. In graphs (a–d), the average value of the series is shown, along with the standard deviation, indicated by a coloured bar (±SD; n = 3). Plot (e) compares the energy increment between series. The bar

chart in Figure 19 shows the energy increment within individual quartiles, as well as the total energy for each specimen.

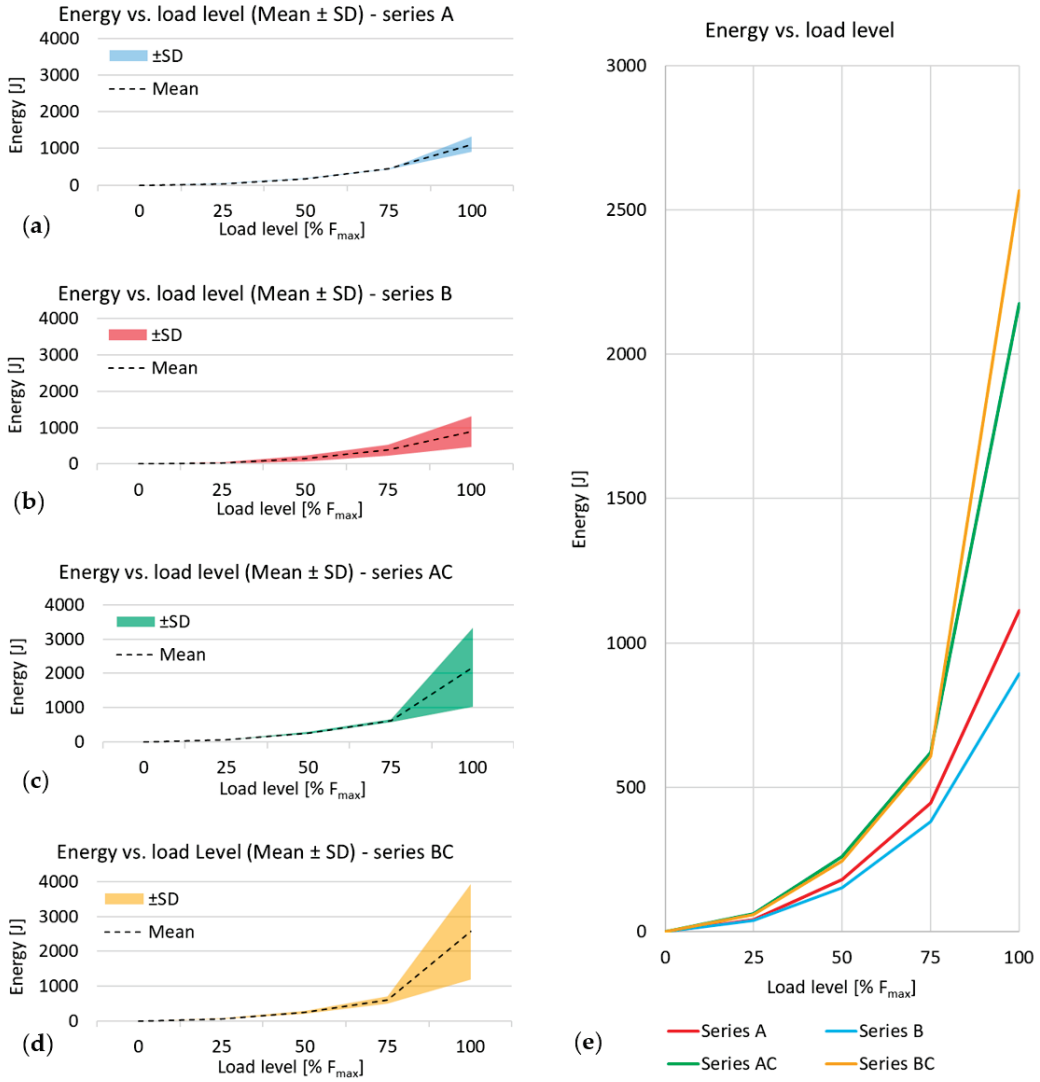

Figure 18. Energy vs. load level: (**a**) CLT panel without joint; (**b**) CLT panel with joint; (**c**) CLT–concrete composite panel without joint; (**d**) CLT–concrete composite panel with joint; (**e**) comparison of all series.

The first two energy increments ($\Delta U_{0\rightarrow 25\%\ Fmax}$; $\Delta U_{25\rightarrow 50\%\ Fmax}$) primarily encompass the elastic phase of loading of the specimens. The subsequent intervals ($\Delta U_{50\rightarrow 75\%\ Fmax}$; $\Delta U_{75\rightarrow 100\%\ Fmax}$) already encompass the post-elastic phase under loading and the associated nonlinear redistribution of internal forces in the specimen during the test. For all specimens, the largest increment occurs in the final interval $\Delta U_{75\rightarrow 100\%\ Fmax}$, which is also reflected by the sharp rise in the curves in Figure 18. As the load level increases, the magnitude of the standard deviation grows markedly.

4.2. Possible Concept of a Theoretical Model of the Joint

Experimental testing has demonstrated the actual behaviour of the moment-resisting, embedded joint of CLT panels from several aspects. The obtained measurements provide a solid basis for the successful application of the proposed solution in practice, particularly when used as part of CLT–concrete composite panels. However, for the practical design of the connection, it is first necessary to at least indicate the concept of a theoretical (mechanical) model, which will be addressed systematically in future analyses. Based on

the premise that common, practical, engineering calculations of simple structural elements should not be primarily based on complex nonlinear numerical models (typically created in research-and-development software such as *ANSYS*, *ABAQUS*, *ADINA*, etc.), at this stage, a concept based on the generally known and widely used component method appears to be more suitable. The component method began to be applied in the 1970s and 1980s, initially on bolted moment-resisting joints of steel structures [56,57]. Later, it was elaborated in detail and became part of Eurocode 3—EN 1993-1-8 [58], where the component method is presented as a separate design framework. The method has also become part of the theory of connections of timber structures and is commonly used in it for the theoretical description of the actual action of connections [59–61]. The method utilises the decomposition of connections (joints) into basic components (compression, tension, and shear), which have their own defined stiffness, resistance, and deformation capacity. In the case we studied, a single type of connection is analysed (see Figure 1), which is, however, used in two different types of structures (ceiling slabs consisting only of CLT panels and CLT–concrete composite slabs). Figure 20 documents the concept of a joint defined using the component method and loaded with a bending moment, both in the case of separate CLT panels (a) and in the case of CLT panels coupled to a reinforced-concrete slab (b, c).

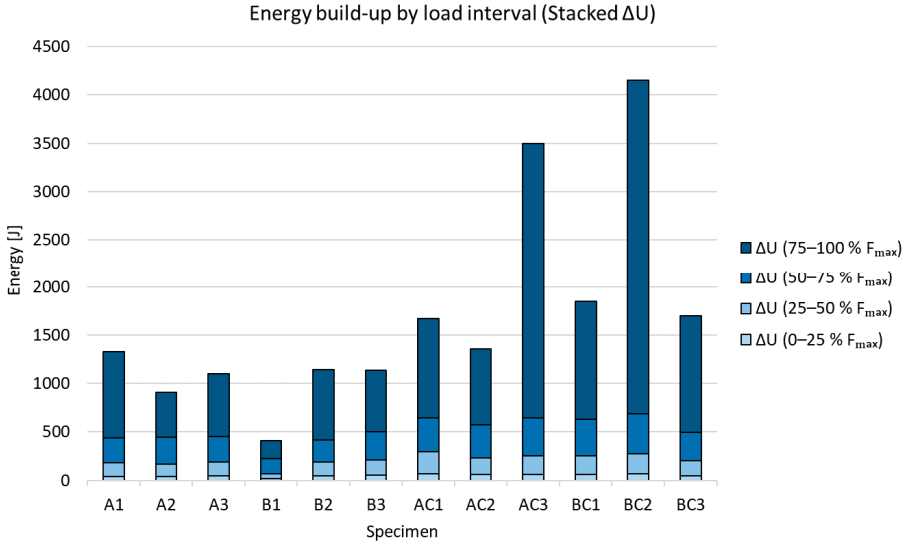

Figure 19. Energy build-up by load interval for all specimens.

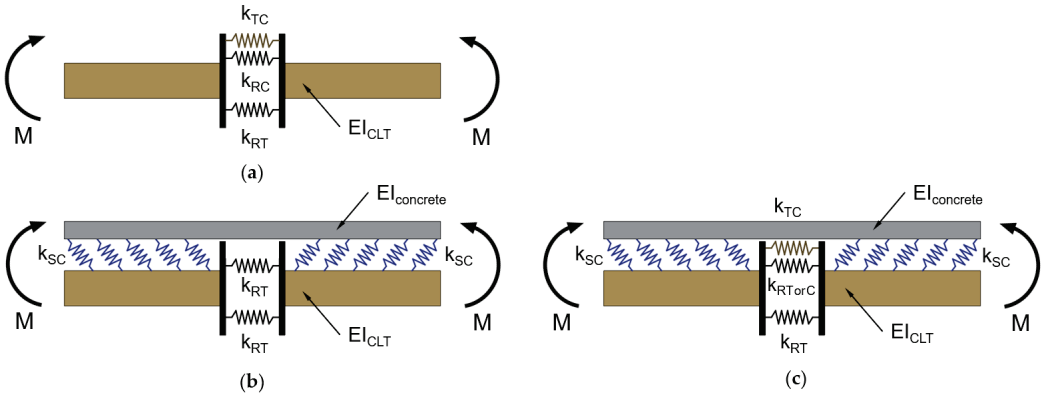

Figure 20. Schematic concept of the joint based on component-method model: (**a**) CLT panel; (**b**) CLT–concrete composite slab—neutral axis lies in concrete part; (**c**) CLT–concrete composite slab—neutral axis lies in CLT panel.

In the case of CLT–concrete composite slabs, the situation is more complicated, since the CLT panel is divided and the reinforced-concrete slab is solid. In addition to determining the stiffness of the connection between the CLT panel and the reinforced-concrete slab (component characterised by stiffness coefficient k_{SC}), the position of the neutral axis of the composite cross-section must be evaluated. The degree of composite action (k_{SC}) influences the neutral-axis position via the effective stiffness but does not determine it directly. In case the neutral axis lies in a reinforced-concrete slab (standard case), the entire CLT panel is stressed in tension, the compression is transmitted only by the reinforced-concrete slab, and the model uses only the stiffness coefficient k_{RT} in this area (representing the action of glued-in steel rods in tension). If the neutral axis falls within the CLT, the timber compression component (characterised by stiffness coefficient k_{TC}) becomes active in the upper part of the CLT; the lower row of glued-in rods is in tension (k_{RT}), while the upper row may be in tension (k_{RT}) or in compression (k_{RC}), depending on the neutral axis position. Further research is needed for the experimental determination of the individual components, especially for the determination of k_{RT} and k_{RC} (predominantly bilinear behaviour [60,62,63]), which are significantly influenced not only by the materials used (steel, adhesive, timber) but also by the position of the glued-in rod within the individual layers of the panel (transverse/longitudinal lamellae) [35]. It will also be necessary to pay attention to the stiffness coefficient k_{TC}, which describes the behaviour of the contact between timber elements parallel to the grain, where predominantly nonlinear behaviour is assumed [64–66].

5. Conclusions

The presented experimental research of the embedded moment-resisting joint of CLT panels with glued-in high-strength steel rods demonstrated sufficient resistance and stiffness of the designed solution.

In the case of simple CLT panels without a reinforced-concrete slab, the joint resistance is approximately 74% of their rolling shear/delamination capacity (pure bending failure of the CLT panels without joint did not occur in any case). The only specimen that significantly reduced the mean resistance of series *B* (CLT panels with a joint) was *B1*—it failed due to joint failure. This reduction in resistance can probably be associated with the potentially imperfect joint execution and/or defects in the timber (or in the CLT panel execution) near the joint. When comparing the initial stiffness K_0, the stiffness of the specimens with the joint reaches approximately 68% of the initial stiffness of the whole CLT panel.

Another important part of this research was the implementation of composite action between the CLT panels and a reinforced-concrete slab, as well as its combination with the moment-resisting joint. The experimental results generally demonstrate the high efficiency of the composite action and its effect on increasing the resistance and stiffness of the tested structural members. For CLT–concrete composite panels without a joint, the ultimate load F_{max} increased, on average, by 121%; for specimens with the joint, the resistance increased by up to 198%. When comparing loads at the serviceability limit deflection *L/300* (i.e., 8.33 mm), the increase in load $F_{L/300}$ due to composite action was up to 242% for specimens without a joint and 442% for specimens with the joint.

In the case of CLT–concrete composite panels, the moment-resisting joint does not significantly limit the resistance of the structural member (because the governing failure mode is again predominantly rolling shear or delamination). The essential finding is that the stiffness of CLT–concrete composite panels with a joint is practically identical to the CLT–concrete composite panels without a joint. The only specimen that failed due to bending stress of the element (in combination with joint failure) was *BC1*, which also reached the highest ultimate load value, F_{max} = 109.71 kN, among all experimentally tested specimens.

Based on the relatively low value of the standard deviation within the series, it is possible to predict that if specimens *BC2* and *BC3* had not failed in rolling shear/delamination, failure would have occurred due to a combination of bending and joint failure, even with a relatively small increase in load.

Based on the assessment of the energy required to achieve ultimate load F_{max}, it is also necessary to point out the sufficient toughness demonstrated by the specimens with the joint compared to the whole CLT panels.

From a practical point of view, it is also necessary to highlight potential risks in joint fabrication based on experience from specimen production. These are primarily related to the joint geometry (maintaining the correct spacing and perpendicularity of the holes, proper alignment of the connected CLT panels), which can be ensured by precise machining and drilling. A second potential risk lies in the correct selection and application of the adhesive—appropriate viscosity must be ensured, together with proper (complete) injection into the holes.

From the perspective of further research, it will be necessary to focus primarily on developing a detailed theoretical model based on the component method and on analysing practical design procedures for this type of joint.

Author Contributions: Conceptualization, M.F.; methodology, M.F. and J.G.; software, M.F.; validation, J.G., P.K. and M.F.; formal analysis, J.G.; investigation, M.F. and J.G.; resources, P.K.; data curation, J.G.; writing—original draft preparation, M.F.; writing—review and editing, J.G.; visualisation, J.G.; supervision, P.K.; project administration, M.F.; funding acquisition, P.K. All authors have read and agreed to the published version of the manuscript.

Funding: This research is supported by the Slovak Research and Development Agency under contract No. APVV-23-0626 and by Research Project No. 1/0321/24 of the Slovak Grant Agency.

Data Availability Statement: The data presented in this study are available on reasonable request from the corresponding author.

Acknowledgments: The material for the specimens was provided by Femada, Ltd.

Conflicts of Interest: The authors declare no conflicts of interest.

References

1. Schickhofer, G. *Starrer und Nachgiebiger Verbund bei Geschichteten, Flächenhaften Holzstrukturen*; Graz University of Technology: Graz, Austria, 2013; ISBN 978-3-85125-268-2.
2. 100 Projects UK CLT. Produced by Waugh Thistleton Architects on behalf of the Softwood Lumber Board & Forestry Innovation Investment. Printed in Canada, 2018. Available online: https://waughthistleton.com/100-projects-uk-clt/ (accessed on 28 September 2025).
3. Swedish Wood. The CLT Handbook. CLT Structures—Facts and Planning. Stockholm, May 2019. Available online: https://www.swedishwood.com/publications/list_of_swedish_woods_publications/the-clt-handbook/ (accessed on 28 September 2025).
4. Karacabeyli, E.; Gagnon, S. Eds. Canadian CLT Handbook. 2019. Available online: https://web.fpinnovations.ca/clt/ (accessed on 28 September 2025).
5. Kremer, P.D.; Guiver, J. Mass Timber Construction in Australia and New Zealand–Status, and Economic and Environmental Influences on Adoption. *Wood Fiber Sci.* **2018**, *50*, 128–138. [CrossRef]
6. Abed, J.; Rayburg, S.; Rodwell, J.; Neave, M. A Review of the Performance and Benefits of Mass Timber as an Alternative to Concrete and Steel for Improving the Sustainability of Structures. *Sustainability* **2022**, *14*, 5570. [CrossRef]
7. Structural Timber Association, Technical Bulletin 01—Timber as a Structural Material—An Introduction. Available online: https://www.structuraltimber.co.uk/ (accessed on 31 July 2025).
8. Harte, A.M. Mass Timber–the Emergence of a Modern Construction Material. *J. Struct. Integr. Maint.* **2017**, *2*, 121–132. [CrossRef]
9. Ibn-Mohammed, T.; Greenough, R.; Taylor, S.; Ozawa-Meida, L.; Acquaye, A. Operational vs. embodied emissions in buildings—A review of current trends. *Energy Build.* **2013**, *66*, 232–245. [CrossRef]
10. Taylor, A.; Gu, H.; Nepal, P.; Bergman, R. Carbon Credits for Mass Timber Construction. *Bioprod. Bus.* **2023**, *8*, 1–12. [CrossRef]

11. Andersen, J.H.; Rasmussen, N.L.; Ryberg, M.W. Comparative life cycle assessment of cross-laminated timber building and concrete building with special focus on biogenic carbon. *Energy Build.* **2022**, *254*, 111604. [CrossRef]
12. Chen, C.X.; Pierobon, F.; Jones, S.; Maples, I.; Gong, Y.; Ganguly, I. Comparative life cycle assessment of mass timber and concrete residential buildings: A case study in China. *Sustainability* **2022**, *14*, 144. [CrossRef]
13. Pierobon, F.; Huang, M.; Simonen, K.; Ganguly, I. Environmental benefits of using hybrid CLT structure in mid-rise non-residential construction: An LCA-based comparative case study in the U.S. Pacific Northwest. *J. Build. Eng.* **2019**, *26*, 100862. [CrossRef]
14. *EN 15804:2012+A2:2019*; Sustainability of Construction Works—Environmental Product Declarations—Core Rules for the Product Category of Construction Products. European Committee for Standardization, CEN: Brussels, Belgium, 2019.
15. *EN 15978:2011*; Sustainability of Construction Works—Assessment of Environmental Performance of Buildings—Calculation Method. European Committee for Standardization, CEN: Brussels, Belgium, 2011.
16. *ASTM E2921–22*; Standard Practice for Minimum Criteria for Comparing Whole Building Life Cycle Assessments for Use with Building Codes, Standards, and Rating Systems. ASTM International: West Conshohocken, PA, USA, 2023.
17. *ISO 14044:2006*; Environmental Management—Life Cycle Assessment—Requirements and Guidelines. International Organization for Standardization: Geneva, Switzerland, 2006.
18. *ISO 21930:2017*; Sustainability in Buildings and Civil Engineering Works—Core Rules for Environmental Product Declarations of Construction Products and Services. International Organization for Standardization: Geneva, Switzerland, 2017.
19. Wallner-Novak, M.; Koppelhuber, J.; Pock, K. *Cross-Laminated Timber Structural Design—Basic Design and Engineering Principles According to Eurocode*, 1st ed.; Working group of the Austrian timber industry for promotion of the application of timber; proHolz: Vienna, Austria, 2014; ISBN 978-3-902926-03-6.
20. Stieb, T.; Maderebner, R.; Dietsch, P. A Timber–Concrete–Composite Edge Connection for Two-Way Spanning Cross-Laminated Timber Slabs—Experimental Investigations and Analytical Approach. *Buildings* **2023**, *13*, 3004. [CrossRef]
21. Hosseini, A.; Shahnewaz, M.; Zhou, J.; Tannert, T. Structural performance of CLT moment connections in the minor strength axis. *Eng. Struct.* **2025**, *328*, 119788. [CrossRef]
22. Ganjali, H.; Pace, A.; Tannert, T. Structural performance of adhesively bonded and hybrid screw-adhesive CLT panel-to-panel floor joints. *Constr. Build. Mater.* **2025**, *475*, 141139. [CrossRef]
23. Lal, R.; Hashemi, A.; Quenneville, P. An innovative connection system for platform-type mass timber buildings. *Resilient Cities Struct.* **2025**, *4*, 14–29. [CrossRef]
24. Piazza, M. Optimization Process in the Use of Wood and Wood-Based Materials in Hybrid and Composite Structures. In *WCTE 2016 e-Book: Containing all Full Papers Submitted to the World Conference on Timber Engineering (WCTE 2016), Vienna, Austria, 22–25 August 2016*; TU Verlag Wien: Vienna, Austria, 2016.
25. Bajzecerová, V. Bending Stiffness of CLT-Concrete Composite Members—Comparison of Simplified Calculation Methods. *Procedia Eng.* **2017**, *190*, 15–20. [CrossRef]
26. Bajzecerová, V.; Kanócz, J.; Rovňák, M.; Kováč, M. Prestressed CLT-concrete composite panels with adhesive shear connection. *J. Build. Eng.* **2022**, *56*, 104785. [CrossRef]
27. Pang, S.J.; Ahn, K.S.; Jeong, S.M.; Lee, G.C.; Kim, H.S.; Oh, J.K. Prediction of bending performance for a separable CLT-concrete composite slab connected by notch connectors. *J. Build. Eng.* **2022**, *49*, 103900. [CrossRef]
28. Zhao, X.; Zhang, B.; Kilpatrick, T.; Sanderson, I. Numerical Analysis on Global Serviceability Behaviours of Tall CLT Buildings to the Eurocodes and UK National Annexes. *Buildings* **2021**, *11*, 124. [CrossRef]
29. Van de Lindt, J.; Amini, M.O.; Rammer, D.; Line, P.; Pei, S.; Popovski, M. *Determination of Seismic Performance Factors for Cross-Laminated Timber Shear Walls Based on FEMA P695 Methodology*; General Technical Report FPL-GTR-281; U. S. Department of Agriculture, Forest Service, Forest Products Laboratory: Madison, WI, USA, 2023; p. 515.
30. Perković, N.; Skejić, D.; Rajčić, V. Numerical Analysis of Fire Resistance in Cross-Laminated Timber (CLT) Constructions Using CFD: Implications for Structural Integrity and Fire Protection. *Forests* **2024**, *15*, 2046. [CrossRef]
31. Dúbravská, K.; Tereňová, Ľ.; Štefková, J. CLT Construction Performance Under Thermal Loading. *Wood Res.* **2020**, *65*, 605–614. [CrossRef]
32. Xing, Z.; Zhang, J.; Aslani, F. CLT two-way slabs fire resistance test; numerical simulation analysis. *J. Build. Eng.* **2025**, *105*, 112529. [CrossRef]
33. Di Bella, A.; Mitrovic, M. Acoustic Characteristics of Cross-Laminated Timber Systems. *Sustainability* **2020**, *12*, 5612. [CrossRef]
34. Schenk, M.; Ohm, J.; Winter, S. Eurocode5: From Mandate to Second Generation—Review, Insight and Outlook. In Proceedings of the 14th World Conference on Timber Engineering 2025 (WCTE 2025), Brisbane, Australia, 22–26 June 2025; pp. 36–45. [CrossRef]
35. Onishi, S.; Karube, Y.; Nasu, H. Study on Control Wooden Joint Rigidity, Strength and Ductility with Combinations of Wooden Fibre Directions. In *WCTE 2016 e-Book: Containing all Full Papers Submitted to the World Conference on Timber Engineering (WCTE 2016), Vienna, Austria, 22–25 August 2016*; TU Verlag Wien: Vienna, Austria, 2016; Available online: https://repositum.tuwien.at/handle/20.500.12708/172 (accessed on 28 September 2025).

36. Joyce, T.; Ballerini, M.; Smith, I. Mechanical behaviour of in-plane shear connections between CLT wall panels. In Proceedings of the CIB Working Commission W18–Timber Structures. 44th Meeting, Alghero, Italy, 29 August–1 September 2011; Available online: https://www.researchgate.net/publication/267244948 (accessed on 28 September 2025).
37. Hossain, A.; Danzig, I.; Tannert, T. Cross-laminated timber shear connections with double-angled self-tapping screw assemblies. *J. Struct. Eng.* **2016**, *142*, 04016099. [CrossRef]
38. Subhani, M.; Shill, S.K.; Al-Deen, S.; Anwar-Us-Saadat, M.; Ashraf, M. Flexural Performance of Splice Connections in Cross-Laminated Timber. *Buildings* **2022**, *12*, 1124. [CrossRef]
39. Sadeghi, M.; Ballerini, M.; Smith, I.; Pedrotti, E. Bending properties of connections in cross laminated timber. In Proceedings of the IABSE Conference: Elegance in Structures, Nara, Japan, 13–15 May 2015; pp. 366–367. [CrossRef]
40. Asselstine, J.; Lam, F.; Zhang, C. New edge connection technology for cross laminated timber (CLT) floor slabs promoting two-way action. *Eng. Struct.* **2021**, *233*, 111777. [CrossRef]
41. Tlustochowicz, G.; Serrano, E.; Steiger, R. State-of-the-art review on timber connections with glued-in steel rods. *Mater. Struct.* **2011**, *44*, 997–1020. [CrossRef]
42. Ayansola, G.S.; Tannert, T.; Vallee, T. Experimental investigations of glued-in rod connections in CLT. *Constr. Build. Mater.* **2022**, *324*, 126680. [CrossRef]
43. Shirmohammadli, Y.; Hashemi, A.; Masoudnia, R.; Quenneville, P. Experimental and numerical investigation of cross-laminated timber joints with multiple glued-in rods. In Proceedings of the World Conference on Timber Engineering (WCTE 2023), Oslo, Norway, 19–22 June 2023; pp. 1389–1396. [CrossRef]
44. Ayansola, G.S.; Tannert, T.; Vallee, T. Glued-in multiple steel rod connections in cross-laminated timber. *J. Adhes.* **2021**, *98*, 810–826. [CrossRef]
45. Azinović, B.; Danielsson, H.; Serrano, E.; Kramar, M. Glued-in rods in cross laminated timber—Numerical simulations and parametric studies. *Constr. Build. Mater.* **2019**, *212*, 431–441. [CrossRef]
46. *EN 1995-1-1:2004+A2:2014*; Eurocode 5: Design of Timber Structures—Part 1-1: General—Common Rules and Rules for Buildings. European Committee for Standardization, CEN: Brussels, Belgium, 2014.
47. Esmaeildoust, S.; Tomlinson, D.; Chui, Y.H. Performance of Timber-Concrete Composite (TCC) Systems Connected with Inclined Screws: A Literature Review. *J. Compos. Sci.* **2025**, *9*, 13. [CrossRef]
48. Du, H.; Hu, X.; Xie, Z.; Wang, H. Study on shear behavior of inclined cross lag screws for glulam-concrete composite beams. *Constr. Build. Mater.* **2019**, *224*, 132–143. [CrossRef]
49. Li, M. Evaluating rolling shear strength properties of cross-laminated timber by short-span bending tests and modified planar shear tests. *J. Wood Sci.* **2017**, *63*, 331–337. [CrossRef]
50. Li, X.; Ashraf, M.; Subhani, M.; Kremer, P.; Li, H.; Anwar-Us-Saadat, M. Rolling shear properties of cross-laminated timber (CLT) made from Australian Radiata Pine–An experimental study. *Structures* **2021**, *33*, 423–432. [CrossRef]
51. Sandoli, A.; Calderoni, B. The rolling shear influence on the out-of-plane behavior of CLT panels: A comparative analysis. *Buildings* **2020**, *10*, 42. [CrossRef]
52. *STN EN 1995-1-1/NA:2019-12*; National Annex to EN 1995-1-1:2004+A2:2014 Eurocode 5: Design of Timber Structures—Part 1-1: General—Common Rules and Rules for Buildings. ÚNMS SR: Bratislava, Slovakia, 2019.
53. *EN 408:2010+A1:2012*; Timber Structures—Structural Timber and Glued Laminated Timber—Determination of Some Physical and Mechanical Properties. European Committee for Standardization, CEN: Brussels, Belgium, 2012.
54. *EN 26891:1991*; Timber Structures—Joints Made with Mechanical Fasteners—General Principles for the Determination of Strength and Deformation Characteristics. European Committee for Standardization, CEN: Brussels, Belgium, 1991.
55. *EN 16351:2021*; Timber Structures—Cross Laminated Timber—Requirements. European Committee for Standardization: Brussels, Belgium, 2021.
56. Zoetemeijer, P. A Design Method for the Tension Side of Statically Loaded, Bolted Beam-to-Column Connections. *Heron* **1974**, *20*, 1–59. Available online: https://resolver.tudelft.nl/uuid:f2dff8e5-dd92-4a3c-89db-c4fa945ea759 (accessed on 28 September 2025).
57. Steenhuis, M.; Jaspart, J.-P.; Gomes, F.; Leino, T. Application of the Component Method to Steel Joints. In Proceedings of the Control of the Semi-Rigid Behaviour of Civil Engineering Structural Connections, Liège, Belgium, 17–19 September 1998.
58. *EN 1993-1-8*; Eurocode 3—Design of Steel Structures—Part 1-8: Design of Joints. CEN: Brussels, Belgium, 2005.
59. Tao, H.; Mao, M.; Yang, H.; Liu, W. Theoretical and experimental behaviour of a hybrid semi-rigid glulam beam-to-column connection with top and seat angles. *Adv. Struct. Eng.* **2020**, *23*, 891–904. [CrossRef]
60. Yang, H.; Liu, W.; Ren, X. A Component Method for Moment-Resistant Glulam Beam–Column Connections with Glued-in Steel Rods. *Eng. Struct.* **2016**, *115*, 42–54. [CrossRef]
61. Buchholz, L.; Kuhlmann, U.; Knobloch, M. Design of Timber Structures in View of Sustainability Based on the Component Method. In Proceedings of the 14th World Conference on Timber Engineering 2025 (WCTE 2025), Brisbane, Australia, 22–26 June 2025. [CrossRef]
62. Hunger, F.; Stepinac, M.; Rajčić, V.; van de Kuilen, J.-W.G. Pull-Compression Tests on Glued-In Metric Thread Rods Parallel to Grain in Glulam and Laminated Veneer Lumber of Different Timber Species. *Eur. J. Wood Wood Prod.* **2016**, *74*, 379–391. [CrossRef]

63. Oh, J.; Ahn, K.-S.; Lee, G.R.; Kim, M.-J.; You, S.-H.; Pang, S.-J.; Kim, C.-K.; Kim, K.-H.; Oh, J.-K. Theoretical Modeling of Pull-Out Stiffness of Glued-In Single Rod in Timber. *Eng. Struct.* **2025**, *325*, 119346. [CrossRef]
64. Totsuka, M.; Jockwer, R.; Aoki, K.; Inayama, M. Experimental study on partial compression parallel to grain of solid timber. *J. Wood Sci.* **2021**, *67*, 39. [CrossRef]
65. Totsuka, M.; Jockwer, R.; Kawahara, H.; Aoki, K.; Inayama, M. Experimental study of compressive properties parallel to grain of glulam. *J. Wood Sci.* **2022**, *68*, 33. [CrossRef]
66. Flaig, M.; Schmidt, T.; Blas, H.J. Compressive strength and stiffness of end-grain contact joints in glulam and CLT. In Proceedings of the International Network on Timber Engineering Research (INTER), Meeting 52, Tacoma, WA, USA, 26–29 August 2019; pp. 313–325; ISSN 2199-9740.

MDPI AG
Grosspeteranlage 5
4052 Basel
Switzerland
Tel.: +41 61 683 77 34

Buildings Editorial Office
E-mail: buildings@mdpi.com
www.mdpi.com/journal/buildings

Academic Open
Access Publishing

mdpi.com

ISBN 978-3-7258-5928-3